Diplomarbeit

Differential emission measures and elemental abundances of stellar coronae

vorgelegt von
Carolin Liefke

Hamburger Sternwarte
Universität Hamburg

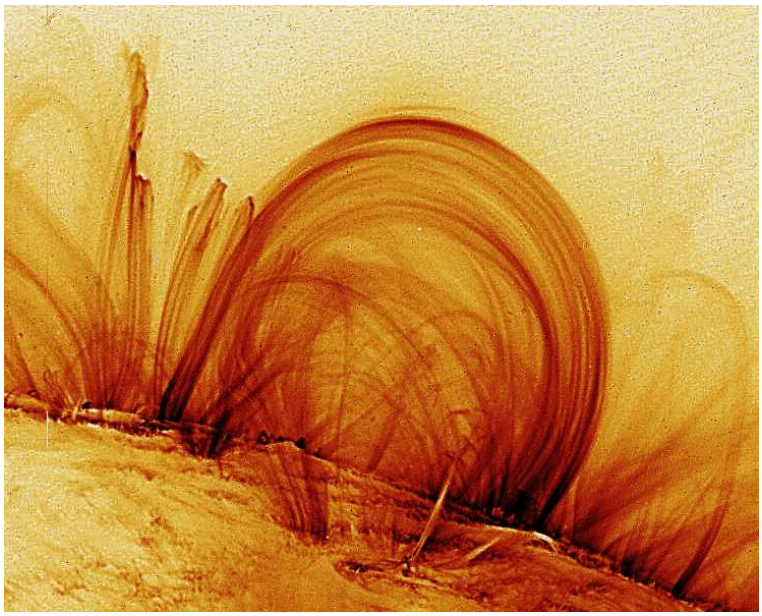

Hamburg
Oktober 2005

Titlepage: An image of coronal loops over the eastern solar limb obtained with the *TRACE* satellite on 6 November 1999 at 2:30 UT in the 171 Å bandpass that includes prominent emission lines of Fe IX and Fe X, corresponding to a characteristic plasma temperature of about 1×10^6 K. Image taken from `http://vestige.lmsal.com/TRACE/POD/TRACEpodarchive.html`

Zusammenfassung

Wasserstoff ist das häufigste Element im Universum. In der uns vertrauten baryonischen Materie macht es einen Massenanteil von etwa 73% aus, gefolgt von Helium mit etwa 25%. Alle weiteren Elemente müssen sich die restlichen 2% teilen, die häufigsten unter ihnen sind wiederum Kohlenstoff, Stickstoff, Sauerstoff und Eisen.

Nicht nur für uns Menschen und das Leben auf der Erde sind aber genau diese Spurenelemente von essentieller Bedeutung. Sie haben auch einen erheblichen Einfluß auf die physikalischen Eigenschaften der Sterne, besonders auf die in ihnen stattfindenden radiativen Prozesse. Bemerkbar machen sich die Metalle dann wieder in den beobachteten Spektren, wo sie ihre Spuren in Form von Absorptions- oder Emissionslinien hinterlassen. Dementsprechend ist es möglich mithilfe dieser Linien die genauen Häufigkeiten der einzelnen Elemente zu rekonstruieren.

Eine solche Elementhäufigkeitsanalyse ist allerdings nicht trivial, sie erfordert die genaue Kenntnis der physikalischen Prozesse, die an der Entstehung der Spektrallinien beteiligt sind, sowie die Bedingungen unter denen sie entstehen. In der Korona, der äußersten Atmosphärenschicht eines sonnenähnlichen Sterns, werden Temperaturen von mehreren Million Kelvin bei gleichzeitig relativ geringen Dichten erreicht. Das Spektrum der Korona ist vorrangig im Röntgenbereich beobachtbar, es ist dominiert von Emissionslinien der schwereren Elemente. Hochauflösende Röntgenspektroskopie mit Hilfe der Satelliten *Chandra* und *XMM-Newton* hat in den letzten Jahren die Untersuchung der Spektren stellarer Koronen in bislang unerreichter Genauigkeit ermöglicht.

Zur Modellierung des Koronaspektrums werden Informationen wie Temperatur, Dichte oder Druck über das koronale Plasma, das diese Linien aussendet, benötigt. Diese Parameter lassen sich allerdings nicht direkt beobachten und werden durch das differentielle Emissionsmaß DEM zusammengefaßt. Es verknüpft den gemessenen Fluß in einer Linie direkt mit der Elementhäufigkeit und den atomaren Daten, die die Linie charakterisieren.

Es gilt daher, zunächst das differentielle Emissionsmaß unabhängig von den Häufigkeiten der Elemente zu bestimmen. In dieser Arbeit wurden zwei entsprechende Methoden angewandt, bei denen das differentielle Emissionsmaß mithilfe von häufigkeitsunabhängigen Verhältnissen von Linien jeweils desselben Elementes bzw. ausschließlich mit Eisenlinien über Polynome verschiedener Ordnungen angenähert wird. Im Anschluß wurden mit diesem differentiellen Emissionsmaß die gemessenen Linienflüsse der zugrundeliegenden Linien synthetisiert und somit die entsprechenden koronalen Elementhäufigkeiten bestimmt.

Diese Methode wurde auf mehrere Datensätze verschiedener Sterne angewandt. Vergleiche des jeweils ermittelten differentiellen Emissionsmaßes und der daraus resultierenden Elementhäufigkeiten mit entsprechenden Daten aus der Literatur zeigen eine gute Übereinstimmung.

Abstract

Hydrogen is not only the simplest and lightest but also by far the most frequent element in the universe. In the baryonic matter we are familiar with it amounts to a mass fraction of about 73%, followed by helium with approximately 25%. The remaining elements, summarized by astrophysicists as "metals", have to share the residual 2%. From these, the most abundant are carbon, nitrogen, oxygen and iron.

These trace elements are not only of vital importance for life on earth, they also have a serious influence of the physical properties of stars, especially on radiative processes running inside. The metals become later visible in observed spectra, where they leave their marks as absorption or emission lines. It is thus possible to reconstruct the precise abundances of the indivual elements from these lines.

Such an analysis of the elemental abundances is nontrivial though, a detailed knowledge of the physical processes and underlying conditions determining the formation of the spectral lines is required. Hence it is not surprising that in recent years even for the Sun, which can be considered as well-known and comparatively easy to study, on occasion revised numbers – sometimes noticeably deviating from the previous ones – for the abundances of individual elements have been released. A corresponding analysis of stars other than the Sun is much more difficult, there is however clear evidence that their abundances only seldom correspond to the solar values.

In the corona, the outermost atmospheric layer of a solar-like star, temperatures of several million Kelvin and comparatively low densities are reached. The coronal spectrum is primarily observable in X-rays, it is dominated by emission lines of the heavier elements. High-resolution X-ray spectroscopy with the *Chandra* and *XMM-Newton* satellites presently enables the analysis of stellar coronae with unrivaled accuracy.

Parameters like temperature, density or pressure of the coronal plasma emitting these emission lines determine the modeling of a coronal spectrum, they are however not directly observable. Instead, they were combined to the soo-called differential emission measure DEM, that connects measured line fluxes directly with the elemental abundance and the atomic data characterizing the line emissivity.

The differential emission measure has thus to be determined independently of the abundances. In this study I applied two methods that approximate the DEM with polynomials of different orders. One approach makes use of abundance-independent line ratios of lines originating from the same element, the other makes use solely of iron lines. Subsequently, the measured line fluxes are reproduced with the underlying DEM and thus the coronal elemental abundances are determined.

This method was applied to several datasets of different stars. A comparison of the differential emission measure and the resulting abundances with corresponding data from the literature shows a good agreement.

Contents

1 Introduction

1.1 The corona of the Sun

The Sun has been observed from time immemorial. Many ancient cultures were aware of its importance for life on earth; the life of the people was centered on the daily recurrence of the Sun and the cycle of seasons. The Sun therefore embodied a divine power and was regarded with awe. Even in Christian Europe up to the end of the middle ages it was a symbol for the perfection of creation and had to be unblemished and unchanging. Thus early observations of sunspots being visible with the naked eye at sunrise or sunset perished or were forgotten.

The invention of the telescope early in the 17th century led, among other things, to definite observations of sunspots. Many scientists of that time, e.g. Galileo Galilei, saw the dark spots in front of the solar disc, but there was disagreement about the nature of this phenomenon. Was it perhaps an illusion, feigned by the telescope? While Galilei was already convinced that the spots were structures on the solar surface, the Jesuit Christoph Scheiner at first thought to see shadows of a planet by then unknown to pass by the Sun. Systematic observations disenchanted the divine and unblemished face of the Sun: The coming and going of the sunspots, their evolution in size and shape, and the changing frequency of their occurrence resulted in momentous conclusions. The Sun had to be rotating for instance to explain these observations. The German pharmacist Heinrich Schwabe deduced in 1843 the 11-year solar cycle from long-term monitoring (Schwabe, 1844). Between Schwabe's observations and the ones of Galilei occurred a period, approximately between 1645 and 1715, where only very few sunspots could be observed. This so-called Maunder Minimum is today associated with a global cold spell ("little ice age"). The changing activity of the Sun on all timescales preoccupies scientists to this day. The term "activity" comprises in this context not only the occurrence of sunspots, but summarizes anything indicating that the Sun is "alive", and not just quiescently shining for eternity.

Other phenomena in connection with the Sun puzzled the astronomers for a long time as well. They wondered for instance whether the corona and prominences visible during total solar eclipses had actually to be assigned to the Sun itself; or whether they were phenomena of the earth's atmosphere, artifacts, or even an atmosphere of the moon that scatters the light of the occulted Sun towards the earth. The new technique of photography helped to exclude the latter possibilities and to assign corona and prominences to the Sun. Admittedly, both of them do not belong anymore to the visible "surface" of the Sun, the so-called photosphere (from Greek *phōs, phōtós*: "light"). Almost the whole visible solar irradiation comes from the photosphere. This layer of the Sun has a thickness of only a few hundreds of kilometers, but all lower-lying layers are not accessible to direct observations because the radiation can not leave them directly. The sunspots are phenomena of the photosphere, but prominences belong to a layer above, the chromosphere (from Greek *chrōma*: "color"). The chromosphere is – without any additional means – only visible at total solar eclipses, where it shows up as small, reddish flame-like structures ("spicules") covering the whole solar limb. The same applies for the weak, white-shimmering corona, that lies again above the chromosphere.

The breakthrough in the identification of the nature of chromosphere and corona came with the application of spectroscopic methods. Moreover it is safe to say that spectroscopy changed the previously phenomenological and observational astronomy to astrophysics. William Wollaston discovered in 1802 that few dark lines divide the colors in the solar photospheric spectrum.

12 years later Josef von Fraunhofer cataloged several hundreds of these absorption lines. The correct identification of Fraunhofer's lines and their assignment to certain elements was enabled by the foundation of spectral analysis by Gustav Kirchhoff and Robert Bunsen in 1859.

First spectroscopic measurements during a solar eclipse were performed in 1868. Norman Lockyer and Pierre Janssen observed for the first time the emission line spectrum of prominences and discovered a bright yellow line whose wavelength did not exactly fit the sodium D line; and it could not be assigned to any other element known at that time. Lockyer proposed the discovery of a new element and called it "helium" (after the Greek sun deity Helios), since it apparently only existed on the Sun. Not until 1895 helium was found on earth, in laboratory experiments with pitchblende, a uranium ore. In the following years Janssen was able to measure Fraunhofer's absorption lines also in the faint continuous spectrum of the corona, an explicit verification of the solar nature of the corona. In 1870 Charles Young noticed that most of the emission lines observed in the spectra of prominences and in the so-called flash spectrum of the chromosphere appear in the photospheric spectrum as dark absorption lines. In the year before though, he had found a green emission line in the spectrum of the corona this finding did not apply to. This green coronal line, among others discovered later, puzzled the spectroscopists the same way as the helium line. They tried to solve the problem also the same way: The new-postulated element got the name "coronium"; and after the discovery of helium on earth the scientists anticipated also the detection of the ominous coronium very soon.

It was not until 1939 that the search for the origin of the coronal emission lines ought to be crowned with success. The elements responsible for them proved indeed to be well known: mainly iron, but also calcium and nickel. The reason why the spectroscopists had not been able to assign the lines to these elements earlier was that they belonged to forbidden transitions in highly ionized states of these elements that were not observable in the laboratory. Inspired by the detailed and elaborated measurements of highly ionized iron by the spectroscopist Bengt Edlén, Walter Grotian derived a very improbable but existent transition in ninefold ionized iron (Fe X) that could explain the red coronal line at a wavelength of 6374 Å (Grotian, 1939). Correspondingly he was able to identify another line, and Edlén himself determined with the same method the appropriate element for many other coronal lines. In this manner the green coronal line at 5303 Å of coronium was eventually assigned to Fe XIV, thus thirteen times ionized iron (Edlén, 1943).

A big amount of energy – thus a very high temperature – is needed to wrest 13 of the 26 electrons of an iron atom: More than one million degrees is the coronal gas required to have. Since the temperature of the photosphere does not exceed 5800 K, the temperature of the outer layers of the Sun must steeply increase again outward. Such a rise of the temperature was completely unexplainable at that time, and even today the mechanisms that heat chromosphere and corona are not understood in detail and are a matter of research and debate.

Hints for extremely high temperatures in the corona have indeed been noted before. Only very high particle velocities – caused by high temperatures – can explain why the coronal gas – contrary to gravitation – is located that far away from the surface of the Sun: On photos of total eclipses the corona appears to be extended to several solar radii. Even with the naked eye the corona seems to have an elongation of about half of the solar radius.

The spectral energy distribution of the coronal light following Planck's law suggested significantly lower temperatures. This is due to the fact that the coronal light consists for the most part of scattered light coming originally from the photosphere. The visible light observed from the solar corona is composed of several components: There is the so-called F-corona (named after the Fraunhofer lines) whose spectrum shows the typical absorption lines of the photosphere. The F-corona is effectively photospheric light, scattered by dust particles in the ecliptic plane. These dust particles also add their own thermal radiation to the coronal light, this so-called T-corona shows up mainly in the infrared. The K-corona (from German *kontinuierlich*) exhibits

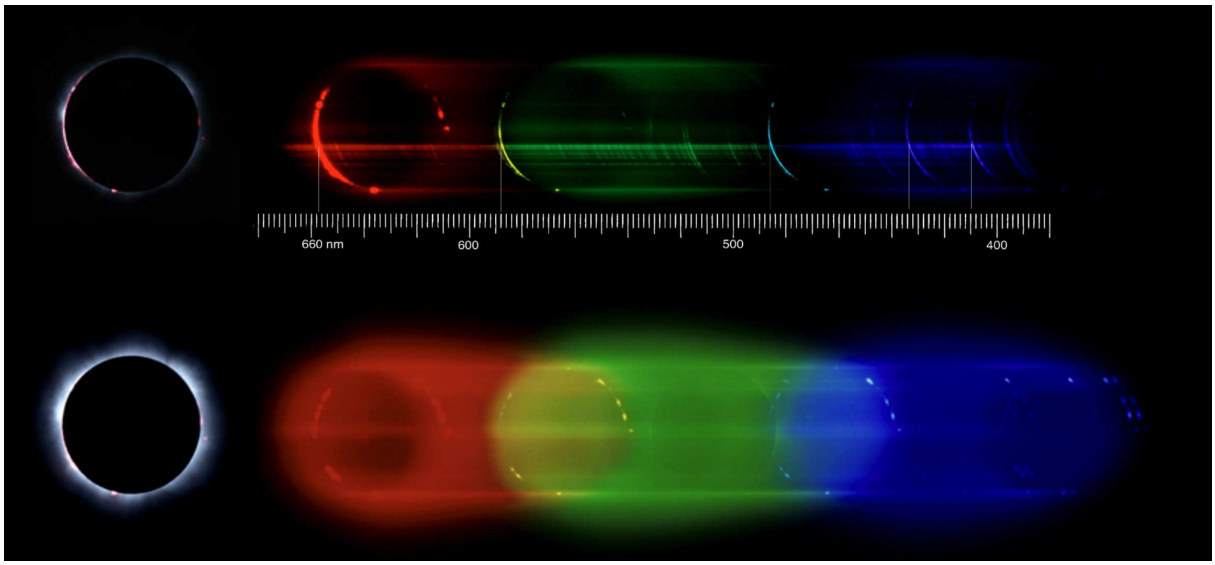

Figure 1.1: Slitless spectrum of the solar chromosphere (top) and corona (bottom) recorded during the eclipse of 11 August 1999. The coronal Fe XIV line at 5303 Å can be distinguished from the lower-temperature hydrogen, helium and calcium lines by the absence of images of the prominences that have a considerably lower temperature than the corona. Pictures taken from `http://www.eurastro.de/webpages/MRSPECT.HTM`

a continuous spectrum without any lines. Again this is scattered light, this time by the particles of the coronal plasma, mostly electrons. Since they move very fast because of the high temperatures in the corona, the absorption lines of the scattered light blur by the effect of Doppler broadening. The only component whose light actually comes directly from the corona itself is the E-corona that shows those emission lines of highly ionized atoms mentioned before.

As a result of the high temperatures the corona radiates essentially in the extreme ultraviolet and in soft X-rays, but the marginal transmission of the earth's atmosphere in this spectral region rules out observations from ground level. Although ground-based observations of the corona in visible light are possible – for instance with narrowband filters centered on the wavelength of one of the coronal lines or with coronagraphs that generate artificial eclipses by covering the solar disk – substantial progress in the investigation of coronal physics started therefore with space flight. Already at test flights with V2 rockets equipped with X-ray detectors in 1949, the Sun – more precisely the corona of the Sun – was detected as an X-ray source. Anyway, it was a long road from the simple verification to detailed analysis with imaging X-ray telescopes and corresponding spectroscopic devices. It was not until the early seventies that the first imaging instruments flew with balloon experiments and sounding rockets, after a decade of successfull monitoring of the solar radiation from UV to Gamma rays by satellites with plain detectors.

X-ray and UV images display a completely different view of the Sun: Chromosphere and corona prove to be much more structured than the photosphere. The dark sunspots seen in visible light become X-ray-bright "active regions", consisting of complex structures of arches ("loops") that can arise several thousands of kilometers above the surface. (See for instance the picture on the title page.) The loop-like structures of the corona were found to follow the uttermost complex solar magnetic field (see Section 2.1). Furthermore, there are the so-called coronal holes – widely extended regions that appear X-ray dark.

In May 1973 the space station *Skylab* was inserted into orbit, equipped with several experiments for analyzing chromosphere and corona, amongst others a coronagraph, an X-ray telescope and spectrographs for the near and far UV and the X-ray spectral range. These in-

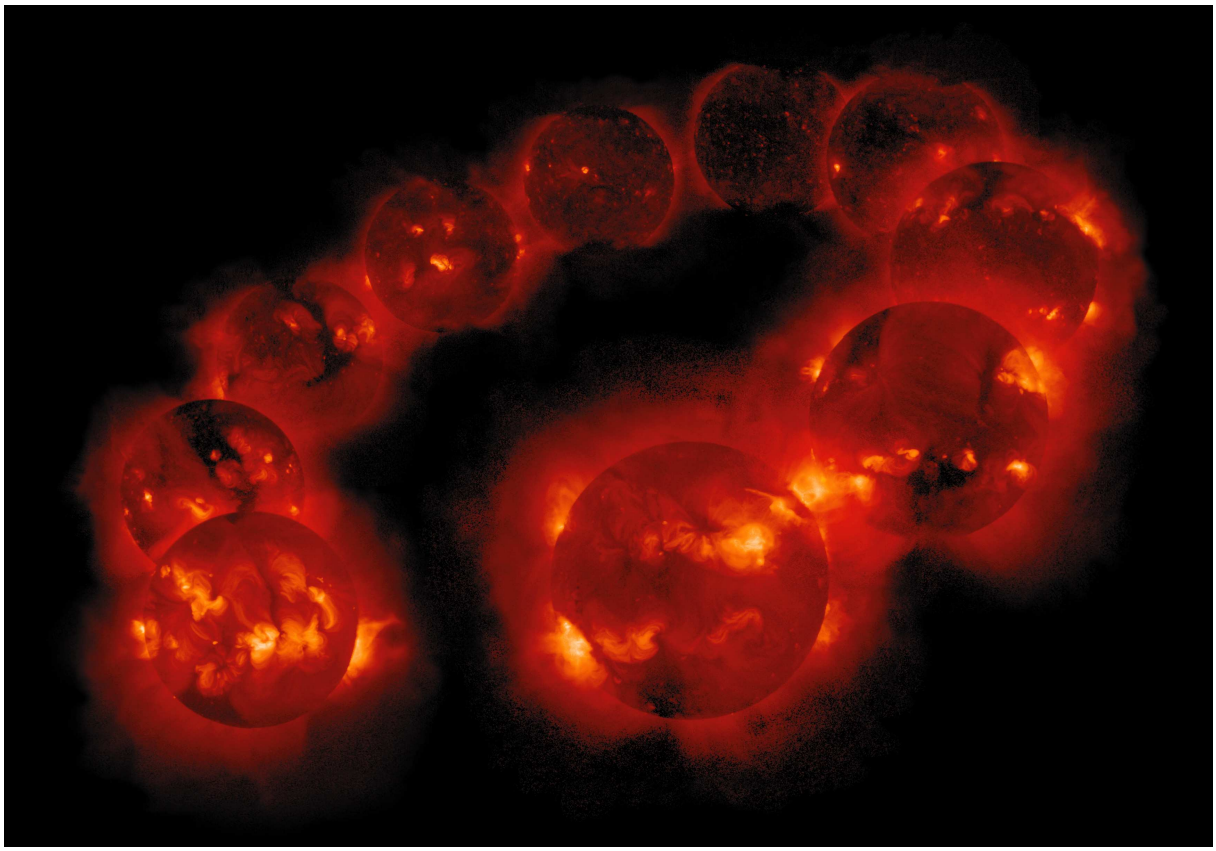

Figure 1.2: A sequence of ten X-ray images of the solar corona from 1991 to 1999, obtained with the Soft X-ray Telescope (SXT) on board the *Yohkoh* satellite. The images, covering almost an entire solar activity cycle, show how the corona changes over the years. From the solar maximum in 1990 to solar minimum in 1995 the brightness in X-rays changes by a factor of 100. Image taken from `http://solar.physics.montana.edu/sxt/`

struments collected data during the nine months of the mission.These data allowed monitoring of the time-dependent evolution of coronal holes and active regions. Outbursts in brightness, so-called flares, that occur quite often in the high-energy spectral region, could be traced. The analysis of the huge amount of data from *Skylab* resulted in a plethora of new insights not only about the corona itself and the solar magnetic field but also about their influence on the earth: Just the coronal holes turned out to be the sources of a steady stream of solar particles, the so-called solar wind, which react with the earth's magnetic field. This leads not only to aurorae, but during periods of increased solar activity interferences in the communication network, radio transmissions or the power supply system may also occur.

In the following a series of satellites was designed to explore the Sun and its outer layers. In contrast to the former mainly spectroscopic missions such as *SMM* and *Hinotori*, the *Yohkoh* ("sunbeam" in English) satellite launched in August 1990 provided again impressive images of the solar corona.*Yohkoh* observed the solar corona for more than ten years, during a complete solar cycle, and was therefore able to track changes in the coronal structure over long timescales. Actually the eleven-year cycle appears even more pronounced in X-rays, the contrast between the bright active regions and loop-like structures at solar maximum and the large-area coronal holes covering nearly the complete solar surface at minimum is eye-catching.

In December 1995 the *Solar and Heliospheric Observatory* (*SOHO*) was launched, equipped with a variety of instruments, amongst others a coronagraph, an imaging XUV telescope and several spectrometers as well as experiments to analyze the solar wind and for helioseismology,

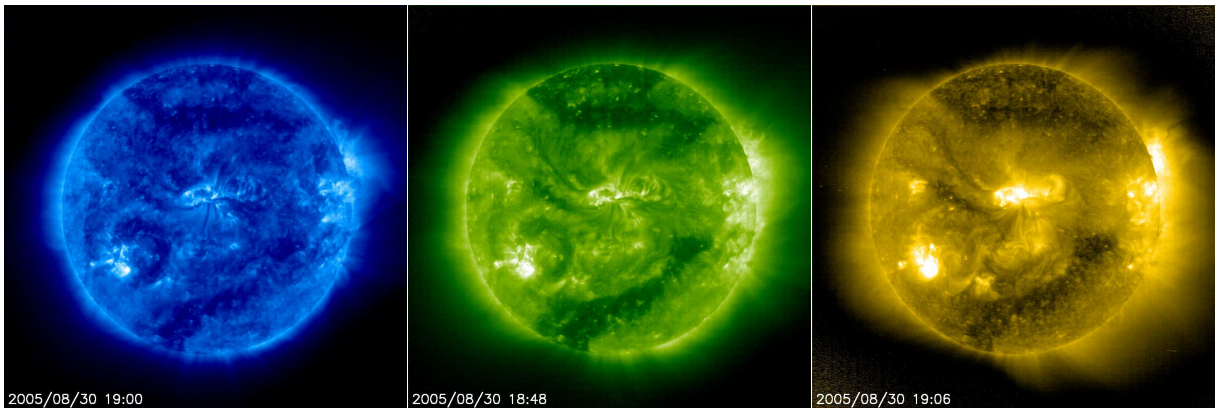

Figure 1.3: Three images of the solar corona in different passbands obtained on 30 August 2005 at intervals of a few minutes with the Extreme ultraviolet Imaging Telescope EIT on board *SOHO*. The sequence corresponds to a temperature series in ascending order from left to right: The left image, taken at a wavelength of 171 Å corresponding to temperatures of ≈1 MK, shows best the fine structure of loops and other features. In the central image, at 195 Å and 2 MK, coronal holes emerge. The active regions appear brightest in the right image (284 Å, 2.5 MK) indicating even higher temperatures. Images taken from `http://sohowww.nascom.nasa.gov/data/realtime-images.html`

a technique which gains information about the solar interior by the analysis of surface waves. The *Transition Region And Coronal Explorer* (*TRACE*) observes the Sun with a small XUV telescope similar to the *SOHO* instrument EIT in multiple narrowband filters centered around strong spectral lines like Fe IX at 171 Å, Fe XII at 195 Å, Fe XV at 284 Å, the hydrogen Lyman α line at 1216 Å or C IV at 1550 Å, or in unfiltered white light in high temporal and spatial resolution. Emission at these wavelengths is associated with certain plasma temperatures in the solar corona – the very temperatures where the mentioned ions form and the associated atomic transitions occur. In the named sequence they correspond to approximately 1 000 000 K, 2 000 000 K, 2 500 000 K, 30 000 K and 100 000 K. The images of *TRACE* and *SOHO* show thus not only the topology but also the temperature structure of chromosphere and corona.

A detailed account of the history of solar observations in general is given in '*The sun. A biography.*' by Whitehouse, and solar coronal observations are treated in more detail in '*The Solar Corona*' by Golub and Pasachoff.

1.2 Coronae of other stars

The Sun is a rather ordinary star. Rated as G2 V in the common spectral classification scheme of the Hertzsprung-Russel diagram, it turns out to be a middle-aged low-mass star – meanwhile one of many with planets. So what about other stars? Do they also have coronae which could be detected in X-rays?

In 1974 the binary star Capella was identified as the first stellar coronal X-ray source – with an X-ray luminosity orders of magnitude higher than the Sun (Catura et al., 1975). Indeed the Sun turned out to be a rather moderate X-ray source in comparison to most of the other stars detected later. Early surveys with the *Einstein* satellite from 1978-81 found stars of almost every spectral type and luminosity class to emit X-rays (Vaiana et al., 1981). The optically faint M-dwarfs turned out to be very active stars, with frequently occurring flares and strong X-ray variability. Moderate to high X-ray emission and therefore stellar coronae seemed to be a common phenomenon among solar-like stars. Main-sequence stars in general emerged to be good

candidates for X-ray emission, with the exception of late A- and early B-type stars, suggesting the absence of coronae for these classes. Furthermore the observed X-ray emission of O- and early B-type stars is assumed to be caused by shocks in stellar winds and not to be of coronal origin. The strongest X-ray emitters were found among the peculiar RS CVn systems – Capella being one of them – very active evolved binary systems, typically consisting of G- or K-type components that are detached but close by. Only a few normal giants are found to show X-ray emission.

Systematic studies of complete samples of nearby stars performed with *ROSAT* in the nineties showed that stellar coronal X-ray emission is ubiquitous among late-type stars (Schmitt (1997), Schmitt and Liefke (2004)), with the minimum X-ray surface flux detected corresponding to the flux level observed in solar coronal holes. The range covered in surface flux however extends to three orders of magnitude beyond. The Sun thus represents just one data point at the lower end of a broad distribution. So how do the coronae of other stars compare to the Sun – and how do they differ and why?

Unfortunately stars other than the Sun cannot directly be observed with spatial resolution – neither in the optical nor in X-rays. Images like Figures 1.2 and 1.3 or even the cover picture are thus unavailable for stars, so alternative ways have to be adopted to gain information about stellar coronae – to ascertain their physical parameters like extent, temperature, density or elemental abundances. Spectroscopic methods – that proved to be very useful in many fields of astronomy – suggest themself. For the Sun high-resolution UV and X-ray spectra that resolved individual emission lines have been available for decades, the instruments to obtain them have been developed even before high-resolution X-ray imaging techniques existed.

Pottasch (1963) introduced the concept of emission measure as a link between the flux observed for these lines and a conceptual model of the emitting plasma. The expression "emission measure", in short EM, characterizes – in simple terms – the amount of material available to produce the measured flux, and is mathematically the product of the square of the electron density integrated over the volume of emission. Apart from elemental abundances of the plasma the other parameters entering the model calculations – excitation and transition probabilities of the atomic transition underlying the particular emission lines – arise from atomic physics.

Gabriel and Jordan (1969) devised a method to infer the density of the solar coronal plasma – the basis of the emission measure – from line ratios of the forbidden lines of helium-like ions. The measurement of line fluxes of single emission lines in the solar coronal spectrum thus enabled indirect determinations of parameters like density, temperature or pressure.

The spectrometers of *Einstein*, the CCD detectors of *ASCA*, and the proportional counters *Einstein*, *ASCA* and *ROSAT* had on board allowed spectroscopy of stellar coronal sources only with low to medium resolution, without the ability to resolve single emission lines. Nevertheless already the thus obtained spectra gave first hints to the properties of the coronal plasma from the investigated stars: Model spectra composed of a vast number of lines can be convolved with the instrumental response and spectral resolution to fit the observed spectra.

Spectral models containing the atomic physics of huge databases of lines are based on an isothermal temperature and a set of elemental abundances. An isothermal temperature is of course a very rough approximation of the actual temperature structure of stellar coronae. A temperature distribution can be approximated by a model consisting of multiple temperature components. The different emission measure values of the single components as represented by respective normalization factors thus give an idea of the temperature structure of the coronal plasma, i.e. the amount of plasma at a certain temperature.

Such "global fits" to the low-resolution spectra of stellar coronal X-ray sources usually contained two or three temperature components; and often temperatures essentially higher than those found in the solar corona or strongly deviating abundances were found to match the data well. Nevertheless, multi-component isothermal models are still an oversimplification of the ac-

tual temperature structure of the coronal plasma. The large uncertainties (arising from both the atomic physics and the quality of the data) and ambiguities (spectral inversion problems are not unique) of these models must be considered as well, so that only rough ideas of the "real" coronae could be devised.

Scaling laws applying to the coronal structures on the Sun allowed the assessment of filling factors and loop lengths also for stars from the values of pressure and temperature derived from the spectral models, assuming the stellar coronae being of similar structure than that of the Sun (Rosner et al., 1978).

The idea of emission measure has been enhanced a lot in the following. Emission measure distributions binned in small temperature intervals provide a more refined temperature structure. This culminates in the application of a differential form of the emission measure in terms of temperature, the "differential emission measure" or DEM. The reconstruction the differential emission measure is an inversion problem even more complex than simple emission measure reconstruction, and is subject to similar mathematical constraints. Reasonable DEM reconstruction requires on the one hand measurements of individual line fluxes and therefore high-resolution spectroscopy and on the other hand detailed and reliable knowledge of the underlying atomic data.

The abundances of the elements that generate the lines serving as input are important parameters entering the calculations. The solar coronal abundances were very early found to deviate strongly from the corresponding photospheric ones, and to scatter over a wide range depending on whether active or quiescent regions of the corona were observed. The general result is that elements with a low first ionization potential (i.e. the energy needed to ionize the neutral atom once) or in short FIP, are overabundant in comparison with those with a high FIP. The separation between low and high FIP is around 10 eV and thus, for example, Fe, Mg and Si are considered low-FIP elements and Ne and Ar are considered high-FIP elements. This abundance anomaly pattern is generally referred to as the "FIP Effect".

Abundances derived from low-resolution spectra of stellar coronae were often inconsistent with both the solar coronal and photospheric abundances. Of course there is no need that they match, since stellar photospheric abundances in many cases deviate also from the solar ones. Moreover stellar photospheric abundances as a reference are hard to measure as well, mostly even harder than those of the corona.

With the current X-ray observatories *XMM-Newton* and *Chandra* the high-resolution spectra required for DEM reconstructions with the methods originally developed for the analysis of the Sun described above and more reliable abundance determinations are now available for stars as well, where investigations involving spatially resolved imaging are still a distant prospect. The topic of stellar coronal research with recent results from *XMM* and *Chandra* were reviewed by Güdel (2004) and Favata and Micela (2003).

In the course of this study I developed and refined two different line-based methods to derive the differential emission measure distribution independently from the abundances, and to deduce these abundances afterwards from the calculated DEM. I applied these methods to the four stars AB Dor, Algol, AU Mic and UX Ari that represent different types of coronal X-ray sources. The basic physics of stellar coronal plasmas and a derivation of the equations needed for emission measure analysis are sketched in Chapter 2. Chapter 3 briefly describes the two X-ray observatories *Chandra* and *XMM-Newton* with which the spectra were obtained this work is based on. My approach on reconstructing the differential emission measure and abundances is explained in detail in Chapter 4, while Chapter 5 presents general results. I also note constraints and limitations as well as feasible future improvements. Chapter 6 gives the detailed results for the individual stars. The appendix contains the source code of the method as implemented in IDL.

2 The physics of stellar coronae

What do we learn from the analysis of the coronae of other stars? Studies like the "Sun in time" project (e.g., Güdel et al. (1997), Ribas et al. (2005), Telleschi et al. (2005)) examined solar-like stars of different ages and arrived at the conclusion that the Sun was much more active in its youth – which must have had serious influence on the conditions in our planetary system at that time. Investigations of stellar coronae therefore provide the opportunity to learn more about the solar corona – and vice versa.

Coronal physics is the subject of intensive current research. There are still several basic aspects of both solar and stellar coronae that are not fully understood. This applies for instance to the details of the heating mechanisms that generate the high temperatures measured in coronal plasmas (Section 2.1). Knowledge of the prevailing conditions for the heating process expressed in physical parameters like pressure, temperature or density is required to develop a self-consistent model of the corona. Emission measure analysis is a tool of fundamental importance to deduce this information from observational data. High-resolution spectroscopy in turn provides the best possible spectra serving as input for the reconstruction of the emission measure (Section 2.2). Another issue is the anomalous coronal abundance pattern of the Sun mentioned above, and – in this context – the abundance patterns of other stars again deviating therefrom (Section 2.3). Again, high-resolution spectroscopy allows detailed studies of abundances measured for individual stars and therefore the comparison of stars of different luminosity, age, and so on; or abundance variations seen during flares.

2.1 Magnetic fields and coronal heating

In the cores of solar-like stars temperatures up to several millions of Kelvin are reached. Thermonuclear reactions convert hydrogen to helium and produce the energy that keeps the star in a state of equilibrium. The high-energy photons released in these fusion reactions travel through the layers sourrounding the core and eventually reach the surface, where they escape softened to mainly visible light. In the radiative zone surrounding the core the material is hot and dense enough that thermal radiation is sufficient to transfer the energy produced in the core outward. In the successive convection zone this mechanism is not efficient, instead the temperature gradient outwards is strong enough to drive convective motions. Packages of hot material (convective cells) ascend to the surface where they cool off and subsequently plunge back downward to the base of the convection zone where they heat up again; and the circuit starts over. At the photosphere the temperatures have cooled down to several thousands of Kelvin, according to the spectral type of the star.

A central question is therefore what mechanisms heat the corona back to temperatures of several million degrees and enables the emission of X-rays. Compared to the bolometric luminosity over all wavelengths – released mainly from the photosphere – the coronal X-ray emission comprises a thousandth part at maximum. Only a small portion of the overall produced energy is therefore needed to heat the corona.

A star is an accumulation of plasma – ionized gas consisting of charged particles – that rotates not as a solid body but differentially, i.e. at the surface the higher latitudes rotate slower than the equator as it can be observed on the Sun. In addition to this latitudinal rotational pattern, helioseismology has revealed that the rotation period of the Sun also changes radially, again with

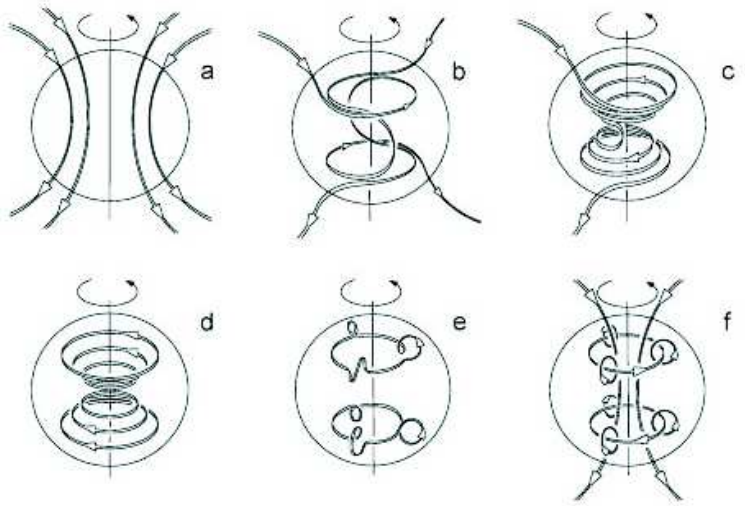

Figure 2.1: The α-ω-dynamo cycle. (a) The initial poloidal field. (b) and (c) Differential rotation wraps the magnetic field around the rotational axis, the ω-effect. (d) A toroidal field emerges. (e) Convective motions lift the field lines up, the Coriolis force twists them so that they experience a magnetic buoyancy, the α-effect. (f) The thus created loops coalesce to the original poloidal field. Figure taken from Love (1999).

different latitudinal patterns. Now magnetic fields come into play since moving charged particles display a current that generates magnetic fields. Changing magnetic fields in turn induce electric fields that govern the motion of charge. The interaction of convective motion and the differential rotation with magnetic fields therefore enables dynamo processes that amplify existing magnetic fields. The fundamental ideas of coronal heating are based on the α-ω-dynamo model, but a complete and self-consistent dynamo theory is still to be developed.

Magnetic fields are – in the approximation of ideal magnetohydrodynamics – embedded ("frozen") in the material, they participate in the motions of the plasma. An initially poloidal field (i.e. oriented parallel to the rotation axis) is stretched and eventually wrapped up by differential rotation because the rotation period further inside is shorter than further outside. Thus a toroidal field (i.e. of helical, annular shape) with increased field strength is generated, this is called the "ω-effect". The convective motions take the field lines along on their way upwards, and eventually the Coriolis force makes the plasma perform a spiral motion that twists the field lines. This results in a poloidal field with reversed polarity, and is called the "α-effect". Together both effects constitute the α-ω-dynamo. See Figure 2.1 for an illustration.

The twisted magnetic fields experience a buoyancy force that lets them frequently "break" trough the surface. The coronal plasma follows the irregularly shaped structure of these magnetic field lines, forming loops and arches as those displayed on the titlepage. At the location of footpoints of these loops the sunspots can be found, marking the positions where the field lines emerge and re-enter the photosphere. Thus arises the connection of visible phenomena on the Sun like sunspots or prominences (cool material caught in flux tubes above the photosphere) with the solar magnetic field.

The scenario of the α-ω-dynamo with its alternating polarity offers an approach to explain the solar cycle which is actually a 22-year cycle of twice the 11-year sunspot cycle but with exchanged polarity of the solar magnetic fields. Also the solar X-ray emission reflects this global change (see Figure 1.2): As the sunspot cycle progresses from maximum to minimum, the Sun's magnetic field changes from a complex structure (the twisted toroidal field) to a simpler configuration

(essentially the poloidal field) with fewer field lines penetrating through the surface that form the X-ray bright active regions.

These active regions are the places of origin of flares. These eruptive processes, leading to high levels of radiation over broad wavelength ranges appear in X-rays usually as a steep rise in luminosity accompanied by spectral hardening. An exponential decay phase follows. The standard model devised for solar flare events (the "two-ribbon flare") starts with motions of the footpoints of magnetic fields emerging from the photosphere. Neighboring field lines of opposite directions start to shear and eventually re-arrange themselves to a simplified configuration in a process called "magnetic reconnection". The abrupt reconnection process transforms magnetic energy into heat and leads to an eruption where the material is heated to extremely high temperatures greater than 10^7 K. Thus flares contribute to the release of magnetic energy. A similar effect on small scales is discussed to contribute significantly to the heating of the corona (nano-flare heating) and therefore to counteract the ever-amplifying dynamo processes.

Since the α-ω-dynamo is based on differential rotation, a connection between magnetic activity and the stellar rotation rate can be expected. Instead, early surveys revealed a quadratic relationship between the X-ray luminosity L_X and the projected rotational velocity $v \sin i$ (Pallavicini et al., 1981). However, for very fast rotators the ratio of L_X to the overall luminosity $L_{\rm bol}$ converges to a constant value of 10^{-3} independent of rotation. This effect is called "saturation". The dependence between stellar activity and rotational velocity leads also to an indirect dependence of the former with the age of the star, because young stars rotate faster. When a star ages the rotation rate slowly diminishes due to angular momentum loss by magnetized winds. The reduction of the rotation rate in turn weakens the dynamo processes and therefore magnetic activity decreases.

The concept of the α-ω-dynamo is though not applicable to all stars: Early-type stars (from spectral type A5 on) should – following model calculations of the stellar interior – have a convective core but no outer convection zone which is essential for the amplification mechanism. These stars should therefore have no possibility to heat up a corona, which is consistent with the observation that essentially no late B- and early A-type stars show X-ray emission. On the other side of the stellar mass scale M-stars later than M3 are expected to be fully convective. Since the toroidal fields generated by the ω-effect arise preferably in the so-called convective overshoot region where radiative and convection zone merge, the α-ω-dynamo should collapse for these stars. However, no fading in X-rays or in activity in general is observed for them, late M-dwarfs are usually even more active and exhibit very distinct flaring. Suggestions to solve this problem must consider the many uncertainties in the models of both the stellar structure and the α-ω-dynamo. A different dynamo mechanism involving turbulent motions has been proposed for these stars as well. After all, at the very bottom of the main sequence, for very low-mass stars and brown dwarfs of spectral types L and T, X-ray emission and other activity indicators seem to decline.

2.2 X-ray emission from coronal plasmas

Photosphere, chromosphere and corona constitute the stellar atmosphere, i.e. the layers of a star emitting electromagnetic radiation. Compared to photosphere and chromosphere, the corona is much hotter and much more tenuous. The underlying conditions have a basic influence on the radiative properties of a plasma and thus the calculation of radiative processes in a corona differs significantly from that of the photosphere and the chromosphere; it is in a sense even easier.

Hot plasmas usually radiate energy very efficiently by emission in isolated spectral lines. In case of a coronal plasma the temperature is so high that the most abundant elements in cosmic matter, hydrogen and helium, are completely ionized. Thus these elements do not contribute to

line emission (i.e. an atomic transition involving an electron bound all the time) and this task is fulfilled by trace elements that are not yet fully ionized but have one or more of their electrons left, like carbon, nitrogen, oxygen, or iron. When extremely high temperatures ($> 10^7$ K) are reached more and more elements are completely ionized and continuum processes involving free electrons contribute significantly to the emission of the plasma.

The radiation of the coronal plasma can schematically be computed as follows: Assume the plasma to consist of a certain mixture of elements at a certain temperature T. Then calculate the number density of the atoms of certain ionization stages and the population of certain energy levels for these ions. The atomic transitions from excited levels to lower-lying levels and thus the emitted photons (together with photons originating from continuum processes) then constitute the coronal spectrum.

The details of this calculation are more complicated though, and usually require numerical approaches. The interplay of ionization and recombination processes at a certain temperature determines the ion fraction of a certain ion and has therefore also an influence on the population of a certain level that is additionally determined by excitation and de-excitation processes. The strengths of certain transitions are therefore not independent.

Usually an equilibrium situation is assumed to describe all these countervailing processes within a consistent framework. This assumption is questionable at least for rapidly changing situations with timescales too short for the involved processes to adjust, for example during flares. A first equilibrium condition affects the ionization stage. A certain ion can be created by ionization from a lower ionization stage and eliminated in the same way by ionization to a higher stage. In return the ion can be re-created by recombination from a higher ionization stage but also recombine to a lower stage. In the low-density, high-temperature coronal plasma ionization processes are usually induced by collisions, mostly with free electrons. The thus required energy increases with ionization stage and atomic number, so the degree of ionization is a function of temperature since the ionization energy must apply to the thermal velocity of the colliding particles. There are essentially two balancing recombination processes. Radiative recombination describes the capturing of a beforehand free electron (usually to an excited level) in combination with the release of a photon (which contributes to the continuum emission) corresponding to the redundant energy. Dielectronic recombination involves an inner electron of the ion that is excited parallel to the recombination process. As a result the ion ends up in a state with two electrons in excited levels.

The population of the individual energy levels of an ion is subject to another equilibrium condition. Again, in coronal plasmas the excitation process is most frequently caused by collisions, here the differentiation of the particle colliding with the ion (electrons, protons or even heavier nuclei are worth considering) is somewhat more important. As mentioned above, recombination processes also contribute to the population of excited levels. Radiative processes, i.e. radiative ionization and excitation, are usually neglected for both equilibrium conditions, the plasma is considered "optically thin". In turn there are various mechanisms de-populating an excited level. Spontaneous emission of a photon together with the transition to a lower level will be the most probable process (stimulated emission is also possible, but very improbable and is thus usually neglected). Collisional processes may lead to a de-excitation to a lower level or to further excitation to an even higher level.

2.2.1 Line emission

The emission of a photon in a certain spectral line corresponding to the transition from an upper level j to a lower level i of the Z times ionized element X is described by the reaction

$$X_j^{Z+} \rightarrow X_i^{Z+} + h\nu_{ji} \qquad \text{bound-bound emission with the photon energy } h\nu_{ji}$$

The emissivity ϵ, i.e. the total power emitted in this transition per unit volume is

$$\epsilon_{ji} = h\nu_{ji}\, A_{ji}\, n_j(X^{Z+}) \tag{2.1}$$

where the Einstein coefficient for spontaneous emission A_{ji} corresponds to the inverse radiative decay time and $n_j(X^{Z+})$ is the number density of atoms of element X in ionization stage $Z+$ that are in the excited state j. The units of ϵ are erg cm^{-3} s^{-1}.

The unknown number density $n_j(X^{Z+})$ can be reduced to the electron density n_e and a set of dimensionless multiplicative factors that can be calculated instead:

$$n_j(X^{Z+}) = \frac{n_j(X^{Z+})}{n(X^{Z+})} \frac{n(X^{Z+})}{n(X)} \frac{n(X)}{n(H)} \frac{n(H)}{n_e}\, n_e \tag{2.2}$$

$\frac{n_j(X^{Z+})}{n(X^{Z+})}$ is the fraction of the specific ion with the outer electron located in level j, or in short the level population. It is determined by solving the statistical equilibrium equations, taking into account all relevant excitation and de-excitation processes mentioned above for ideally all levels but in practice often only for the most important, lower-lying levels.

$\frac{n(X^{Z+})}{n(X)}$ is the fraction of atoms of element X located in ionization stage $Z+$, or in short the ion fraction of the specific ion. Similar to the level population the ionization balance is determined by solving the coresponding equilibrium equations.

$\frac{n(X)}{n(H)}$ is the abundance of element X relative to hydrogen.

$\frac{n(H)}{n_e}$ is the hydrogen abundance relative to the electron density, also called the proton-to-electron ratio. Since most electrons originate from hydrogen and helium that are completely ionized it is usually set to a constant value of ≈ 0.83. Due to the remaining electrons from the other elements it is actually a weak function of temperature and abundances.

The energy flux measured with any arbitrary detector is proportional to ϵ_{ji} integrated over the emitting volume

$$F_{ji} = \frac{1}{4\pi d^2} \int \epsilon_{ji}\, dV \tag{2.3}$$

with the distance d. The units of F_{ji} are erg cm^{-2} s^{-1}. With Equation 2.2 this becomes

$$F_{ji} = \frac{h\nu_{ij}}{4\pi d^2} \int A_{ji} \frac{n_j(X^{Z+})}{n(X^{Z+})} \frac{n(X^{+Z})}{n(X)} \frac{n(X)}{n(H)} \frac{n(H)}{n_e}\, n_e\, dV$$

which can be summarized to

$$F_{ji} = \frac{h\nu_{ij}}{4\pi d^2} \int G(T)\, DEM(T)\, dT \tag{2.4}$$

with the so-called contribution function $G(T)$

$$G(T) = A_{ji} \frac{n_j(X^{Z+})}{n(X^{Z+})} \frac{n(X^{Z+})}{n(X)} \frac{n(X)}{n(H)} \frac{n(H)}{n_e} \frac{1}{n_e} \tag{2.5}$$

and the differential emission measure $DEM(T)$

$$DEM(T) = n_e^2 \frac{dV}{dT} \tag{2.6}$$

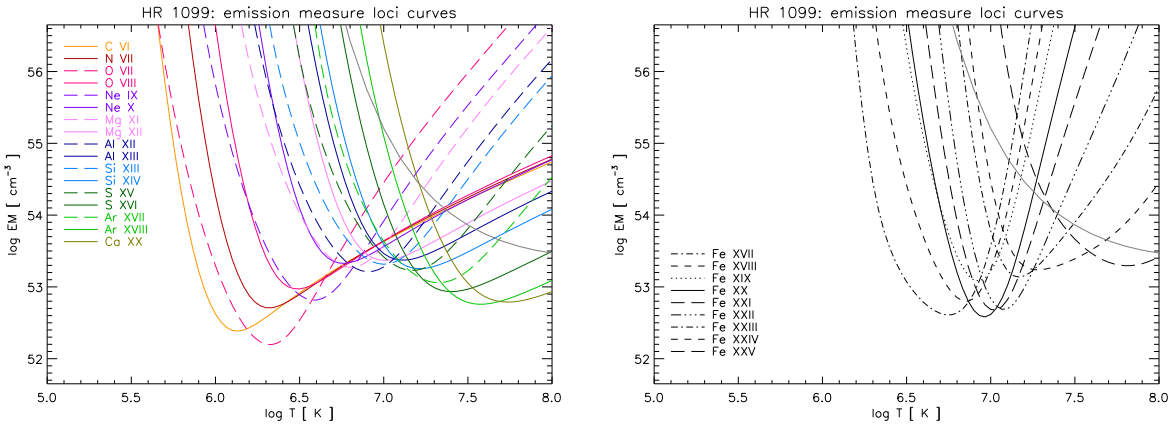

Figure 2.2: Emission measure loci curves for HR 1099 calculated with CHIANTI 5.0 applying the ionization balance of Mazzotta et al. (1998). H-like and He-like lines of various elements (left) have broad contribution functions while iron lines (right) from most ionization stages have a narrower shape. Both graphs also show a corresponding curve arising from continuum between 2-3 Å (see below). Note the logarithmic scale of the y-axis.

The contribution function $G(T)$ contains the atomic physics parameters of the particular transition and has the units erg cm^3 s^{-1}. $G(T)$ describes in simple terms the efficiency of the formation of the particular line as a function of temperature and is usually sharply peaked. Its overall shape (in terms of slopes and width) depends essentially on the ionization equilibrium (the formation temperature of the corresponding ion determines the temperature range where the line can occur) but also on the level population. Figure 2.2 shows emission measure loci curves, i.e. inverse contribution functions multiplied by the measured line flux from two different sets of lines.

The DEM in turn describes the properties of the emitting plasma and is a function unique for each line. It comes in cm^{-3} K^{-1}. The exact physical meaning of the differential emission measure is though not that straightforward. Mathematically one deals with a temperature-gradient-weighted electron density n_e. The applied electron density is a value averaged over the whole emitting volume, i.e. in case of a star the whole corona towards the observer. In reality different coronal structures (for instance active regions vs. coronal holes) may of course have different densities and a different temperature structure (see Figure 1.3). A certain coronal region may thus contribute to the emission in a certain temperature interval and another one may not while both may contribute at another temperature; i.e. the "filling factor" varies. Even for the Sun, where different regions can be observed separately, the DEM cannot distinguish between a large low-density volume and a small high-density volume emitting a certain flux.

A reconstruction of the DEM from measured line fluxes and theoretical calculations of the atomic physics included in $G(T)$ is based on the inversion of the integral equation 2.4. The fundamental problems arising from this approach have been analyzed by many authors, e.g. Craig and Brown (1976), Craig (1977); see Kashyap and Drake (1998) for a recent discussion. To obtain a reliable DEM covering an appropriate temperature range a set of lines with contribution functions widely distributed over the temperature interval is required. While few lines will result in a DEM with poor resolution in temperature, the problem becomes ill-conditioned when using many lines with contribution functions overlapping in temperature. As a result the solutions are ambiguous and unstable to perturbations, i.e. there is a strong dependence on the particular lines serving as input data. Further limitations concern the atomic data entering the calculations, i.e. the ionization balance, the level population and collision strengths (see below). Therefore additional constraints like artificial smoothness or positivity must be forced or further

simplifications often must be made.

The emission measure EM(units cm^{-3}) corresponding to the DEM is

$$EM = \int n_e^2 \, dV = \int DEM(T) \, dT \tag{2.7}$$

The isothermal approximation thus would simplify Equation 2.4 to

$$F_{ji} = \frac{h\nu_{ij}}{4\pi d^2} \langle EM \rangle \int G(T) \, dT$$

with an averaged emission measure $\langle EM \rangle$

The coronal approximation

A frequently used simplification is the so-called coronal approximation. This includes a strict compliance of the equilibrium conditions and the assumption that the plasma is optically thin. Furthermore level j is assumed to be populated exclusively from the ground level g by collisions with electrons. Radiative decay to lower levels should be the only process to de-populate level j. Less frequent processes like collisional de-excitation and population of level j by radiative cascades from higher levels are neglected. In "normal" coronal plasmas, i.e. at lower temperatures and densities, the coronal approximation may be applied, but e.g. during flares these conditions are not fulfilled.

The statistical equilibrium of processes populating and de-populating level j is thus described by

$$n_e \, n_g(X^{+Z}) C_{gj} = n_j(X^{+Z}) \sum_{k<j} A_{jk} \tag{2.8}$$

where the collision rate coefficient C_{gj} determines the excitation from the ground state to level j. The definition of the collision rate coefficients is similar to that of the Einstein coefficients, but a reasonable calculation of the C_{gj} requires further assumptions: Usually the velocities of the electrons are assumed to follow a Maxwellian distribution. It is then possible to approximate C_{gj} via a "collision strength" deduced from cross sections.

The excitation rate depends on the density of the colliding counterparts, i.e. electrons and ions of the ground state. It is balanced by radiative decays from the upper level to all lower-lying levels k. Inserting Equation 2.8 into Equation 2.1 gives

$$\epsilon_{jg} = h\nu_{jg} \, A_{jg} \, n_j(X^{Z+}) = h\nu_{jg} \, \frac{A_{jg} \, C_{gj}}{\sum\limits_{k<j} A_{jk}} \, n_g(X^{Z+}) \, n_e$$

together with Equation 2.2 one has

$$\epsilon_{jg} = h\nu_{jg} \, \frac{A_{jg} \, C_{gj}}{\sum\limits_{k<j} A_{jk}} \, \frac{n_g(X^{Z+})}{n(X^{Z+})} \frac{n(X^{Z+})}{n(X)} \frac{n(X)}{n(H)} \frac{n(H)}{n_e} \, n_e^2$$

Further simplifications include that the decay back to the ground state dominates the sum of possible radiative decays, i.e. $\sum_{k<j} A_{jk} \approx A_{jg}$, and that almost all ions are located in the ground state g, i.e. $n_g(X^{Z+})/n(X^{Z+}) \approx 1$. Together with the assessment of the proton-to-electron ratio to a constant factor (see above), this results in

$$\epsilon_{jg} = h\nu_{jg} \, C_{gj} \frac{n(X^{Z+})}{n(X)} \frac{n(X)}{n(H)} \cdot 0.83 \cdot n_e^2$$

and thus it can be pointed out how the collisional excitation rate enters the contribution function. Equation 2.5 becomes

$$G(T) = 0.83 \, C_{gj} \frac{n(X^{Z+})}{n(X)} \frac{n(X)}{n(H)}$$

Other definitions

The derivation of the DEM and related quantities given here follows essentially Mason and Fossi (1994). Various other definitions of the differential emission measure DEM, the corresponding emission measure EM and the underlying contribution function can be found in the literature. It is quite common to define the DEM as

$$DEM(T) = n_e\, n(H)\, \frac{dV}{dT}$$

i.e. the proton-to-electron ratio is excluded from the contribution function and assigned to the differential emission measure. Equation 2.5 thus becomes

$$G(T) = A_{ji} \frac{n_j(X^{Z+})}{n(X^{Z+})} \frac{n(X^{Z+})}{n(X)} \frac{n(X)}{n(H)} \frac{1}{n_e}$$

In solar physics where individual structures can be spatially resolved and observed separately an emission measure over height or a column emission measure instead of the volume emission measure (Equations 2.6 and 2.7) is applied:

$$DEM(T) = n_e^2\, \frac{dh}{dT}$$

has in turn the units $\mathrm{cm}^{-5}\ \mathrm{K}^{-1}$. The corresponding EM has accordingly cm^{-5}. Instead of fluxes the line intensity (units erg $\mathrm{cm}^{-2}\ \mathrm{s}^{-1}\ \mathrm{sr}^{-1}$) may be measured:

$$I_{ji} = h\nu_{ij} \int G(T)\, DEM(T)\, dT$$

Especially in X-rays there is no need to normalize and convert spectra to energy units since the measured counts directly correspond to single X-ray photons. Instead of the energy flux given in Equation 2.4 a photon flux without the factor $h\nu_{ij}$ (units photons $\mathrm{cm}^{-2}\ \mathrm{s}^{-1}$) can be considered:

$$f_{ji} = \frac{1}{4\pi d^2} \int G(T)\, DEM(T)\, dT \tag{2.9}$$

2.2.2 Continuum emission

Free-free emission, free-bound emission and two-photon radiation are the three main processes contributing to continuum emission in a hot plasma. Figure 2.3 shows their emissivity for two diffreent coronal temperatures. Free-free radiation or bremsstrahlung originates from the interaction of free electrons with heavier charged particles, mostly with protons (due to their high abundance), but also with alpha particles and rarely heavier ions. The main fraction of these electrons arise from hydrogen and helium which are fully ionized in X-ray emitting plasmas. Only a small number of them is determined by the other elements. The impact of the abundance of these elements on the free-free emission is therefore minor. Free-free radiation produces a featureless spectrum with a maximum shifting to lower wavelengths for higher temperatures.

Free-bound emission rises from recombination processes of electrons with heavier ions. The frequency of these recombinations is of course dependent on the abundance of these ions. The shape of a free-bound spectrum is dominated by edges whose wavelengths are determined by the level energy of the captured electron. The strength of these features depends not only on the elemental abundance but also on the level population (and therefore on the temperature).

Two-photon radiation is a possible and sometimes the only way to return to the ground state for excited metastable states in low-density plasmas where collisions that depopulate these levels are rare. Instead of a single photon with a discrete energy two photons may be emitted with

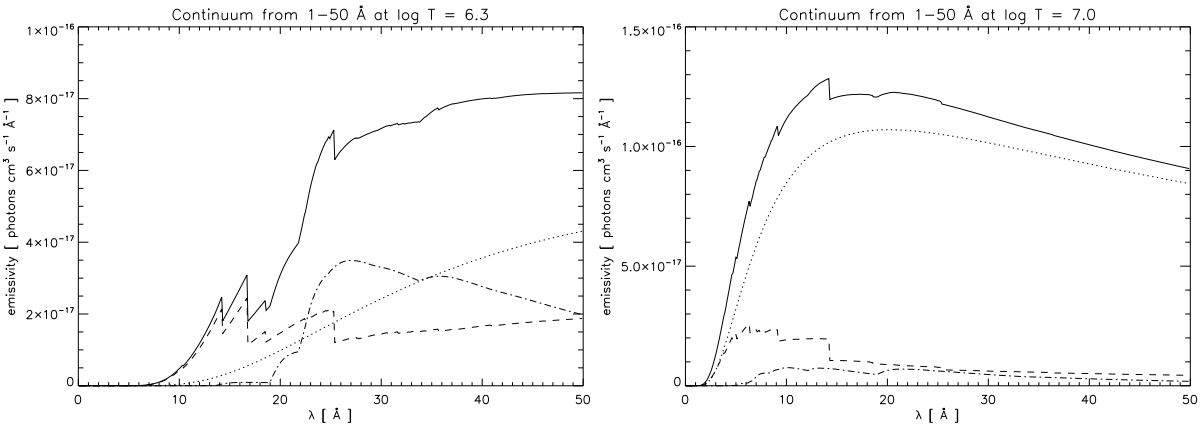

Figure 2.3: Theoretical continuum emissivity from 1-50 Å at 2 MK (left) and 10 MK (right) respectively with solar photospheric abundances after Asplund et al. (2005), calculated with CHIANTI routines. The relative fractions of the three constituents are also shown, the dotted line represents free-free emission, the dashed line free-bound, and the dash-dotted line two-photon emission. At higher temperatures, the emission is dominated by free-free processes while at lower temperatures free-bound and two-photon processes control the shape of the continuum at certain wavelengths.

the sum of both photon energies being equal to the energy difference between the two levels. The particular energies of the two photons follow a certain distribution that can be modeled. Two-photon processes arise essentially from H-like and He-like ions: The hydrogen-like $2^1S_{1/2}$ state (in contrast to the $2^1P_{1/2}$ and $2^1P_{3/2}$ states) is a metastable level with a very long direct decay time to the ground state $1^1S_{1/2}$ so that two-photon processes are possible. For He-like ions a two-photon process is the only possibility (apart from collisional de-excitation) for the 2^1S_0 state to return to the 1^1S_0 ground state since a transition with a single photon would require a strictly forbidden $J = 0 \rightarrow J = 0$ transition. The distinctness of structures in the two-photon continuum also depends on the abundances.

In principle, a mathematical formalism similar to the one presented above for line emission can be derived for the processes contributing to continuum emission

$$
\begin{aligned}
X^{Z+} + e &\rightarrow X^{Z+} + e' + h\nu && \text{free-free emission} \\
X^{(Z+1)+} + e &\rightarrow X_j^{Z+} + h\nu && \text{free-bound emission} \\
X_j^{Z+} &\rightarrow X_i^{Z+} + h\nu_{jk^*} + h\nu_{k^*i} && \text{two-photon emission, } k^* \text{ is a virtual level}
\end{aligned}
$$

The total continuum emissivity in a certain wavelength interval as a function of temperature can be calculated analogously to the line emissivity. A corresponding continuum contribution function can be defined that – convoluted with the differential emission measure – gives the continuum flux in the respective wavelength interval. The shape of such a continuum contribution function differs though from that of an emission line. It is a function monotonically increasing in temperature without extrema since an increase in temperature will always result in an increase in continuum emission. The same DEM applies to both line and continuum emission.

2.3 Coronal abundances

As can be seen from Equations 2.4 and 2.5 the amount of flux emitted in a certain line of a particular element is proportional to the abundance of that element. At first glance one would assume that the elemental abundances are uniformly distributed at least in the atmosphere of

a certain star or the Sun. Pottasch (1964a) adopted the emission measure method to deduce the abundances of several elements in solar coronal UV and XUV spectra and found significant deviations from the photospheric composition. (See also Pottasch, 1964b)

Further measurements established what is today called the FIP effect as mentioned in the introduction, i.e. that elements with a low first ionization potential show an enhancement relative to high-FIP elements. Furthermore variations in the magnitude of the FIP effect where found, dependent on the coronal regions observed. See Feldman and Laming (2000) for a review on solar observations and corresponding pre-*Chandra* and *XMM* investigations of solar-like stars. There are different ways to explain the fractionation process underlying the FIP effect, for instance a draining of high-FIP elements of the coronal material or a process easing the enhancement of low-FIP elements. Its actual cause must originate in the cooler, lower lying layers of the solar atmosphere, where the affected elements are not ionized so that the first ionization potential can have a great importance. See Laming (2004) for a recent approach.

For stellar coronal sources the situation is even more sophisticated. Inactive, solar-like stars show abundance patterns similar to the solar FIP effect (e.g. Raassen et al., 2003) or no FIP bias (e.g. Raassen et al., 2002), while the coronae of more active stars, especially RS CVn binaries seemed to show an inverse FIP effect (e.g. Brinkman et al. (2001), Audard et al. (2003)). The discussion is nevertheless somewhat meaningless since stellar coronal abundance determinations are usually carried out relative to solar photospheric abundances, lacking appropriate stellar photospheric abundances as a reference. Sanz-Forcada et al. (2004) find that for the stars in their sample, the abundance patterns differ considerably when stellar photospheric abundances are consulted.

Even the solar photospheric abundances are subject to continuous modifications. A standard set of solar photospheric abundances, still the most prevalent in use in the literature, was devised by Anders and Grevesse (1989). A revision by Grevesse and Sauval (1998) resulted in notably reduced abundances for nitrogen, oxygen and iron. In the recent past further approaches of improvements by many authors have been undertaken and the new set compiled by Asplund et al. (2005) can be considered to be the most suitable matching both observational data and 3D hydrodynamical modeling although some discrepancies with helioseismological data occurred. Drake and Testa (2005) proposed to solve this problem by adjusting the solar neon abundance to the level found in most stellar coronae. A measurement of the abundances of noble gases like helium, neon and argon for the solar photosphere is difficult since these elements show no photospheric lines. Estimates are therefore based on coronal data. A neon overabundance relative to these solar values is indeed found for most stars analyzed with the *Chandra* and *XMM-Newton* gratings. (See e.g. Drake et al., 2001)

3 High-resolution X-ray spectroscopy with Chandra and XMM-Newton

More than 25 years ago, the Focal Plane Crystal Spectrometer on board the *Einstein* satellite observed a few bright celestial X-ray sources with high spectral resolution but low efficiency. The FCPS was a Bragg crystal spectrometer, restricted to small wavelength segments centered on specific spectral features. Capella was the only coronal X-ray source observed with the FCPS (Vedder and Canizares, 1983) and barely resolving individual spectral features also with *Einstein's* Objective Grating Spectrometer OGS (Mewe et al., 1982), but these early measurements only made the stellar X-ray astronomers look forward to the wealth of high-resolution broadband X-ray spectra now available from the currently operating *Chandra* and *XMM-Newton* satellites. Both constitute the next generation of X-ray observatories – *Chandra* being the successor of *Einstein* – and high-resolution spectroscopy of stellar coronae is one of their central points. The corresponding spectra are generated with diffraction and reflection gratings respectively that follow essentially the same functional principle as gratings for optical spectroscopy and can be manufactured in a similar manner.

X-ray imaging devices, however, must be built differently from optical telescopes, because X-ray photons – due to their high energy – would penetrate the lenses or mirrors the telescopes are made of. Only when hitting a mirror with very small incidence angles (a few degrees at most), X-rays could be reflected. Several difficulties arise from this "grazing incidence": The mirror reflectivity with small incidence angles is not very high, also strong abberations occur off the principal axis.

A system invented by the German physicist Hans Wolter solves these problems. Two mirrors are arranged successively, the first of paraboloidal, the second of hyperboloidal shape. The twofold reflection on this two-mirror system focuses an infinitely far-off object and simultaneously minimizes abberations. The X-rays encounter at first the paraboloid and then the hyperboloid, each time in grazing incidence. To increase the efficiency of such an X-ray telescope several of these mirror pairs can be nested, increasing the effective reflecting area. The quality of X-ray optics depends heavily on the smoothness of the mirror surface – the fabrication tolerance is much lower than for "normal" optics because the surface roughness must be small against the wavelength.

Another important aspect affects the detection of X-rays. Astronomical detectors for visible light operate (usually) in a "photon-collecting" mode, i.e. the detector is illuminated for the entire exposure time; the resulting image has lost any temporal information and the contribution of a single photon to the overall signal cannot be distinguished. X-ray detectors instead operate in a "photon-counting" mode, they are recurrently read out and are therefore normally able to measure individual photons that are recorded afterwards in so-called event lists. The timing resolution of such a detector of course depends on read-out and dead times.

The American mission *Chandra* and its European counterpart *XMM-Newton* are complementary in terms of scientific objectives. While the former is adjusted to accomplish the highest spatial resolution, the latter focuses on sensitivity. Nevertheless both satellites are allround observatories, with high-end imaging and spectroscopy capabilities.

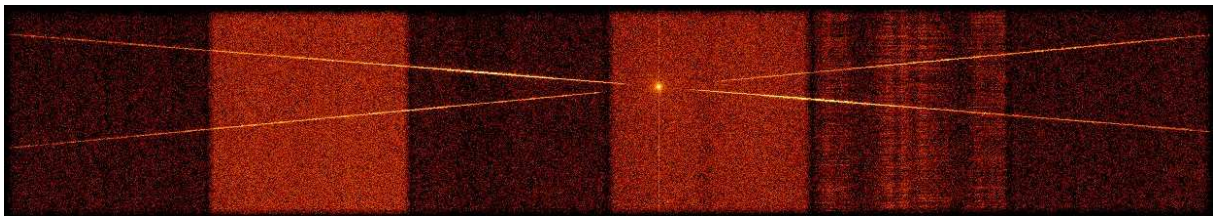

Figure 3.1: A typical CCD image of an HETGS spectrum on the ACIS-S detector. The two HEG and MEG spectra (upper left to lower right and lower left to upper right respectively) of positive and negative orders form an X-shaped figure with the 0th order image in the center. Note the slightly varying instrumental background on the six CCD chips.

3.1 Chandra

The *Chandra* X-ray observatory, named after the late astrophysicist Subrahmanyan Chandrasekhar, was launched in July 1999. Its telescope system, the High Resolution Mirror Assembly (HRMA), consists of four nested pairs of Wolter-type mirrors with a focal length of 10 m and made of iridium-coated Zerodur, a glass-ceramic famous for its very low thermal expansion and therefore predestined as a material for telescope mirrors. Great care was taken on grinding, polishing and coating their surfaces as well as on their exact alignment. Together with the large diameter of the outermost mirror shell of 1.20 m this allows for X-ray imaging of the highest quality reached so far, with an angular resolution of $0.5''$.

Two different types of instruments serve as detectors in the focal plane: The Advanced Charged Couple Imaging Spectrometer (ACIS) consists – as the name suggests – of 10 CCD chips with 1024×1024 pixel each, arranged in two arrays. An array of 2×2 chips (ACIS-I) is optimized for X-ray imaging, six chips arranged in-line (ACIS-S) for recording dispersed spectra. A CCD is basically a semiconductor electronic device composed primarily of silicon pixel cells. Photoelectric absorption of an X-ray photon in silicon results in the release of a number of electrons proportional to the photon energy absorbed. Immediately after the charge is confined by electric fields to a small volume near the interaction site, a gate structure allows the confined charge to be passed down to a serial readout at one edge by clocking the applied voltages. An X-ray CCD detector provides therefore, additional to the imaging capabilities and the recording of the photon arrival time, the ability to measure the energy of each incoming X-ray photon with intermediate resolution without additional means. The spectral resolution depends upon an accurate determination of the total charge deposited by a single photon. This in turn is determined by the efficiency of the charge collecting material and the readout amplifiers, the fraction of charge lost in the transfer from pixel to pixel during read-out (charge transfer inefficiency CTI), as well as on read-out noise.

The second kind of detector on board *Chandra* is the High Resolution Camera (HRC) made of microchannel plates (MCP). Again, there are two detectors, one for imaging and the other one for recording dispersed spectra, HRC-I and HRC-S. The HRC-I consists of a quadratic cluster of 10 cm edge length with 69 million tiny lead-oxide glass tubes with 10 μm in diameter, covering a field of view of $31' \times 31'$ in total. Three separate 27×100 mm rectangular segments of identical design form a narrow and long device optimized as a detector for grating spectra. The microchannel plate tubes act like miniatures of a photomultiplier: Electrons are released when the tubes are struck by X-rays, they are accelerated down the tube by high voltage, releasing more electrons when hitting the sides of the tube. Thus a single X-ray photon is amplified to millions of electrons. A crossed grid of wires detects this electronic signal and allows the position of the original X-ray to be determined with high precision. The HRC provides the highest spatial resolution imaging, it has essentially no energy resolution but a good time resolution of about

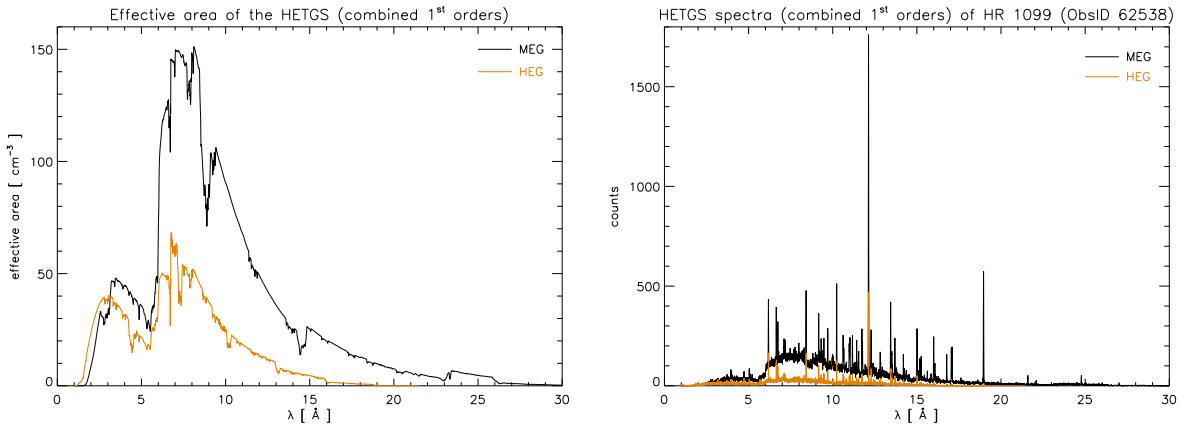

Figure 3.2: Left: Representative effective area of the instrument combination HETG + ACIS-S in first order. Effective areas for positive and negative orders are summed up. Right: Instancing HEG and MEG count spectra of HR 1099. The steep rise of the source continuum at 6 Å reflects the rise of the effective area.

16 μs instead. Unfortunately a technical defect of the HRC-S results in high background count rates for this instrument that induces an additional background noise in the spectra.

Eventually there are two additional gratings dedicated to high-resolution spectroscopy: the High Energy Transmission Grating (HETG) and the Low Energy Transmission Grating (LETG). Either of them can be positioned in the optical path behind the mirrors. The two gratings in combination with the different detectors have complementary capabilities.

3.1.1 The High-Energy Transmission Grating Spectrometer HETGS

The HETG is usually operated with the ACIS-S, both form the High-Energy Transmission Grating Spectrometer (HETGS). The HETGS achieves a resolving power E/ΔE up to 1000 in the energy band between 0.4 keV and 10.0 keV (corresponding to wavelengths of $\approx$ 1.5 Å to 30 Å).

The HETG itself consists of two sets of gratings with different periods. The first set, the Medium Energy Grating (MEG), intercepts the X-rays from the two outer HRMA shells and – as its name implies – is optimized for medium energies. The second one, the High Energy Gratings (HEG), accordingly intercepts the X-rays from the two inner shells and is optimized for high energies. The resolution is 0.015 Å FWHM and 0.025 Å FWHM for HEG and MEG respectively. (See also Figures 4.3 and 4.4 for a comparison of the spectral resolution of the grating spectra used in this study.)

Both grating sets, consisting of 192 and 144 small facets, are mounted on a single support structure and therefore used concurrently, but both sets are mounted with their dispersion directions being offset by 10°; the dispersed spectra can therefore be easily distinguished on the detector (see Figure 3.1).

The MEG gratings have a period of 0.4 μm, the corresponding period of the HEG gratings is 0.2 μm. The gratings are composed of gold bars; their height and width are nominally chosen to maximize the first-order intensities and to simultaneously reduce the intensity of higher spectral orders and of the zeroth-order image, similar to the "blazing" technique of reflection gratings.

An important parameter describing the efficiency of a combination grating + detector (or one of them alone) as a function of energy or wavelength of the infalling X-rays is the effective area, the functional equivalent to the aperture. The HEG effective area in first order combined for both gating arms starts rising at $\approx$ 1.5 Å with a decline towards $\approx$ 5.5 Å followed by a new rise to maximum values of $\approx$ 70 cm^2 at $\approx$ 7 Å. From that on, the effective area basically decreases,

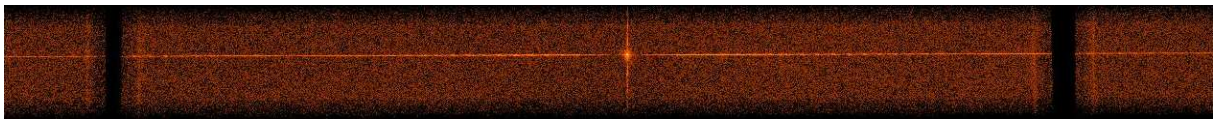

Figure 3.3: Central portion of a typical detector image of an LETGS spectrum on the HRC-S. The whole spectrum covers the three equal sized microchannel plate elements. The broad gaps between the detector elements are easily visible as missing parts in spectrum and background.

arriving at zero at ≈ 19 Å. The shape of the effective area of the individual arms is similar, but slightly shifted in wavelength due to the offset position of the zeroth order image on the ACIS-S detector (a centered image would fall on the gap between the chips).

The MEG effective area has a similar shape, with a small shift to longer wavelengths at the short-wavelength boundary but a much steeper increase at ≈ 6 Å to maximum values of ≈ 150 cm^2. Zero values after the decline are therefore reached at wavelengths of ≈ 29 Å. Some of the larger structures in the effective area are caused by absorption edges in the detector material (e.g. the Silicon K-edge at 6.76 Å). The exact wavelength position of small-scale features caused by bad pixels and chip gaps depends on the location of the 0th order image and is different for each observation. (See Figure 3.2 for a graph of the HETGS effective areas and corresponding spectra.)

The wavelength or energy of each photon from the spectrum imaged on the detector is determined by its dispersion angle (corresponding to the radial distance from the zeroth order image on the detector) and its spectral order. The different orders overlap on the detector and thus photons originating from higher orders would be assigned to the wrong wavelength when they are considered as first order photons. The intrinsic energy resolution of a CCD detector like ACIS provides the opportunity to distinguish between the orders: A plot of the dispersion angle of the detected photons versus their energy leads to an order-sorting image (though it is rather a schematic plot than a real image) where the single orders are easily resolved, the so-called banana plot. See also the right panel of Figure 3.5. The application of narrow extraction regions to the banana plots provide an additional background filtering technique for grating spectra so that HETGS spectra usually have a negligible background.

3.1.2 The Low-energy Transmission Grating Spectrometer LETGS

The Low Energy Transmission Grating Spectrometer LETGS comprises the LETG and a focal plane imaging detector. The HRC-S is the primary detector designed in particular for use with the LETG but ACIS-S can also be used. In combination with the HRC-S wavelengths from 5 Å to 175 Å are observable, with ACIS-S the accessible wavelength range is limited from 5 Å to 45 Å due to the smaller dimensions of the ACIS-S and its low sensitivity at lower energies. The long-wavelength part of the initially available spectrum is thus lost. Usage of ACIS-S would however allow for order separation via the intrinsic energy resolution of the CCDs as described above for the HETGS. This is not possible with microchannel plates, so that a first order spectrum obtained with the HRC-S will always suffer from a contamination with higher orders. In this study only LETGS spectra obtained with the HRC were used, the term LETGS will therefore always denote the instrument combination LETG + HRC-S in the following.

The LETGS provides high-resolution spectroscopy ($E/\Delta E > 1000$) for XUV wavelengths ($\approx 80 - 175$ Å or $0.07 - 0.15$ keV) and a more moderate resolving power at shorter wavelengths for soft X-rays, the nominal resolution is ≈ 0.06 Å FWHM.

The LETG gratings are made of fine gold wires with a period of 1 μm. Similar to the HETGS, the thickness of the wires is designed to maximize the first order intensity and to suppress higher orders. The strongest contaminations from higher orders arise from 3rd and 6th order, even

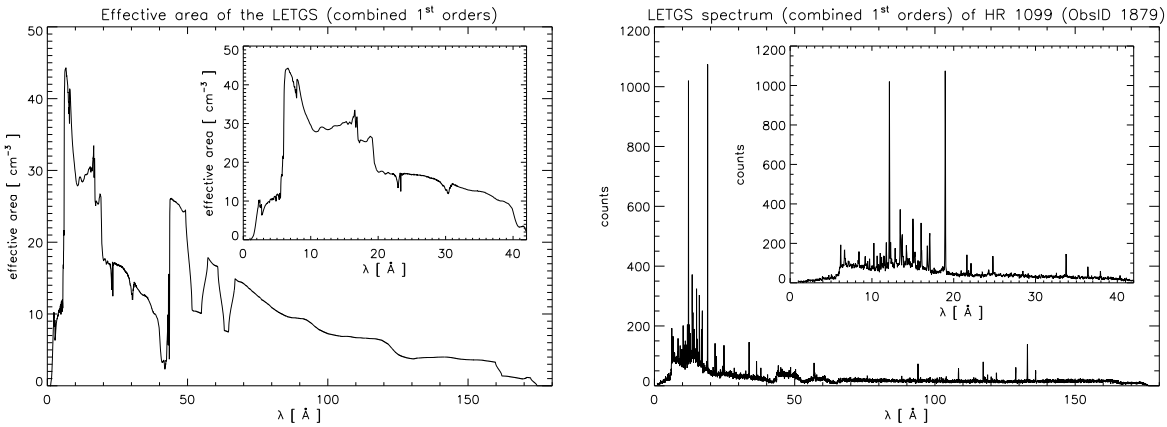

Figure 3.4: Left: Representative effective area of the instrument combination LETG + HRC-S. Effective areas for positive and negative side are summed up. Right: An instancing LETG count spectrum of HR 1099. The shape of the source continuum follows clearly the effective area.

orders are generally weaker than odd orders. The gratings of the LETG, just like those of the HETG, consist of small facets that are mounted onto a toroidal ring structure matching the Chandra mirrors, both grating assemblies thus look very similar.

The three segments of the HRC-S are divided by relatively broad gaps that cover wavelength intervals of approximately 8 Å. In standard operation, the position of the central zeroth order image is put slightly offset so that different spectral regions fall onto these gaps on the positive and negative sides. The total wavelength interval covered thus ranges from approximately 165 Å on the negative side to 175 Å on the positive side in first order. This wavelength range can be shifted somewhat by offset pointing, and thus wavelength coverage up to 210 Å can be forced but is accompanied by a steep decline in spectral resolution.

The effective area of the LETGS (Figure 3.4) in the described standard operation and added up for a combined first order spectrum is low for wavelengths between ≈ 2 and 5 Å. Considering the low resolving power for short wavelengths measurements of individual lines are practically impossible and this part of the spectrum is normally unusable. A steep rise follows at ≈ 5.5 Å and maximum values of ≈ 45 cm^2 are reached. The LETGS effective area then decreases like those of HEG and MEG, but with a different shape. A minimum is reached at ≈ 43 Å, where the carbon edge is located. Another steep rise to values of ≈ 35 cm^2 succeeds. The following smooth decline is interrupted by two dips caused by the detector gaps that are usually located around 54 Å and 63 Å. The effective area eventually reaches zero at ≈ 175 Å.

The LETGS is the only instrument taken into account in this study that covers additional to the soft X-ray range also part of the XUV. Unfortunately the wavelength calibration degrades for the longer wavelengths. The enhanced instrumental background of the HRC-S also affects especially wavelengths greater than 100 Å.

More technical details about *Chandra* and its instrumentation can be found in the "The Chandra Proposers' Observatory Guide", Version 7.0 (2004)

3.2 XMM-Newton

XMM-Newton, launched in December 1999, is equipped with three identical co-aligned X-ray telescopes with a diameter of 70 cm and a focal length of 7.50 m. Contrary to *Chandra*, they do not consist of a few thick mirrors but of thin gold-coated nickel shells. Each of the telescopes has 58 of these reflecting shells. The large mirror surface area thus provides *XMM*'s large effective area and high sensitivity. The disadvantage of the thin metal mirrors is that their surface cannot

be manufactured as precisely as that of customary mirrors. As a result, the point spread function (PSF) that describes the instrumental broadening of the image of a point-like source is much broader for *XMM* compared with *Chandra*.

The three telescopes are equipped with imaging CCD detectors (European Photon Imaging Camera, EPIC) of two different types. One of the telescopes comes solely with the EPIC PN camera, the other two that come with the EPIC MOS detectors also have integrated reflective gratings and corresponding detectors (Reflection Grating Spectrometer, RGS) for high-resolution spectroscopy. In addition to the X-ray telescopes the Optical Monitor (OM), a 30 cm Ritchey-Chrétien telescope provides observations in the UV or in visible light to monitor the observed X-ray sources simultaneously at longer wavelengths and to ease the identification of unknown X-ray sources with optical counterparts. All six instruments (the EPIC PN, the two EPIC MOS and RGS, and the OM) can be operated simultaneously and thus provide multiple measurements of the same target at once.

3.2.1 The European Photon Imaging Camera EPIC

The EPIC CCDs have an intrinsic energy resolution of $E/\Delta E \approx 20 - 50$ in the energy range between 0.2 and 15.0 keV and therefore provide imaging spectroscopy with intermediate spectral resolution (similar to *Chandra* ACIS). Several operation modes allow to adjust the size of the imaging frame and accordingly optimize the read-out time. Three filters of different thickness block optical and UV radiation. The field of view of all EPIC instruments extends to $\approx 30'$

The EPIC PN is named after its fully depleted p-n junction and consists of 12 chips integrated on a single wafer with 6×6 cm in size, each with 200×64 pixels with an edge length of 150 μm, and thus a nominal angular resolution of $3.3''$. The PN operates in the energy range of 0.2 to 15.0 keV and offers the best quantum efficiency of the EPIC instruments. For an example of an EPIC PN spectrum see Figure 4.11. Since no additional grating retains part of the infalling photons it also has the highest effective area, reaching ≈ 900 cm^2 at maximum. The PN together with its mirror module is therefore by far the most sensitive X-ray imaging device available at all. Additionally it has a very good timing resolution.

The other two EPIC instruments on *XMM-Newton* consist of arrays of Metal-Oxide-Silicon (MOS) technology. Seven CCD chips with one in the center of the field of view and the other six surrounding it, each with an imaging area of 2.5×2.5 cm and 600×600 pixels with a pixel size of 40 μm, corresponding to $1.1''$ nominal resolution. The angular resolution of the two MOS detectors is better than that of the PN, with MOS 1 surpassing MOS 2 somewhat. The MOS CCDs can operate in the energy range of 0.2 to 12.0 keV, with a slightly better spectral resolution than that of the PN. However, quantum efficiency and effective area (that reaches only ≈ 400 cm^2 at maximum due to obscuration by the gratings) and therefore the sensitivity are lower. The two MOS detectors are offset by 90° so that sources falling on chip boundaries in one of the exposures are imaged without problems in the other one.

Due to the high sensitivity of the EPIC instruments the effect of pile-up must at any rate be considered for sources with higher count rates. The term pile-up describes the phenomenon that two or even more photons are detected as a single event when they arrive within one read-out interval on the same pixel. This effect applies to all X-ray CCD detectors (therefore as well for *Chandra* ACIS) and falsifies count rate measurements and especially spectra extracted for these sources because the energy of the spuriously measured piled event corresponds to the sum of the energies of the individual photons of which it is comprised. The spectra thus "loose" events at lower energies and get a high-energy tail instead. The first step to deal with pile-up is of course to avoid it, i.e. for *XMM* to choose an operating mode with adequate timing resolution or for *Chandra* to insert an additional grating. Subsequent pile-up correction is based on the fact that the central pixels of the point-spread function are affected more often and that piled events often

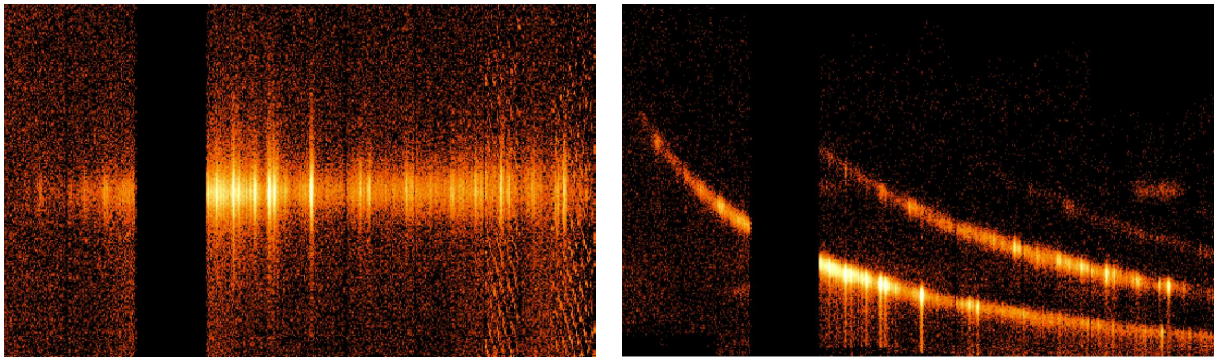

Figure 3.5: Left: RFC image of the RGS 1 spectrum of Capella from dataset 0134720801. Right: Banana plot corresponding to the spatial image with the dispersion angle increasing from left to right and the intrinsic energy increasing from bottom to top. The distinct orders split up and become bent-shaped. Three orders can easily be recognized, but the photons are concentrated in first and second order.

cover more pixel than single-photon events. The exclusion of events with such pixel patterns is one possibility, another one is to adopt an annular source extraction region and therefore to exclude the central portion of the PSF.

3.2.2 The Reflection Grating Spectrometer RGS

The two X-ray telescopes with a MOS imaging detector are also equipped with Reflection Grating Spectrometers (RGS). Each RGS incorporates an array of reflection gratings (the Reflection Grating Array, RGA) that are placed in the optical path behind the mirror modules and a strip of CCD elements (the RFC) to record the dispersed spectra.

An RGA contains 182 identical diffraction gratings, each measuring about 10×20 cm. The gratings are mounted in a configuration where the incident and diffracted rays lie in a plane which is perpendicular to the grating grooves. These have a period of $\approx 1.5\,\mu$m and a blazed profile that corresponds to a blaze wavelength of 15 Å in the negative first order. The grating facets were replicated from an identical set of master gratings onto thin substrate and covered with a thin gold coating.

The gratings intercept roughly half of the X-ray photons, while the undeflected photons pass through and are intercepted by the MOS detectors in the focal plane. The diffracted X-rays are detected with the RFC, a strip of nine CCD chips (similar to ACIS-S). The CCDs have an area of 384×1024 pixels with a pixel size of 27 μm. The pixels are binned on-chip by 3×3.

Images of RGS spectra differ somewhat from *Chandra* LETGS or HETGS spectra since the RFC only records the negative orders of the spectrum, the zeroth order image is also not included (see Figure 3.5). Thus the wavelength scale of the resulting spectrum has no fixed point and its lower and upper limits depend sensitively on the source position. Usually a wavelength interval from 5 Å to 38 Å is covered in first order, corresponding to energies between 0.35 and 2.5 keV. A resolving power of $E/\Delta E$ of 200 to 800 and a spectral resolution of ≈ 0.06 Å is reached, the latter one being comparable to *Chandra* LETGS. The blazing angle concentrates the intensity to the negative first order but higher orders are not suppressed as with the *Chandra* gratings. Their separation is accomplished the same way as for *Chandra* ACIS-S, by using the intrinsic energy resolution of the CCDs. For brighter sources the second order spectra provide additional useful data, with an improved spectral resolution of ≈ 0.03 Å but lower effective area. Furthermore the usable wavelength range covered is smaller, lasting from ≈ 5 Å to 19 Å, the exact upper limit depends again on the source position. (As a result, the O VIII line at 18.97 Å is sometimes included in the spectra, and sometimes not, see Figure 3.6.)

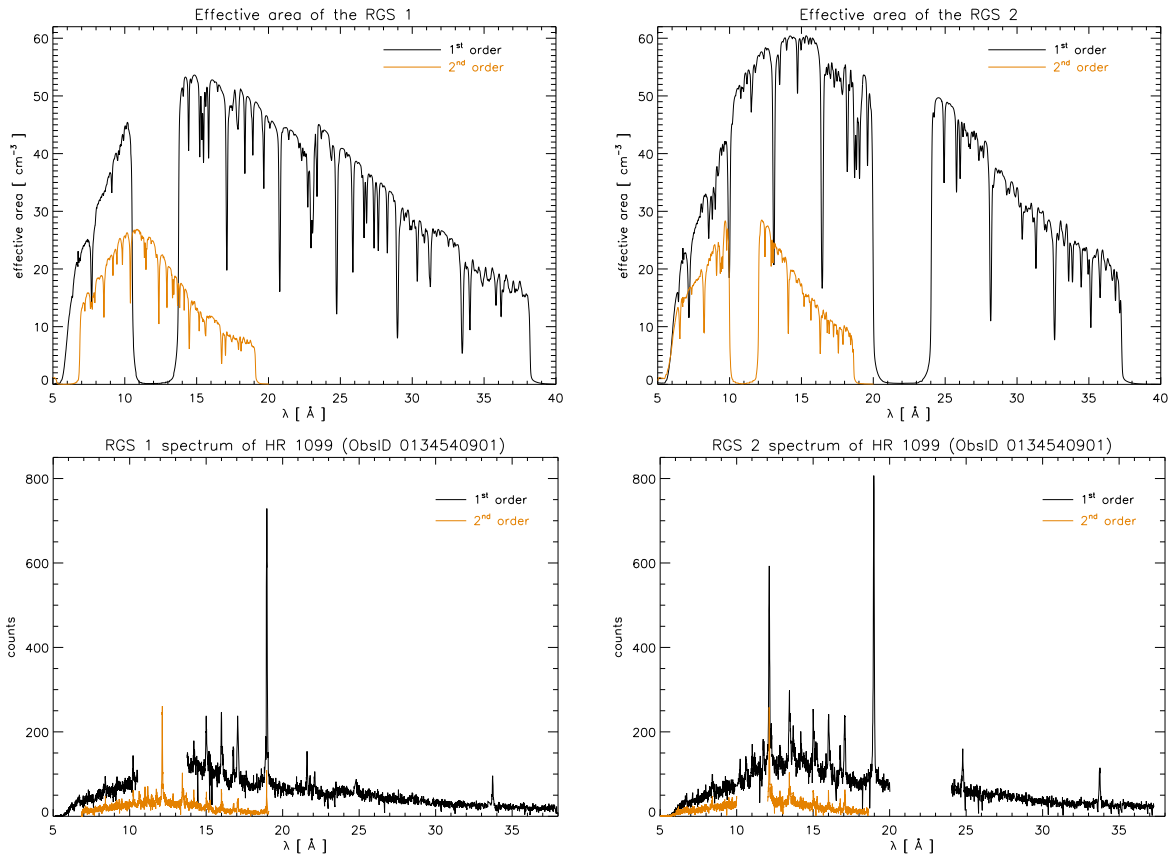

Figure 3.6: Effective area (upper panel) and spectra (lower panel) of the coronal X-ray source HR 1099 for RGS 1 (left panel) and RGS 2 (right panel) in first and second order. Note the slight shift in wavelength of the effective area.

Unfortunately, in both RFCs one of the nine CCD chips failed shortly after *XMM* started operating. In RGS 1 this affects CCD 7 and in RGS 2 CCD 4. This is unfavorable since both CCDs cover wavelength intervals usually including important emission lines in first order, for CCD 3 these are the Ne IX and X lines, and for CCD 6 this concerns the O VII triplet. In addition to the gaps between the single CCDs the RGS spectra suffer from a great number of bad pixels that must be excluded from the data, these gaps in the spectra strongly affect the analysis of single lines or even make a reasonable measurement impossible like with the O VIII line at 18.97 Å in RGS 2. The gaps and bad pixels determine the fine structure of the effective area of the RGS as shown in Figure 3.6. Apart from that the effective area is a smooth function that – in first order – starts rising at ≈ 6 Å, with a maximum at 15 Å followed by a slow decline and a drop to zero at ≈ 38 Å. The exact maximum values reached depend strongly on the off-axis angle of the source. Values between 45 cm^2 and 60 cm^2 at 15 Å are typical for small positional offsets, the RGS 2 has always a slightly higher effective area. The effective area for the second order is of similar shape, the maximum though is reached at 11 Å and does not exceed 30 cm^2.

XMM-Newton and its instruments are described in more detail in the "XMM-Newton Users' Handbook", Issue 2.3 (2005).

4 Modeling abundances and differential emission measure

The aim of this work is to reconstruct differential emission measures from a set of measured line fluxes and an inversion of the corresponding set of equations (see Equation 2.9). The reconstruction should be independent from the elemental abundances to reduce the number of free parameters; and the abundances should be determined afterwards. I applied two different methods based on different sets of X-ray and XUV lines described in Sections 4.3.1 and 4.3.2, the first approach involves abundance-independent ratios of two lines of the same element (Section 4.5), the second approach makes use exclusively of iron lines so that only the iron abundance enters the calculation (Section 4.6).

4.1 Data processing

The X-ray data used in this study are entirely archival and were downloaded from the corresponding online data archives, the *Chandra* Data Archive (`http://cxc.harvard.edu/cda/`) and the *XMM-Newton* Science Archive (`http://xmm.vilspa.esa.es/external/xmm_data_acc/xsa/`).

In case of *Chandra* HETGS and LETGS data, X-ray spectra were created directly from the pipeline-processed data products. Two scripts, `heggarf` and `leggarf`, originally provided by Jan-Uwe Ness and slightly modified for my purposes, were used to compute the response matrices and effective areas for each individual observation by means of the *Chandra* Interactive Analysis of Observations (CIAO) software package, Version 3.2 (in the course of this work patched to 3.2.2 without resulting in significant changes). The scripts apply the two tools `mkgrmf` and `fullgarf` on the positive and negative 1st orders of the spectra. Both were combined afterwards by two IDL scripts (`read_hetg` and `read_letg`) which generate ASCII files containing wavelength, source and background counts and corresponding errors as well as the effective areas and the exposure time. These ASCII files serve as input to the CORA line fitting program.

Since the wavelength grid of *Chandra* grating observations is fixed, it is quite simple to add up several datasets of the same source to a combined spectrum with higher signal-to-noise. The count numbers in each wavelength bin are summed, and a joint effective area is calculated by averaging the effective areas, weighted by the corresponding exposure times. Thus it was possible to create for example LETGS and HETGS spectra of Capella with total exposure times of 431.6 ks and 326.6 ks respectively. Ness et al. (2003a) used accordingly generated spectra for their analysis of iron contamination of the Ne IX triplet.

A greater deal of work had to be done concerning the *XMM* data. Pipeline-processed *XMM* RGS spectra are inappropriate for an analysis with CORA because they are background-subtracted, apart from that the calibration applied to these data is often obsolete and the proposal coordinates of the targets are occasionally shifted. The observation datafiles (ODF) of the particular datasets were therefore reprocessed with the *XMM-Newton* Science Analysis System (SAS), version 6.0. The metatask `rgsproc` was used to create non-background-subtracted spectra and the corresponding response matrices. A way round through xspec must be gone to create the spectrum files for the analysis since there is no easy way to compute count spectra and matching effective areas for a specified wavelength grid. xspec is able to output the desired data as ancillary ASCII files from the FITS files produced by `rgsproc`. The CORA spectrum

files for 1st and 2nd order each have been created from these ancillary files with another IDL script (`read_rgs`), which was as well as the method via xspec developed by Jan-Uwe Ness and later highly modified by myself.

Medium resolution spectra obtained from *XMM* EPIC images were used to obtain continuum measurements at higher energies. The EPIC data have also been reprocessed: Newly created event lists with high-background periods resulting from proton flares excluded were used instead of the pipeline products to extract the spectra. The main reason for the reprocessing was again the insufficient calibration status of the archival data. The images were produced with the SAS metatasks `epproc` and `emproc` using standard settings. Spatial images have been created and spectra from the source and adjacent background regions were extracted. The objects I have concentrated on in this work are rather strong X-ray sources and pile-up in their EPIC exposures is quite common. I therefore used the SAS tasks `epatplot` to inspect the created source spectra for pile-up contamination; I changed the shape of the extraction region from a circle to an annulus to exclude the pile-up contamined center of the line spread function if necessary. Response matrices and lightcurves were created afterwards. The SAS tasks for EPIC analysis were performed semi-automatically by the two scripts `EPIC_check` and `EPIC_ana`, provided by Jan Robrade.

4.2 Line fitting with CORA

The emission lines in the high-resolution HETG, LETG and RGS spectra were fitted with the stand-alone version of CORA line fitting tool (Ness and Wichmann, 2002), versions 3.2 and 3.4. The CORA program fits analytical line profiles to discretized, non-background-subtracted count spectra, using a maximum likelihood algorithm and applying Poisson statistics as it is most convenient for the analysis of low-count spectra.

CORA provides a lot of possibilities to constrain the fit, various parameters can be varied or fixed, included in the fit or excluded. I usually treated the central wavelength of the line as a free parameter since small wavelength shifts within the scope of the wavelength calibration are always possible, additional to the uncertainty in the absolute calibration of the wavelength scale for RGS data. Although the line widths of the four gratings are well-known and it is quite common to fix them I decided to treat them as free parameters as well. I took them as a quality indicator for the fit instead: Much to small or much to large fitted line widths indicate that other parameters, usually the source background, are erroneous. Lines whose fits did not converge in line width were thus rejected. If multiple lines were fitted at once I fixed the wavelength spacing and demanded an identical line width. CORA includes a χ^2 minimization and a parameterized median function to fit the source background underlying the emission lines. Both methods have their field of application as described in Ness et al. (2004), nevertheless from time to time they fail and the source background must be determined by eye.

The line fitting procedure is usually unproblematic with HETG and LETG spectra. The line spread function of the *Chandra* gratings can as a first approximation be described by a simple Gaussian; detailed investigations have lately revealed that a "β-model"

$$I(\lambda) = I_{max}\left(1 + \left(\frac{\lambda - \lambda_0}{\Delta\lambda}\right)^2\right)^{-\beta} \tag{4.1}$$

reproduces the measured line profile slightly better (see the Proposer's Observatory Guide). The β-model corresponds to a modified Lorentzian, with an exponent $\beta = 1$ resulting in a normal Lorentzian profile. For the *Chandra* gratings β was found to have a value of 2.5, and I adopted this value and the modified Lorentzian line profile. Admittedly – at least with the naked eye – I could not recognize a difference between the two fits or their quality.

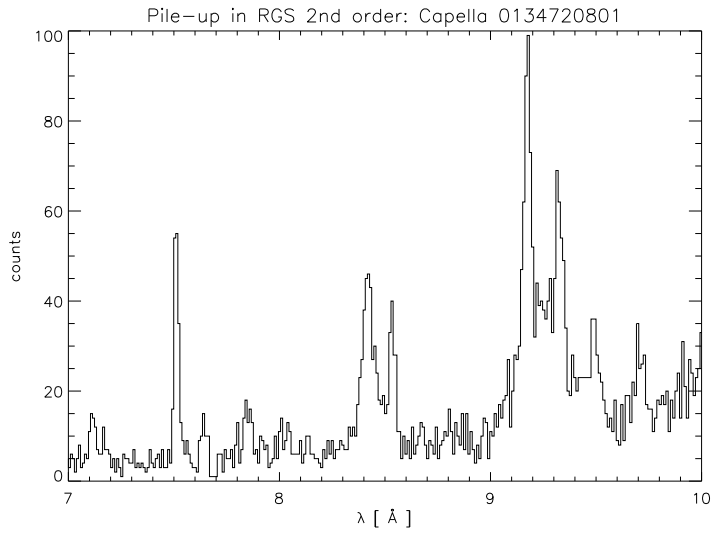

Figure 4.1: Wavelength interval from 7 Å to 10 Å in the RGS 1 spectrum of Capella in 2nd order. Additional to the Mg XII and VI lines, the pile-up caused features at 7.5 Å and 8.5 Å with a peculiarly small line width can easily be recognized.

HEG spectra often contain only few counts per bin as a result of the small binsize with many bins sampling the high spectral resolution. Multiple rebinning even for strong sources is therefore often required to get a reliable number of counts per bin. The same applies often to the XUV part of the LETGS spectra or to RGS in 2nd order and of course in general to underexposed spectra.

RGS spectra were for several reasons less easier to fit. On the one hand there are the many bad pixels on the RFC CCDs already mentioned in Chapter 3 that disturb the fitting process. Sometimes CORA can handle them, but there are several fatal cases where the resulting fit is bad or does not even converge. In the worst case the central portion of the line spread function is located on bad pixels what makes the fit impossible. On the other hand there is the instrumental line profile itself. A simple Lorentzian, i.e. $\beta = 1$, is usually considered for RGS spectra. Such a Lorentzian has broad wings complicating the assessment of the source background. Uncertainties and errors in the source background do not enter the error calculated by CORA, and thus it must be clearly stated here that the error introduced to the measured line counts due to an erroneous background level can exceed the statistical error by far. The full extent of this problem becomes clear in spectral regions with lots of lines like the wavelength range from 10 Å to 17 Å. The sum of the broad wings of the many lines there result in a "pseudo-continuum" as it can be recognized for instance by comparison of the fluxed HETG and RGS spectra of AU Mic (Figures 6.17 and 6.19), a source that has a rather weak true continuum. Such a pseudo-continuum arises – due to the finite line width and the wealth of unresolved weak lines – also for the *Chandra* gratings but the effect is much smaller.

When investigating the RGS second order spectra of a smaller sample of stars I discovered three at first sight unidentifiable lines at 7.5 Å, 8.53 Å, and 9.5 Å in the spectra of Capella. These lines were recognized to be caused by pile-up: Two simultaneously arriving photons from the strong Fe XVII lines at 15.01 Å or 17.05/17.09 Å or O VIII at 18.97 Å were detected as one event with the double energy. The order sorting mechanism by the intrinsic energy resolution of the CCDs therefore assigns these photons, whose location on the chip would attribute them to their original wavelength in first order, to the second order and half the wavelength. The resulting effects on the measured line fluxes in first order are small however: The doubled number of

counts contained in these lines (corresponding to the number of counts missing in the first order spectra) constitute less than 3% of those measured in first order for Capella, which is the only star from the sample where this effect was clearly visible at all. Pile-up in grating spectra is not topical in the literature, probably because the effects are very small for most sources, and few authors ever analyze the 2nd order spectra.

4.3 The lines used in this study

The strongest lines in astronomical X-ray spectra are associated either with iron lines of ionization stages suitably to the prevailing temperatures or with lines of the hydrogen and helium isoelectronic sequences of the most abundant elements.

Hydrogen is the simplest atom, consisting just of a proton – the nucleus – and a single electron. Its atomic transitions can as a first approach be calculated even with semi-classical physics. Quantum mechanics is needed to do this for helium, the next element in the periodic table of elements, possessing a second electron and a more massive nucleus. The equations yielding energy levels and describing atomic transitions can still be solved analytically for hydrogen and helium – this is too sophisticated for any other atom possessing more than two electrons and thus numerical methods are required.

The physics of hydrogen and helium atoms – especially concerning atomic transitions – is assumed to be well-known. For hydrogen- and helium-like ions, i.e. ions stripped up to one or two electrons respectively, similar considerations should apply. While hydrogen and helium themselves are totally ionized in X-ray emitting plasmas, H- and He-like ions of elements such as carbon, nitrogen, oxygen, neon, and so on exist and are actually quite frequent.

Theoretical emissivities for the lines I used in this study rest upon the CHIANTI database for emission lines developed by Dere et al. (1997) and extended to X-ray wavelengths in version 3.0 (Dere et al., 2001). For calculations in the development and verification phase of the methods used in this study CHIANTI version 4.2 (Young et al., 2003) was applied. The final calculations were made with the then available version 5.0 (Landi et al., 2005) that includes extended level population calculations considering dielectronic recombination and resulting radiative cascades especially for several iron ions, resulting in much longer times needed to calculate the emissivities but accordingly better results. The database contains wavelengths, radiative transition probabilities and excitation rate coefficients for a large number transitions of ions used in astrophysics as well as ionization equilibrium calculations; see the corresponding papers for further references.

4.3.1 H-like Ly α lines and He-like resonance lines

The energy needed to ionize elements to hydrogen- and helium-like states rises with increasing atomic number, this is also and in particular valid for the ionization process transforming the He-like ion to the H-like ion. Since these energies are realized in coronal plasmas by high temperatures, ratios measured of emission lines from both the He-like and the H-like states are a monotonic function of temperature. These ratios were utilized in the first DEM modeling approach.

The strongest emission lines arising from H-like ions belong to the Lyman series, and the strongest one of them is the Lyman α line, corresponding to the transition from the first excited level to the ground state. For the He-like ions a similar resonance line exists which forms in low-density plasmas a line triplet with two metastable lines, the intercombination and forbidden lines. The ratio formed by the two metastable lines was recently extensively used for density diagnostics. I concentrated my measurements and modeling attempts instead on the

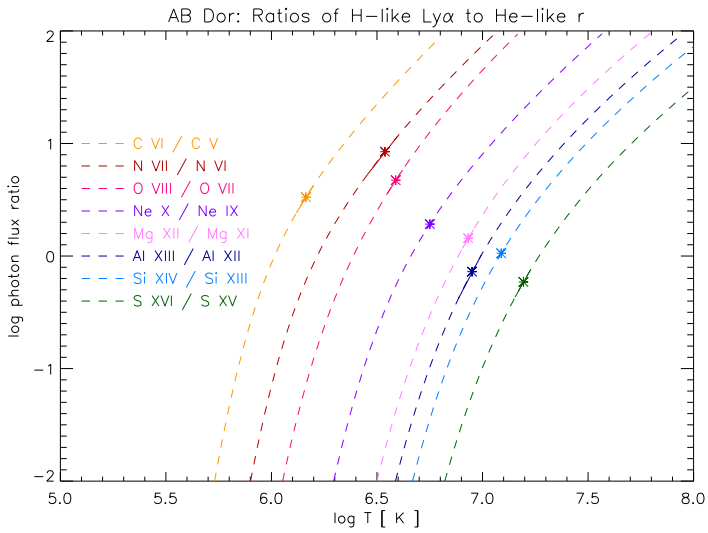

Figure 4.2: Theoretical temperature dependence of the photon flux ratio of H-like and He-like lines of several elements together with measured data points from AB Dor.

hydrogen- and helium-like resonance lines and therefore the terms "H-like" and "He-like line" and corresponding ratios refer to these lines in the following if not stated otherwise.

Typical stellar coronal sources exhibit too low temperatures to form hydrogen-like iron, apart from the fact that both the H-like Ly α line and the He-like resonance line are difficult to measure with the *XMM* and *Chandra* gratings (see also Section 4.3.2 below), this makes the measurement of a corresponding H-like to He-like ratio impossible.

The Ly α lines of Ca XX and Ar XVIII have wavelengths of 3.02 Å and 3.73 Å, the corresponding He-like resonance lines of Ca XIX and Ar XVII are found at 3.18 Å and 3.95 Å. These lines cover the high-temperature tail of the emission measure distribution since temperatures of at least 10 MK are needed even to form the corresponding ions. *Chandra* HEG and MEG exclusively provide the ability to detect these lines but measurements are still problematic: Their emissivity is low due to the generally low abundances of calcium and argon and the high required temperatures, resulting in low signal-to-noise. Thus even with the high spectral resolution of the HEG it is impossible to resolve the three components of the He-like triplets (the intercombination and forbidden lines of Ca and Ar being located at 3.19 Å and 3.21 Å, and 3.97 Å and 3.99 Å respectively). I therefore measured these lines where possible but only for later abundance assignments. Resulting ratios did not enter the *DEM* determinations.

Similar but less fatal problems arise for sulfur and aluminium, so that ratios of these two elements could hence serve as input for the *DEM* fitting. Sulfur is one of the more abundant elements, allowing often the measurements of the S XVI Ly α line at 4.73 Å and the S XV resonance line at 5.04 Å with HEG and MEG. Aluminium, though less abundant, benefits from the high effective area especially of the MEG at the corresponding wavelengths of 7.17 Å and 7.76 Å for the Al XIII Ly α line and the Al XII resonance line. Measurements with RGS and LETGS are not possible because both He-like triplets would not be resolved, the same applies for Al XIII and the neighboring Mg XII Ly β line at 7.11 Å. Furthermore, the effective area of both instruments is too low for the sulfur lines.

The aluminium and sulfur lines share a problem with the calcium and argon lines: Features corresponding to these lines are often clearly visible in the spectra but the noise level and therefore the underlying background is easily underestimated. This has on the one hand a non-negligible influence on the deduced ratios, on the other hand it leads to systematically

overestimated abundances for these elements.

Silicon H-like and He-like ions are in their formation arranged between sulfur and aluminium on the temperature scale. Measurements of the Si XIV Ly α line or the Si XVIII resonance line at 6.18 Å and 6.65 Å profit from both an increased effective area with now all four gratings and instruments and a relative high abundance level. Problems with silicon lines arise primarily through detector calibration issues: Absorption edges and other features caused by silicon contained in the detector material have to be well-modeled in the instrumental response.

Mg XIV at 8.42 Å is a single, unblended line easy to measure in all detectors. Testa et al. (2004) examined the contamination of the Mg XI triplet with lines arising from iron and the neon Lyman series with *Chandra* HETGS data. Since the resulting effects limited on the resonance line are small compared to other error sources I neglected any blending of this line in my measurements and calculations. It must be noticed that the Si XIII and Mg XI triplets are still difficult to resolve with RGS and LETGS.

Neon lines cover intermediate temperatures of ≈ 6 MK. The Ne X Ly α line at 12.134 Å is frequently one of the strongest lines in stellar coronal X-ray spectra. In RGS and LETGS it is blended with Fe XVII at 12.124 Å, but the resulting effects can normally be neglected. The whole Ne IX triplet suffers from strong contamination with several iron lines, even the resonance line at 13.447 Å is severely blended, mostly with lines from Fe XIX.

A special treatment is necessary to get a reliable measurement for this line, especially with the RGS and the LETGS that can not resolve all the emerging lines. Ness et al. (2003a) tackled this problem for Capella, where the blending effects are extremely strong due to a relatively high iron abundance in combination with low temperatures. In order to get reliable density measurements – the weak Ne IX intercombination line at 13.55 Å suffers most from the blending – they fitted all lines (about 20 iron lines, arising from ionization stages XVII to XXII, and some nickel lines) in that spectral region they could identify in a combined *Chandra* HEG spectrum composed of most of the Capella HETGS datasets available at that time. The measured line fluxes of the contamining lines where then artificially broadened to fit the spectral resolution of the other instruments, and the fit of the neon lines was performed leaving the relative strengths of the contamining lines fixed. A good agreement between the different datasets was achieved.

This method could in principle also be applied to other stars. The problem is though to obtain the basic HEG spectrum with a satisfactory signal-to-noise level. Instead the Capella HEG spectrum could be taken – assuming the temperature structure of Capella and the new star being the same when leaving the relative strengths of the lines constant. The single three neon lines as well as an overall normalization factor for all the contamining lines in total could then be fitted to the observed spectrum. Jan-Uwe Ness incorporated this approach with the IDL version of CORA and made the script available to me. I generalized and automated the routine (called thereafter `ne_fit`) and in particular added the possibility to remove part of the initial lines from the fit, since I was not interested in fitting the whole triplet but only in the resonance line. It is therefore possible to concentrate only on the neighboring Fe XIX lines to abandon the assumption of the coinciding temperature structure. Figures 4.3 and 4.4 show that this worked very well.

Oxygen H- and He-like lines mark the transition to lower temperatures around 2 MK in stellar coronae such as they are typical for the sun. Both the O VIII Ly α line at 18.97 Å and the whole O VII triplet with the resonance line at 21.6 Å are easy to measure and are relatively unblended apart from some satellite lines, the O VIII line is usually one of the strongest lines in the spectrum similar to Ne X Ly α. Unfortunately the effective area of the HEG drops to zero in this wavelength region, it is impossible to measure O VII with the HEG and also O VIII is only rarely measurable despite the high emissivity of the line.

The same applies for nitrogen, which can be accounted to even lower temperatures, in combination with the MEG, also because the N VII line at 24.78 Å and the N VI triplet lines located at

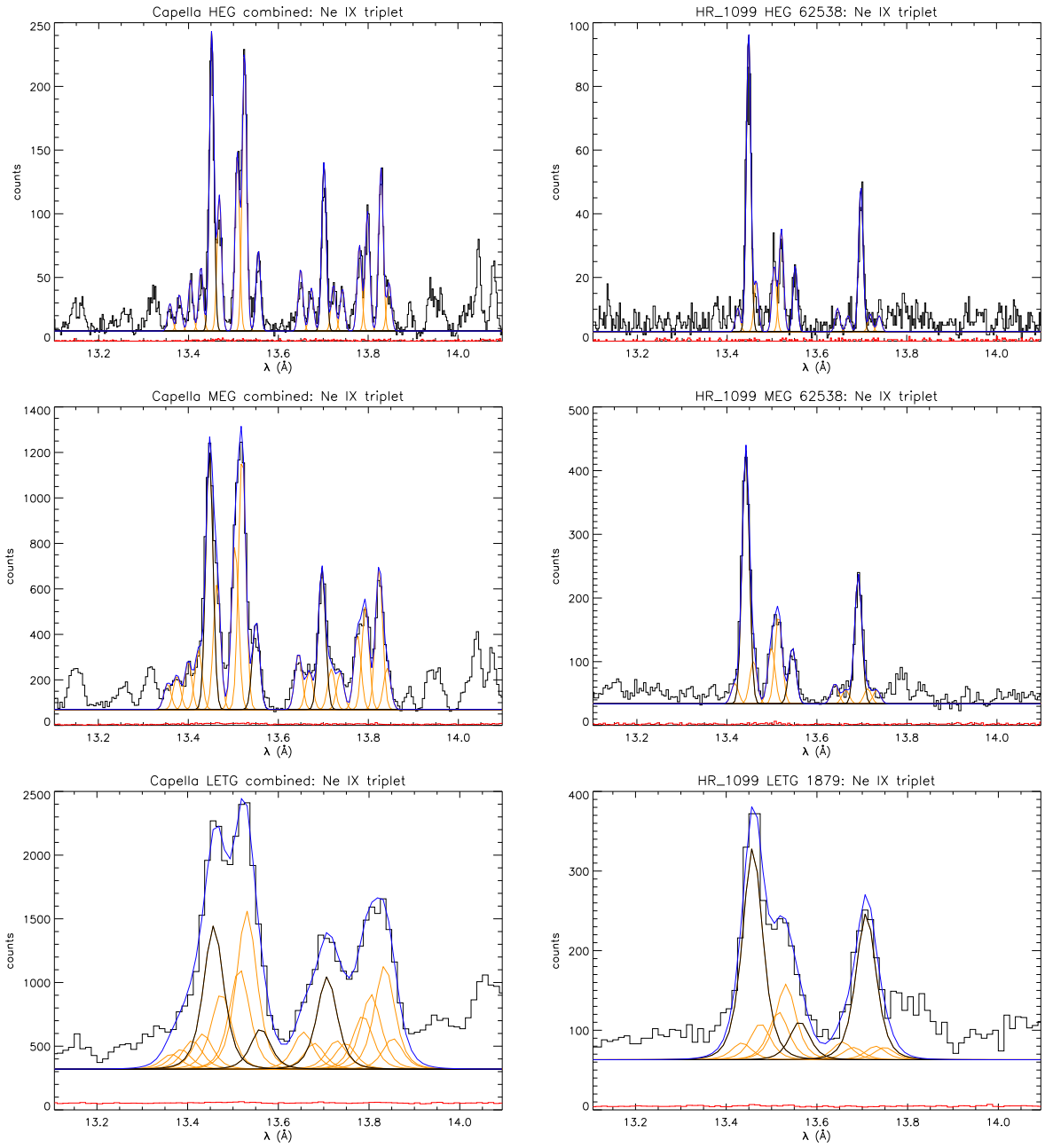

Figure 4.3: Output of the `ne_fit` routine for *Chandra* spectra. The left panel shows the fits to the Ne IX triplet for Capella, where the iron contamination is very strong. For HR 1099 (right panel), the effects are less momentous. Part of the lines were excluded from the fit (especially the Fe XVII line at 13.83 Å that is strong in Capella, leaving essentially only Fe XIX lines) to account for the differing temperature structures of the two stars. The upper panel gives the HEG spectra, so the upper left plot shows the initial Capella HEG fit all further measurements are based on. Middle and lower panel display the MEG and LETG spectra. While it is still possible to distinguish between the single lines with the MEG, they merge to an unresolved conglomerate in the LETGS.

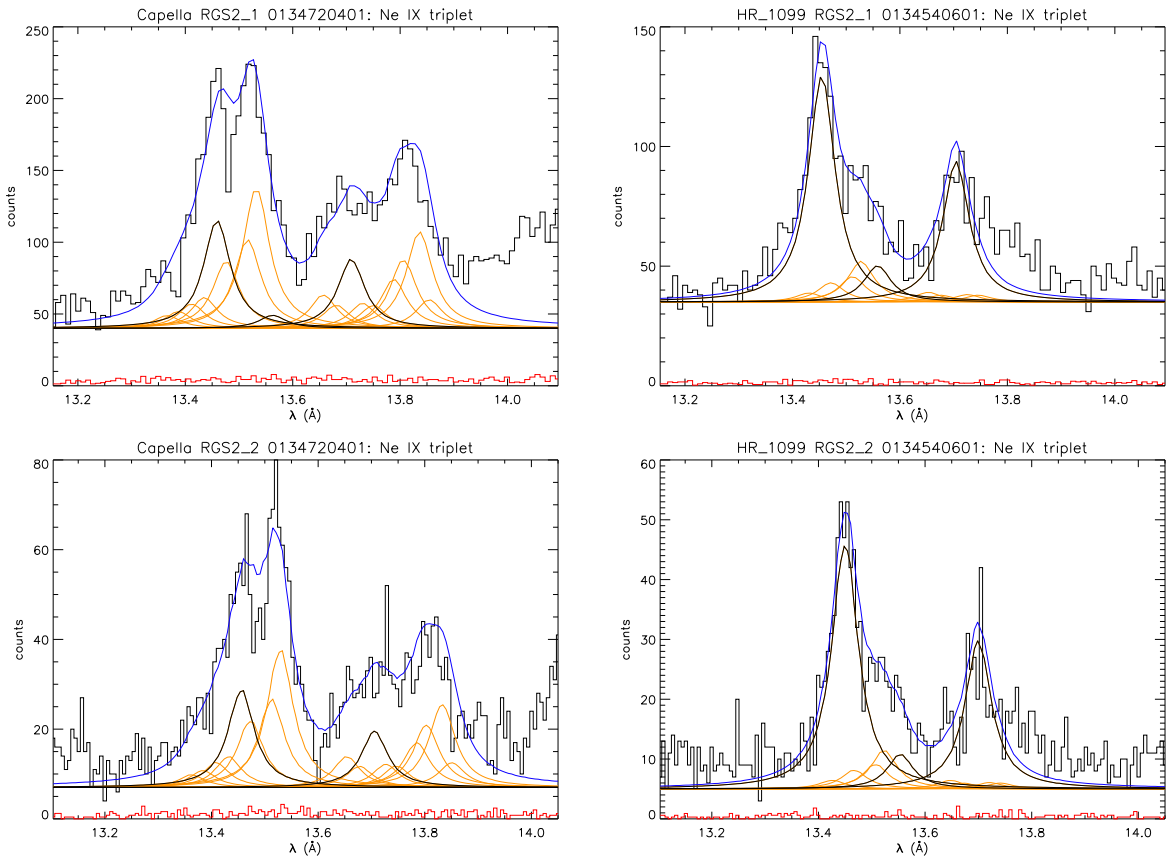

Figure 4.4: Same as in Figure 4.3 but for *XMM-Newton* RGS 2 spectra in first and second order. Only a very low iron abundance would allow reasonable measurements of the neon lines without additional means. In second order the advantage of smaller line width is compensated by the lower effective area, so that measurements in the second order seldomly lead to improved measurements.

28.787 Å, 29.082 Å, and 29.534 Å are in general not that strong compared to oxygen and neon.

Only RGS in 1st order and LETGS allow the measurement of the very low-temperature carbon lines, i.e. C VI Ly α at 33.74 Å and the C V triplet with the resonance line at 40.268 Å. The latter is even only measurable with the LETGS where it suffers from low effective areas and contamination with the Ne IX triplet in 3rd order. The C V resonance line itself is heavily blended with the Ne IX resonance line and the sourrounding iron lines. The results of the `ne_fit` routine described above were therefore enlisted to assess the degree of contamination of the carbon triplet by the neon and iron lines. The estimated blending, deduced by scaling the counts measured in the Ne IX triplet, is subtracted from the source counts and assigned to the instrumental background. The C V lines are fitted afterwards, whenever they are measurable. This method was in a more simplified manner and including less iron lines applied to Capella by Ness et al. (2001). The procedure was generalized to adopt the results of the corresponding fit to the neon triplet for any arbitrary LETGS dataset and became part of the `ne_fit` routine.

4.3.2 Iron lines

In general, the atomic data for iron lines are not as reliable as for H-like and He-like lines. Vast improvements have been achieved by incorporating the calculations of Gu (2003) including among other things dielectronic and radiative recombination processes. When I switched from CHIANTI 4.2 to 5.0 (the latter includes the data from Gu, the older version did not) several

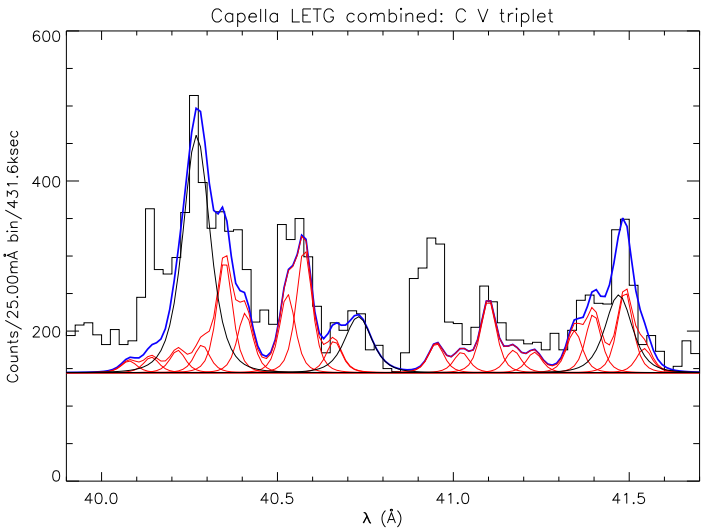

Figure 4.5: Fit to the C V triplet of Capella with all available *Chandra* LETGS obserations summed up. The underlying fit to the Ne IX triplet is shown in the lower left plot of Figure 4.3. The fit reproduces whole triplet quite well, when it is considered that the Fe XVI line visible at 40.15 Å and the Si XII line at 40.91 Å are not included in the fit.

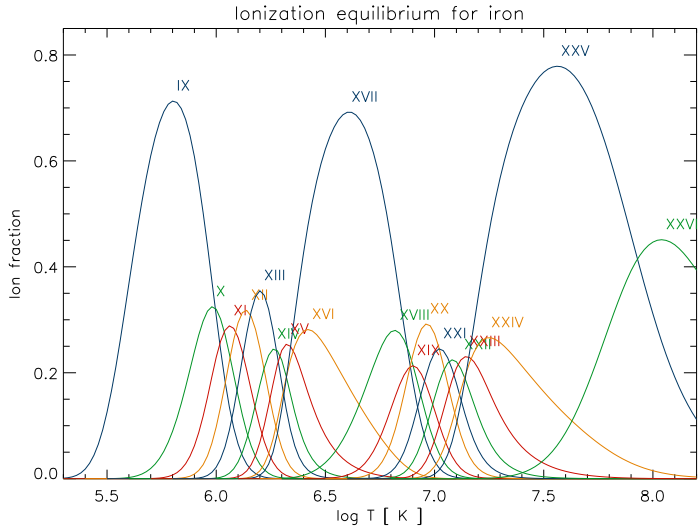

Figure 4.6: Ionization equilibrium for Fe IX to Fe XXVI after Mazzotta et al. (1998), as implemented in the CHIANTI database. The ions having noble gas configuration, i.e. Fe IX, Fe XVII, and Fe XXV, comprise the main fraction of occurrence and form over broad temperature ranges while the other ionization stages are less frequent and persist at smaller temperature intervals.

inconsistencies disappeared, theoretical line ratios of certain lines fitted the measured ones much better but are still far from perfection.

Fig. 4.6 shows that H-like Fe XXVI does not form until extremely high temperatures ($\gtrapprox$ 50 MK, peak formation temperature $\approx$ 100 MK) are reached. Furthermore, up to 80 MK the dominant ion species is He-like Fe XXV with a peak formation temperature of approx. 40 MK, so it is very unlikely to detect Fe XXVI lines such as Ly α at 1.78 Å in the spectra of stellar coronae since such high temperatures are quite unusual and only reached in flaring states. Given this fact

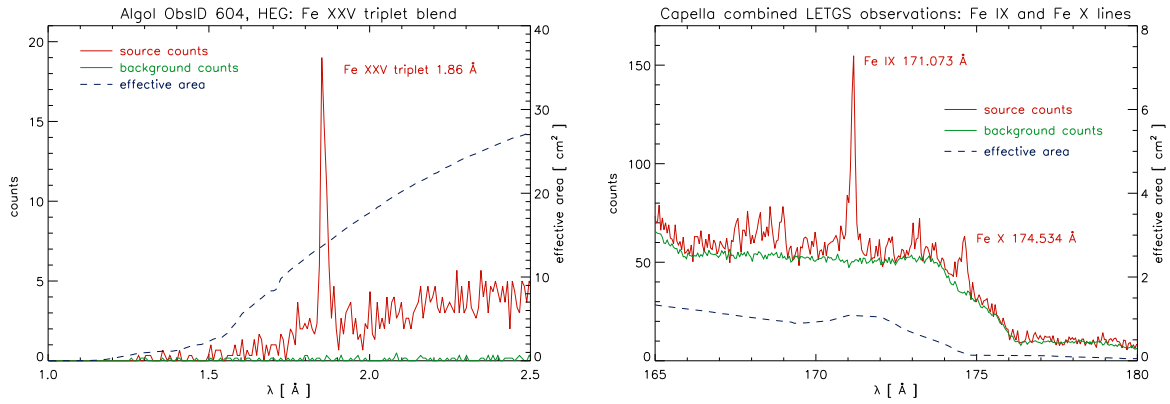

Figure 4.7: Iron lines at the boundaries of the temperature range. Left: The Fe XXV triplet at 1.86 Å. Right: Fe IX and Fe X at 171.1 Å and 174.5 Å respectively.

it is not very remarkable that I was never able to distinguish the Fe XXV Ly α line from the background in *Chandra* HEG spectra.

The Fe XXV triplet at 1.86 Å can be observed however, if temperatures exceed 15 MK and the signal-to noise is high enough in the HEG and sometimes also in the MEG spectra. The triplet must be measured as a whole, the individual resonance, intercombination and forbidden lines can not be resolved. The right panel of Figure 4.7 shows the Fe XXV triplet in the HEG spectrum of Algol. The line is clearly visible but some issues affect the measurement of the line flux: First, the effective area of the HEG just starts to increase to reasonable values which raise the line over the noise level. The instrumental background is not a problem but the correct placement of the continuum level because of the steep slope resulting from the increase of the effective area. Furthermore, the triplet itself is severely blended by a multitude of weaker lines of highly ionized iron whose contribution to the line complex can not be assessed. A simple measurement of the counts contained in the line will therefore overestimate the flux of the triplet. The treatment of this line was thus the same as for the calcium and argon lines described above. MEG spectra sometimes also show the Fe XXV triplet, but measurements are even more dubious because of the very low effective area of the MEG at that wavelength. All other lines of Fe XXV are too weak to measure.

Fe XXIV has a much lower peak formation temperature of 18 MK, but the ion fraction reaches 27% at maximum. The strongest lines of Fe XXIV appear in the wavelength range of 10 Å to 12 Å, e.g. at 10.619 Å, 11.029 Å, 11.171 Å, and 11.426 Å. Unfortunately this spectral region is quite crowded with other lines of highly ionized iron (see Figure 4.8), and the line at 11.171 Å is the only one that is hardly affected by blending. I included this line in my calculations, but measurements with the LETGS and the RGS are somewhat questionable.

The strongest lines of Fe XXIII are also found in the wavelength domain around 11 Å, namely at 10.981 Å, 11.018 Å, 11.736 Å, and 12.175 Å. None of these lines is without blending, but with HEG and MEG it is possible to separate the line at 11.736 Å from the Fe XXII line at 11.769 Å, both lines will in this case be included in the calculations. In LETGS spectra a strong line can be found at 132.91 Å. Unfortunately, it is blended with a strong Fe XX line at 132.84 Å, and this blend is usually unresolvable. It is possible to calculate the contribution of the Fe XX line to the blend: Its theoretical photon flux ratio relative to the Fe XX line at 121.84 Å stays constant at ≈ 0.7 independent of density and temperature (see the left panel of Figure 4.9). The corresponding ratio of the effective area of the LETGS at the two wavelengths is ≈ 1.45. The measured counts of the line at 121.84 Å had therefore to be multiplied by 0.98 and the result to be subtracted from the measured counts at 132.9 Å to obtain the fraction of Fe XXIII

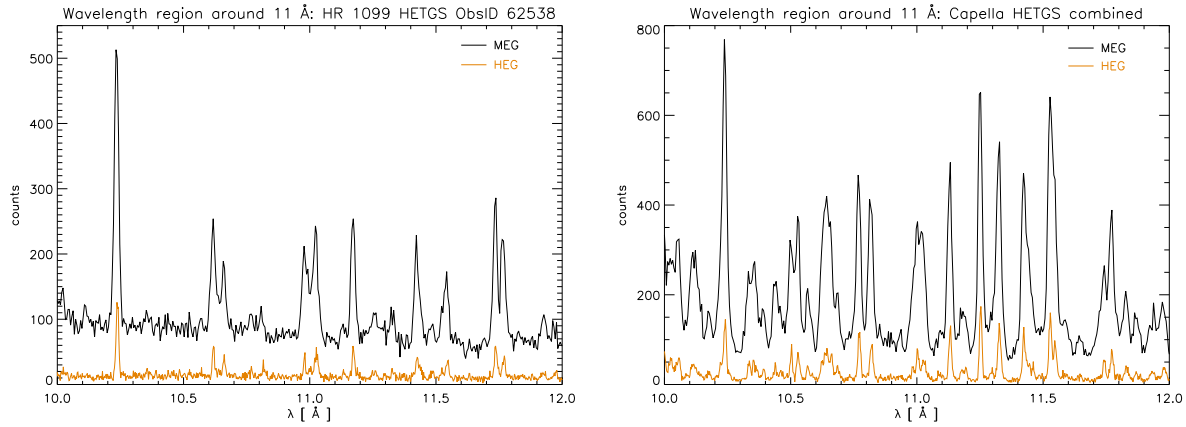

Figure 4.8: The crowded wavelength region from 10 Å to 12 Å. Left: HETGS spectra of the high-temperature RS CVn binary HR 1099. The strongest line is Ne X Ly β at 10.239 Å, the other lines arise from higher ionization stages of iron. Right: The same spectral region for Capella, which exhibits a higher iron abundance and lower temperatures than HR 1099. Additional strong lines from lower-temperature ionization stages of iron such as Fe XVII and Fe XIX as well as lines from nickel appear and complicate the isolation of individual lines; adequate measurements with LETGS and RGS become impossible.

to the blend. I applied this method to several spectra and it led to consistent results (the iron abundance calculated from the Fe XXIII line at 132.91 Å applying a DEM calculated from the H-like / He-like ratios matched that of the other iron lines) but it should be kept in mind that the indirect measurement of this line introduces new uncertainties to the iron line DEM fit at higher temperatures.

The peak formation temperature reduces to 12 MK for Fe XXII. Strong lines in the short wavelength range include the ones at 11.427 Å, 11.769 Å, 11.921 Å, 11.936 Å, and 12.757 Å. All of them are blended, the treatment of the 11.769 Å line is described above. In the long wavelength range two strong lines can be observed with the LETGS at 117.15 Å and 135.79 Å.

Some of the XUV lines of Fe XXI can be used as density indicators (cf. Ness et al., 2002a). I used the two strongest ones which can can be found at 128.75 Å and 117.5 Å. At shorter wavelengths, stronger lines can be found at 9.475 Å, 12.282 Å, 12.327 Å, 12.395 Å, 12.499 Å, 13.507 Å and 14.008 Å. Again, all of suffer from blending. The strongest one of them is the line at 12.282 Å, its blend with an Fe XVII line at 12.264 Å can sometimes be resolved with MEG and HEG, therefore I included this line in my calculations.

Three strong lines of Fe XX at 12.812 Å, 12.827 Å and 12.845 Å group to a blend that can be measured with all instruments. In my calculations I neglect the contribution of a line of Fe XXI 12.823 Å to that conglomeration. The strong line at 121.84 Å was already mentioned in connection with the treatment of the XUV Fe XXII line. I also selected this one together with another line at 118.68 Å for the calculations.

As described above, many Fe XIX lines are found within and in the immediate vicinity of the Ne IX triplet, the strongest ones are found at 13.456 Å, 13.506 Å, 13.525 Å and 13.799 Å (see also Figure 4.3). Some of these lines may be fit directly in HEG and MEG spectra but this is impossible for LETGS and RGS spectra. The best alternative is to use the global fit to the iron lines by the `ne_fit` routine, but this introduces similar problems to the calculations as does the treatment of the XUV Fe XXIII line. In particular theoretical ratios of some of these lines do not exactly fit the measured ratios in the Capella reference spectrum (see the right panel of Figure 4.9), even with CHIANTI 5. Nevertheless, I applied this method, because the other stronger lines in the short wavelength range, located at 14.669 Å, 15.081 Å, 15.208 Å and 16.11 Å, are

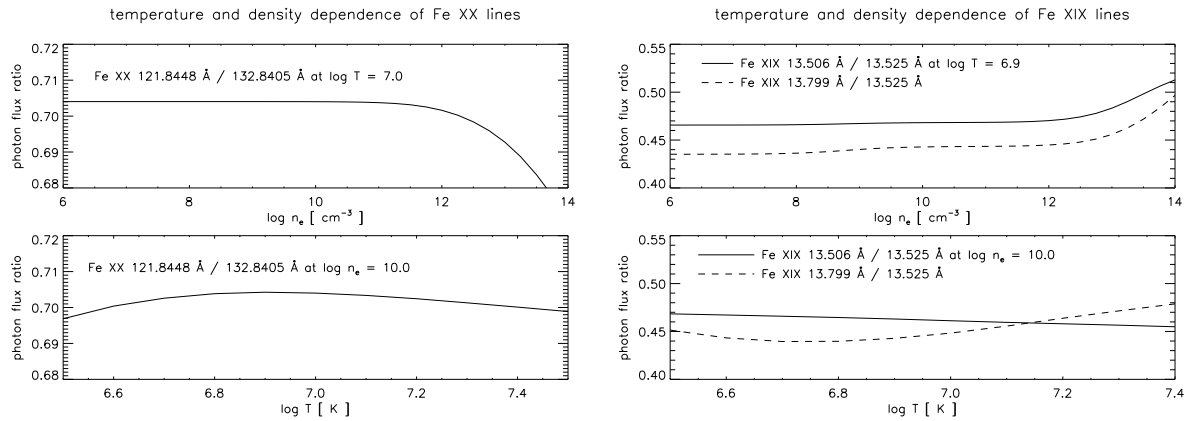

Figure 4.9: Left: Theoretical line ratio of the two Fe XX lines at 121.84 Å and 132.84 Å and its variation with density and temperature, calculated with CHIANTI. The ratio as a function of temperature is calculated over the temperature range where Fe XX forms (cf. Figure 4.6). Note the very small range of the ordinate, the ratio is next to constant. Right: Theoretical line ratios of the three Fe XIX lines at 13.506 Å, 13.525 Å and 13.799 Å. While the ratio 13.799 Å / 13.525 Å fits the measured ratio of 0.44 in the combined Capella HEG spectrum (used as a reference in the `ne_fit` routine) quite well, the 13.506 Å / 13.525 Å ratio deviates from the measured value of 0.64.

also affected by blending. In the long wavelength range, Fe XIX lines at 101.55 Å and 108.36 Å can be taken instead. The differences between theoretical and predicted fluxes for these lines have been investigated by Ness et al. (2003a) and more recently by Desai et al. (2005).

With a further decrease in the peak formation temperature from 8 MK for Fe XIX to 6.5 MK Fe XVIII is reached. The two strongest lines of this ion are found at 14.207 Å and 16.007/16.076 Å. Measurements of the two lines near 16 Å are strongly affected by O VIII Ly β at 16.006 Å. Fe XX at 14.26 Å is in RGS and LETGS unresolvable from the line at 14.2 Å but gives only a minor contribution, therefore this line will be included in the calculations. At longer wavelengths, the strongest Fe XVIII line is found at 93.92 Å, but a blend with Fe XX at 93.78 Å may not be resolved in case of low signal-to-noise. Therefore I preferred the measurement of the somewhat weaker line at 103.94 Å whereever possible. Desai et al. (2005) also investigated the reliability of recent atomic data for Fe XVIII.

The Ne-like Fe XVII is the most frequent iron ion in stellar coronae and the strongest iron lines in coronal spectra normally come from Fe XVII. It forms over the broad temperature range from 2 to 8 MK, with a peak formation temperature of 4 MK. Five very pronounced lines located at 15.015 Å, 15.262 Å, 16.777 Å, 17.05 Å and 17.095 Å can be detected, and because in RGS spectra they are, together with the Fe XVIII line at 14.2 Å, often the only iron lines that can be measured with reasonable accuracy, I included all of them in the calculations. I summarized the measured counts of latter two, since they are not resolvable in the LETGS and in RGS 1st order. Fe XVII benefits in particular from the inclusion of the calculations by Gu (2003). While test fits based on CHIANTI 4.2 resulted in considerable discrepancies between these lines, the final calculations done with CHIANTI 5.0 give a much more consistent view. Several authors, e.g. Ness et al. (2003c) and Matranga et al. (2005), used ratios of these lines as an opacity indicator. Ness et al. (2003c) arrive at somewhat contradictory results with the atomic data available at that time. It would be interesting to adopt their results to the new atomic data.

With Fe XVI and its peak formation temperature of ≈2.5 MK the domain of lower coronal temperatures is definitely reached. The much less frequent Fe XVI has its strongest lines at

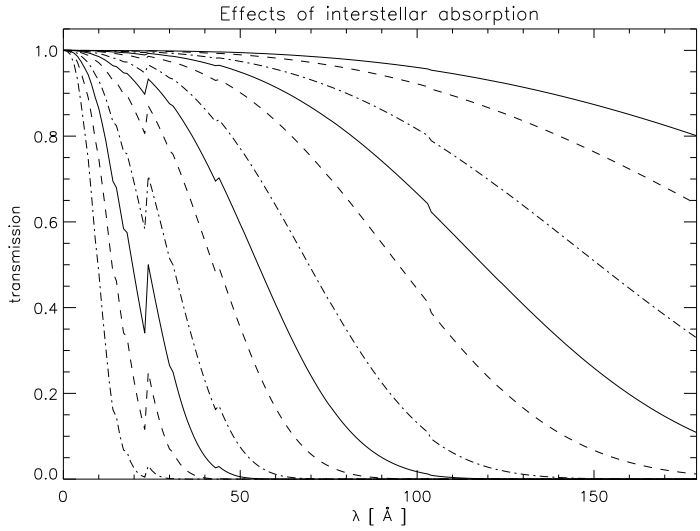

Figure 4.10: Transmission coefficients as a function of wavelength for different values of hydrogen column density increasing from 1×10^{18} cm^2 to 5×10^{21} cm^2. The solid lines correspond to a multiplicative factors of 1, the dashed lines to a factor of 2, and for the dash-dotted lines the factor is 5. Note the pronounced oxygen edge at 22.9 Å for column densities around 10^{21} cm^2, the carbon edge is also visible at lower column densities.

54.71 Å, 62.87 Å, 63.71 Å and 66.36 Å, so they are exclusively observable with the LETGS. Each of them is located in one of the two detector gaps of the HRC-S though, and therefore they suffer from a significant decrease in effective area. (See Figures 3.3 and 3.4). The line at 66.36 Å is contamined by the forbidden line of the O VII triplet in 3rd order. I measured the stronger one at 63.71 Å whereever possible but it is usually not included in the calculations; I suspect the either the atomic data of the Fe XVI lines or the LETGS calibration to be poor because these lines provide systematically lower iron abundances.

Seldomly Fe XV allows the measurement of the only stronger line in the available wavelength range at 69.68 Å. The low-temperature ions Fe XI to Fe XIV instead do not show strong lines measureable with the *XMM* and *Chandra* gratings. The measurement of the Fe X line at 174.5 Å despite the very low effective area and the high instrumental background of the LETGS at that wavelength (see the right panel of Figure 4.7) is an indicator for low temperature plasma, since the peak formation temperature reduces to 0.9 MK for Fe X.

The Ar-like Fe IX line at 171.1 Å, although at first sight suggesting even lower temperatures because of the peak formation temperature of 0.65 MK, is nonetheless easier to measure because of the higher ion fraction and the broader temperature range covered. Unfortunately, the *Chandra* LETGS is not particularly suitable to observe in that wavelength range. Due to the low effective area (cf. Figure 4.7 and Chapter 3) count statistics are not very good which introduces large errors to the calculations.

4.3.3 Interstellar absorption

Although the objects I studied in the course of this work are close by in the sense of astronomical distances, attenuation by interstellar absorption must be taken into account for the lines with longer wavelengths, especially for iron lines in the XUV range. The measured column densities for the stars treated in Chapter 6 range from $\approx 1 - 5 \times 10^{18}$ cm^2, so noticeable effects become visible for wavelengths $\gtrapprox 100$ Å as can be read off from Figure 4.10.

CHIANTI does not provide the facility to compute the interstellar absorption for certain wavelengths, thus I adopted the IDL routine `ismtau` from the Package for the Interactive Analysis of Line Emission (PINTofALE, Kashyap and Drake, 2000) that computes the absorption cross sections of the ISM in the X-ray and XUV range as a function of wavelength. This routine combines the calculations of several authors and is described in more detail in Chapter 3.2 of the PINTofALE User's Book, Version 2.0, 2004.

4.4 Continuum measurements

Continuum measurements are necessary to provide a normalization to the reconstruction of theDEMM. There are essentially two methods to assess the level of the source continuum for a stellar coronal X-ray source whose spectral emissivity is in general dominated by emission lines: On the one hand one could look for regions in the spectrum that are free of strong lines and take the average level of measured counts per Ångstrøm as a measure of the continuum flux at a certain wavelength, on the other hand the line fluxes and the underlying continuum fluxes can be fitted in one step.

Both possibilities suffer essentially from the same problem: the treatment of the pseudo-continuum produced by weak, unresolved lines. Concerning the first method, there are no spectral regions that are totally free of lines, and even in those regions where no strong lines appear, weaker lines are known and should actually be considered by an additional but unassessed level of emission. Also the current atomic databases include a wealth of weaker lines but another bulk of them must be considered unidentified or even unknown, apart from the uncertainty of the atomic data of the already incorporated lines. Hence global fitting routines based on the second method such as xspec or SPEX are also affected. Both methods would of course improve from a combination with each other or iterative fitting procedures.

My own continuum measurement methods are rather simple and somehow primitive. Spectral regions where only few weak lines are listed in CHIANTI are found at wavelengths of 2-3 Å, 19-20.5 Å and around 25.5 Å. The latter two regions are at lower temperatures dominated by free-bound emission with striking edges from the oxygen K series (see Figure 2.3), so the continuum flux there is slightly abundance dependent. *Chandra* HEG spectra provide enough effective area for a reliable measurement in the first mentioned region while for LETG spectra one of the latter two can be selected. I chose the region from 19.5-20.5 Å because there are fewer lines listed than in the region around 25.5 Å. I cut the range from 19.0-19.5 Å since the emission there is dominated by the wings of the strong O VIII line. The continuum flux is computed by summing the measured source counts in these spectral regions, subtracting the background counts and dividing by exposure time and the effective area at the central wavelength. The contamination by existing lines is not considered, and no iterative steps to account for them are applied. Of course, this procedure will always overestimate the true continuum flux.

I did not apply this technique to RGS spectra since the first wavelength interval is uneligble due to low effective area and the latter two were considered to be heavily contamined by the neighboring stronger lines because of the broad wings of the lorentzian-shaped line spread function of the RGS. Instead, I tried a different approach here: Medium-resolution spectra were created from the corresponding EPIC images as described above. These spectra were fitted in xspec with APEC models with two or three temperature components and variable elemental abundances. After successful and reliable fitting the abundances of the elements S, Ar, Ca, Fe and Ni were set to zero, leaving the model flux at energies >2 keV limited to pure continuum emission. Fluxes between 1-2 Å, 2-3 Å, and 3-4 Å (corresponding to the energy ranges 3.098-4.131 keV, 4.131-6.198 keV, and 6.198-12.396 keV) were calculated. This method to assess the continuum flux is of course heavily dependent on the prior fitted spectral model.

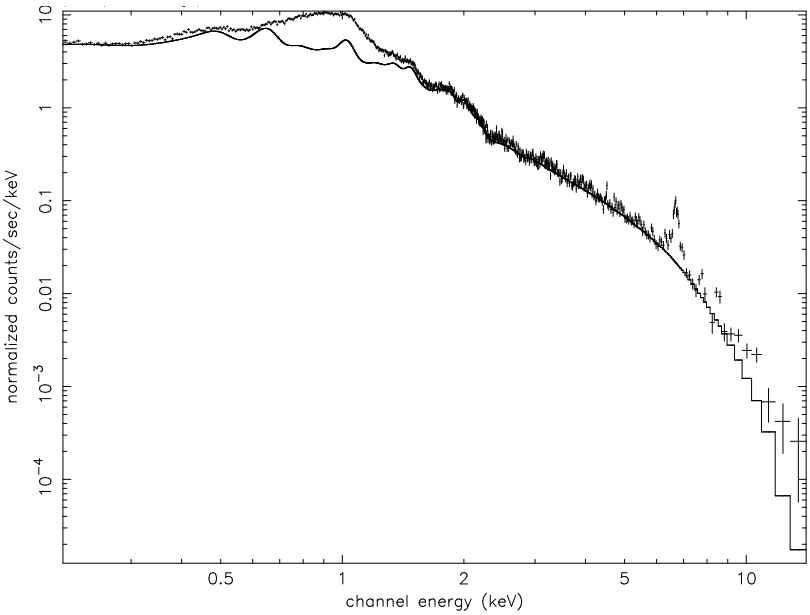

Figure 4.11: Medium-resolution EPIC PN spectrum of Algol and the adapted model with the abundances of S, Ar, Ca, Fe and Ni set to zero. The most significant deviations occur due to iron lines, as well at lower energies around 0.7-1.0 keV ($\approx 10 - 17$ Å) which are not of importance here, and at 6.7 keV (1.7-1.9 Å, Fe XXV and Fe XXVI).

4.5 Differential emission measure from ratios of H-like to He-like lines

Various methods to reconstruct the differential emission measure from high-resolution X-ray and UV spectra can be found in the literature, see Güdel (2004) for an overview. Actually most approaches make use of "emission measure distributions", i.e. discrete emission measures binned in temperature. In this respect probably the most refined technique is the `MCMC_DEM` routine incorporated in the PINTofALE software package (Kashyap and Drake, 2000). It is based on a Monte Carlo method developed by Kashyap and Drake (1998) and provides also the statistical uncertainties of the best-fit emission measure distribution. More details can be found in the PINTofALE User's Book.

The mathematical realization of the inversion problem introduced by a set of equations in the form of Equation 2.9 can be achieved with several techniques. Most of them bring along additional constraints to improve the stability of the fit and to avoid ambiguities, such as positivity, artificial smoothness or a certain shape. The physical meaning and validity of these constraints must be critically evaluated though. Many of these methods make use of iterative optimization techniques.

One basic approach is to apply matrix inversion methods, usually involving regularization, to the set of equations. Another one is to fit analytical functions to the DEM or to parts of it (e.g. their slopes), for instance power laws with certain cutoffs in temperature have been discussed to approximate the DEM of coronal structures. A way inbetween is realized by spline-fitting techniques interpolating a smooth DEM between measured data points, see for instance the routine `CHIANTI_DEM` that is part of the software package appended to the CHIANTI database and described in more detail in the CHIANTI Users Guide, Version 5.0, 2005.

All these DEM reconstruction techniques are usually – parallel to the integral inversion problem – also confronted with a set of additional free parameters in the fit: the elemental

abundances. Schmitt and Ness (2004) adopted the idea to make use of abundance-independent line ratios applied for example by McIntosh (2000) before and thus to separate DEM reconstruction and abundance fitting. Schmitt and Ness (2004) approximated the DEM determined by H-like to He-like ratios by a sum of Chebyshev polynomials and assumed several boundary conditions such as a maximum and a minimum temperature. García-Alvarez et al. (2005) and Argiroffi et al. (2004) used such abundance independent ratios as input to the Monte Carlo method of Kashyap and Drake (1998). Unfortunately they refer to a publication for a detailed description of their method that is not existent.

The first of my approaches also makes use of the abundance-independent H-like to He-like ratios and is in general similar to the one of Schmitt and Ness (2004).

4.5.1 Implementation

In the following calculations I used another notation for the contribution function and the photon flux (Equations 2.5 and 2.9) to consider the specification of the abundances in terms of solar photospheric ones. While other authors sometimes detach the abundance totally from the contribution function, I split it up into the solar photospheric value and a multiplicative factor describing the deviation from this value

$$\frac{n(X)}{n(H)} = Ab(X)\,\frac{n(X)}{n(H)}_{\odot} \tag{4.2}$$

The solar photospheric value is included in the contribution function

$$G(T) = A_{ji}\,\frac{n_j(X^{Z+})}{n(X^{Z+})}\,\frac{n(X^{Z+})}{n(X)}\,\frac{n(X)}{n(H)}_{\odot}\,\frac{n(H)}{n_e}\,\frac{1}{n_e} \tag{4.3}$$

while the multiplicative factor $Ab(X)$ enters the flux as an additional parameter:

$$f_{ji} = \frac{1}{4\pi d^2}\,Ab(X)\int G(T)\,DEM(T)\,dT \tag{4.4}$$

The contribution function as defined in Equation 4.3 was calculated by the CHIANTI routine `g_of_t`, see the CHIANTI User Guide for further details. It requires the specification of the underlying abundances, an ionization equilibrium and a value for the electron density n_e. I adopted the solar photospheric values of Asplund et al. (2005) and the ionization equilibrium computed by Mazzotta et al. (1998) that has been extrapolated to temperatures up to $\log T = 9$. The electron density was set to 10^{10} cm^{-3}.

Practical considerations concerning the inversion of Equation 4.4 resulted in the application of logarithmic scales. At first T was substituted by $\log T$ to handle smaller numbers. Besides, `g_of_t` computes the contribution functions in a $\log T$ grid. With

$$\frac{d\log T}{dT} = \frac{1}{T\cdot\ln 10}$$

Equation 4.4 alters to

$$f = \frac{\ln 10}{4\pi d^2}\,Ab(X)\int G(\log T)\cdot T\cdot DEM(\log T)\,d\log T \tag{4.5}$$

Second, I decided to model $\log DEM(\log T)$ instead of $DEM(\log T)$. This ensures positivity of the DEM; a negative DEM would definitely be unphysical. The application of Chebyshev polynomials as an approximation of the DEM as undertaken by Schmitt and Ness (2004) has certain mathematical advantages like orthonormality and a simple normalization. Anyway, other

functions may be used instead. I decided on simple polynomials of order N, with N varying from 2 to 8. Contrary to the Chebyshev polynomials such a simple polynomial has the disadvantage that the higher order coefficients are not necessarily small, "their sequence does not converge". Furthermore I tried to avoid setting further constraints and boundary conditions on the DEM as maximum and minimum temperatures. Instead I denoted confidence ranges in $\log T$ for each computed DEM where the measured line ratios and continuum fluxes were well-reproduced by the corresponding theoretical values.

$$\log DEM(\log T) = a_0 + a_1(\log T) + a_2(\log T)^2 + ... + a_N(\log T)^N = \sum_{i=0}^{N} a_i(\log T)^i \tag{4.6}$$

and thus

$$DEM(\log T) = 10^{\sum_{i=0}^{N} a_i(\log T)^i} \tag{4.7}$$

The flux ratio of two H-like and He-like lines of a certain element becomes

$$r_{theo} = \frac{f_H}{f_{He}} = \frac{\int G_H(\log T) \cdot T \cdot DEM(\log T)\, d\log T}{\int G_{He}(\log T) \cdot T \cdot DEM(\log T)\, d\log T} \tag{4.8}$$

where the multiplicative factor $Ab(X)$ cancels down together with the star's distance. Considering the components of Equation 4.3, the electron density, the proton-to-electron ratio and the solar abundances also cancel down when assuming them to be temperature-independent so that they can be taken out of the integral, leaving only the Einstein coefficient A_{ji}, the ion fractions of the H-like and He-like ions and the level population of the upper level of the atomic transition.

Inserting Equation 4.7 in Equation 4.8 gives

$$r_{theo} = \frac{\int G_H(\log T) \cdot T \cdot 10^{\sum_{i=0}^{N} a_i(\log T)^i}\, d\log T}{\int G_{He}(\log T) \cdot T \cdot 10^{\sum_{i=0}^{N} a_i(\log T)^i}\, d\log T} \tag{4.9}$$

The constant coefficient a_0 makes a factor of 10^{a_0} turn up in both integrals that can be truncated. The coefficient a_0 that provides a "normalization level" can thus not be deduced from the ratios and the resulting polynomial is undetermined. Instead of a_0 the factor T enters the exponent as $10^{\log T}$

$$r_{theo} = \frac{\int G_H(\log T) \cdot 10^{\log T + \sum_{i=1}^{N} a_i(\log T)^i}\, d\log T}{\int G_{He}(\log T) \cdot 10^{\log T + \sum_{i=1}^{N} a_i(\log T)^i}\, d\log T} \tag{4.10}$$

The missing normalization is provided by the continuum measurements that have only a weak dependence on the applied abundances. The flux of the continuum in a certain wavelength interval can in principle be described by Equation 4.4 as well, with $G_c(T)$ now being the continuum contribution function.

$$c_{theo} = \frac{\ln 10}{4\pi d^2} \int G_c(\log T) \cdot T \cdot DEM(\log T)\, d\log T \tag{4.11}$$

$$= \frac{\ln 10}{4\pi d^2} \int G_c(\log T) \cdot 10^{\log T + \sum_{i=0}^{N} a_i(\log T)^i}\, d\log T \tag{4.12}$$

CHIANTI provides the routines `freefree`, `freebound` and `two_photon` to calculate the emissivities of the three constituents of the continuum as a function of wavelength and temperature.

The first two routines make use of previous calculations of gaunt factors and cross sections from the literature. The corresponding references as well as short descriptions of these routines can be found in the CHIANTI User Guide.

The polynomial coefficients a_i are determined by minimization of a χ^2-like expression

$$\chi^2 = \sum_j \frac{(r_{j,mes} - r_{j,theo})^2}{r_{err,j}} + \sum_k \frac{(c_{k,mes} - c_{k,theo})^2}{c_{err,i}} \tag{4.13}$$

This mathematical formalism (together with additional subroutines that read ASCII files with measured continuum fluxes and line counts, convert the latter into fluxes, compute error-weighted means when required and assign the calculation of the contribution functions) was implemented in an IDL routine called `fit_dem`. The minimization is performed by the Powell minimization procedure (Press et al., 1992) as implemented in IDL.

4.5.2 Abundance determination

Once a set of polynomial coefficients a_i is returned by the Powell procedure, the abundances $Ab(X)$ can be calculated by forcing the theoretical flux to reproduce the measured line flux for each line, i.e.

$$f_{theo} = \frac{\ln 10}{4\pi d^2}\, Ab(X) \int G(\log T) \cdot 10^{\log T + \sum_{i=0}^{N} a_i (\log T)^i}\, d\log T \stackrel{!}{=} f_{mes}$$

Thus the abundance is given by

$$Ab(X) = \frac{4\pi d^2}{\ln 10}\, \frac{f_{mes}}{\int G(\log T) \cdot T \cdot DEM(\log T)\, d\log T} \tag{4.14}$$

Assuming that the only variables in this equation having errors are the measured line fluxes, i.e. neither the distance of the star and the hydrogen column density towards it contain measurement errors, nor have the polynomial coefficients a_i errors, a simple error propagation results in

$$Ab(X)_{err} = \frac{4\pi d^2}{\ln 10}\, \frac{f_{err}}{\int G(\log T) \cdot T \cdot DEM(\log T)\, d\log T} \tag{4.15}$$

Moreover also the atomic data underlying the calculation of the contribution function, i.e. ionization equilibrium, level population, collision rate coefficients etc. are supposed to be well-determined and have no errors. These assumptions are of course a massive oversimplification of the real situation and the thus deduced errors will be systematically too small. A more comprehensive consideration of possible errors is nevertheless on the one hand not that easy (for instance concerning the errors of the polynomial coefficients) and on the other hand these errors are very difficult to assess (especially concerning the atomic parameters). A more detailed discussion is found in Chapter 5.

Since normally more than one emission line is available for each element (two for those where ratios could be built, and typically many more in case of iron) a mean value must be calculated. An error-weighted mean including the lines i of element X is given by

$$\overline{Ab(X)} = \frac{\sum_i \frac{Ab(X)_i}{Ab(X)^2_{err,i}}}{\sum_i \frac{1}{Ab(X)^2_{err,i}}} = \frac{4\pi d^2}{\ln 10}\, \frac{\sum_i \frac{f_{mes} \cdot \int G(\log T) \cdot T \cdot DEM(\log T)\, d\log T}{f^2_{err,i}}}{\sum_i \frac{(\int G(\log T) \cdot T \cdot DEM(\log T)\, d\log T)^2}{f^2_{err,i}}} \tag{4.16}$$

A minimization procedure leads to the same formula.

It arose that the thus computed absolute elemental abundances have a certain "normalization problem", i.e. different sets of abundances of the same star, obtained even from the same observational data differ by a common multiplicative factor. Hence additionally relative abundances avoiding this problem were computed. I chose oxygen that provides usually reliable flux measurements as the reference element. The relative abundances and their errors are obtained from

$$X/O \pm X/O_{err} = \frac{Ab(X)}{Ab(O)} \pm \frac{\sqrt{Ab(X)_{err}^2 + Ab(O)_{err}^2 \cdot \left(\frac{Ab(X)}{Ab(O)}\right)^2}}{Ab(O)} \tag{4.17}$$

Corresponding calculations are appended to the `fit_dem` routine.

To convert later between the thus abundances relative to Asplund et al. (2005) and other sets of reference abundances used in the literature a simple multiplication with certain conversion factors must be performed. Anyway, sometimes abundances are given in the logarithmic notation, i.e.

$$[X/O] \pm [X/O]_{err} = \log \frac{Ab(X)}{Ab(O)} \pm \frac{\sqrt{Ab(X)_{err}^2 + Ab(O)_{err}^2 \cdot \left(\frac{Ab(X)}{Ab(O)}\right)^2}}{\ln 10 \cdot Ab(X)} \tag{4.18}$$

4.6 Differential emission measure from iron lines

Preliminary test versions of the `fit_dem` routine based on the H-like and He-like ratios included additional ratios from iron lines of different ionization stages. These iron line ratios (based on CHIANTI 4.2 atomic data) were however not compatible with each other and with the H-like to He-like ratios and therefore they were removed from the fit. The search for an independent cross check of the differential emission measures and abundances determined with the ratio method led to a different application of these lines and finally to a second approach to fit the $DEMs$.

A consistency check for the determined differential emission measure should originate from similar basic requirements: The DEM should cover a broad temperature range and must be determined independent from the set of elemental abundances. This can be achieved by using exclusively lines of a single element but of various ionization stages. Again a normalization with continuum measurements is required, and the abundance of the used element becomes an additional fit parameter.

In practice, the only element this method can be applied to is iron, since it is the only heavier element that – due to its relatively high abundance – provides enough lines that are strong enough. Lighter elements such as carbon, nitrogen, or oxygen cover only the lower temperatures. Several authors made use of this approach, e.g. Linsky et al. (2002), Ness et al. (2003a) and Sanz-Forcada et al. (2002)

Confined to the X-ray spectral range observable with the *Chandra* and *XMM-Newton* gratings, the temperature range of $\log T = 5.5$ to 8.0 is covered by lines of Fe IX to Fe XXV. It is however usually not possible to measure all the available lines, i.e. HEG spectra of stars with very hot coronae will show the Fe XXV triplet but LETGS spectra of the same star will probably not show the low-temperature Fe IX line and vice versa. Nevertheless the input to the iron line fit usually consists of several more lines than ratios are available for the corresponding ratio fit. The (supposed) greater uncertainties and errors in the atomic data of the single iron lines have thus the chance to cancel and average out.

The mathematical implementation of the DEM reconstruction follows exactly the same scheme as applied to the ratio fit, only with different input data. Instead of the ratios a set of

iron line fluxes from the lines described in Section 4.3.2 is used

$$f_{\mathrm{Fe}} = \frac{\ln 10}{4\pi d^2}\, Ab(\mathrm{Fe}) \int G_{\mathrm{Fe}}(\log T) \cdot T \cdot DEM(\log T)\, d\log T \tag{4.19}$$

The differential emission measure should again be represented by analytical functions – again by simple polynomials as defined in Equation 4.7. The coefficients a_i – together with the iron abundance – are determined by the minimization of the corresponding expression

$$\chi^2 = \sum_{\mathrm{Fe}} \frac{(f_{\mathrm{Fe},mes} - f_{\mathrm{Fe},theo})^2}{f_{err,\mathrm{Fe}}} + \sum_{k} \frac{(c_{k,mes} - c_{k,theo})^2}{c_{err,i}} \tag{4.20}$$

As soon as the DEM is determined by the polynomial coefficients the abundances of the elements other than iron can be determined as described above.

The whole iron line fit method also became part of the `fit_dem` routine that now applies the two methods concurrently.

5 Results and discussion

5.1 Stability of the fit

The numerical evaluation of the integrals in Equations 4.10, 4.12 and 4.19 with $\log T$ ranging from 5 to 9 by the Powell procedure requires the numerical handling of high numbers due to the terms $10^{(\log T)^i}$, especially for polynomials of higher orders. To prevent the procedure from being caught into a numerical overflow loop I introduced a shift in the temperature variable $\log T$. This shifting parameter (called `tshift`) was usually set to -7 so that the temperature range was centered around zero. An even greater shift could lead to numerical underflows instead. Additional to this substitution the routine was assigned to do all calculations in double precision.

Concerning the fit of the H-like to He-like ratios, lower order polynomials, i.e. the parabola and the 3rd order polynomial, usually gave a "reliable" result in the sense that these polynomials show a maximum somewhere in between $T = 1$ MK to 15 MK, with $\log DEM$ values ranging from 44 to 47 cm^{-3} K^{-1}.

Depending on the available number of ratios and continuum intervals, polynomials up to the 8th order could be fitted, but not always a numerically stable fit was possible, i.e. the Powell procedure ran into an overflow loop or the fit did not converge even with an increased number of maximum allowed iterations. From 4th order upwards the polynomials should be able to show a more differentiated structure, i.e. two or later even more maxima. The ratio fits are in this respect somewhat inert due to the the broad temperature range covered by each ratio and the small number of ratios available at all. Even if these fits show more features than one maximum these structures are typically not very pronounced.

The stability of the iron line fit depends extremely on the lines used and on their number and distribution in temperature, i.e. five lines originating only from Fe XVII and Fe XVIII – in some RGS datasets the only available iron lines – have most likely not the ability to reproduce a reasonable DEM. In the HETGS and LETGS spectra typically many more iron lines with a broad distribution of ionization stages and thus covered temperature can be measured. Thus polynomials with much higher orders than applied in the ratio fits could be fitted if it had not been for numerical overflow problems. The individual contribution functions of the iron lines sample a narrower temperature range than do the H-like to He-like ratios (see Figure 2.2) and thus the iron line fit easily forms structures at higher temperatures. The question is however how reliable these structures are since too many lines overlapping in temperature oversample the temperature range. As a result discrepancies between the individual lines can amplify to oscillations at higher order N, see e.g. Figure 6.30.

Here also uncertainties in the atomic data come into play because they are most likely the reason for the initial scatter of the lines and thus the amplification process. This correlation is clearly revealed by a comparison of the CHIANTI versions 4.2 and 5.0. While the iron line fit only seldomly converged to reasonable results with CHIANTI 4.2, the same measured line fluxes gave much more plausible $DEMs$ with version 5.0 in the majority of cases. There are however some datasets that did not provide a reliable DEM reconstruction even with CHIANTI 5.0 applied, see e.g. Figure 6.21. In this case even the parabola does not have a maximum in the considered temperature interval, and the normalization of the fitted polynomials from individual orders varies enormously. The polynomials from the iron line fit tend to oscillate at higher orders

or the fit did not converge still with CHIANTI 5.0. Thus a restriction to lower orders, at least to the maximum order of the corresponding ratio fit is advisable.

5.2 Influence of constraints and initial conditions

There are various parameters that enter the DEM and abundance calculations. Most of them have only minor or even no influence on the final results. For instance, the `tshift` parameter mentioned above that has an influence on the fit stability. It results in a shifting of the fitted polynomial, but as soon as the shift is substituted, different `tshift` values give identical $DEMs$. The contribution functions calculated by the `g_of_t` routine are no analytical functions but tabulated on a temperature grid. The width of this grid is by default $\Delta \log T = 0.1$, but it can be varied. A smaller width samples the contribution function somewhat better and thus leads to a more precise computation of the integrals in Equations 4.10, 4.12 and 4.19. Too small values however just oversample the temperature grid what decelerates the calculation of the integrals and does not lead to improved results. The chosen temperature grid has therefore a minor influence.

However, the solution of an integral equation like Equation 2.9 always depends on initial conditions, and iterative processes like the Powell minimization procedure depend on initial values for the iterated parameters. The resulting effects and discrepancies can be very conspicuous.

5.2.1 Initial values of the polynomial coefficients

The Powell procedure requires initial values of all the parameters entering the minimization, i.e. the polynomial coefficients a_0, $a_1, \ldots, a_N$, and in case of the iron line fit additionally an initial iron abundance $Ab(Fe)$. Concerning the polynomial coefficients, I set $a_0 = 45$ and $a_i = 0$ with $i = 1, \ldots, N$. This gives a reasonable normalization but no other restrictions. The initial iron abundance in the iron line fit was set $Ab(Fe) = 1$.

The setting of these parameters has a definite influence on the final set of minimized parameters returned be the procedure, since the Powell procedure may run into a local minimum during the iteration it cannot escape from. This problem occurs especially with higher order polynomials where the parameter space can have various local minima while at lower polynomial orders usually only few pronounced minima exist. I tested several sets of initial values for the polynomial coefficients, and parabola and 3rd order fit always gave the same final result. From 4th order on though, different initial values yielded different polynomials.

These polynomials can have very different coefficients but usually look similar restricted to typical $\log T$ intervals. This is a problem arising from the fact that in an approximation by simple polynomials the higher-order coefficients are not necessary small and converge to zero as they would do for instance for Chebyshev polynomials or other sets of orthogonal functions. It is thus difficult to give unambiguous initial values for the higher-order coefficients.

I eventually implemented a successive calculation of the polynomials with increasing order in the `fit_dem` routine. It takes the parameters resulting from a previous fit as initial values for a new fit with the order N incremented by one, with the highest coefficient initially set to zero. A parabola or a 3rd order polynomial (given by the parameter `startorder`) with initial values as described above was usually applied as the starting order for this chain. As a result, the fit sometimes "converges" to a certain shape (i.e. the highest coefficient was fitted to a very small number and the other coefficients do not change much, see e.g. the fourth and fifth order polynomials in Figure 6.2). In some cases however, the fit "escapes" from this local minimum in the next higher order, see e.g. the fourth and fifth as well as the sixth and seventh order fits in Figure 6.15. This method will however not always provide the real minimum set of parameters.

5.2.2 Constraining the slopes of the DEM at the temperature boundaries

The overall shape of a polynomial is determined by its order, i.e. a parabola will always have a rising and a falling slope and one extremum, a third order polynomial has two extrema and so on. The polynomial coefficients a_i scale height and width and determine the position of these features in a certain coordinate plane.

The DEM reconstruction restricts this coordinate plane to a certain area of interest – ranging in this study from approximately 5.5 to 8 in the $\log T$ direction and from 43 to 48 in the $\log DEM$ direction. The shape of the polynomial outside this area is not of interest. The individual lines, ratios and continuum fluxes in turn cover again only a small portion of the mentioned temperature interval and can determine the shape of the polynomial representing the DEM only at these temperatures. A complete coverage of the temperature interval is seldomly achieved, especially the boundaries are often only poorly determined.

As a result, undesired effects like rising slopes towards the high- and low-temperature edges can occur. Such an – artifical – increase has unphysical consequences for a real differential emission measure: Towards very low temperatures ($\log T \ll 5$) a rise of the DEM is actually possible, the resulting emission measure is however not related to the corona and though not of interest here. If such an increase towards lower temperatures starts even at $\log T = 6$ (see e.g. Figures 6.10 and 6.12), the emission measure of the low-temperature corona, of the chromosphere and of the transition region in between will be overestimated. On the other hand an unceasing increase of the DEM towards extremely high temperatures cannot reflect real physical conditions since the coronal plasma must have a maximum temperature above that no emission measure exists ("cutoff temperature").

Hence the question arose how to deal with polynomials showing such rising slopes. With CHIANTI 4.2 the available ionization equilibrium tables were limited from $\log T = 4$ to 8. This was very unfavorable for the calculation of the differential emission measure at temperatures higher than $\log T = 7$ because the continuum measurements have a certain influence on the shape of the DEM at these temperatures. As mentioned in Section 2.2, a real continuum contribution function is not bounded above in temperature, but the boundary at $\log T = 8$ emulates such a temperature cutoff. Thus a DEM with less emission measure between $\log T = 7$ and 7.5 but increasing from $\log T = 7.5$ upwards can artificially reproduce the measured continuum fluxes since no ratios or iron lines cover the high temperatures of $\log T > 7.5$.

This problem occurred quite often and I attempted to solve it by forcing the slope of the DEM at $\log T = 8$ to be negative. Following this principle I also introduced the possibility to constrain the slope at lower temperatures to positive values. This approach did not work though. Constraining one or even both of the slopes often prevented the whole fit from converging, and if the fit converged it just gave a poor reproduction of the measured continuum flux instead of redirecting the emission measures. I therefore abandoned the attempt to force the slopes of the DEM to a certain shape and decided instead to define a confidence interval in temperature for each fit that is well-covered by H-like to He-like ratios or iron lines respectively so that the reconstructed DEM is reliable in between.

The possibility finally to avoid the rising slope towards higher temperatures came unexpectedly with CHIANTI 5.0. The new database includes an ionization balance table based on the calculations by Mazzotta et al. (1998) but extended up to $\log T = 9$. The calculation of the continuum contribution functions up to these high temperatures prevents the fitted $DEMs$ from rising towards higher temperatures since this would require a much higher measured continuum flux. Since this extended ionization equilibrium is applied none of the reconstructed $DEMs$ shows a rise towards higher temperatures.

5.3 Quality of the DEM fit and the deduced abundances

A fundamental assumption underlying the `fit_dem` routine is that real-existing differential emission measures of stellar coronae can be modeled with simple polynomials. The questions in this respect are if a polynomial is generally able reproduce the shape of a true differential emission measure and if the `fit_dem` routine provides the ability to perform a reasonable approximation from the available input data.

The physical information provided at least by low-order polynomials is limited since the shape of the thus reconstructed DEM is determined by the properties of the polynomial, i.e. a parabola cannot contain more information than a simple axially symmetric rise and decay. Nevertheless even such simple analytical functions like a parabola contain the basic information underlying the DEM, i.e. a temperature of maximum emission measure and a temperature interval providing a certain level of emission measure at all.

The higher the order N of the polynomial the better existing structures in the differential emission measure like maxima, minima and slopes can be reproduced. It it however difficult to assess to what extent real differential emission measures are structured at all, and if so how pronounced these features are. Other issues are whether the available measurement data – the high resolution spectra obtained with *Chandra* and *XMM*– have sufficient quality to contain the information about this structuring and whether the atomic data underlying the spectral modeling – that are at most based on theoretical calculations – have sufficient quality to extract this information in the modeling process. The current high resolution X-ray spectra have some calibrational uncertainties, their spectral resolution is of course technically limited, but otherwise the fundamental limit of Poisson statistics is reached. The assessment of uncertainties in the atomic data is much more difficult, see the discussion below. An estimate of the arising errors confirms that the DEM reconstruction is limited rather by the quality the atomic data and not by the input spectra.

Considering this it makes no sense to fit polynomials with orders higher and higher, since they will not provide new information. If the reduced χ^2 values provided by Equation 4.13 and 4.20 are taken seriously, polynomials with orders ranging between 3 and 5 often provide the best fit results. From the sample of different stars and datasets I investigated I would conclude that it is usually not necessary to fit polynomials with orders greater than 6, even if the number of available H-like to He-like ratios / iron lines and continuum fluxes allows these fits with respect to the existing degrees of freedom.

In general these fits provide polynomials with a reasonable shape within the confidence interval in temperature to represent the differential emission measures. The fit to the H-like to He-like ratios usually reproduces the measured ratios and continuum fluxes within the measurement errors. The fit to the iron lines provides similar values for the iron abundances deduced from the individual iron lines lines and reproduces the continuum fluxes. A certain problem arises however from the fact that continuum measurements at short wavelengths affect the DEM only at higher temperatures. Thus the shape of a reconstructed DEM may be "divided", i.e. at lower to intermediate temperatures it is determined by ratios or iron lines and at higher temperatures it depends exclusively on the continuum when corresponding ratios are missing. An alleviated version of the problem previously leading to the rising slopes towards the high-temperature boundary could thus occur. Since the normalization of the whole differential emission measure depends on the continuum measurements it is thus possible to obtain a DEM with a shifted normalization level.

As a result the complete set of abundances $Ab(X)$ derived from the reconstructed differential emission measure is systematically deviating by a multiplicative factor corresponding to this shift in normalization, i.e. if the whole $\log DEM$ is too low by 0.3 cm^{-3} K^{-1} the resulting abundances are too high by a factor of 2. It is a priori unknown if such a normalization problem

biases the determined absolute abundances, and if so by what order of magnitude. I therefore additionally calculated relative abundances with oxygen as the reference element. These relative abundance are independent of this normalization problem.

The relative abundances deduced with polynomials of different orders or from different datasets of the same star usually compare well with each other. Thus even if they do not match the results from an independent global fit with xspec, or values reported in the literature I consider the relative abundances in general to be very reliable since the literature values – even when obtained from the same star and dataset but with different methods – show occasionally also a broad distribution.

5.4 Error analysis

Errors and uncertainties from various sources enter the DEM reconstruction and abundance calculation as described in Sections 4.5 and 4.6. Unfortunately only few of them can be considered when evaluating the errors of the deduced abundances and the only errors I introduced into error propagation calculations are the statistical uncertainties of the measured line counts and continuum fluxes. Complicating cases like upper limit measurements have never been taken into account.

Further values having measurement errors are the distances and column densities taken from the literature. The stars in the sample studied here are nearby and relatively bright. The parallax errors listed for these stars in the *Hipparcos* catalog range from only 1% to 6%, and are thus more or less negligible. Concerning the adopted hydrogen column densities, Wood et al. (2005) specify a general uncertainty of 10% for their measurements, the value adopted from Sanz-Forcada et al. (2002) should have the same order of magnitude. The biggest problems in this respect arise for Algol, where only contradictory values from various global fits to low-resolution X-ray spectra were available so that I had to estimate an appropriate value. I did however not consider these uncertainties in the `fit_dem` routine.

On the other hand there are several parameters that must be set in the course of the fitting procedure and that have a certain influence on the final results as mentioned in Section 4.5. There is for instance the density assumed to calculate line and continuum emissivities. I fixed it to 1×10^{10} cm^{-3} in all calculations, which is a relatively low value. The H- and He-like lines and most of the iron lines are resonance lines, the dependence of their line emissivity on the density is similar and relatively weak for lower densities. Not until extremely high density values ($\geq 10^{13}$ cm^{-3}) are reached, the emissivities of these lines start to increase strongly. The vast number of density measurements for many stars published in the literature in recent years suggest that such extremely high densities are not common in stellar coronal plasmas in quiescent state, see for instance Ness et al. (2003b) and Testa et al. (2004). Thus it seems to be justified to assume such a low density value.

Of course, the densities stated here, also those explicitly contained in the differential emission measure, are average values assuming the density to be constant in the whole coronal plasma, although the coronal plasma must not necessarily be in such an equilibrium state. Density and and also the elemental abundances can vary locally or even with temperature as it is observed on the Sun. We are however not in a position to distinguish such circumstantial situations from spatially unresolved stellar measurements. Emissivity calculations with CHIANTI are based on the ionization equilibrium condition. In case of strong flares, this condition may not be fulfilled. Calculations outside the ionization equilibrium are difficult to implement and are however beyond the scope of this work. Nevertheless even individual ionization balance calculations differ, and the contribution functions depend on the ionization balance adopted. From those available in the CHIANTI database the one calculated by Mazzotta et al. (1998) is the latest updated and most commonly used. As mentioned above I made use of an extended version that is new

in CHIANTI 5, covering temperatures up to $\log T = 9$. Gu (2003) showed that the detailed consideration of recombination processes can change the ionization equilibrium significantly, it is therefore questionable whether the one of Mazzotta et al. is still up to date.

The coronal plasma is assumed to be optically thin, i.e. no resonant scattering should occur. Non-zero optical depths would extremely complicate the calculations and require a treatment with much more sophisticated coronal model. The question if resonant scattering occurs in stellar coronal plasmas is still unanswered, Ness et al. (2003c) argued that strong resonant scattering is unlikely for the stars in their sample but it could not be excluded. Photoexcitation effects originating from radiation fields can thus clearly considered to be negligible. The resonance lines are not involved in transitions that can be stimulated by the stellar photospheric radiation field, the only possible photoexcitation processes correspond would to resonant scattering.

Even the initially assumed set of abundances has a certain influence on the calculations since they directly enter the continuum contribution functions. The only possibility to avoid this is an iterative process where the abundances deduced after the DEM fitting enter a new calculation of the continuum contribution functions. Such an iteration scheme is not yet implemented in the `fit_dem` routine.

The abundances by Asplund et al. (2005) that I adopted constitute the latest and most consistent collection of solar photospheric abundances, but they do not necessarily fit stellar abundances, neither photospheric nor coronal. A comparison of the deduced stellar coronal abundances relative to the corresponding photospheric ones as it was done e.g. by Sanz-Forcada et al. (2004) would be the ideal case to give a statement concerning FIP or inverse FIP effects, but stellar photospheric abundances can also only be determined with great difficulty, especially for the crucial elements carbon, nitrogen and oxygen, for neon it is even impossible.

The really crucial uncertainties arise however from the atomic physics data underlying the line emissivity calculations. It is extremely difficult to measure collision rate coefficients, decay rates and so on for highly ionized atoms under the conditions predominating in stellar coronal plasmas (i.e. very high temperatures and very low densities) in the laboratory. The only remaining way to obtain these numbers is to perform theoretical calculations. Such calculations are of course the more precise the more physical processes are included. Thus the population of a single level depends on the interplay of various populating and de-populating processes that link thousands of other levels of the same ion and of the neighboring ionization stages. These calculations require considerable numerical resources, and they must be restricted to a certain number of important levels and processes. It is however difficult to assess these relevant processes and levels and the influence of further extensions of these calculations. As a consequence it is often unknown how to evaluate the quality of the atomic data now available from databases like CHIANTI or APED.

I got a feeling of the impact of the quality of the atomic data by the change from CHIANTI 4.2 to 5.0. The significant improvements im my fits due to the application of the new data and extended calculations were eye-catching, in particular concerning the agreement of results obtained from different iron lines. However, it is still difficult to assess the absolute level of goodness and to determine errors. The emissivities of H-like and He-like lines are considered to have small errors, at least smaller than those of the iron lines, but assumed error ranges reported in the literature range from 10% to 30%.

Even if one wants to include these errors in the minimization procedure it must be considered that the uncertainties in the atomic data are systematic errors rather than statistical errors that do not follow a normal distribution and thus do not fit the mathematical formalism of χ^2 statistics. (Strictly speaking the Poisson distributed errors in the line counts do not either.) Sanz-Forcada et al. (2003) argued that the uncertainties in their reconstructed emission measure distributions are dominated by errors in the line emissivities rather than by the errors of the line counts. Relative Poissionian errors are the smaller the stronger the regarded line, but the

strongest lines do not necessarily have the better known atomic data. Therefore Sanz-Forcada et al. rejected a minimization with χ^2 and applied a method giving all lines the same weight instead. Such an approach is worth discussing.

Apart from the consideration of various errors entering the DEM fitting procedure it is just as difficult to determine the errors resulting from the fitting. As a matter of fact, the polynomial coefficients returned by the Powell procedure have errors that ought to enter the subsequent abundance calculations and thus increase the derived errors of the abundances. There is however no simple way to calculate the errors of the polynomial coefficients, the only reasonable approach is given by the variation of the input data with a Monte Carlo method as it was done by Kashyap and Drake (1998) in their emission measure distribution reconstruction method. The application of a Monte Carlo method to the `fit_dem` routine is however additionally complicated if not even ruled out by the fact that very different sets of coefficients may reproduce the original DEM equally well while a slight variation of one of the coefficients may result in a polynomial with a very different shape in the temperature confidence interval. This is the main reason why I did not implement such an approach.

5.5 Open issues and possible improvements

The `fit_dem` routine is still far from perfection and offers several approaches for further improvements and extensions. I was not able to perform a final cross-check of the calculated DEM and the deduced abundances that includes the application of the polynomial DEM and the derived set of abundances as input to CHIANTI's `make_chianti_spec` routine that computes synthetic spectra for lack of time. The thus obtained synthetic spectra could be compared to the observed data.

It is surely worth testing if functions other than simple polynomials as a representation of the DEM give strongly deviating and/or better results. A set of orthogonal functions would show convergence for the higher-order coefficients which provides several mathematical advantages.

It would be very simple to combine the two fitting methods presented here to a single method. The resulting combined fit may join the positive properties of both approaches, i.e. the better stability of the ratio fit and the better ability of the iron line fit to reproduce fine structure in the DEM. (On the other hand the opposite may happen.)

Especially the ratio fit is often limited by the small number of available H-like to He-like ratios. It would be simple to extend the list of temperature-dependend but abundance-independent ratios, for example with ratios of Ly α to Ly β. Thus it may be possible to cover temperature ranges inaccessible with certain datasets before, e.g. the RGS does not provide the measurement of the carbon H-like to He-like ratio but would allow the measurement of carbon Ly α to Ly β.

Also for the lack of time I was not able to implement an iterative process to consider the abundance dependence of the continuum as mentioned above. The current treatment of the continuum in general requires further improvements though, since it is probably the cause of the normalization problem mentioned above. A more reliable continuum measurement must at least provide more data points whose continuum contribution functions also cover lower temperatures, i.e. they have to be located at longer wavelengths. In combination with an iterative process aligning the abundances a correct normalization in the whole temperature confidence interval might be achieved. Another possibility would be to exclude the now applied continuum measurements from the fit and use instead the source background of the individual lines measured with CORA. A non-normalized DEM (i.e. with an unknown polynomial coefficient a_0) can thus be scaled so that the reproduced continuum fluxes agree on average with the data. Such an approach is probably much better than simple photon counting in few spectral regions supposed to be free of lines, although it still would not consider the pseudo-continuum created by unresolved lines.

6 Individual stars

I have studied several stars with the method described in Chapter 4. Here I provide the detailed results on a small selection distributed over the Hertzsprung-Russel-diagram. For each of the chosen stars multiple observations, obtained with more than one instrument, are available so that the results acquired from the single datasets can be compared. I also took the opportunity to combine the measurements of different instruments to increase the number of measured lines and therefore to extend the temperature range covered by the fit. A discussion whether this is reasonable in the individual cases is appended, since big spaces of time may lie inbetween the distinct observations and different stages of activity may be covered.

For each of the listed observations additionally the lightcurve and a fluxed spectrum are given to evaluate the short-term variability of the source and to compare the state of activity of all the datasets of the same star. The lightcurves of *Chandra* HETGS and LETGS observations were obtained from the counts contained in the 0th order image and the dispersed spectra, LETGS lightcurves were dead-time-factor corrected. For datasets obtained with *XMM-Newton*, the lightcurves were usually determined from the data of the EPIC PN detector running parallel to RGS and MOS. Effects of pile-up on the lightcurve were not considered since the overall shape of a lightcurve will be influenced by pile-up only when enormous changes in count rate occur, besides the lightcurves have only minor relevance for the subject of this work. The lightcurves were grouped in bins of 300 s if not stated otherwise. The fluxed spectra were in case of *Chandra* data directly calculated from count spectra, effective area and exposure time, positive and negative 1st order summed up. RGS spectra were created with the SAS task `rgsfluxer` and contain the merged data from both RGS instruments in 1st and 2nd order. The binsize of the spectra is 0.0125 Å, 0.015 Å, 0.0375 Å and 0.0103 Å for HEG, MEG, LETGS and RGS respectively.

Considering the single observations, HETGS datasets were always regarded completely, i.e. line counts of HEG and MEG spectra are fitted separately but the line fluxes for each line were averaged and overall differential emission measure distributions and abundances were calculated. The spectra of RGS 1 and 2, in 1st and 2nd order, were also treated together the same way. This procedure should be reasonable since the mentioned detectors operate parallely.

For each of the analyzed datasets I show plots of the calculated DEMs – normally as well from the fit of the H-like to He-like ratios as from the iron lines, plotted in black and red respectively. For better clarity, the $DEMs$ from each available polynomial are plotted separately but with the same ranges and scales. The minimum order is usually 2, representing thus a simple parabola. The maximum order of the fitted polynomials is constrained either by the ability of the fit to converge or by the available degrees of freedom, the latter is the prevalent case for the ratio fits. The plots of the differential emission measures are arranged in increasing order from left to right and top down.

The quality of each single DEM fit can be evaluated from the prediction of the measured line fluxes, ratios and continuum fluxes the fit is initially based on. The values of reduced χ^2 are also given. For the ratio fits they are based on Equation 4.13 and thus on the H-like to He-like ratios and the continuum fluxes. The corresponding value for the iron line fits – although listed again with the ratios – is based on Equation 4.20, i.e. on the iron lines and continuum fluxes. The column belonging to the polynomial with the minimum χ^2 is highlighted in grey, also in the following tables, where the deduced abundances are listed. The abundances are itemized relative

to oxygen and also absolutely, despite the uncertain normalization as mentioned in Chapter 5. For comparison, I give also the abundances obtained from a global fit to the high resolution spectra with two or three temperature components accomplished with xspec. For consistency checks I eventually list the abundances derived for each line individually. This helps to identify problematic lines, i.e. significantly deviating lines or those with large errors, especially within the bunch of iron lines. Iron lines that were not included in the fit are marked with asterisks.

If the derived ratios or abundances exceed the value of 100 (which is very unreliable) they are replaced by asterisks. Admittedly, even once these values reach 15 or 20, they become untrustworthy. Especially with iron line fits based on very few lines values of zero and NaN (representing infinity) also occur, clarifying that the DEM fit is definitely not credible in the corresponding temperature interval or that the normalization is wrong.

For the calculations two additional numbers were needed: The first is the distance of the star, the second is the hydrogen column density N_H towards it. For all stars treated in the following Hipparcos parallaxes were adopted (Perryman and ESA, 1997). The hydrogen column density towards AB Dor and UX Ari was taken from Sanz-Forcada et al. (2002), for AU Mic I adopted the value derived by Wood et al. (2005).

6.1 The zero-age main sequence star AB Dor

On the night sky AB Dor is an inconspicuous star with $m_V = 6\overset{m}{.}9$ in brightness, located not far from the Large Magellanic Cloud in the constellation of Doradus. Yet it is an interesting object to observe in X-rays, since it was classified as a zero-age main sequence star. Statements concerning its spectral type and luminosity class in the literature vary from K0–2 and III–V. Its age was estimated to be approximately 20–30 Myr. With a distance of 14.9 pc, AB Dor is thus the nearest K-type ZAMS star. It is a fast rotator with $v \sin i = 90$ km s^{-1}, resulting in a rotation period of 0.5148 d. Strong magnetic fields arise that have been studied with Zeeman Doppler imaging techniques. Hence it is no wonder that AB Dor is a very luminous X-ray source that has been extensively studied with almost every X-ray satellite since its discovery in X-rays in 1981. Rotational modulation has been detected in various wavelength bands and Doppler imaging campaigns revealed the existence of dark spots, in particular a long-lived, extended polar spot. Further details on AB Dor can be found in García-Alvarez et al. (2005) and references therein.

The X-ray emission of AB Dor is with a luminosity of $\approx 10^{30}$ erg s^{-1} very close to the saturation limit – not unusual for such a young and rapidly rotating object. The observed level of activity ranges from periods of relative quiescence and slow variation to extremely strong and repeated flaring, with flaring periods being recurrent. Rotational modulation in X-rays at levels up to 15% has been verified, indicating that at least part of the X-ray emission originates from spatially limited regions on the star. The sizes of the X-ray emitting coronal structures are calculated to occupy only small fractions of the stellar surface but raising to heights of the order of the stellar radius (Sanz-Forcada et al. (2003), Hussain et al. (2005)).

AB Dor has two companions, the dM4e star AB Dor B at a distance of $10''$ and a very low-mass star close by. With *Chandra*, AB Dor A and B can be clearly separated, while in the *XMM* EPIC images the source appears just elongated and in the RGS a separation is not also possible. Sanz-Forcada et al. (2003) argue from the analysis of *Chandra* HETGS data that the contribution of the two late-type companions to the total X-ray emission is negligible, they compute the contribution of AB Dor B to the overall X-ray luminosity not to exceed 4%.

The emission measure distribution of AB Dor is found to be concentrated between $\log T \approx 6.5 - 7.5$ (Sanz-Forcada et al. (2003), García-Alvarez et al. (2005)) with the shape of the DEM being similar at different activity levels. Early abundance calculations indicate a sub-solar metallicity. Sanz-Forcada et al. (2003) find an intermediate behavior between the FIP effect and the inverse FIP effect from *XMM* and *Chandra* data while García-Alvarez et al. (2005) do not confirm this trend and report an overall inverse FIP effect. The observed abundance anomalies are however less extreme than observed in very active stars.

6.1.1 The HETGS dataset ObsID 16

Chandra observed AB Dor with the HETGS on 9 October 1999 for 52.3 ks. This dataset has among others been discussed by Sanz-Forcada et al. (2003) and García-Alvarez et al. (2005), the latter derive emission measure distributions and abundances from line ratios of H-like to He-like lines in combination with iron lines as input to the algorithm developed by Kashyap and Drake (1998). Since the underlying method is very similar to the one I used, a comparison between their results and those I obtain is quite interesting.

Figure 6.1 shows the lightcurve and the fluxed HEG and MEG spectra of the observation. The lightcurve is – with regard to AB Dor's usual behavior – comparatively quiescent, showing only one moderate flare. The spectra reveal a not very distinct continuum, indicating moderate temperatures; and the strongest lines arise from Ne X and O VIII.

The HEG and MEG spectra allowed the measurement of H-like to He-like ratios from all elements well-covered by the HETG wavelength range, i.e. oxygen, neon, magnesium, aluminium,

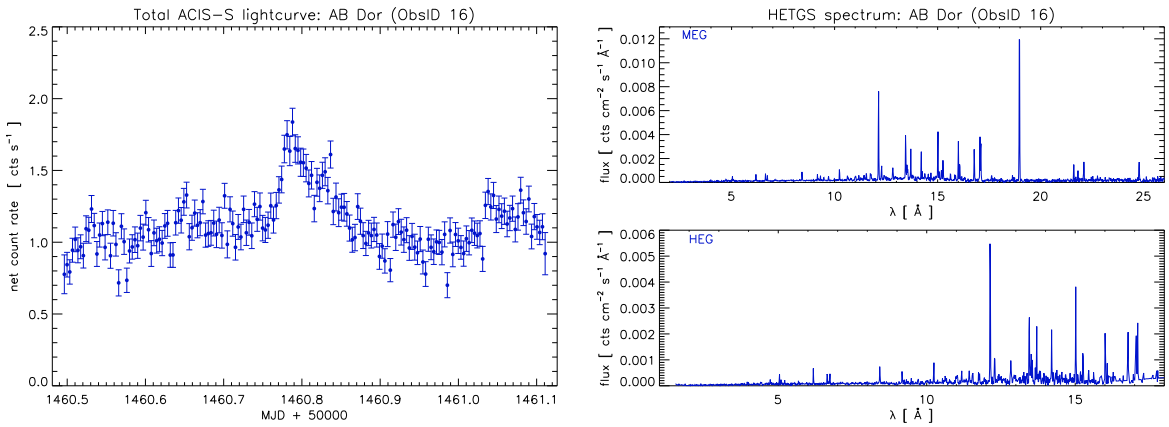

Figure 6.1: Lightcurve (left) and spectrum (right) of the *Chandra* HETGS observation 16, targetting AB Dor.

silicon and sulfur, whereas the oxygen ratio has a relatively large error (cf. Table 6.1). The DEM reconstructed from these ratios can thus be valid only for higher temperatures ranging from $\approx$ 4 MK to 20 MK ($\log T$ from 6.6 to 7.3). The available iron lines (Fe XVII to Fe XXIV, not counting the Fe XXV triplet, cf. Table 6.6) cover essentially the same temperature range.

The respective parabolas, the simplest fitted polynomials, look very similar for both the ratio and the iron line fit, with a maximum at $\log T \approx 6.8$. This changes considerably for the third order polynomial, where the normalization of the DEM from the ratios lowers in contrast to the iron line fit, where the DEM is lifted up. Consistency is reached only for lower temperatures where the fit would not be valid. The two forth order polynomials show a similar structure (two peaks with the second one an order of magnitude lower) but they are shifted in temperature and normalization. The first maximum is located at 5 MK for the ratio fit and at 7 MK for the iron line fit. The second peak is correspondingly located at 20 MK and 45 MK respectively, the latter is definitely outside the reliable temperature range. However both fits seem to converge in 4th order, the fifth order ratio fit is virtually identical to the fourth order fit, and the iron line fit differs only a little.

Table 6.1 shows that the overall fit results are in general better for the ratio fit, while the iron line fits with orders greater 3 are not able to reproduce the oxygen, neon and sulfur ratios. The iron abundances (when omitting the Fe XXV triplet and the Fe XX line that clearly deviate from the other lines) deduced from the ratio fit (Table 6.4) scatter with a factor of $\approx$ 2.5. Both parabolas reproduce the ratios moderately but a parabola must be considered to be a poor fit to the DEM. The 4th order ratio fit appears to provide the best solution.

The absolute abundances deduced from the $DEMs$ of the ratio fits (Table 6.5) differ by multiplicative factors due to the different normalizations of the $DEMs$. Neither of the 4 sets matches those derived from the global fit with xspec. The resulting relative abundances instead agree with each other within the errors but they match only few from the global fit. The largest deviations arise for argon what is reducible to a questionable measurement of the Ar XVII line as mentioned in Section 4.3.1, but the other abundances also differ by factors up to 2.

The absolute abundance derived from the iron line fit scatter similar to those from the ratio fit, the values of the higher orders are significantly too high, indicating that the normalization of the ratio fit for 4th and 5th order is better. The parabola gives absolute abundances that match the global fit best (see Table 6.7), additionally the relative abundances of the higher orders (Table 6.3) match the global fit quite well.

The individual abundances derived from the DEM fit of iron lines (Table 6.6) scatter more for the non-iron lines, the iron lines though scatter less than in the ratio fit. The Fe XX line

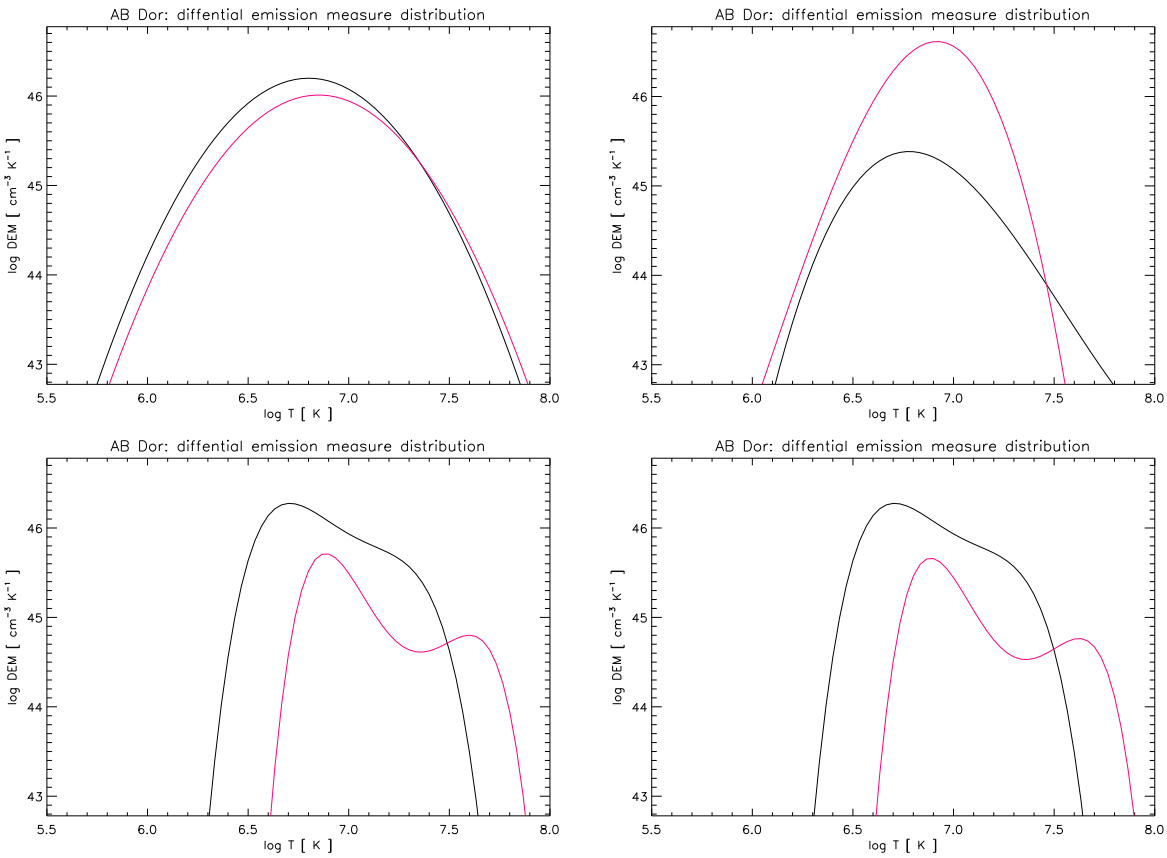

Figure 6.2: Differential emission measures for AB Dor with the polynomial order ranging from 2 to 5, calculated from the HETGS dataset 16.

clearly deviates, in both the ratio and the iron line fit, indicating a measurement problem. In a second run of the fit the line was therefore excluded from the iron line fit.

When transforming the calculated DEM of the best-fit 4th order polynomial from the H-like to He-like ratios to an emission measure distribution (units cm^{-3}, see the left panel of Figure 6.8) its overall shape compares not that well with those derived by García-Alvarez et al. (2005), which is somewhat astonishing since I used the same lines and a very similar method. Instead it matches the fit of Sanz-Forcada et al. (2003), who also reconstructed emission measure distributions from this dataset.

Sanz-Forcada et al. (2003) give logarithmic abundances relative to solar photospheric abundances derived by Anders and Grevesse (1989), García-Alvarez et al. (2005) use Grevesse and Sauval (1998) as a reference. Both authors give more than one set of abundances from different fits, and these sets have a broad scatter. A conversion to the non-logarithmic scale and relative to the abundances of Asplund et al. (2005) places the relative values from my calculations in the same range. In general, I can confirm the trend of an inverse FIP effect from the elements I investigated here. I did not obtain data for the low-FIP elements calcium and nickel where Sanz-Forcada et al. (2003) find an increase.

	measured	2nd order	3rd order	4th order	5th order
O VIII / O VII	9.403±1.505	6.045 (7.162)	7.417 (14.484)	9.410 (28.037)	9.410 (28.257)
Ne X / Ne IX	2.264±0.103	2.345 (2.688)	2.329 (3.462)	2.265 (4.930)	2.265 (4.967)
Mg XII / Mg XI	1.460±0.292	1.413 (1.623)	1.310 (1.519)	1.325 (1.770)	1.325 (1.782)
Al XIII / Al XII	0.726±0.303	1.063 (1.220)	0.999 (0.975)	1.089 (1.199)	1.089 (1.208)
Si XIV / Si XIII	1.015±0.129	0.867 (0.999)	0.853 (0.684)	0.966 (1.038)	0.966 (1.051)
S XVI / S XV	0.588±0.157	0.514 (0.599)	0.664 (0.287)	0.608 (1.038)	0.608 (1.085)
2-3 Å	1.291±0.129	1.291 (1.291)	1.291 (1.291)	1.291 (1.291)	1.291 (1.291)
red. χ^2		2.10 (8.74)	1.68 (8.12)	0.91 (6.45)	1.82 (8.59)

Table 6.1: Fit results from H-like to He-like ratios from the AB Dor HETGS dataset 16: Photon flux ratios and continuum flux [10^{-4} cts s^{-1} cm^{-2}] from 2-3 Å. The corresponding results from the iron line fit are given in brackets.

abundance	2nd order	3rd order	4th order	5th order	2T fit
N / O	1.790±0.318	1.824±0.264	1.868±0.257	1.868±0.257	1.578
Ne / O	2.595±0.308	2.464±0.149	2.372±0.094	2.372±0.094	1.478
Mg / O	0.545±0.074	0.548±0.049	0.538±0.041	0.538±0.041	0.275
Al / O	1.085±0.255	1.108±0.233	1.064±0.220	1.064±0.220	0.309
Si / O	0.559±0.074	0.577±0.051	0.559±0.035	0.559±0.035	0.334
S / O	1.458±0.233	1.549±0.191	1.343±0.153	1.343±0.153	0.594
Ar / O	6.896±1.469	8.111±1.516	5.922±1.073	5.922±1.073	1.715
Fe / O	0.453±0.063	0.417±0.044	0.399±0.039	0.399±0.039	0.314

Table 6.2: Abundances relative to oxygen derived from the DEM calculated from H-like to He-like ratios and a corresponding global fit with two temperature components for the AB Dor HETGS dataset 16.

abundance	2nd order	3rd order	4th order	5th order	2T fit
N / O	1.787±0.266	1.853±0.285	1.860±0.372	1.859±0.372	1.578
Ne / O	2.421±0.233	2.007±0.355	1.787±0.537	1.785±0.540	1.478
Mg / O	0.455±0.043	0.363±0.037	0.292±0.048	0.291±0.048	0.275
Al / O	0.883±0.239	0.736±0.159	0.583±0.171	0.581±0.173	0.309
Si / O	0.466±0.039	0.362±0.059	0.314±0.050	0.314±0.050	0.334
S / O	1.105±0.141	1.083±0.268	0.680±0.209	0.667±0.219	0.594
Ar / O	4.961±0.943	6.334±1.229	3.196±0.742	3.208±0.746	1.715
Fe / O	0.439±0.041	0.359±0.034	0.349±0.054	0.351±0.055	0.314

Table 6.3: Abundances relative to oxygen derived from the DEM calculated iron lines and a corresponding global fit with two temperature components for the AB Dor HETGS dataset 16.

element	wavelength	2nd order	3rd order	4th order	5th order
N VII	24.782	0.615±0.082	4.711±0.627	0.722±0.096	0.722±0.096
O VII	21.601	0.230±0.036	2.070±0.323	0.387±0.060	0.387±0.060
O VIII	18.969	0.358±0.013	2.625±0.093	0.387±0.014	0.387±0.014
Ne IX	13.446	0.915±0.037	6.502±0.260	0.917±0.037	0.917±0.037
Ne X	12.134	0.884±0.019	6.322±0.139	0.917±0.020	0.917±0.020
Mg XI	9.1688	0.182±0.034	1.290±0.240	0.192±0.036	0.192±0.036
Mg XII	8.4209	0.188±0.014	1.438±0.105	0.211±0.015	0.211±0.015
Al XII	7.7572	0.450±0.112	3.327±0.829	0.504±0.126	0.504±0.126
Al XIII	7.1729	0.307±0.103	2.417±0.810	0.336±0.113	0.336±0.113
Si XIII	6.6479	0.187±0.011	1.447±0.084	0.214±0.012	0.214±0.012
Si XIV	6.1830	0.219±0.025	1.721±0.194	0.225±0.025	0.225±0.025
S XV	5.0387	0.488±0.060	4.119±0.505	0.523±0.064	0.523±0.064
S XVI	4.7300	0.559±0.132	3.648±0.863	0.506±0.120	0.506±0.120
Ar XVII	3.9488	2.367±0.421	20.941±3.726	2.289±0.407	2.289±0.407
Fe XVII	15.015	0.131±0.006	0.895±0.038	0.128±0.005	0.128±0.005
Fe XVII	17.075	0.158±0.025	1.081±0.172	0.154±0.024	0.154±0.024
Fe XVII	15.262	0.196±0.014	1.340±0.094	0.192±0.013	0.192±0.013
Fe XVII	16.777	0.148±0.010	1.012±0.067	0.144±0.010	0.144±0.010
Fe XVIII	14.204	0.214±0.013	1.486±0.089	0.232±0.014	0.232±0.014
Fe XIX	13.520	0.296±0.020	2.158±0.147	0.358±0.024	0.358±0.024
Fe XX*	12.829	0.056±0.071	0.432±0.544	0.072±0.090	0.072±0.090
Fe XXI	12.284	0.218±0.017	1.770±0.138	0.274±0.021	0.274±0.021
Fe XXII	11.767	0.150±0.019	1.288±0.162	0.176±0.022	0.176±0.022
Fe XXIII	11.736	0.183±0.024	1.643±0.214	0.188±0.024	0.188±0.024
Fe XXIV	11.170	0.284±0.061	2.599±0.556	0.262±0.056	0.262±0.056
Fe XXV*	1.8559	1.193±0.430	5.215±1.879	1.328±0.478	1.328±0.478

Table 6.4: Abundances derived for individual lines from the DEM calculated from H-like to He-like ratios for the AB Dor HETGS dataset 16.

element	2nd order	3rd order	4th order	5th order	2T fit
N	0.615±0.082	4.711±0.627	0.722±0.096	0.722±0.096	1.062
O	0.343±0.040	2.582±0.148	0.387±0.013	0.387±0.013	0.673
Ne	0.891±0.017	6.362±0.123	0.917±0.018	0.917±0.018	0.995
Mg	0.187±0.013	1.414±0.096	0.208±0.014	0.208±0.014	0.185
Al	0.372±0.076	2.861±0.579	0.411±0.084	0.411±0.084	0.208
Si	0.192±0.012	1.490±0.100	0.216±0.011	0.216±0.011	0.225
S	0.500±0.055	3.999±0.436	0.519±0.057	0.519±0.057	0.400
Ar	2.367±0.421	20.941±3.726	2.289±0.407	2.289±0.407	1.154
Fe	0.155±0.012	1.078±0.095	0.154±0.014	0.154±0.014	0.211

Table 6.5: Absolute abundances derived from the *DEM* calculated from H-like to He-like ratios and as well from a global fit with two temperature components, for the AB Dor HETGS dataset 16.

element	wavelength	2nd order	3rd order	4th order	5th order
N VII	24.782	0.968±0.129	0.407±0.054	4.746±0.632	5.357±0.713
O VII	21.601	0.421±0.066	0.334±0.052	7.522±1.174	8.560±1.336
O VIII	18.969	0.552±0.020	0.217±0.008	2.523±0.090	2.849±0.101
Ne IX	13.446	1.506±0.060	0.636±0.025	9.272±0.371	10.538±0.421
Ne X	12.134	1.269±0.028	0.416±0.009	4.258±0.094	4.803±0.106
Mg XI	9.1688	0.271±0.050	0.082±0.015	0.885±0.165	1.001±0.186
Mg XII	8.4209	0.243±0.018	0.079±0.006	0.730±0.053	0.821±0.060
Al XII	7.7572	0.635±0.158	0.185±0.046	1.951±0.486	2.205±0.549
Al XIII	7.1729	0.377±0.126	0.138±0.046	1.181±0.396	1.325±0.444
Si XIII	6.6479	0.251±0.015	0.076±0.004	0.806±0.047	0.912±0.053
Si XIV	6.1830	0.255±0.029	0.112±0.013	0.789±0.089	0.881±0.099
S XV	5.0387	0.601±0.074	0.224±0.027	2.160±0.265	2.460±0.302
S XVI	4.7300	0.590±0.140	0.459±0.109	1.225±0.290	1.334±0.316
Ar XVII	3.9488	2.686±0.478	1.391±0.248	8.157±1.451	9.243±1.644
Fe XVII	15.015	0.208±0.009	0.071±0.003	0.809±0.034	0.918±0.039
Fe XVII	17.075	0.253±0.040	0.088±0.014	1.034±0.165	1.174±0.187
Fe XVII	15.262	0.312±0.022	0.106±0.007	1.223±0.086	1.388±0.097
Fe XVII	16.777	0.237±0.016	0.083±0.005	0.974±0.065	1.106±0.073
Fe XVIII	14.204	0.321±0.019	0.090±0.005	0.882±0.053	0.996±0.060
Fe XIX	13.520	0.423±0.029	0.110±0.007	1.084±0.074	1.221±0.083
Fe XX*	12.829	0.077±0.097	0.020±0.025	0.216±0.273	0.243±0.307
Fe XXI	12.284	0.285±0.022	0.080±0.006	0.964±0.075	1.089±0.085
Fe XXII	11.767	0.188±0.024	0.061±0.008	0.773±0.097	0.879±0.110
Fe XXIII	11.736	0.214±0.028	0.091±0.012	0.938±0.122	1.077±0.140
Fe XXIV	11.170	0.310±0.066	0.197±0.042	0.884±0.189	0.986±0.211
Fe XXV*	1.8559	1.046±0.377	3.481±1.254	0.625±0.225	0.612±0.221

Table 6.6: Abundances derived for individual lines from the DEM calculated from iron lines for the AB Dor HETGS dataset 16.

element	2nd order	3rd order	4th order	5th order	2T fit
N	0.968±0.129	0.407±0.054	4.746±0.632	5.357±0.713	1.062
O	0.541±0.036	0.220±0.017	2.552±0.380	2.881±0.431	0.673
Ne	1.311±0.091	0.441±0.070	4.560±1.192	5.143±1.354	0.995
Mg	0.246±0.017	0.080±0.005	0.745±0.051	0.838±0.057	0.185
Al	0.478±0.125	0.162±0.033	1.488±0.377	1.673±0.430	0.208
Si	0.252±0.013	0.080±0.011	0.802±0.042	0.905±0.047	0.225
S	0.598±0.065	0.238±0.056	1.734±0.466	1.923±0.562	0.400
Ar	2.686±0.478	1.391±0.248	8.157±1.451	9.243±1.644	1.154
Fe	0.238±0.015	0.079±0.004	0.891±0.040	1.010±0.045	0.211

Table 6.7: Absolute abundances derived from the DEM calculated from iron lines and a corresponding global fit with two temperature components for the AB Dor HETGS dataset 16.

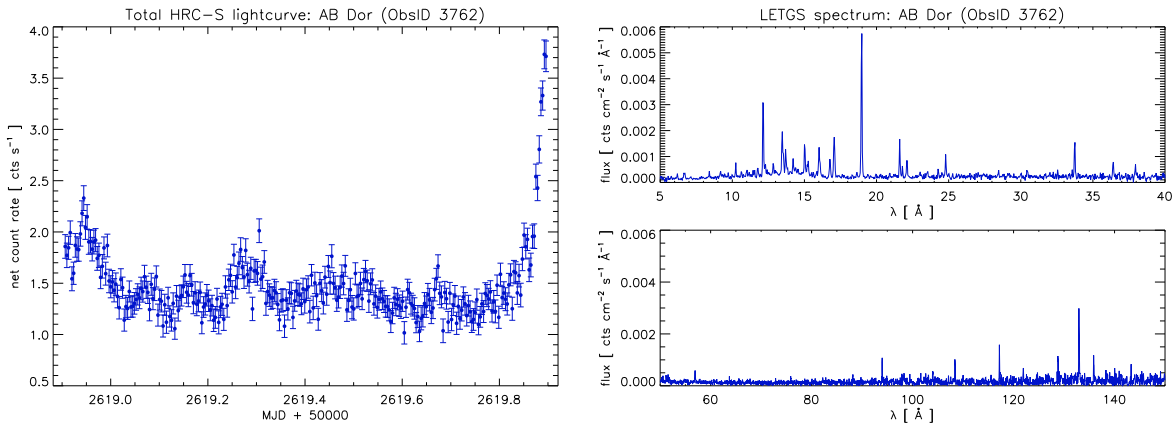

Figure 6.3: Lightcurve (left) and spectrum (right) of AB Dor from 10/11 December 2002 obtained with the LETGS and HRC-S onboard *Chandra*.

6.1.2 The LETGS dataset ObsID 3762

Hussain et al. (2005) use the LETGS dataset of AB Dor to verify rotational modulation in X-rays and to measure Doppler shifts in order to determine the size of coronal structures. The observation, lasting for 88.1 ks, covers nearly two rotational periods. The lightcurve shown in Figure 6.3 is moderately quiescent apart from a strong flare beginning at the end of the observation. The short-wavelength part of the fluxed spectrum compares quite well to the MEG spectrum shown in Figure 6.1, the high-temperature iron lines in the long-wavelength part are not that well-pronounced.

Nevertheless these iron lines could be measured together with five H-like to He-like ratios, from ranging from carbon to silicon, i.e. temperatures from $\approx$ 1 MK to 16 MK are covered. Only polynomials up to the forth order could be fitted to these ratios and the results are not really satisfactory. 3rd and 4th order polynomials reproduce at least most of the ratios well, apart from the higher-temperature silicon and magnesium (cf. Table 6.8). The rise of the DEM at lower temperatures is suspicious, though it is at the boundary of the reliable temperature range. Nevertheless the deduced iron abundance of the low-temperature Fe XVI is systematically too low (see Table 6.11). Again, the iron lines show a broad scatter.

The iron lines (Fe XVI to Fe XXIV) cover somewhat higher temperatures ranging from 2.5 MK to 20 MK, but the thus obtained $DEMs$ do not provide better fits. They can in no way reproduce the line ratios of the H-like and He-like lines, and especially in 4th order the normalization is gone wrong. The shape of neither the $DEMs$ from the iron lines nor of those from the ratios, shown in Figure 6.4, matches the HETG fit. The two-peaked structure does not develop either.

The abundances derived from a global fit with two temperature components to the LETGS data differ somewhat from the corresponding global fit to the HETGS data. The abundances derived from the $DEMs$ fitted to the LETGS data match the global fit not that well, neither absolute nor relative to oxygen, as can be read off from Tables 6.12, 6.9, 6.14 and 6.10. The iron lines seem to provide partly more reasonable values, but not for all elements. In general the abundances seem at least to retain the general trend of an inverse FIP effect, apart from the values for oxygen. The overall order of magnitude of the relative values derived from HETGS and LETGS data agrees up to a certain degree.

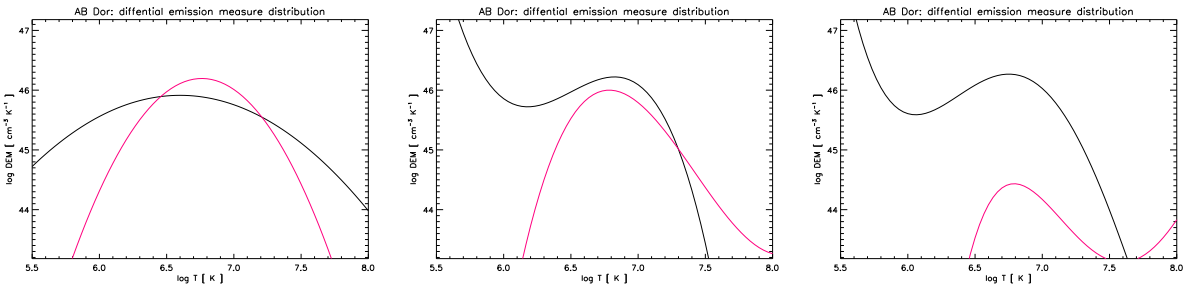

Figure 6.4: Second to forth order polynomials representing the differential emission measures for AB Dor calculated from the LETGS dataset 3762. The two parabolas (left) differ considerably, the one from iron is clearly better. The third (middle) and fourth (right) order polynomials diverge at the boundaries of the appointed valid temperature ranges. At least for the the maximum value at $\log T$ approximates the first peak found in the HETGS data.

	measured	2nd order	3rd order	4th order
C VI / C V	3.106±0.869	6.580 (23.991)	3.142 (***)	3.092 (***)
O VIII / O VII	4.452±0.262	3.313 (5.337)	4.431 (***)	4.533 (***)
Ne X / Ne IX	2.172±0.092	2.110 (2.102)	2.167 (***)	2.101 (33.615)
Mg XII / Mg XI	0.976±0.193	1.738 (1.254)	1.231 (***)	1.346 (32.223)
Si XIV / Si XIII	1.281±0.274	1.366 (0.762)	0.648 (***)	1.097 (51.034)
19.5-20.5 Å	6.497±1.299	6.497 (6.497)	6.497 (6.497)	6.497 (6.481)
red. χ^2		16.99 (5.53)	3.55 (4.10)	4.80 (4.44)

Table 6.8: Fit results from H-like to He-like ratios from the AB Dor LETGS dataset 3762: Photon flux ratios and continuum flux [10^{-4} cts s^{-1} cm^{-2}] in specified wavelength bands. The corresponding results from the iron line fit are given in brackets.

element	2nd order	3rd order	4th order	2T fit
C / O	1.006±0.151	1.079±0.065	1.162±0.070	1.340
N / O	1.821±0.220	1.925±0.136	1.934±0.136	1.554
Ne / O	3.240±0.329	2.816±0.076	2.889±0.078	1.826
Mg / O	0.556±0.153	0.553±0.061	0.584±0.088	0.391
Si / O	0.605±0.083	0.762±0.261	0.757±0.072	0.338
Fe / O	0.386±0.047	0.328±0.016	0.365±0.020	0.166

Table 6.9: Abundances relative to oxygen derived from the DEM calculated from H-like to He-like ratios and a corresponding global fit with two temperature components for the AB Dor LETGS dataset 3762.

abundance	2nd order	3rd order	4th order	2T fit
C / O	1.344±0.261	1.228±0.486	1.269±0.488	1.340
N / O	2.017±0.171	1.980±0.670	2.020±0.657	1.554
Ne / O	2.776±0.151	1.793±1.481	1.883±1.422	1.826
Mg / O	0.556±0.071	0.160±0.137	0.167±0.137	0.391
Si / O	0.747±0.193	0.101±0.069	0.106±0.070	0.338
Fe / O	0.327±0.021	85.441±***	2.852±0.912	0.166

Table 6.10: Abundances relative to oxygen derived from the DEM calculated from iron lines and a corresponding global fit with two temperature components for the AB Dor LETGS dataset 3762.

element	wavelength	2nd order	3rd order	4th order
C V	40.268	1.142±0.312	0.405±0.111	0.365±0.100
C VI	33.737	0.539±0.032	0.401±0.024	0.367±0.022
N VII	24.782	0.987±0.067	0.715±0.049	0.610±0.042
O VII	21.602	0.421±0.023	0.370±0.021	0.321±0.018
O VIII	18.970	0.566±0.010	0.372±0.007	0.315±0.006
Ne IX	13.447	1.725±0.058	1.045±0.035	0.892±0.030
Ne X	12.134	1.775±0.046	1.047±0.027	0.923±0.024
Mg XI	9.1688	0.475±0.074	0.241±0.037	0.232±0.036
Mg XII	8.4210	0.267±0.033	0.191±0.024	0.168±0.021
Si XIII	6.6480	0.344±0.063	0.201±0.037	0.214±0.039
Si XIV	6.1830	0.323±0.035	0.398±0.043	0.250±0.027
Fe XVI	63.711	0.116±0.031	0.080±0.021	0.066±0.018
Fe XVII	15.015	0.212±0.009	0.108±0.005	0.097±0.004
Fe XVII	17.075	0.251±0.009	0.131±0.005	0.116±0.004
Fe XVII	15.262	0.271±0.025	0.139±0.013	0.124±0.011
Fe XVII	16.777	0.234±0.014	0.122±0.007	0.108±0.006
Fe XVIII	14.205	0.320±0.026	0.147±0.012	0.143±0.012
Fe XVIII	93.923	0.205±0.018	0.097±0.009	0.092±0.008
Fe XVIII	103.93	0.425±0.064	0.202±0.031	0.190±0.029
Fe XIX*	13.521	0.535±0.036	0.245±0.017	0.257±0.017
Fe XIX	108.35	0.293±0.027	0.133±0.012	0.136±0.013
Fe XIX	101.55	0.331±0.067	0.151±0.030	0.154±0.031
Fe XX	121.84	0.187±0.025	0.089±0.012	0.096±0.013
Fe XXI	128.75	0.168±0.021	0.089±0.011	0.101±0.012
Fe XXII	117.15	0.193±0.016	0.123±0.010	0.143±0.012
Fe XXII	135.79	0.232±0.029	0.148±0.018	0.172±0.021
Fe XXIII	132.90	0.140±0.008	0.126±0.007	0.145±0.008
Fe XXIV	11.171	0.316±0.055	0.633±0.110	0.677±0.118

Table 6.11: Abundances derived for individual lines from the DEM calculated from H-like to He-like ratios for the AB Dor LETGS dataset 3762.

element	2nd order	3rd order	4th order	2T fit
C	0.545±0.061	0.401±0.023	0.366±0.021	0.607
N	0.987±0.067	0.715±0.049	0.610±0.042	0.704
O	0.542±0.054	0.372±0.007	0.315±0.006	0.453
Ne	1.756±0.036	1.047±0.021	0.911±0.019	0.827
Mg	0.301±0.077	0.206±0.022	0.184±0.028	0.117
Si	0.328±0.031	0.283±0.097	0.239±0.022	0.153
Fe	0.209±0.014	0.122±0.005	0.115±0.006	0.075

Table 6.12: Absolute abundances derived from the DEM calculated from H-like to He-like ratios and a corresponding global fit with two temperature components for the AB Dor LETGS dataset 3762.

element	wavelength	2nd order	3rd order	4th order
C V	40.268	4.074±1.114	16.152±4.417	***
C VI	33.737	0.527±0.031	0.003±0.000	3.870±0.229
N VII	24.782	0.795±0.054	0.005±0.000	6.165±0.421
O VII	21.602	0.466±0.026	1.238±0.069	79.177±4.417
O VIII	18.970	0.389±0.007	0.003±0.000	3.039±0.056
Ne IX	13.447	1.073±0.036	1.817±0.061	85.932±2.906
Ne X	12.134	1.108±0.028	0.005±0.000	5.553±0.143
Mg XI	9.1688	0.261±0.041	0.344±0.053	16.541±2.569
Mg XII	8.4210	0.203±0.025	0.000	0.501±0.062
Si XIII	6.6480	0.220±0.040	0.169±0.031	12.788±2.346
Si XIV	6.1830	0.370±0.040	0.000	0.321±0.035
Fe XVI	63.711	0.082±0.022	0.168±0.045	8.067±2.165
Fe XVII	15.015	0.114±0.005	0.191±0.008	7.634±0.339
Fe XVII	17.075	0.137±0.005	0.231±0.008	9.328±0.330
Fe XVII	15.262	0.146±0.013	0.244±0.023	9.800±0.905
Fe XVII	16.777	0.127±0.007	0.215±0.012	8.682±0.503
Fe XVIII	14.205	0.163±0.013	0.261±0.021	10.124±0.826
Fe XVIII	93.923	0.106±0.009	0.171±0.015	6.667±0.589
Fe XVIII	103.93	0.219±0.033	0.355±0.054	13.828±2.095
Fe XIX*	13.521	0.282±0.019	0.454±0.031	17.867±1.204
Fe XIX	108.35	0.151±0.014	0.243±0.022	9.478±0.872
Fe XIX	101.55	0.171±0.035	0.275±0.055	10.718±2.164
Fe XX	121.84	0.103±0.014	0.167±0.022	6.708±0.901
Fe XXI	128.75	0.102±0.012	0.171±0.021	7.028±0.861
Fe XXII	117.15	0.135±0.011	0.232±0.020	9.680±0.822
Fe XXII	135.79	0.163±0.020	0.279±0.034	11.636±1.438
Fe XXIII	132.90	0.125±0.007	0.216±0.013	8.562±0.497
Fe XXIV	11.171	0.487±0.085	0.216±0.038	8.700±1.511

Table 6.13: Abundances derived for individual lines from the DEM calculated from iron lines for the AB Dor LETGS dataset 3762.

element	2nd order	3rd order	4th order	2T fit
C	0.530±0.099	0.003±0.001	3.871±0.835	0.607
N	0.795±0.054	0.005±0.000	6.165±0.421	0.704
O	0.394±0.020	0.003±0.001	3.051±0.971	0.453
Ne	1.095±0.022	0.005±0.003	5.746±3.936	0.827
Mg	0.219±0.026	0.000	0.510±0.384	0.117
Si	0.295±0.075	0.000	0.324±0.186	0.153
Fe	0.129±0.005	0.217±0.007	8.702±0.295	0.075

Table 6.14: Absolute abundances derived from the DEM calculated from iron lines and a corresponding global fit with two temperature components for the AB Dor LETGS dataset 3762.

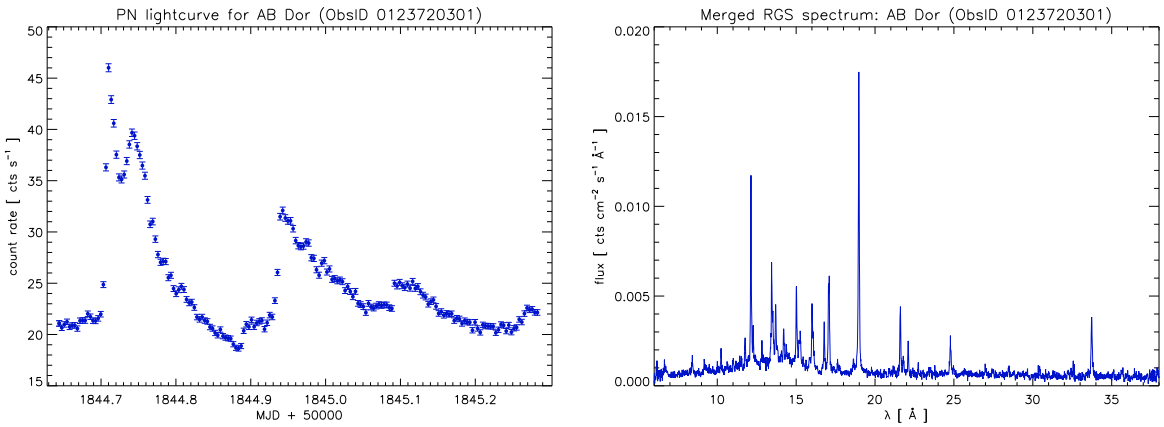

Figure 6.5: Lightcurve (left) and spectrum (right) of AB Dor from 27/28 October 2000 obtained with EPIC-PN and RGS onboard *XMM* respectively.

6.1.3 The RGS dataset ObsID 0123720301

AB Dor is used as a calibrational target for *XMM*, and especially for the wavelength calibration of the RGS. It has therefore been extensively observed during the commissioning and calibration phase of the satellite and is still regularly observed. More than 1000 ks of observing time with the RGS have been gathered together to date, which would result in a high resolution X-ray spectrum of incomparable quality and signal-to-noise when combined with the SAS 6.5 task `rgscombine`. Results from early data have been presented by Güdel et al. (2001), Sanz-Forcada et al. (2003) examine selected datasets covering different states of activity.

Since SAS 6.5 was not available when I sifted the existing data for processing and analyzing, I could only select single RGS datasets to include in this study. For AB Dor I chose the – relatively early – dataset 0123720301 with a total exposure time of 55.1 ks in RGS 1. This dataset has not been discussed in the literature before.

The lightcurve of the observation shows that AB Dor was caught in a very active state, displaying multiple flares. The fluxed spectrum though compares again quite well to the previously described datasets. The PN dataset covers a somewhat longer time interval of 58.9 ks.

The RGS dataset 0123720301 allowed the measurement of the H-like to He-like ratios from nitrogen, oxygen, neon, magnesium and silicon, i.e. of all ratios typically measureable with the RGS. The nitrogen ratio has a relatively high measurement error. I would therefore constrain the reasonable temperature range covered by the ratios from 2 MK to 13 MK. Iron lines are only available from ionization stages XVII to XX, so that the confidence range for the iron line fit would not exceed 3 MK to 10 MK. Higher temperatures are however covered by the three continuum measurements, thus an extension to higher temperatures should be possible.

The parabola and the third order polynomial obtained from both the ratio and the iron line fit are almost identical for temperatures exceeding 6 MK. These polynomials have a simple shape and maxima located approximately at $\log T = 6.7 - 6.8$, similar to the corresponding fits to the HETGS data. The reconstructed $DEMs$ are somewhat broader though. The 4th order evolves – for both the ratio and the iron line fit – to the two-peaked shape already known from the HETGS fits. The iron line fit looks almost identical, apart from the normalization. The RGS ratio fit leads to a broader DEM than in the HETGS fit. The ratio fit has its first maximum at ≈ 4 MK, and the not very well pronounced second peak at ≈ 25 MK. The corresponding iron line fit peaks at 6.5 MK and 30 MK. Only minor changes in the shape of the reconstructed $DEMs$ result for 5th and 6th order polynomials.

Thus the 4th order polynomial gives the best fit in the sense of reduced χ^2. Nevertheless,

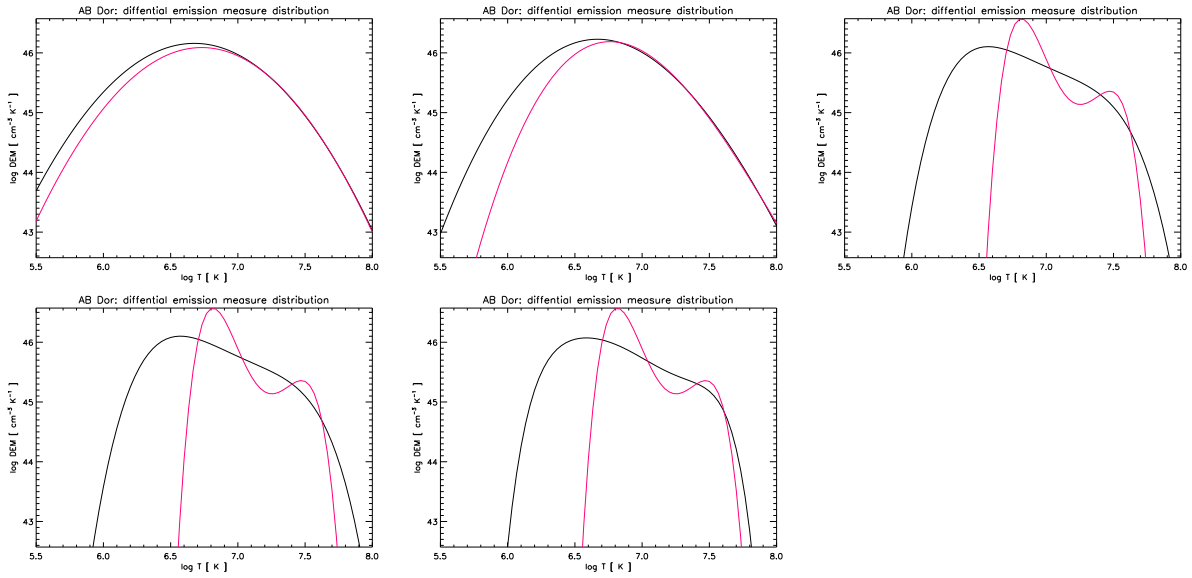

Figure 6.6: Differential emission measures for AB Dor with the polynomial order ranging from 2 to 6, calculated from the RGS dataset 0123720301.

all polynomials obtained from th ratio fits reproduce the measured ratios and continuum fluxes well, see Table 6.15. The iron abundances reconstructed from these fits (Table 6.20) show the typical scatter.

The averaged absolute abundances per element (Table 6.19) are relatively stable compared with the results from the HETGS and LETGS fits. The values obtained from the 2nd and 3rd order fit are systematically lower than for the higher orders and they do not match the results from the global fit with two temperature components. This discrepancy remains also for the values derived relative to oxygen that are listed in Table 6.16. While the values from all polynomials compare well with each other, they do not match the global fit results. Instead they are compatible with the relative abundances deduced from the HETGS and LETGS DEM reconstructions, apart from magnesium that is enhanced by a factor of two. In general, the values of the low-FIP elements, i.e. magnesium, silicon and iron, are increased compared to he HETGS and LETGS datasets that are not dominated by strong flares while this RGS observation is characterized by flaring activity.

The iron line fit does not reproduce the H-like to He-like ratios well, see Table 6.17. The best results are obtained from the parabola that was very similar to the ratio fit parabola (Figure 6.6), but the best fit with regard to the iron lines is obtained by the 4th order polynomial. These higher order iron line fits reproduce none of the ratios within the errors, the strongest discrepancies arise from the low temperature elements like oxygen and nitrogen.

The abundances deduced from the iron lines however fit the scheme built up by the former measurements. The absolute values listed in Table 6.21 are somewhat higher than for the ratio fit but still do not match the global fit. The values relative to oxygen in Table 6.18 match the results from the global fit better than does the ratio fit, even the values of the low-FIP elements are reduced. back to the values in the HETGS and LETGS fits.

	measured	2nd order	3rd order	4th order	5th order	6th oder
N VII / N VI	9.145±3.350	5.398	5.759	7.066	7.014	7.063
O VIII / O VII	3.817±0.179	3.733	3.798	3.840	3.841	3.838
Ne X / Ne IX	1.823±0.116	1.965	1.899	1.796	1.797	1.802
Mg XII / Mg XI	1.360±0.222	1.409	1.333	1.472	1.468	1.441
Si XIV / Si XIII	1.559±0.499	0.996	0.939	1.213	1.215	1.225
3-4 Å	3.129±0.092	3.185	3.190	3.126	3.125	3.111
2-3 Å	2.015±0.059	1.967	1.953	2.017	2.018	2.032
1-2 Å	0.769±0.014	0.770	0.771	0.768	0.768	0.767
red. χ^2		1.06	1.14	0.40	0.60	1.13

Table 6.15: Fit results from H-like to He-like ratios from the AB Dor RGS dataset 0123720301: Photon flux ratios and continuum flux [10^{-4} cts s^{-1} cm^{-2}] in specified wavelength bands.

abundance	2nd order	3rd order	4th order	5th order	6th oder	2T fit
C / O	1.106±0.047	1.139±0.048	1.239±0.053	1.235±0.052	1.238±0.053	1.139
N / O	1.796±0.176	1.814±0.152	1.859±0.103	1.858±0.103	1.856±0.103	1.712
Ne / O	3.136±0.105	3.154±0.099	3.318±0.104	3.314±0.104	3.299±0.103	1.716
Mg / O	1.027±0.073	1.069±0.076	1.104±0.079	1.104±0.079	1.111±0.079	0.357
Si / O	0.788±0.170	0.823±0.199	0.853±0.138	0.854±0.138	0.867±0.140	0.345
Fe / O	0.523±0.036	0.513±0.036	0.561±0.044	0.559±0.044	0.551±0.043	0.337

Table 6.16: Abundances relative to oxygen derived from the DEM calculated from H-like to He-like ratios and a corresponding global fit with two temperature components for the AB Dor RGS dataset 0123720301.

	measured	2nd order	3rd order	4th order	5th order	6th oder
N VII / N VI	9.145±3.350	6.421	9.716	35.834	35.834	35.834
O VIII / O VII	3.817±0.179	4.300	5.551	18.824	18.824	18.824
Ne X / Ne IX	1.823±0.116	2.145	2.229	3.249	3.249	3.249
Mg XII / Mg XI	1.360±0.222	1.503	1.418	1.070	1.070	1.070
Si XIV / Si XIII	1.559±0.499	1.041	0.942	0.664	0.664	0.664
3-4 Å	3.129±0.092	3.177	3.201	3.129	3.129	3.129
2-3 Å	2.015±0.059	1.972	1.945	2.015	2.015	2.015
1-2 Å	0.769±0.014	0.770	0.771	0.768	0.768	0.768
red. χ^2		4.86	5.88	3.39	5.09	10.19

Table 6.17: Fit results from iron lines from the AB Dor RGS dataset 0123720301: Photon flux ratios and continuum flux [10^{-4} cts s^{-1} cm^{-2}] in specified wavelength bands.

abundance	2nd order	3rd order	4th order	5th order	6th oder	2T fit
C / O	1.143±0.074	1.261±0.206	1.483±0.724	1.483±0.724	1.483±0.724	1.139
N / O	1.813±0.144	1.886±0.316	2.150±1.071	2.150±1.071	2.150±1.071	1.712
Ne / O	2.849±0.217	2.579±0.445	1.876±0.965	1.876±0.965	1.876±0.965	1.716
Mg / O	0.889±0.077	0.822±0.143	0.644±0.321	0.644±0.321	0.644±0.321	0.357
Si / O	0.678±0.136	0.627±0.180	0.525±0.325	0.525±0.325	0.525±0.325	0.345
Fe / O	0.490±0.041	0.432±0.074	0.274±0.134	0.274±0.134	0.274±0.134	0.337

Table 6.18: Abundances relative to oxygen derived from the DEM calculated from iron lines for the AB Dor RGS dataset 0123720301.

element	2nd order	3rd order	4th order	5th order	6th oder	2T fit
C	0.438±0.016	0.401±0.015	0.620±0.023	0.622±0.023	0.653±0.024	1.079
N	0.710±0.068	0.639±0.052	0.931±0.047	0.935±0.048	0.978±0.050	1.621
O	0.396±0.009	0.352±0.008	0.501±0.011	0.503±0.011	0.527±0.011	0.947
Ne	1.241±0.032	1.110±0.025	1.661±0.037	1.668±0.038	1.739±0.039	1.625
Mg	0.406±0.028	0.376±0.026	0.553±0.038	0.556±0.038	0.586±0.040	0.338
Si	0.312±0.067	0.290±0.070	0.427±0.068	0.430±0.069	0.457±0.073	0.327
Fe	0.207±0.014	0.181±0.012	0.281±0.021	0.282±0.021	0.291±0.022	0.319

Table 6.19: Absolute abundances derived from the DEM calculated from H-like to He-like ratios and a corresponding global fit with two temperature components for the AB Dor RGS dataset 0123720301.

element	wavelength	2nd order	3rd order	4th order	5th order	6th oder
C VI	33.737	0.438±0.016	0.401±0.015	0.620±0.023	0.622±0.023	0.653±0.024
N VI	28.787	0.429±0.156	0.410±0.149	0.725±0.263	0.723±0.262	0.761±0.276
N VII	24.782	0.727±0.037	0.650±0.033	0.938±0.048	0.943±0.049	0.986±0.051
O VII	21.602	0.390±0.015	0.351±0.014	0.503±0.020	0.506±0.020	0.529±0.021
O VIII	18.970	0.398±0.010	0.353±0.009	0.500±0.013	0.502±0.013	0.526±0.014
Ne IX	13.447	1.324±0.078	1.150±0.068	1.640±0.097	1.647±0.097	1.722±0.101
Ne X	12.134	1.228±0.030	1.104±0.027	1.665±0.041	1.672±0.041	1.742±0.043
Mg XI	9.1688	0.418±0.060	0.370±0.053	0.588±0.085	0.591±0.085	0.613±0.088
Mg XII	8.4210	0.403±0.031	0.378±0.029	0.544±0.042	0.547±0.042	0.578±0.045
Si XIII	6.6480	0.273±0.058	0.252±0.054	0.390±0.083	0.393±0.084	0.419±0.090
Si XIV	6.1830	0.428±0.102	0.419±0.100	0.502±0.119	0.505±0.120	0.533±0.127
Fe XVII	15.015	0.193±0.011	0.168±0.010	0.258±0.015	0.259±0.015	0.267±0.015
Fe XVII	17.075	0.221±0.011	0.192±0.009	0.292±0.014	0.293±0.014	0.303±0.015
Fe XVII	15.262	0.163±0.039	0.141±0.033	0.218±0.052	0.219±0.052	0.225±0.053
Fe XVII	16.777	0.170±0.017	0.147±0.015	0.225±0.023	0.226±0.023	0.233±0.024
Fe XVIII	14.205	0.267±0.017	0.236±0.015	0.394±0.025	0.395±0.025	0.405±0.025
Fe XIX	13.521	0.316±0.030	0.284±0.027	0.488±0.046	0.491±0.046	0.509±0.048
Fe XX	12.830	0.171±0.024	0.157±0.022	0.265±0.037	0.267±0.038	0.284±0.040

Table 6.20: Abundances derived for individual lines from the DEM calculated from H-like to He-like ratios for the AB Dor RGS dataset 0123720301.

element	2nd order	3rd order	4th order	5th order	6th oder	2T fit
C	0.552±0.020	0.568±0.021	0.795±0.029	0.795±0.029	0.795±0.029	1.079
N	0.875±0.051	0.849±0.043	1.154±0.121	1.154±0.121	1.154±0.121	1.621
O	0.483±0.026	0.450±0.072	0.536±0.261	0.536±0.261	0.536±0.261	0.947
Ne	1.376±0.075	1.162±0.077	1.007±0.167	1.007±0.167	1.007±0.167	1.625
Mg	0.429±0.029	0.370±0.025	0.345±0.037	0.345±0.037	0.345±0.037	0.338
Si	0.327±0.063	0.283±0.068	0.281±0.108	0.281±0.108	0.281±0.108	0.327
Fe	0.237±0.015	0.195±0.012	0.147±0.006	0.147±0.006	0.147±0.006	0.319

Table 6.21: Absolute abundances derived from the DEM calculated from iron lines for the AB Dor RGS dataset 0123720301.

element	wavelength	2nd order	3rd order	4th order	5th order	6th oder
C VI	33.737	0.552±0.020	0.568±0.021	0.795±0.029	0.795±0.029	0.795±0.029
N VI	28.787	0.622±0.226	0.902±0.327	4.503±1.633	4.503±1.633	4.503±1.633
N VII	24.782	0.886±0.046	0.849±0.044	1.149±0.059	1.149±0.059	1.149±0.059
O VII	21.602	0.527±0.021	0.607±0.024	2.472±0.097	2.472±0.097	2.472±0.097
O VIII	18.970	0.468±0.012	0.418±0.011	0.501±0.013	0.501±0.013	0.501±0.013
Ne IX	13.447	1.587±0.094	1.389±0.082	1.725±0.102	1.725±0.102	1.725±0.102
Ne X	12.134	1.349±0.033	1.136±0.028	0.968±0.024	0.968±0.024	0.968±0.024
Mg XI	9.1688	0.465±0.067	0.383±0.055	0.291±0.042	0.291±0.042	0.291±0.042
Mg XII	8.4210	0.421±0.033	0.367±0.028	0.371±0.029	0.371±0.029	0.370±0.029
Si XIII	6.6480	0.289±0.062	0.246±0.053	0.240±0.051	0.240±0.051	0.240±0.051
Si XIV	6.1830	0.433±0.103	0.407±0.097	0.563±0.134	0.563±0.134	0.563±0.134
Fe XVII	15.015	0.222±0.013	0.183±0.010	0.138±0.008	0.138±0.008	0.138±0.008
Fe XVII	17.075	0.256±0.013	0.212±0.010	0.166±0.008	0.166±0.008	0.166±0.008
Fe XVII	15.262	0.188±0.045	0.155±0.037	0.117±0.028	0.117±0.028	0.117±0.028
Fe XVII	16.777	0.197±0.020	0.163±0.017	0.128±0.013	0.128±0.013	0.128±0.013
Fe XVIII	14.205	0.295±0.018	0.238±0.015	0.149±0.009	0.149±0.009	0.149±0.009
Fe XIX	13.521	0.341±0.032	0.276±0.026	0.199±0.019	0.199±0.019	0.199±0.019
Fe XX	12.830	0.181±0.026	0.150±0.021	0.146±0.021	0.146±0.021	0.146±0.021

Table 6.22: Abundances derived for individual lines from the DEM calculated from iron lines for the AB Dor RGS dataset 0123720301.

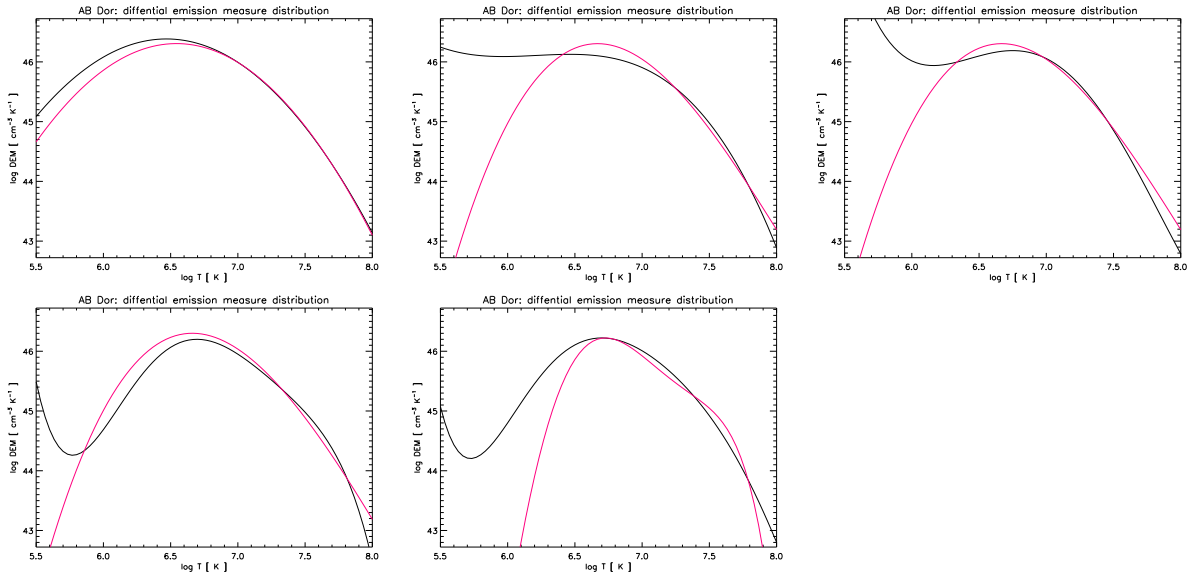

Figure 6.7: Differential emission measures for AB Dor with the polynomial order ranging from 2 to 6 for all dataset combined.

6.1.4 Combined datasets

The HETGS and the LETGS datasets caught AB Dor in a state of moderate activity, while the chosen RGS dataset shows the star continuously flaring. Nevertheless, both the HETGS and the RGS datasets produce $DEMs$ with a two-peaked structure and comparable relative abundances. A combination of the data from these two datasets should thus give similar results. The LETGS dataset reproduced $DEMs$ with a different shape, probably because the high temperatures where the second maximum is located in the two other fits is not that well covered with LETGS data that instead provide information about the lower temperatures from the carbon and nitrogen lines. After all, similar abundances arise from all datasets. A combination of them thus leads to fits covering a broader temperature range.

Figure 6.7 shows the polynomials representing the reconstructed $DEMs$ from the corresponding fits. The parabolas from iron line and ratio fit are broader than those from the HETGS and RGS fits, and slightly shifted to lower temperatures in their maximum, probably due to the influence of the LETGS data. Again both parabolas are very similar. Third and fourth order ratio fit show a rise towards lower temperatures as it could be seen in the corresponding LETGS fits. For temperatures greater than 10 MK they are however still very similar to the iron line fits that decrease towards lower temperatures. The maximum is shifted back to $\log T \approx 6.7$. In fifth order the DEM from the ratio fit at last also lowers up to 1 MK, where the boundary of the reliable temperature interval is reached. Additionally at ≈ 30 MK the second peak slowly forms although it is not very pronounced. Iron line and ratio fit look again very similar. The ratio fit does not change much from 5th to 6th order, and the iron line fit now also shows the convexity suggesting the second peak.

Especially the polynomials with orders 4 to 6 from the ratio fit can reproduce the measured ratios and continuum fluxes quite well (see 6.23). The best-fit model arises from the fifth order. The reproduced iron abundances in Table 6.26 exhibit the well-known scatter, suspicious lines like Fe XVI, Fe XIX at 13.52 Å and Fe XXV show the greatest discrepancies.

The fit results from the iron lines are not that good in terms of χ^2, the parabola gives the best result (see 6.27). The corresponding $DEMs$ can however for the first time reproduce the H-like to He-like ratios within the errors apart from the low-temperature carbon ratio.

As expected the relative abundances given in Tables 6.24 and 6.28 derived from these fits match

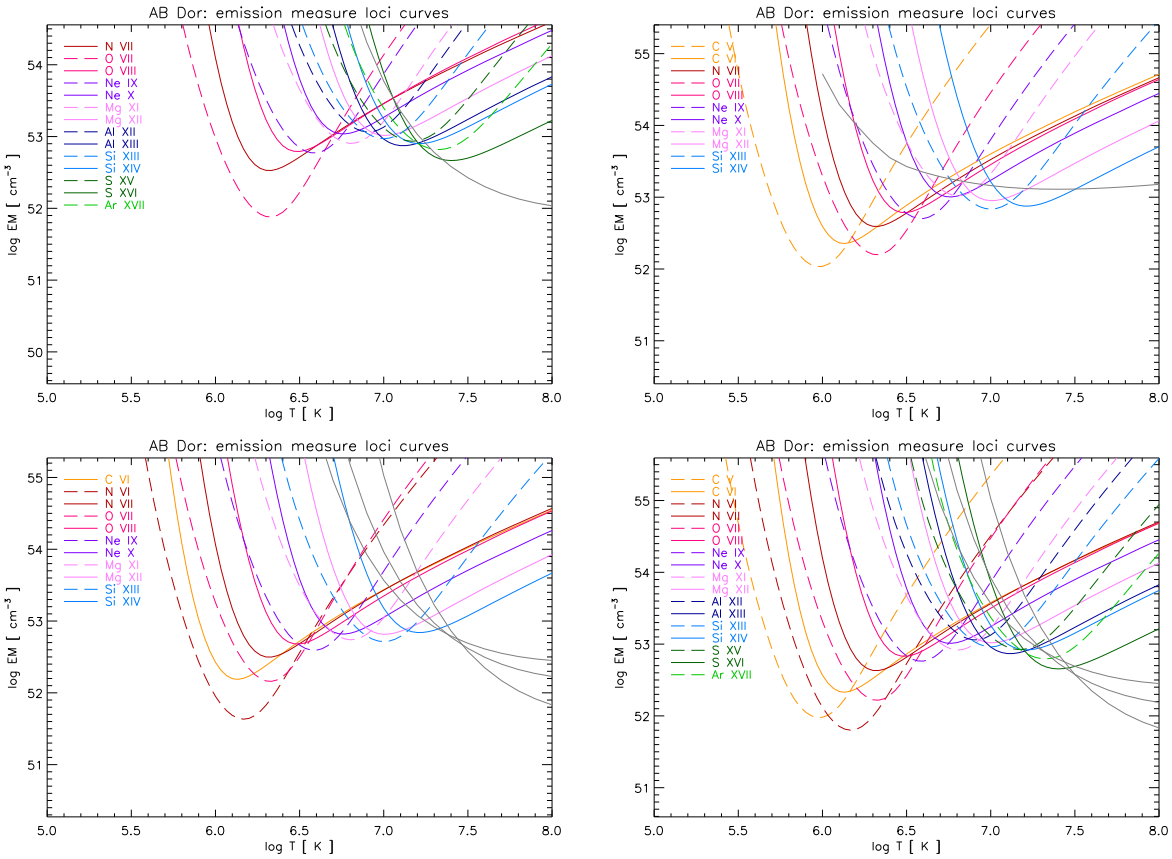

Figure 6.8: Shapes of emission measure distributions constructed from the best-fit $DEMs$ and abundances as a lower limit from the mission measure loci curves for AB Dor. From upper left to lower right: The best-fit polynomial from the HETGS, the LETGS, the RGS and all datasets combined.

the previous determined values from the single datasets, at least those from the polynomials with orders 4 to 6. The corresponding absolute abundances (Tables 6.28 and 6.28) also compare well with each each other.

Aside from the different shapes of the reconstructed $DEMs$ from the different datasets for AB Dor it could be stated as a general result that AB Dor's differential emission measure has its maximum at $\log T \approx 6.7 - 6.8$ with probably a less pronounced second peak around $\log T \approx 7.3 - 7.5$. The corresponding emission measure distributions (see Figure 6.8) thus compare quite well with those calculated by Sanz-Forcada et al. (2003).

The abundances deduced from the fits to the single datasets agree with each other and indicate a moderate inverse FIP effect as it was derived by García-Alvarez et al. (2005).

	measured	2nd order	3rd order	4th order	5th order	6th oder
C VI / C V	3.334±0.919	5.456	4.046	3.532	3.335	3.334
N VII / N VI	8.449±3.133	3.358	3.184	4.103	7.879	7.451
O VIII / O VII	4.715±1.102	2.533	2.727	3.598	4.659	4.515
Ne X / Ne IX	1.921±0.191	1.542	1.840	2.072	1.971	1.997
Mg XII / Mg XI	1.439±0.268	1.186	1.459	1.424	1.321	1.349
Al XIII / Al XII	0.726±0.303	0.995	1.212	1.114	1.078	1.087
Si XIV / Si XIII	1.057±0.116	0.891	1.071	0.937	0.959	0.950
S XVI / S XV	0.588±0.157	0.632	0.730	0.591	0.692	0.663
3-4 Å	3.129±0.092	3.088	3.129	3.126	3.117	3.121
2-3 Å	1.834±0.185	1.906	1.963	1.856	1.952	1.900
1-2 Å	0.769±0.014	0.771	0.766	0.768	0.767	0.768
red. χ^2		2.50	1.54	1.06	0.64	0.76

Table 6.23: Fit results from H-like to He-like ratios from all mentioned AB Dor datasets combined: Photon flux ratios and continuum flux [10^{-4} cts s^{-1} cm^{-2}] in specified wavelength bands.

element	2nd order	3rd order	4th order	5th order	6th oder
C / O	0.870±0.113	0.830±0.089	0.977±0.054	1.311±0.062	1.284±0.061
N / O	1.377±0.433	1.363±0.451	1.600±0.338	1.900±0.157	1.874±0.155
Ne / O	3.401±0.530	3.155±0.349	2.817±0.172	2.772±0.149	2.777±0.149
Mg / O	0.809±0.124	0.655±0.088	0.565±0.056	0.587±0.055	0.580±0.055
Al / O	1.611±0.379	1.196±0.333	1.055±0.232	1.123±0.232	1.102±0.228
Si / O	0.861±0.120	0.654±0.074	0.564±0.037	0.605±0.035	0.592±0.034
S / O	2.153±0.350	1.436±0.215	1.366±0.160	1.430±0.163	1.420±0.162
Ar / O	9.801±2.106	6.235±1.280	6.235±1.143	6.366±1.152	6.482±1.173
Fe / O	0.505±0.069	0.410±0.051	0.353±0.029	0.375±0.027	0.369±0.027

Table 6.24: Abundances relative to oxygen derived from the DEM calculated from H-like to He-like ratios for all mentioned AB Dor datasets combined.

element	2nd order	3rd order	4th order	5th order	6th oder
C	0.214±0.010	0.322±0.011	0.341±0.011	0.508±0.017	0.456±0.015
N	0.339±0.098	0.528±0.166	0.558±0.115	0.736±0.056	0.665±0.050
O	0.246±0.030	0.387±0.040	0.349±0.015	0.387±0.013	0.355±0.012
Ne	0.837±0.083	1.222±0.052	0.982±0.042	1.074±0.045	0.985±0.042
Mg	0.199±0.019	0.254±0.022	0.197±0.017	0.227±0.020	0.206±0.018
Al	0.397±0.080	0.463±0.120	0.368±0.079	0.435±0.089	0.391±0.080
Si	0.212±0.015	0.253±0.012	0.197±0.010	0.234±0.011	0.210±0.010
S	0.530±0.058	0.556±0.061	0.476±0.052	0.554±0.061	0.504±0.055
Ar	2.413±0.429	2.416±0.430	2.174±0.387	2.467±0.439	2.300±0.409
Fe	0.124±0.008	0.159±0.011	0.123±0.009	0.145±0.009	0.131±0.009

Table 6.25: Absolute abundances derived from the DEM calculated from H-like to He-like ratios for all mentioned AB Dor datasets combined.

element	wavelength	2nd order	3rd order	4th order	5th order	6th oder
C V	40.268	0.349±0.096	0.389±0.107	0.361±0.099	0.508±0.139	0.456±0.125
C VI	33.736	0.213±0.007	0.321±0.011	0.340±0.011	0.508±0.017	0.456±0.015
N VI	28.787	0.156±0.057	0.235±0.085	0.296±0.107	0.689±0.250	0.591±0.214
N VII	24.781	0.392±0.030	0.622±0.048	0.609±0.047	0.739±0.057	0.670±0.052
O VII	21.601	0.137±0.032	0.230±0.053	0.268±0.062	0.383±0.089	0.340±0.079
O VIII	18.969	0.254±0.009	0.397±0.013	0.352±0.012	0.388±0.013	0.355±0.012
Ne IX	13.446	0.718±0.062	1.183±0.103	1.042±0.091	1.095±0.095	1.016±0.088
Ne X	12.134	0.895±0.043	1.236±0.060	0.966±0.047	1.068±0.052	0.977±0.047
Mg XI	9.1688	0.178±0.027	0.256±0.039	0.196±0.030	0.215±0.033	0.198±0.030
Mg XII	8.4209	0.216±0.023	0.253±0.027	0.198±0.021	0.235±0.025	0.211±0.023
Al XII	7.7572	0.460±0.115	0.612±0.153	0.458±0.114	0.530±0.132	0.480±0.119
Al XIII	7.1729	0.336±0.112	0.367±0.123	0.299±0.100	0.357±0.120	0.320±0.107
Si XIII	6.6479	0.205±0.011	0.254±0.014	0.192±0.010	0.229±0.012	0.206±0.011
Si XIV	6.1830	0.243±0.023	0.251±0.024	0.216±0.021	0.253±0.024	0.229±0.022
S XV	5.0387	0.539±0.066	0.590±0.072	0.477±0.058	0.578±0.071	0.519±0.064
S XVI	4.7300	0.502±0.119	0.475±0.113	0.475±0.112	0.491±0.116	0.461±0.109
Ar XVII	3.9488	2.413±0.429	2.416±0.430	2.174±0.387	2.467±0.439	2.302±0.409
Fe XVI	63.710	0.041±0.011	0.070±0.019	0.068±0.018	0.074±0.020	0.068±0.018
Fe XVII	15.015	0.115±0.010	0.181±0.016	0.143±0.013	0.150±0.013	0.139±0.013
Fe XVII	17.075	0.129±0.012	0.205±0.020	0.165±0.016	0.172±0.016	0.160±0.015
Fe XVII	15.262	0.127±0.012	0.200±0.019	0.159±0.015	0.166±0.016	0.154±0.015
Fe XVII	16.777	0.112±0.008	0.178±0.012	0.143±0.010	0.149±0.010	0.138±0.009
Fe XVIII	14.204	0.191±0.015	0.275±0.021	0.203±0.015	0.224±0.017	0.205±0.016
Fe XVIII	93.922	0.092±0.008	0.137±0.012	0.103±0.009	0.111±0.010	0.102±0.009
Fe XVIII	103.93	0.190±0.029	0.283±0.043	0.214±0.032	0.230±0.035	0.212±0.032
Fe XIX	13.520	0.288±0.015	0.383±0.020	0.275±0.014	0.324±0.017	0.291±0.015
Fe XIX	108.35	0.147±0.013	0.201±0.018	0.145±0.013	0.167±0.015	0.151±0.014
Fe XIX	101.54	0.166±0.033	0.227±0.046	0.164±0.033	0.189±0.038	0.171±0.034
Fe XX	121.84	0.103±0.014	0.132±0.018	0.095±0.013	0.115±0.015	0.102±0.014
Fe XX	12.829	0.083±0.058	0.104±0.073	0.075±0.053	0.092±0.065	0.082±0.057
Fe XXI	128.75	0.102±0.012	0.122±0.015	0.089±0.011	0.112±0.014	0.099±0.012
Fe XXI	12.284	0.259±0.020	0.304±0.024	0.224±0.017	0.285±0.022	0.250±0.019
Fe XXII	117.15	0.131±0.011	0.147±0.012	0.111±0.009	0.142±0.012	0.125±0.011
Fe XXII	135.79	0.157±0.019	0.177±0.022	0.133±0.016	0.171±0.021	0.150±0.018
Fe XXII	11.767	0.178±0.022	0.196±0.025	0.150±0.019	0.193±0.024	0.169±0.021
Fe XXIII	132.90	0.110±0.006	0.116±0.007	0.093±0.005	0.118±0.007	0.104±0.006
Fe XXIII	11.736	0.205±0.027	0.210±0.027	0.175±0.023	0.217±0.028	0.193±0.025
Fe XXIV	11.170	0.289±0.042	0.278±0.040	0.262±0.038	0.290±0.042	0.275±0.040
Fe XXV	1.8559	0.601±0.217	0.567±0.204	0.754±0.272	0.554±0.199	0.619±0.223

Table 6.26: Abundances derived for individual lines from the DEM calculated from H-like to He-like ratios for all mentioned AB Dor datasets combined.

ratio	measured	2nd order	3rd order	4th order	5th order	6th oder
C VI / C V	3.334±0.919	6.617	15.022	15.022	14.518	46.332
N VII / N VI	8.449±3.133	3.876	6.403	6.403	6.245	14.863
O VIII / O VII	4.715±1.102	2.849	3.963	3.963	3.887	7.178
Ne X / Ne IX	1.921±0.191	1.660	1.835	1.835	1.822	2.148
Mg XII / Mg XI	1.439±0.268	1.249	1.242	1.242	1.243	1.279
Al XIII / Al XII	0.726±0.303	1.037	0.997	0.997	1.002	1.040
Si XIV / Si XIII	1.057±0.116	0.920	0.867	0.867	0.873	0.945
S XVI / S XV	0.588±0.157	0.643	0.593	0.593	0.600	0.731
3-4 Å	3.129±0.092	3.125	3.120	3.120	3.119	3.107
2-3 Å	1.834±0.185	1.925	1.893	1.893	1.899	1.970
1-2 Å	0.769±0.014	0.767	0.768	0.768	0.768	0.768
red. χ^2		7.56	7.93	8.43	8.99	9.55

Table 6.27: Fit results from iron lines from all mentioned AB Dor datasets combined: Photon flux ratios and continuum flux [10^{-4} cts s^{-1} cm^{-2}] in specified wavelength bands.

abundance	2nd order	3rd order	4th order	5th order	6th oder
C / O	0.870±0.113	0.830±0.089	0.977±0.054	1.311±0.062	1.284±0.061
N / O	1.377±0.433	1.363±0.451	1.600±0.338	1.900±0.157	1.874±0.155
Ne / O	3.401±0.530	3.155±0.349	2.817±0.172	2.772±0.149	2.777±0.149
Mg / O	0.809±0.124	0.655±0.088	0.565±0.056	0.587±0.055	0.580±0.055
Al / O	1.611±0.379	1.196±0.333	1.055±0.232	1.123±0.232	1.102±0.228
Si / O	0.861±0.120	0.654±0.074	0.564±0.037	0.605±0.035	0.592±0.034
S / O	2.153±0.350	1.436±0.215	1.366±0.160	1.430±0.163	1.420±0.162
Ar / O	9.801±2.106	6.235±1.280	6.235±1.143	6.366±1.152	6.482±1.173
Fe / O	0.505±0.069	0.410±0.051	0.353±0.029	0.375±0.027	0.369±0.027

Table 6.28: Abundances relative to oxygen derived from the DEM calculated from iron lines for all mentioned AB Dor datasets combined.

element	2nd order	3rd order	4th order	5th order	6th oder
C	0.214±0.010	0.322±0.011	0.341±0.011	0.508±0.017	0.456±0.015
N	0.339±0.098	0.528±0.166	0.558±0.115	0.736±0.056	0.665±0.050
O	0.246±0.030	0.387±0.040	0.349±0.015	0.387±0.013	0.355±0.012
Ne	0.837±0.083	1.222±0.052	0.982±0.042	1.074±0.045	0.986±0.042
Mg	0.199±0.019	0.254±0.022	0.197±0.017	0.227±0.020	0.206±0.018
Al	0.397±0.080	0.463±0.120	0.368±0.079	0.435±0.089	0.391±0.080
Si	0.212±0.015	0.253±0.012	0.197±0.010	0.234±0.011	0.210±0.010
S	0.530±0.058	0.556±0.061	0.476±0.052	0.554±0.061	0.504±0.055
Ar	2.413±0.429	2.416±0.430	2.174±0.387	2.467±0.439	2.302±0.409
Fe	0.124±0.008	0.159±0.011	0.123±0.009	0.145±0.009	0.131±0.009

Table 6.29: Absolute abundances derived from the DEM calculated from iron lines for all mentioned AB Dor datasets combined.

element	wavelength	2nd order	3rd order	4th order	5th order	6th oder
C V	40.268	0.528±0.144	1.623±0.444	1.623±0.444	1.561±0.427	9.314±2.547
C VI	33.736	0.266±0.009	0.360±0.012	0.360±0.012	0.358±0.012	0.670±0.023
N VI	28.787	0.212±0.077	0.409±0.148	0.409±0.148	0.399±0.145	1.615±0.586
N VII	24.781	0.463±0.036	0.540±0.042	0.540±0.042	0.540±0.042	0.918±0.071
O VII	21.601	0.173±0.040	0.249±0.058	0.249±0.058	0.245±0.057	0.667±0.154
O VIII	18.969	0.286±0.010	0.296±0.010	0.296±0.010	0.298±0.010	0.438±0.015
Ne IX	13.446	0.814±0.071	0.829±0.072	0.829±0.072	0.834±0.073	1.209±0.105
Ne X	12.134	0.942±0.046	0.867±0.042	0.867±0.042	0.879±0.043	1.081±0.052
Mg XI	9.1688	0.188±0.029	0.172±0.026	0.172±0.026	0.175±0.026	0.217±0.033
Mg XII	8.4209	0.217±0.023	0.199±0.022	0.199±0.022	0.202±0.022	0.244±0.026
Al XII	7.7572	0.476±0.119	0.430±0.107	0.430±0.107	0.437±0.109	0.540±0.134
Al XIII	7.1729	0.333±0.112	0.313±0.105	0.313±0.105	0.316±0.106	0.377±0.126
Si XIII	6.6479	0.209±0.011	0.189±0.010	0.189±0.010	0.192±0.010	0.238±0.013
Si XIV	6.1830	0.240±0.023	0.231±0.022	0.231±0.022	0.233±0.022	0.267±0.026
S XV	5.0387	0.536±0.066	0.502±0.062	0.502±0.062	0.508±0.062	0.614±0.075
S XVI	4.7300	0.490±0.116	0.499±0.118	0.499±0.118	0.498±0.118	0.494±0.117
Ar XVII	3.9488	2.370±0.422	2.321±0.413	2.321±0.413	2.334±0.415	2.564±0.456
Fe XVI	63.710	0.048±0.013	0.053±0.014	0.053±0.014	0.053±0.014	0.090±0.024
Fe XVII	15.015	0.125±0.011	0.117±0.011	0.117±0.011	0.119±0.011	0.151±0.014
Fe XVII	17.075	0.142±0.014	0.134±0.013	0.134±0.013	0.135±0.013	0.174±0.017
Fe XVII	15.262	0.139±0.013	0.130±0.013	0.130±0.013	0.131±0.013	0.167±0.016
Fe XVII	16.777	0.123±0.008	0.116±0.008	0.116±0.008	0.117±0.008	0.151±0.010
Fe XVIII	14.204	0.201±0.015	0.179±0.014	0.179±0.014	0.182±0.014	0.220±0.017
Fe XVIII	93.922	0.098±0.009	0.088±0.008	0.088±0.008	0.090±0.008	0.109±0.010
Fe XVIII	103.93	0.203±0.031	0.183±0.028	0.183±0.028	0.186±0.028	0.227±0.034
Fe XIX	13.520	0.296±0.015	0.261±0.013	0.261±0.013	0.266±0.014	0.326±0.017
Fe XIX	108.35	0.152±0.014	0.134±0.012	0.134±0.012	0.137±0.013	0.166±0.015
Fe XIX	101.54	0.172±0.035	0.152±0.031	0.152±0.031	0.154±0.031	0.188±0.038
Fe XX	121.84	0.105±0.014	0.093±0.012	0.093±0.012	0.094±0.013	0.118±0.016
Fe XX	12.829	0.084±0.059	0.075±0.053	0.075±0.053	0.076±0.054	0.096±0.068
Fe XXI	128.75	0.102±0.013	0.092±0.011	0.092±0.011	0.093±0.011	0.120±0.015
Fe XXI	12.284	0.259±0.020	0.234±0.018	0.234±0.018	0.238±0.019	0.307±0.024
Fe XXII	117.15	0.130±0.011	0.119±0.010	0.119±0.010	0.121±0.010	0.156±0.013
Fe XXII	135.79	0.156±0.019	0.143±0.018	0.143±0.018	0.145±0.018	0.187±0.023
Fe XXII	11.767	0.176±0.022	0.163±0.020	0.163±0.020	0.165±0.021	0.213±0.027
Fe XXIII	132.90	0.108±0.006	0.102±0.006	0.102±0.006	0.104±0.006	0.129±0.008
Fe XXIII	11.736	0.201±0.026	0.192±0.025	0.192±0.025	0.194±0.025	0.237±0.031
Fe XXIV	11.170	0.282±0.041	0.282±0.041	0.282±0.041	0.283±0.041	0.301±0.043
Fe XXV	1.8559	0.596±0.215	0.634±0.228	0.634±0.228	0.624±0.225	0.529±0.190

Table 6.30: Abundances derived for individual lines from the DEM calculated from iron lines for all mentioned AB Dor datasets combined.

6.2 Algol, the eclipsing binary

Algol or β Persei, the second brightest star in the constellation of Perseus is an eclipsing binary consisting of a B8 V main sequence star (Algol A) and a K0 IV subgiant (Algol B). (A third component of spectral type F with an orbital period of ≈ 1.8 yr is considered as unimportant in this context.) It has an apparent magnitude m_V of $2\overset{m}{.}12$ outside eclipse which decreases to about $3\overset{m}{.}5$ during the eclipse of the main sequence star whose overall luminosity is more than one order of magnitude higher.

The name Algol, deduced from Arabic *Rhas al-Ghûl* for "head of the demon", is based on the classical depiction of the constellation Perseus, where the Greek hero holds the head of the Medusa. The star Algol was said to be dangerous and ill-fated since ancient times. This indicates that observers noticed the unexplainable alternation in brightness a long time ago, although there is no documentary evidence for that. First specifications of Algol's variability arise in 1667, and in 1782 John Goodricke quantified the period of 2.8674 days. From the shape of the lightcurve he also reasoned correctly the partial eclipse of the star by a fainter companion, which was proved spectroscopically in 1889. See also Burnham, p. 1409 ff.

Algol is an evolved close-binary system: The secondary was initially the more massive star of the system and evolved first. As soon as it filled its Roche lobe a mass transfer towards the initially less massive primary started. By now the secondary has lost the biggest part of its initial mass, especially from its outer layers. This implies that now the original core is unveiled. The chemical composition of the core material had been modified by fusion processes, i.e. in case of the high-mass progenitor of Algol B by the CNO cycle that transforms hydrogen into helium in a catalytic reaction via carbon, nitrogen and oxygen. From all the partial reactions involved in the CNO cycle the longest-lasting is the one that converts ^{14}N to ^{15}O. The resulting bottleneck leads to an enhancement of nitrogen and a parallel deficiency of carbon that could be measured in terms of the abundances of what is now Algol B's photosphere and corona. While photospheric measurements performed in the optical will focus on the more luminous A component, coronal studies in X-rays will concentrate on Algol B since the A component is considered to be X-ray dark. Actually Schmitt and Ness (2002) found evidence for a nitrogen enhancement and a carbon depletion from Algol's LETGS spectrum. These results were confirmed by Drake (2003), who examined the coronal carbon and nitrogen abundances of Algol and a corresponding dataset of the RS CVn system HR 1099 to deduce Algol's anomalous carbon and nitrogen abundances from a comparison of the otherwise very similar spectra. Schmitt and Ness (2004) eventually derive a continuous differential emission measure based on Chebyshev polynomials from ratios of H-like to He-like lines from the LETGS dataset and thus measured a nitrogen enhancement by a factor of 2 and a carbon depletion by at least a factor of 25 relative to cosmic abundances after Allen (1973).

Algol is known as an X-ray source already since 1976. At first, the high level of X-ray emission was interpreted as being due to accretion of matter on the B-star. This model is in conflict with X-ray observations of the eclipses though, since one would expect to see a decrease in X-ray luminosity parallel to the optical primary minimum. Actually the situation is opposite: Primary eclipses are not observed but on occasion the secondary eclipses. This is a definite evidence for the origin of the X-ray emission being located on the K-type secondary. Nowadays it is assumed that Algol B harbors an very hot corona that causes the high X-ray luminosity. It is under debate to what extend this corona is influenced or even supported by the vicinity of the B-star, i.e. whether even larger magnetic structures such as interbinary loops, as they are suggested for RS CVn systems, exist. (See for instance Chung et al. (2004), who find the corona of Algol B to be distorted towards the A component.) At least the two stars are tidally locked, which results in a short rotation period and thus a triggered dynamo mechanism.

Eclipse observations (the inclination angle of the system is $\approx 81.4°$) allow the reconstruction

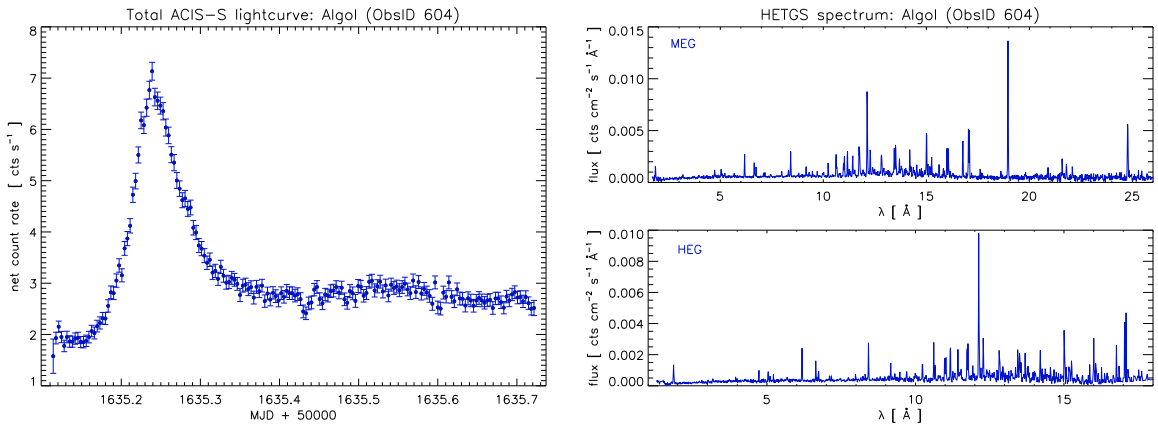

Figure 6.9: Lightcurve (left) and spectrum (right) of Algol obtained with the HETGS onboard *Chandra* with a total exposure time of 51.7 ks.

of size and shape of coronal structures on Algol B from geometrical considerations (see Schmitt and Favata (1999), Schmitt et al. (2003)). Algol and α CrB, where the occultation is even total in X-rays, are the only eclipsing binary systems with an X-ray-dark component where this works.

The Algol system is known to produce huge flares (see Schmitt and Favata (1999), Favata and Schmitt (1999) for the analysis of a giant flare observed with *BeppoSAX*, and Favata et al. (2000) for a summary on further flare observations). Temperatures as high as 100 MK can be reached during these flares, making the flaring plasma dominate an integrated X-ray spectrum. The occurrence of such a strong flare would thus require and perhaps permit (in terms of data quality) a separate analysis of the DEM of both the quiescent and the flaring state.

The assessment of the hydrogen column density towards Algol is somewhat puzzling: The results from various global fits to earlier low-resolution X-ray spectra reported in the literature require considerably high column densities up to $\log N_H > 21$. Such high values are definitely incompatible with the observed spectrum at higher wavelengths. If so, essentially no flux from wavelengths greater 50 Å should be measureable, contrary to the LETGS spectrum with ObsID 2. However, global fits with the hydrogen column density as a free parameter performed with the available LETGS, RGS and EPIC spectra resulted in column densities with similarly high values of $\log N_H = 19.52$, 20.56 and 19.59 respectively, revealing obvious contradictions in these global fits. Eventually I decided to fix the $\log N_H$ value for Algol at 18.5, which results in more or less coinciding iron abundances for lines from both the long and the short wavelength range.

6.2.1 The HETGS dataset ObsID 604

A *Chandra* HETGS observation of Algol was obtained on 1 April 2000. It covers the phase interval from 0.49 to 0.69 ad therefore part of the secondary minimum. The occurrence of a flare makes the interpretation of this part of the observation ambiguous (see Figure 6.9), the flaring region is obviously not totally occulted, but a partial eclipse is possible. This subject is discussed by Chung et al. (2004), who also measure Doppler shifts resulting from orbital motion and line broadening with these data. The spectrum, as well as the spectra of the other Algol datasets analyzed here, shows a well-pronounced source continuum over a broad wavelength range, indicating the high temperatures typical for Algol.

Only polynomials with a maximum order of 4 could be fitted to this dataset, they are shown in Figure 6.10. Even the simple parabolas from ratio and iron line fit indicate the high temperatures typical for Algol, their maxima are located at 10 MK and 14 MK respectively. (Ness et al. (2002a) found a bremsstrahlung model with a temperature of 15 MK as a best-fit to Algol's observed

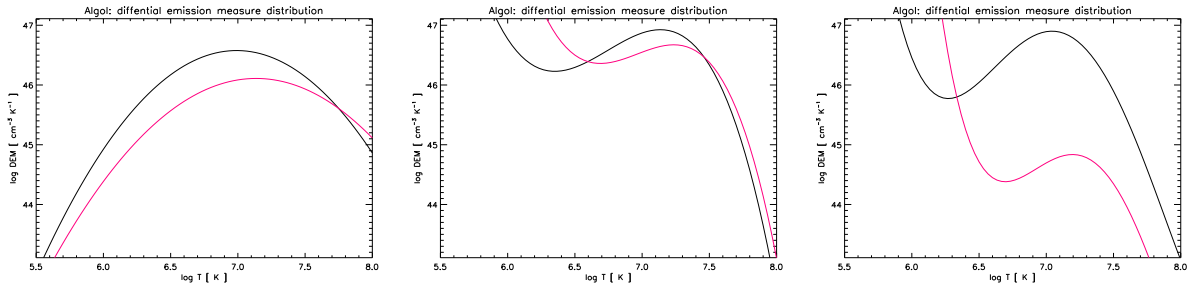

Figure 6.10: Differential emission measures for Algol with polynomials of order 2 to 4, calculated from the HETGS dataset 604.

continuum.) Additionally the DEM maxima from the ratio fits reach values up to one order of magnitude higher than those of AB Dor. The iron lines measured in Algol's HETGS spectrum however show a broad scatter in their normalization.

The 3rd and 4th order ratio fits keep the maximum at temperatures higher than 10 MK and form an additional minimum at temperatures of ≈ 1.8 MK followed by a rise towards even lower temperatures. This artifical rise is induced by the absence of the carbon and nitrogen ratios in the input data to the fit, I would thus confine the reliable temperature range of these fits to temperatures of 2.5 MK and upwards. The corresponding iron line fits are computed from the ionization stages XVII to XXIV and thus should be considered from temperatures greater 3 MK.

Table 6.31 however implies that these iron line fits are not able to reproduce the H-like to He-like ratios. Especially the 4th order fit produces unreasonable values due to a really bad normalization. Since this also applies to the absolute (Tables 6.36 and 6.37) and relative (Table 6.33) abundances deduced from this polynomial, I will not discuss it any further. The relative abundances calculated from the 3rd order fit are also unreasonably high, as a result of a much too low oxygen abundance. This in turn is due to the rise of the underlying DEM towards lower temperatures that here already stars at the formation temperatures of the oxygen ad nitrogen lines and thus assigns misleading values to these elements. The other absolute abundances have at least the same order of magnitude as the global fit with two temperature components to this dataset. The parabola gives relative abundances that at least partly match the global fit.

The $DEMs$ calculated from the H-like to He-like ratios reproduce their input data well, the 4th order fit gives even an unreasonably low value of reduced χ^2. The absolute abundances (Tables 6.34 and 6.35) already indicate a clear nitrogen overabundance. The normalization of the parabola matches the global fit somewhat better than do the 3rd and 4th order fits. Relative to oxygen the abundances from these three polynomials compare well with each other, see Table 6.32. With regard to the global fit, almost all elements show a systematic enhancement. For certain elements like calcium, argon sulfur or aluminium this may be explained by erroneous measurements (see Section 4.3.1). When transforming the abundances derived by Schmitt and Ness (2004) to the solar values by Asplund et al. (2005), they compare better to the abundances deduced from the DEM fit than to the global fit.

For this particular dataset I also investigated DEM fits an the coresponding abundances including the weak calcium and argon lines. The changes introduced to the shapes of the DEM polynomials and the reconstructed abundances were only minor, so I do not list the results from these fits here.

	measured	2nd order	3rd order	4th order
O VIII / O VII	7.305±1.379	8.633 (11.724)	7.483 (0.019)	7.306 (0.000)
Ne X / Ne IX	5.123±0.634	3.785 (5.156)	4.716 (2.994)	5.073 (0.000)
Mg XII / Mg XI	2.696±0.477	2.611 (3.625)	3.049 (3.390)	2.842 (***)
Si XIV / Si XIII	1.703±0.136	1.777 (2.491)	1.747 (2.185)	1.686 (***)
S XVI / S XV	1.220±0.235	1.210 (1.745)	0.971 (1.273)	1.238 (***)
2-3 Å	9.743±0.974	9.743 (9.743)	9.743 (9.743)	9.743 (9.682)
red. χ^2		1.90 (4.86)	1.10 (4.74)	0.12 (5.18)

Table 6.31: Fit results from H-like to He-like ratios from the Algol HETGS dataset 604: Photon flux ratios and continuum flux [10^{-4} cts s^{-1} cm^{-2}] in specified wavelength bands. The corresponding results from the iron line fit are given in brackets.

abundance	2nd order	3rd order	4th order	2T fit
N / O	7.893±0.658	7.563±0.630	8.030±0.669	8.453
Ne / O	2.640±0.407	2.897±0.214	2.865±0.211	1.998
Mg / O	1.121±0.060	0.964±0.052	0.959±0.052	0.774
Al / O	2.991±0.303	2.505±0.254	2.589±0.262	1.023
Si / O	1.072±0.058	0.897±0.049	0.927±0.050	0.668
S / O	0.956±0.092	0.857±0.099	0.885±0.085	0.686
Ar / O	5.498±1.203	5.626±0.868	4.474±2.084	2.429
Ca / O	5.234±0.729	5.329±1.482	3.542±2.371	2.286
Fe / O	0.890±0.071	0.900±0.055	0.864±0.067	0.843

Table 6.32: Abundances relative to oxygen derived from the DEM calculated from H-like to He-like ratios and a corresponding global fit with two temperature components for the Algol HETGS dataset 604.

abundance	2nd order	3rd order	4th order	2T fit
N / O	7.909±0.869	***	***	8.453
Ne / O	2.964±0.305	***	***	1.998
Mg / O	0.918±0.089	***	***	0.774
Al / O	2.244±0.278	***	***	1.023
Si / O	0.899±0.181	***	***	0.668
S / O	0.589±0.100	***	***	0.686
Ar / O	2.833±1.228	***	***	2.429
Ca / O	2.734±0.449	***	***	2.286
Fe / O	1.005±0.089	***	***	0.843

Table 6.33: Abundances relative to oxygen derived from the DEM calculated iron lines and a corresponding global fit with two temperature components for the Algol HETGS dataset 604.

element	2nd order	3rd order	4th order	2T fit
N	3.302±0.241	1.833±0.134	2.174±0.158	5.173
O	0.418±0.017	0.242±0.010	0.271±0.011	0.612
Ne	1.105±0.164	0.702±0.043	0.776±0.048	1.223
Mg	0.469±0.017	0.234±0.008	0.260±0.009	0.474
Al	1.252±0.116	0.607±0.056	0.701±0.065	0.626
Si	0.448±0.016	0.217±0.008	0.251±0.009	0.409
S	0.400±0.035	0.208±0.023	0.240±0.021	0.420
Ar	2.300±0.495	1.363±0.203	1.211±0.562	1.487
Ca	2.190±0.292	1.292±0.355	0.959±0.641	1.399
Fe	0.372±0.025	0.218±0.010	0.234±0.016	0.516

Table 6.34: Absolute abundances derived from the DEM calculated from H-like to He-like ratios and a corresponding global fit with two temperature components for the Algol HETGS dataset 604.

element	wavelength	2nd order	3rd order	4th order
N VII	24.782	3.302±0.241	1.833±0.134	2.174±0.158
O VII	21.602	0.491±0.090	0.248±0.046	0.271±0.050
O VIII	18.970	0.416±0.017	0.242±0.010	0.271±0.011
Ne IX	13.447	0.989±0.084	0.677±0.058	0.772±0.066
Ne X	12.134	1.339±0.120	0.735±0.066	0.780±0.070
Mg XI	9.1688	0.455±0.079	0.263±0.046	0.273±0.047
Mg XII	8.4210	0.470±0.017	0.233±0.008	0.259±0.009
Al XIII	7.1730	1.252±0.116	0.607±0.056	0.701±0.065
Si XIII	6.6480	0.454±0.019	0.219±0.009	0.250±0.011
Si XIV	6.1830	0.435±0.029	0.213±0.014	0.253±0.017
S XV	5.0387	0.398±0.064	0.180±0.029	0.242±0.039
S XVI	4.7300	0.401±0.041	0.226±0.023	0.239±0.025
Ar XVII	3.9488	2.823±0.510	1.356±0.245	2.160±0.390
Ar XVIII	3.7330	1.833±0.482	1.381±0.363	0.878±0.231
Ca XIX	3.0212	2.137±0.325	1.206±0.183	2.196±0.334
Ca XX	3.1773	2.411±0.665	2.774±0.765	0.627±0.173
Fe XVII	15.015	0.291±0.012	0.203±0.009	0.205±0.009
Fe XVII	17.075	0.381±0.015	0.268±0.010	0.274±0.011
Fe XVII	15.262	0.376±0.030	0.262±0.021	0.265±0.021
Fe XVII	16.777	0.342±0.023	0.241±0.016	0.246±0.017
Fe XVIII	14.205	0.329±0.024	0.204±0.015	0.195±0.014
Fe XIX	13.521	0.730±0.038	0.403±0.021	0.389±0.020
Fe XX	12.830	0.446±0.040	0.224±0.020	0.225±0.020
Fe XXI	12.285	0.395±0.017	0.182±0.008	0.196±0.008
Fe XXII	11.767	0.511±0.035	0.221±0.015	0.265±0.018
Fe XXIII	11.736	0.527±0.022	0.227±0.010	0.315±0.013
Fe XXIV	11.171	0.591±0.055	0.292±0.027	0.487±0.045
Fe XXV*	1.8560	1.172±0.113	1.419±0.137	1.740±0.168

Table 6.35: Abundances derived for individual lines from the DEM calculated from H-like to He-like ratios for the Algol HETGS dataset 604.

element	2nd order	3rd order	4th order	2T fit
N	9.356±0.682	0.628±0.046	0.000	5.173
O	1.183±0.097	0.001±0.003	0.000	0.612
Ne	3.507±0.217	0.813±0.210	0.000	1.223
Mg	1.086±0.057	0.374±0.016	0.140±0.029	0.474
Al	2.655±0.247	0.922±0.086	0.296±0.028	0.626
Si	1.064±0.196	0.356±0.042	0.081±0.126	0.409
S	0.697±0.104	0.275±0.024	0.037±0.023	0.420
Ar	3.351±1.427	1.636±0.246	0.081±0.117	1.487
Ca	3.235±0.460	1.512±0.280	0.045±0.079	1.399
Fe	1.189±0.040	0.367±0.011	26.425±0.776	0.516

Table 6.36: Absolute abundances derived from the DEM calculated from iron lines and a corresponding global fit with two temperature components for the Algol HETGS dataset 604.

element	wavelength	2nd order	3rd order	4th order
N VII	24.782	9.356±0.682	0.628±0.046	0.000
O VII	21.602	1.877±0.346	0.001±0.000	0.000
O VIII	18.970	1.169±0.048	0.282±0.012	0.000
Ne IX	13.447	3.517±0.299	0.696±0.059	0.000
Ne X	12.134	3.495±0.314	1.191±0.107	0.511±0.046
Mg XI	9.1688	1.448±0.251	0.467±0.081	7.591±1.314
Mg XII	8.4210	1.077±0.039	0.372±0.014	0.140±0.005
Al XIII	7.1730	2.655±0.247	0.922±0.086	0.296±0.028
Si XIII	6.6480	1.245±0.053	0.390±0.017	20.961±0.893
Si XIV	6.1830	0.851±0.057	0.304±0.020	0.080±0.005
S XV	5.0387	0.930±0.151	0.283±0.046	11.073±1.794
S XVI	4.7300	0.651±0.067	0.272±0.028	0.037±0.004
Ar XVII	3.9488	5.594±1.010	1.841±0.332	37.764±6.817
Ar XVIII	3.7330	2.443±0.642	1.390±0.365	0.080±0.021
Ca XIX	3.0212	3.581±0.545	1.419±0.216	10.398±1.581
Ca XX	3.1773	2.624±0.724	2.356±0.650	0.044±0.012
Fe XVII	15.015	1.039±0.044	0.321±0.014	23.732±1.001
Fe XVII	17.075	1.369±0.053	0.409±0.016	28.471±1.098
Fe XVII	15.262	1.343±0.108	0.413±0.033	30.262±2.431
Fe XVII	16.777	1.229±0.084	0.367±0.025	25.686±1.756
Fe XVIII	14.205	1.112±0.080	0.391±0.028	31.353±2.252
Fe XIX	13.521	2.341±0.122	0.812±0.042	60.971±3.170
Fe XX	12.830	1.357±0.123	0.449±0.041	32.120±2.905
Fe XXI	12.285	1.129±0.048	0.351±0.015	24.553±1.051
Fe XXII	11.767	1.347±0.091	0.398±0.027	27.983±1.894
Fe XXIII	11.736	1.217±0.051	0.358±0.015	26.641±1.121
Fe XXIV	11.171	1.104±0.102	0.385±0.036	26.543±2.464
Fe XXV*	1.8560	1.251±0.120	1.210±0.117	0.234±0.023

Table 6.37: Abundances derived for individual lines from the DEM calculated from iron lines for the Algol HETGS dataset 604.

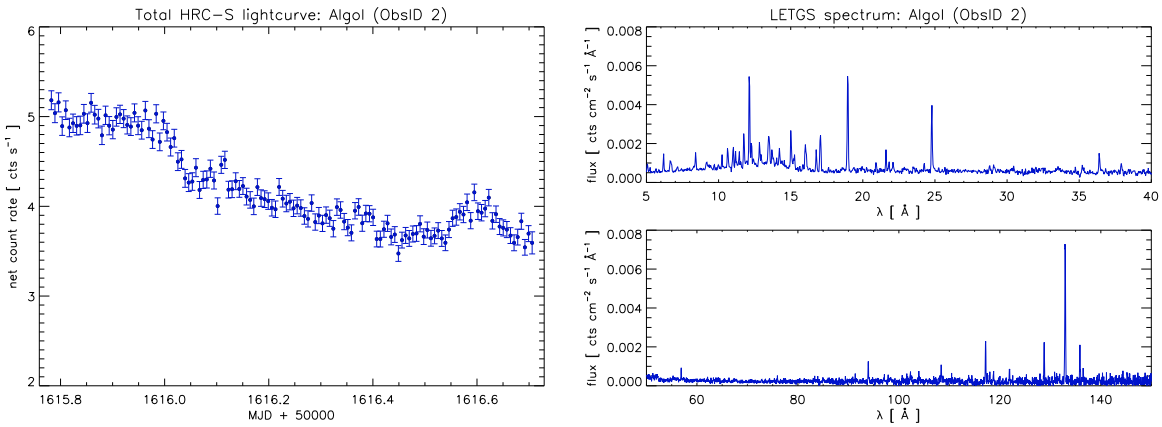

Figure 6.11: Lightcurve (left) and spectrum (right) of Algol from 12/13 March 2000 obtained with the LETGS on board *Chandra*. The lightcurve is binned with 600 s, the total exposure time is 79.5 ks.

6.2.2 The LETGS dataset ObsID 2

Figure 6.11 shows that Algol was relatively quiescent with a slow decay during the *Chandra* LETGS observation 2, which covers the primary but not the secondary eclipse. This dataset was discussed in detail by Ness et al. (2002a), focussing on density and temperature diagnostics. It also serves as input to the studies of Schmitt and Ness (2002) and Drake (2003). The strongest line in Algol's LETGS spectrum is the iron line located at 132.9 Å. In case of Algol it is clearly dominated by Fe XXIII what again illustrates the existence of a high-temperature corona. Among the stronger lines in the short-wavelength part of the spectrum the N VII line is very conspicuous.

The DEM reconstruction method applied to this dataset by Schmitt and Ness (2004) is probably the most similar to mine available in the literature, and a comparison of the results is essential, as well concerning the shape of the emission measure distribution as the deduced abundances.

The polynomials representing the $DEMs$ from the ratio fits to this dataset resemble their complements from the HETGS fit: They have the same shape and their maxima and minima are located at the same temperatures although Algol was apparently in different states of activity during these two observations. Apart from the 4th order fit, similar considerations apply to the iron line fits, though the rise towards lower temperatures of the 3rd order fit leads not to that strongly deviating values for the reconstructed abundances of oxygen and nitrogen. The polynomial obtained from the 4th order iron line fit however differs considerably. The reconstructed DEM is very narrow, covering temperatures from $\log T = 6.5 - 7.2$ and develops a two-peaked structure with the first, slightly weaker maximum located at 5 MK and the second peak located at 25 MK.

The differential emission measures from the iron line fits can however again not reproduce the H-like to He-like ratios (Table 6.38) while the scatter of the iron abundances deduced for the individual iron lines from the ratio fits (Table 6.41) keeps within reasonable limits, apart from the short-wavelength Fe XIX line, that was therefore excluded from the iron line fit. From the three ratio fits the third order polynomial gives the best fit result. Both 3rd and 4th order polynomials can reproduce the measured ratios apart from magnesium within the errors.

A comparison shows that these two reconstructed $DEMs$ resemble the fourth order Chebyshev polynomials derived by Schmitt and Ness (2004) in the temperature confidence range from $\log T = 6.2$ upwards quite closely in shape and the location of the maximum at ≈ 13 MK (cf. their Figure 6). However it seems that I measured systematically lower ratios.

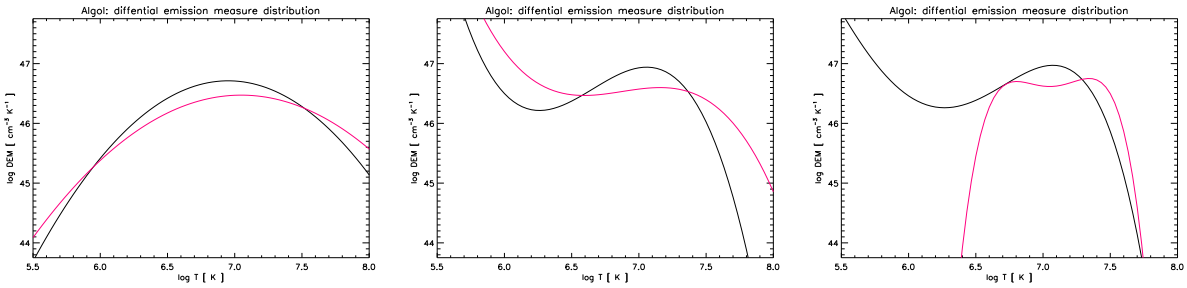

Figure 6.12: Differential emission measures for Algol with polynomials of order 2 to 4, calculated from the LETGS dataset 2.

	measured	2nd order	3rd order	4th order
N VII / N VI	7.463±1.275	10.628 (10.868)	7.087 (2.142)	7.281 (41.795)
O VIII / O VII	7.187±0.640	7.111 (7.756)	7.523 (3.272)	7.361 (20.373)
Ne X / Ne IX	4.117±0.194	3.461 (4.163)	3.985 (3.445)	4.029 (4.622)
Mg XII / Mg XI	2.028±0.314	2.517 (3.235)	2.477 (3.077)	2.488 (2.910)
Si XIV / Si XIII	1.448±0.155	1.782 (2.397)	1.405 (2.206)	1.363 (2.077)
19.5-20.5 Å	19.422±3.88	19.421 (19.421)	19.421 (19.421)	19.421 (19.421)
red. χ^2		8.22 (4.65)	1.48 (4.81)	2.74 (5.00)

Table 6.38: Fit results from H-like to He-like ratios from the Algol LETGS dataset 2: Photon flux ratios and continuum flux between 19.5 and 20.5 Å in 10^{-4} cts s^{-1} cm^{-2}. The corresponding results from the iron line fit are given in brackets.

A conversion of the averaged absolute abundances listed in Table 4 of Schmitt and Ness (2004) to the solar photospheric reference of Asplund et al. (2005) gives values of 3.02, 0.36, 1.14, 0.39, 04.6, and 0.28 for N, O, Ne, Mg, Si, and Fe respectively. Thus I obtained in general slightly lower absolute abundances (see Table 6.40), caused by a different normalization. The abundances I derived for the individual lines (Table 6.41) show much less scattering than those listed in Table 2 of Schmitt and Ness (2004).

The 3rd and 4th order polynomials from the HETGS and LETGS ratio fits give very similar absolute abundances with a clear nitrogen enhancement. Assuming the absolute normalization level to be correct the other elements are sub-solar except for neon. Again, the abundances derived from the reconstructed $DEMs$ do not match those from the global fit well, neither those deduced from the ratios nor those from the iron lines as can be seen from Tables 6.40 and 6.43. Additionally the global fit of the LETGS data shows distinct discrepancies compared to the global fit of the HETGS data, even for the relative abundance values.

The abundances relative to oxygen listed in Tables 6.39 and 6.42 though compare quite well with those of Schmitt and Ness (2004) for all three available polynomials from the ratio fits and for the parabola and the 4th order fit from the iron line fit. Nitrogen that is somewhat lower in all my measurements is the only exception.

element	2nd order	3rd order	4th order	2T fit
N / O	7.176±0.453	7.042±0.277	7.019±0.276	8.998
Ne / O	3.268±0.264	3.166±0.090	3.173±0.090	2.570
Mg / O	1.043±0.076	0.932±0.064	0.924±0.064	0.660
Si / O	1.116±0.096	1.075±0.053	1.074±0.053	0.653
Fe / O	0.659±0.031	0.579±0.029	0.572±0.030	0.648

Table 6.39: Abundances relative to oxygen derived from the DEM calculated from H-like to He-like ratios and a corresponding global fit with two temperature components for the Algol LETGS dataset 2.

element	2nd order	3rd order	4th order	2T fit
N	2.260±0.136	1.811±0.062	1.760±0.060	3.599
O	0.315±0.006	0.257±0.005	0.251±0.005	0.400
Ne	1.029±0.080	0.814±0.017	0.796±0.016	1.028
Mg	0.328±0.023	0.240±0.016	0.232±0.015	0.264
Si	0.351±0.030	0.276±0.013	0.269±0.012	0.261
Fe	0.207±0.009	0.149±0.007	0.143±0.007	0.259

Table 6.40: Absolute abundances derived from the DEM calculated from H-like to He-like ratios and a corresponding global fit with two temperature components for the Algol LETGS dataset 2.

element	wavelength	2nd order	3rd order	4th order
N VI	28.787	3.190±0.534	1.724±0.288	1.719±0.288
N VII	24.782	2.240±0.078	1.815±0.063	1.762±0.061
O VII	21.602	0.312±0.027	0.269±0.023	0.257±0.022
O VIII	18.970	0.315±0.006	0.257±0.005	0.250±0.005
Ne IX	13.447	0.911±0.037	0.795±0.033	0.783±0.032
Ne X	12.134	1.084±0.026	0.821±0.019	0.800±0.019
Mg XI	9.1688	0.398±0.057	0.286±0.041	0.278±0.040
Mg XII	8.4210	0.321±0.019	0.234±0.014	0.227±0.013
Si XIII	6.6480	0.416±0.039	0.270±0.025	0.258±0.024
Si XIV	6.1830	0.338±0.018	0.278±0.015	0.274±0.014
Fe XVII	15.015	0.159±0.007	0.131±0.006	0.130±0.006
Fe XVII	17.075	0.202±0.007	0.169±0.006	0.168±0.006
Fe XVII	15.262	0.237±0.021	0.196±0.018	0.194±0.018
Fe XVII	16.777	0.231±0.011	0.194±0.010	0.193±0.009
Fe XVIII	14.205	0.194±0.017	0.141±0.012	0.138±0.012
Fe XVIII	93.923	0.205±0.015	0.156±0.011	0.154±0.011
Fe XIX*	13.521	0.516±0.025	0.338±0.016	0.326±0.016
Fe XIX	108.35	0.241±0.020	0.163±0.014	0.158±0.013
Fe XX	121.84	0.187±0.019	0.117±0.012	0.112±0.011
Fe XX	118.68	0.198±0.027	0.124±0.017	0.119±0.016
Fe XXI	128.75	0.190±0.014	0.114±0.009	0.107±0.008
Fe XXI	117.50	0.188±0.037	0.112±0.022	0.106±0.021
Fe XXII	117.15	0.210±0.011	0.125±0.006	0.117±0.006
Fe XXII	135.79	0.214±0.018	0.127±0.011	0.119±0.010
Fe XXIII	132.90	0.257±0.008	0.164±0.005	0.155±0.005
Fe XXIV	11.171	0.274±0.025	0.248±0.022	0.249±0.023

Table 6.41: Abundances derived for individual lines from the DEM calculated from H-like to He-like ratios for the Algol LETGS dataset 2.

abundance	2nd order	3rd order	4th order	2T fit
N / O	7.097±0.470	4.890±2.509	7.728±1.740	8.998
Ne / O	3.298±0.094	3.992±1.048	2.976±0.465	2.570
Mg / O	0.915±0.128	1.186±0.332	0.828±0.154	0.660
Si / O	0.865±0.163	1.143±0.339	0.812±0.166	0.653
Fe / O	0.716±0.026	0.865±0.218	0.589±0.089	0.648

Table 6.42: Abundances relative to oxygen derived from the DEM calculated from iron lines and a corresponding global fit with two temperature components for the Algol LETGS dataset 2.

element	2nd order	3rd order	4th order	2T fit
N	3.479±0.220	1.483±0.665	2.825±0.478	3.599
O	0.490±0.010	0.303±0.076	0.366±0.054	0.400
Ne	1.616±0.033	1.211±0.097	1.088±0.053	1.028
Mg	0.448±0.062	0.360±0.045	0.303±0.034	0.264
Si	0.424±0.079	0.347±0.056	0.297±0.041	0.261
Fe	0.351±0.011	0.262±0.008	0.215±0.006	0.259

Table 6.43: Absolute abundances derived from the DEM calculated from iron lines and a corresponding global fit with two temperature components for the Algol LETGS dataset 2.

element	wavelength	2nd order	3rd order	4th order
N VI	28.787	5.020±0.840	0.564±0.094	15.720±2.631
N VII	24.782	3.448±0.120	1.964±0.068	2.807±0.097
O VII	21.602	0.527±0.046	0.156±0.014	1.023±0.089
O VIII	18.970	0.488±0.010	0.342±0.007	0.361±0.007
Ne IX	13.447	1.630±0.067	1.070±0.044	1.191±0.049
Ne X	12.134	1.612±0.038	1.278±0.030	1.061±0.025
Mg XI	9.1688	0.690±0.099	0.527±0.075	0.421±0.060
Mg XII	8.4210	0.432±0.025	0.347±0.020	0.293±0.017
Si XIII	6.6480	0.657±0.061	0.497±0.046	0.403±0.038
Si XIV	6.1830	0.397±0.021	0.326±0.017	0.281±0.015
Fe XVII	15.015	0.291±0.013	0.217±0.010	0.177±0.008
Fe XVII	17.075	0.370±0.013	0.273±0.009	0.229±0.008
Fe XVII	15.262	0.433±0.039	0.322±0.029	0.264±0.024
Fe XVII	16.777	0.423±0.021	0.312±0.015	0.261±0.013
Fe XVIII	14.205	0.351±0.030	0.277±0.024	0.209±0.018
Fe XVIII	93.923	0.373±0.027	0.291±0.021	0.221±0.016
Fe XIX*	13.521	0.908±0.043	0.718±0.034	0.574±0.027
Fe XIX	108.35	0.427±0.035	0.339±0.028	0.264±0.022
Fe XX	121.84	0.323±0.032	0.253±0.025	0.211±0.021
Fe XX	118.68	0.342±0.047	0.268±0.037	0.223±0.031
Fe XXI	128.75	0.317±0.024	0.243±0.018	0.210±0.016
Fe XXI	117.50	0.313±0.061	0.239±0.047	0.207±0.041
Fe XXII	117.15	0.333±0.017	0.248±0.013	0.210±0.011
Fe XXII	135.79	0.339±0.029	0.252±0.022	0.214±0.018
Fe XXIII	132.90	0.372±0.011	0.271±0.008	0.218±0.007
Fe XXIV	11.171	0.314±0.028	0.248±0.022	0.210±0.019

Table 6.44: Abundances derived for individual lines from the DEM calculated from iron lines for the Algol LETGS dataset 2.

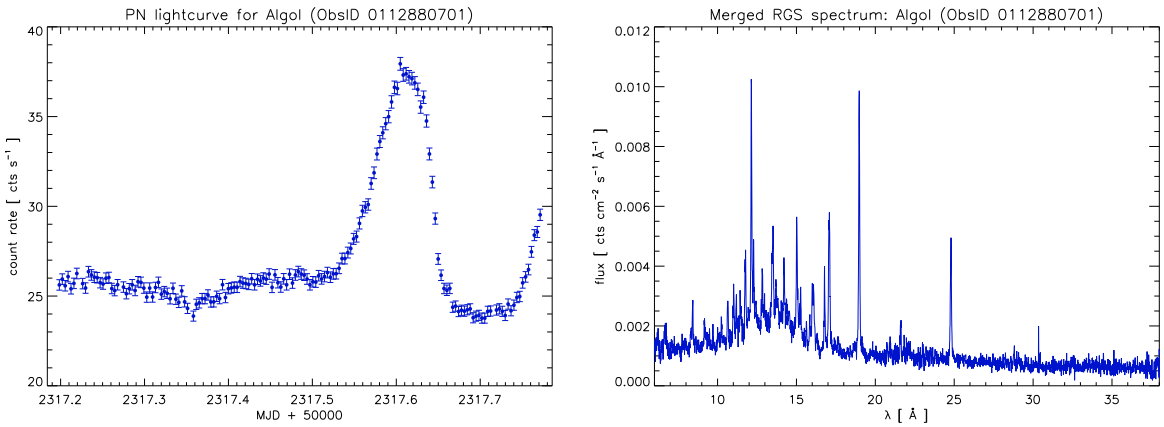

Figure 6.13: Lightcurve (left) and spectrum (right) of Algol obtained with EPIC PN and RGS onboard *XMM* respectively. Though total exposure time of the PN is reduced compared to MOS and RGS (45 ks vs. 51.4 ks), the data from PN detector was taken to create the lightcurve because of its higher sensitivity.

6.2.3 The RGS dataset ObsID 0112880701

Algol was also observed with *XMM-Newton* on 12 February 2002. The observation is centered on phase 0.46 and also covers the secondary minimum. Figure 6.13 exhibits another strong flare, occurring just before the time of the eclipse, Algol was thus in a state of activity similar to that covered by the HETGS dataset. The flaring region on the K-star was apparently occulted and allowed Schmitt et al. (2003) to reconstruct a spatially resolved "image" with eclipse mapping techniques.

It was difficult to measure the silicon lines in Algol's RGS spectrum, thus one ratio less than from the LETGS data is available for the ratio fit. Additionally some of the ratio measurements deviate considerably from the previous datasets, see Table 6.45. The nitrogen ratio is higher and the neon and magnesium ratios are found to be much lower than in the HETGS and LETGS datasets. It is thus no wonder that the polynomials representing the DEM differ from those of the other datasets.

The $DEMs$ reconstructed from the H-like to He-like ratios do not really suit the properties known for Algol's corona from the previous datasets. The high level of $\log DEM \approx 47$ at maximum is maintained but the maximum shifted to lower temperatures of ≈ 6.5 MK in case of the parabola. The 3rd and 4th order polynomials look very similar and they do barely differ from the parabola. The thus reconstructed $DEMs$ are relatively broad and peak at low temperatures with respect to what is typical for Algol. The 5th order ratio fit got a different shape: Additional to the dominating low temperature maximum a second peak at ≈ 40 MK develops. An auxiliary minimum at 0.7 MK followed by a rise towards very low temperatures is definitely outside the temperature range covered by the input ratios. From $\log T = 6.2$ upwards these $DEMs$ may be trustworthy but I am hesitating to rely on them at all. The values of reduced χ^2 for he ratio fits (see Table 6.45) are generally quite good so any fatal errors must arise from the measured ratios.

The iron line fits are not well-determined since only lines from Fe XVII and Fe XVIII are available, see Table 6.46. The deduced parabola gives the best-fit result and actually matches the parabolas from the previous datasets better than does the ratio fit, with the maximum located at 12 MK. The following three polynomials are virtually identical, the fit is converged due to the poor temperature coverage of the available iron lines. From the reproduced ratios in Table 6.45 and the broad scatter in the deduced individual abundances (see Table 6.59) it is clear that

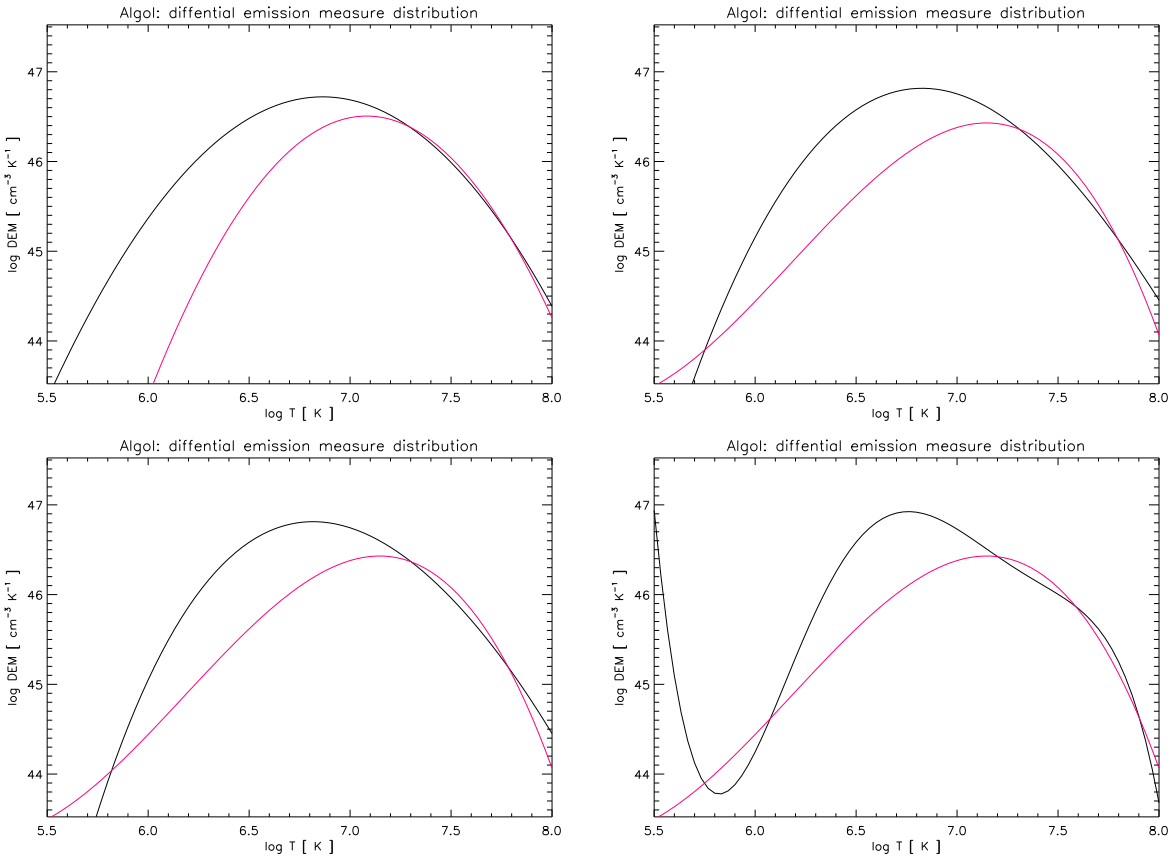

Figure 6.14: Differential emission measures for Algol with polynomials of order 2 to 5, calculated from the RGS dataset 011288070.

these fits do not provide good results.

A global fit with three temperature components was required to fit the Algol RGS dataset well. The abundances deduced from these fits however resemble those from the LETGS global fit apart from a somewhat lower nitrogen abundance. The absolute abundances reconstructed from the ratio fits (Table 6.53) are systematically lower, and those from the iron line fits (Table 6.57) – although probably not reliable – are systematically higher.

Aside from magnesium the relative abundances resulting from the ratio fits match those deduced from the previous datasets. The same applies astonishingly for the relative abundances from the poor iron line fit, the deviating value is here the iron abundance itself. Thus the overall level of abundances is similar for all datasets: For N / O, Ne / O, Mg / O, Si / O and Fe / O typical values are 7.1, 3.2, 0.9, 0.9 and 0.7 respectively.

The very similar $DEMs$ from the HETGS and LETGS datasets recommend a combination of the data to enlarge the covered temperature range and increase the signal-to-noise. The question is whether it makes sense to add also the RGS dataset. Both the RGS and the HETGS lightcurves show a flare while the LETGS dataset covers a phase of quiescence. Flares are typical for Algol, even much stronger flares than those observed in these datasets. And also with respect to abundances, all three datasets give similar results. Thus a combination of all three datasets should at least not lead to contradictory abundances.

	measured	2nd order	3rd order	4th order	5th order
N VII / N VI	8.807±1.457	9.401 (32.114)	10.026 (24.291)	10.123 (24.291)	8.805 (24.291)
O VIII / O VII	7.079±0.783	6.097 (17.305)	6.110 (15.027)	6.076 (15.027)	7.201 (15.027)
Ne X / Ne IX	2.664±0.385	2.851 (5.285)	2.668 (5.571)	2.637 (5.571)	2.425 (5.571)
Mg XII / Mg XI	1.292±0.347	1.988 (3.048)	1.812 (3.406)	1.802 (3.406)	1.537 (3.406)
3-4 Å	8.397±0.188	8.490 (8.422)	8.498 (8.399)	8.491 (8.399)	8.442 (8.399)
2-3 Å	6.059±0.157	5.950 (6.022)	5.917 (6.057)	5.927 (6.057)	5.990 (6.057)
1-2 Å	2.812±0.158	2.846 (2.838)	2.894 (2.814)	2.890 (2.814)	2.862 (2.814)
red. χ^2		1.69 (3.69)	1.94 (4.89)	2.90 (7.34)	1.25 (14.69)

Table 6.45: Fit results from H-like to He-like ratios from the Algol RGS dataset 0112880701: Photon flux ratios and continuum flux [10^{-4} cts s^{-1} cm^{-2}] in specified wavelength bands. The corresponding results from the iron line fit are given in brackets.

element	wavelength	2nd order	3rd order	4th order	5th order
N VI	28.787	1.521±0.246	1.373±0.222	1.392±0.225	1.162±0.187
N VII	24.782	1.425±0.052	1.206±0.044	1.211±0.044	1.162±0.042
O VII	21.602	0.183±0.019	0.154±0.016	0.153±0.016	0.166±0.017
O VIII	18.970	0.212±0.008	0.178±0.007	0.178±0.007	0.163±0.006
Ne IX	13.447	0.917±0.117	0.735±0.094	0.734±0.094	0.622±0.080
Ne X	12.134	0.857±0.058	0.734±0.049	0.741±0.050	0.683±0.046
Mg XI	9.1688	0.467±0.111	0.386±0.092	0.390±0.093	0.345±0.082
Mg XII	8.4210	0.303±0.038	0.275±0.034	0.279±0.035	0.290±0.036
Fe XVII	15.015	0.170±0.017	0.135±0.014	0.136±0.014	0.111±0.011
Fe XVII	17.075	0.169±0.005	0.135±0.004	0.135±0.004	0.110±0.003
Fe XVII	15.262	0.176±0.015	0.140±0.012	0.140±0.012	0.115±0.010
Fe XVII	16.777	0.096±0.019	0.077±0.015	0.077±0.015	0.063±0.012
Fe XVIII	14.205	0.209±0.033	0.171±0.027	0.172±0.027	0.148±0.023

Table 6.46: Abundances derived for individual lines from the DEM calculated from H-like to He-like ratios and a corresponding global fit with three temperature components for the Algol RGS dataset 0112880701.

element	wavelength	2nd order	3rd order	4th order	5th order
N VI	28.787	11.986±1.935	10.351±1.671	10.351±1.671	10.351±1.671
N VII	24.782	3.287±0.120	3.753±0.137	3.753±0.137	3.753±0.137
O VII	21.602	1.105±0.115	1.115±0.116	1.115±0.116	1.115±0.116
O VIII	18.970	0.452±0.017	0.525±0.019	0.525±0.019	0.525±0.019
Ne IX	13.447	2.845±0.364	3.513±0.450	3.513±0.450	3.513±0.450
Ne X	12.134	1.434±0.096	1.680±0.113	1.680±0.113	1.680±0.113
Mg XI	9.1688	0.934±0.222	1.173±0.279	1.173±0.279	1.173±0.279
Mg XII	8.4210	0.396±0.049	0.445±0.055	0.445±0.055	0.445±0.055
Fe XVII	15.015	0.461±0.047	0.601±0.062	0.601±0.062	0.601±0.062
Fe XVII	17.075	0.474±0.014	0.616±0.018	0.616±0.018	0.616±0.018
Fe XVII	15.262	0.480±0.041	0.625±0.054	0.625±0.054	0.625±0.054
Fe XVII	16.777	0.270±0.052	0.350±0.068	0.350±0.068	0.350±0.068
Fe XVIII	14.205	0.448±0.070	0.588±0.092	0.588±0.092	0.588±0.092

Table 6.47: Abundances derived for individual lines from the DEM calculated from iron lines for the Algol RGS dataset 0112880701.

abundance	2nd order	3rd order	4th order	5th order	3T fit
N / O	6.872±0.418	6.952±0.419	6.963±0.431	7.094±0.351	7.129
Ne / O	4.178±0.323	4.210±0.324	4.231±0.331	4.076±0.281	1.995
Mg / O	1.541±0.252	1.656±0.223	1.677±0.225	1.824±0.212	0.824
Fe / O	0.801±0.058	0.761±0.055	0.761±0.056	0.664±0.043	0.782

Table 6.48: Abundances relative to oxygen derived from the DEM calculated from H-like to He-like ratios and a corresponding global fit with three temperature components for the Algol RGS dataset 0112880701.

element	2nd order	3rd order	4th order	5th order	3T fit
N	1.429±0.051	1.213±0.043	1.217±0.043	1.162±0.041	2.880
O	0.208±0.010	0.174±0.008	0.175±0.009	0.164±0.006	0.404
Ne	0.869±0.052	0.735±0.044	0.740±0.044	0.667±0.040	0.806
Mg	0.320±0.050	0.289±0.036	0.293±0.036	0.299±0.033	0.333
Fe	0.167±0.009	0.133±0.007	0.133±0.007	0.109±0.006	0.316

Table 6.49: Absolute abundances derived from the DEM calculated from H-like to He-like ratios and a corresponding global fit with three temperature components for the Algol RGS dataset 0112880701.

abundance	2nd order	3rd order	4th order	5th order	3T fit
N / O	7.139±1.820	7.021±1.580	7.021±1.580	7.021±1.580	7.129
Ne / O	3.282±0.991	3.307±0.989	3.307±0.989	3.307±0.989	1.995
Mg / O	0.905±0.303	0.874±0.300	0.874±0.300	0.874±0.300	0.824
Fe / O	0.994±0.202	1.111±0.202	1.111±0.202	1.111±0.202	0.782

Table 6.50: Abundances relative to oxygen derived from the DEM calculated from iron lines and a corresponding global fit with two temperature components for the Algol RGS dataset 0112880701.

element	2nd order	3rd order	4th order	5th order	3T fit
N	3.320±0.536	3.797±0.536	3.797±0.536	3.797±0.536	2.880
O	0.465±0.092	0.541±0.095	0.541±0.095	0.541±0.095	0.404
Ne	1.527±0.349	1.789±0.433	1.789±0.433	1.789±0.433	0.806
Mg	0.421±0.114	0.473±0.139	0.473±0.139	0.473±0.139	0.333
Fe	0.462±0.023	0.601±0.030	0.601±0.030	0.601±0.030	0.316

Table 6.51: Absolute abundances derived from the DEM calculated from iron lines and a corresponding global fit with three temperature components for the Algol RGS dataset 0112880701.

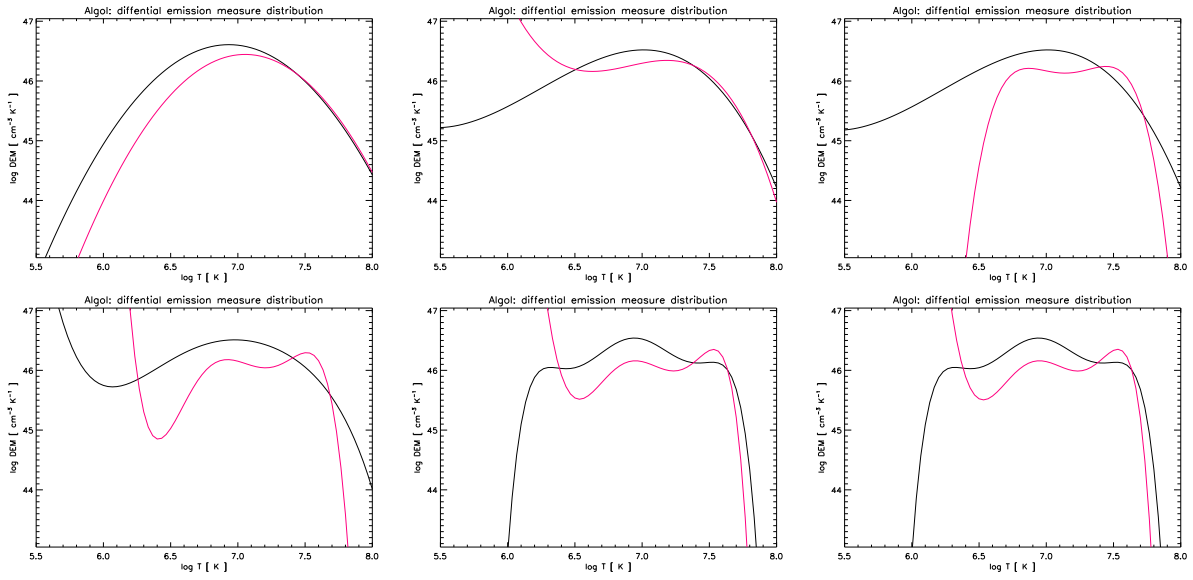

Figure 6.15: Differential emission measures for Algol with polynomials of order 2 to 7, calculated from all available datasets combined.

6.2.4 Combined datasets

Polynomials up to the 7th order can be calculated from the combined datasets. The resulting lower-order $DEMs$ look a little bit like a mixture between the HETGS and LETGs datasets on the one hand and the RGS dataset on the other hand. The parabola from the ratio fit has its maximum at $\log T = 6.9$, the corresponding iron line fit provides a somewhat narrower DEM with the maximum shifted to $\log T = 7.1$. The high-temperature slopes of the two parabolas are identical. Third and fourth order ratio fit are almost identical. They show a maximum at 10 MK, towards higher temperatures they resemble the parabolas. Towards lower temperatures they flatten and thus they are broader than the polynomials. The third order iron line fit is very similar to its HETGS and LETGS counterparts, with a maximum at 15 MK and a minimum at 4 MK. The fourth order iron line fit shows the same two-peaked structure as the fourth order iron line fit from the LETGS dataset, though the two peaks are somewhat shifted towards higher temperatures and now located at $\log T = 6.8$ and 7.5. It keeps these two maxima also in fifth order, the second peak is now a little more pronounced and a minimum at $\log T = 6.4$ occurs. The following rise towards lower temperatures is again not covered by the available iron lines. The fifth order ratio fit also keeps its one-peaked structure with the maximum at 10 MK, the additional new minimum at 1 MK is due to the absence of the carbon ratio only barely covered by the nitrogen ratio.

In sixth order even the ratio fit gives a DEM with multiple peaks. The first one is located at $\log T = 6.2$, the other two at $\log T = 6.9$ and 7.5, exactly where also the maxima of the iron line fit are found. Instead of the first peak there is a minimum at $\log T = 6.5$ (vaguely where the minimum between first and second peak of the ratio fit are located) followed by a steep rise towards lower temperatures. Both ratio and iron line fit DEM change only marginally from 6th to 7th order.

All ratio fits give a good fit in terms of reduced χ^2, most of the values are even much smaller than one and thus "too good", cf. Table 6.52. The best fit is given by the 3rd order polynomial, but the second-best value comes from the 6th order fit. I consider the structures evolving at the higher order fits very credible, at least the two higher-temperature peaks, since they are also reproduced by the iron line fit. Additionally Schmitt and Ness (2004) compute a 7th order Chebyshev polynomial with two peaks at 10 MK and 45 MK from the LETGS dataset that

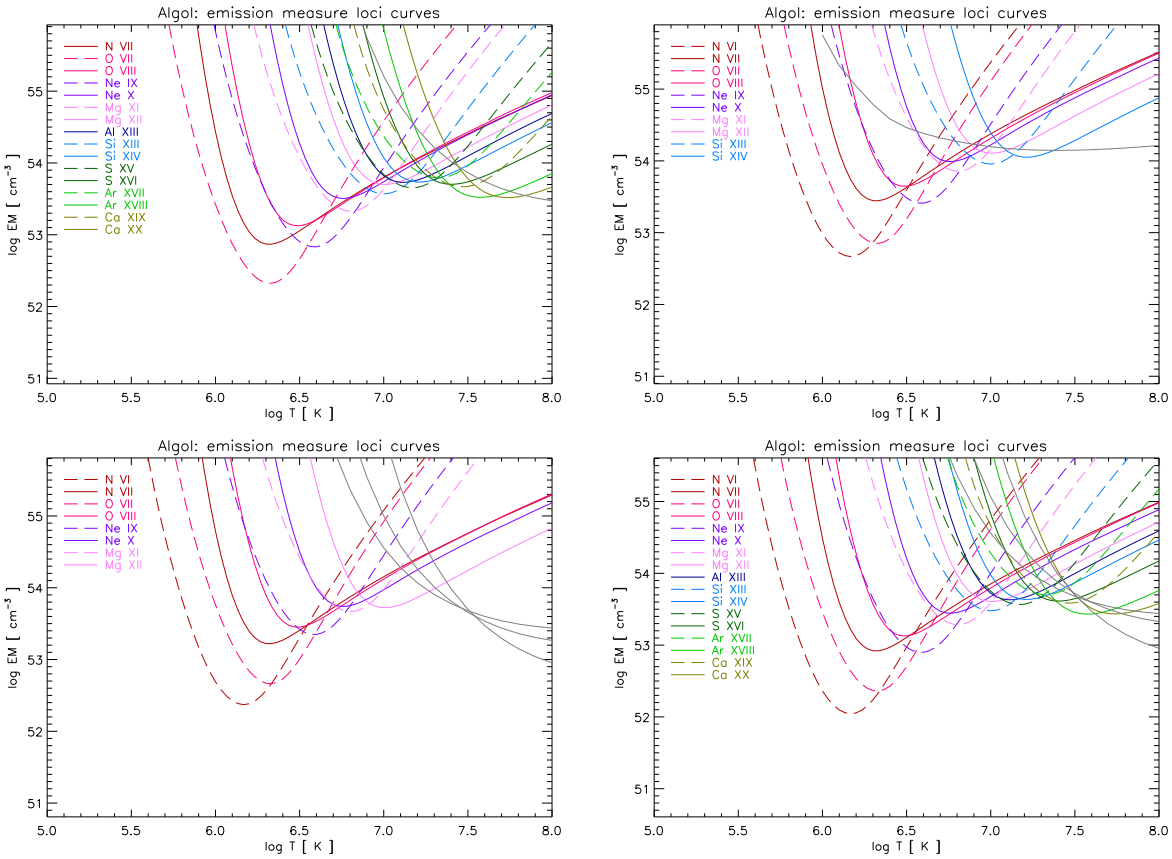

Figure 6.16: Shapes of emission measure distributions constructed from the best-fit $DEMs$ and abundances as a lower limit from the mission measure loci curves for Algol. From upper left to lower right: The best-fit polynomial from the HETGS, the LETGS, the RGS and all datasets combined.

resembles the 6th and 7th order ratio fits very well. The high-temperature peak would enable the development of Algol's strong continuum.

The absolute abundances deduced from the ratio fits (Table 6.53) are very stable and thus the usual normalization problem seems to be overcome in this fit with all datasets. Apart from nitrogen the values are slightly higher than those derived by Schmitt and Ness (2004). The corresponding values relative to oxygen in listed Table 6.54 are also higher, again apart from nitrogen. As can be seen in Table 6.55, the iron abundances derived from the ratio fit have the typical scatter, but the short-wavelength lines may be slightly systematically higher, indicating that the chosen hydrogen column density was too low. The strongly deviating Fe XIX line at 13.52 Å and the Fe XXV triplet were not taken into account.

Table 6.56 shows the the iron line fits cannot reproduce the measured ratios well. Especially the lower-temperature elements give poor results. In the higher orders this is due to rise towards lower temperatures, here are the fits particularly bad. It is thus no wonder that the abundances given in Table 6.59 show a broad scatter for the individual lines; and also averaged for each element (Table 6.57) they do not match the values deduced from the ratio fit. Due to the misleading values for oxygen, the relative abundances given in Table 6.58 are useless for the higher orders. The values in 2nd and 4th order have at least the right order of magnitude.

	measured	2nd order	3rd order	4th order	5th order	6th oder	7th order
N VII / N VI	9.372±2.671	12.357	9.296	9.308	9.071	9.337	9.343
O VIII / O VII	6.735±1.217	7.682	6.919	6.917	7.081	6.759	6.756
Ne X / Ne IX	3.801±0.472	3.320	3.577	3.575	3.546	3.782	3.782
Mg XII / Mg XI	2.409±0.298	2.245	2.540	2.539	2.502	2.435	2.436
Si XIV / Si XIII	1.677±0.127	1.507	1.692	1.692	1.698	1.668	1.668
S XVI / S XV	1.220±0.235	1.005	1.097	1.098	1.126	1.260	1.259
3-4 Å	8.397±0.188	8.348	8.415	8.415	8.415	8.415	8.415
2-3 Å	6.980±0.927	5.997	6.016	6.016	6.042	6.147	6.146
1-2 Å	2.812±0.158	2.966	2.834	2.834	2.832	2.827	2.827
red. χ^2		1.32	0.37	0.46	0.57	0.43	0.87

Table 6.52: Fit results from H-like to He-like ratios from all mentioned Algol datasets combined: Photon flux ratios and continuum flux [10^{-4} cts s^{-1} cm^{-2}] in specified wavelength bands.

element	2nd order	3rd order	4th order	5th order	6th oder	7th order
N	2.584±0.359	2.694±0.371	2.696±0.371	2.725±0.375	2.998±0.413	2.998±0.413
O	0.344±0.030	0.389±0.033	0.389±0.033	0.398±0.034	0.436±0.038	0.436±0.038
Ne	1.184±0.078	1.413±0.084	1.413±0.084	1.428±0.085	1.580±0.093	1.580±0.093
Mg	0.458±0.025	0.514±0.028	0.514±0.028	0.524±0.029	0.566±0.031	0.566±0.031
Al	1.411±0.131	1.475±0.137	1.476±0.137	1.514±0.141	1.678±0.156	1.678±0.156
Si	0.500±0.026	0.528±0.019	0.529±0.019	0.542±0.020	0.601±0.022	0.601±0.022
S	0.493±0.045	0.490±0.043	0.490±0.043	0.498±0.043	0.535±0.047	0.535±0.047
Ar	3.092±0.463	2.987±0.448	2.987±0.448	2.993±0.450	2.958±0.744	2.959±0.743
Ca	2.958±0.402	2.824±0.393	2.824±0.392	2.823±0.379	2.773±0.370	2.773±0.370
Fe	0.315±0.020	0.371±0.019	0.371±0.019	0.379±0.020	0.414±0.025	0.414±0.025

Table 6.53: Absolute abundances derived from the DEM calculated from H-like to He-like ratios for all mentioned Algol datasets combined.

abundance	2nd order	3rd order	4th order	5th order	6th oder	7th order
N / O	7.505±1.227	6.926±1.125	6.931±1.126	6.847±1.112	6.882±1.118	6.884±1.118
Ne / O	3.439±0.373	3.633±0.380	3.633±0.380	3.588±0.375	3.627±0.379	3.628±0.379
Mg / O	1.329±0.136	1.321±0.135	1.321±0.135	1.317±0.135	1.299±0.133	1.299±0.133
Al / O	4.098±0.520	3.791±0.480	3.793±0.481	3.804±0.482	3.851±0.488	3.852±0.488
Si / O	1.452±0.146	1.358±0.127	1.359±0.127	1.362±0.127	1.379±0.129	1.379±0.129
S / O	1.431±0.180	1.259±0.154	1.259±0.154	1.251±0.153	1.228±0.151	1.228±0.151
Ar / O	8.983±1.552	7.678±1.329	7.678±1.329	7.520±1.304	6.790±1.805	6.793±1.804
Ca / O	8.592±1.382	7.261±1.188	7.261±1.187	7.095±1.132	6.364±1.011	6.367±1.012
Fe / O	0.916±0.097	0.952±0.095	0.953±0.095	0.952±0.096	0.951±0.100	0.951±0.100

Table 6.54: Abundances relative to oxygen derived from the DEM calculated from H-like to He-like ratios for all mentioned Algol datasets combined.

element	λ	2nd order	3rd order	4th order	5th order	6th oder	7th order
N VI	28.787	3.152±0.712	2.681±0.605	2.684±0.606	2.671±0.603	2.991±0.676	2.993±0.676
N VII	24.782	2.390±0.415	2.703±0.470	2.703±0.470	2.759±0.479	3.002±0.522	3.002±0.522
O VII	21.602	0.377±0.055	0.396±0.058	0.396±0.058	0.412±0.060	0.437±0.064	0.436±0.064
O VIII	18.970	0.331±0.035	0.385±0.041	0.385±0.041	0.391±0.042	0.435±0.046	0.435±0.046
Ne IX	13.447	1.091±0.109	1.360±0.137	1.359±0.136	1.367±0.137	1.575±0.158	1.575±0.158
Ne X	12.134	1.249±0.091	1.445±0.106	1.446±0.106	1.465±0.107	1.583±0.116	1.583±0.116
Mg XI	9.1688	0.435±0.046	0.534±0.056	0.534±0.056	0.539±0.057	0.570±0.060	0.570±0.060
Mg XII	8.4210	0.467±0.030	0.507±0.033	0.507±0.033	0.519±0.034	0.564±0.037	0.564±0.037
Al XIII	7.1730	1.411±0.131	1.475±0.137	1.476±0.137	1.514±0.141	1.678±0.156	1.678±0.156
Si XIII	6.6480	0.468±0.029	0.531±0.032	0.532±0.032	0.546±0.033	0.599±0.037	0.599±0.037
Si XIV	6.1830	0.521±0.024	0.527±0.024	0.527±0.024	0.540±0.024	0.602±0.027	0.602±0.027
S XV	5.0387	0.434±0.070	0.456±0.074	0.456±0.074	0.471±0.076	0.547±0.089	0.547±0.089
S XVI	4.7300	0.528±0.055	0.507±0.052	0.507±0.052	0.511±0.053	0.530±0.055	0.530±0.055
Ar XVII	3.9488	3.378±0.610	3.338±0.603	3.339±0.603	3.412±0.616	3.802±0.686	3.801±0.686
Ar XVIII	3.7330	2.703±0.711	2.551±0.671	2.551±0.671	2.511±0.660	2.302±0.605	2.303±0.605
Ca XIX	3.0212	2.802±0.426	2.674±0.407	2.674±0.407	2.681±0.408	2.674±0.407	2.674±0.407
Ca XX	3.1773	3.997±1.102	3.851±1.062	3.849±1.062	3.733±1.030	3.253±0.897	3.254±0.897
Fe XVII	15.015	0.233±0.014	0.299±0.019	0.299±0.019	0.298±0.018	0.321±0.020	0.321±0.020
Fe XVII	17.075	0.261±0.019	0.336±0.025	0.336±0.025	0.334±0.024	0.364±0.027	0.364±0.027
Fe XVII	15.262	0.283±0.019	0.364±0.024	0.364±0.024	0.363±0.024	0.392±0.026	0.392±0.026
Fe XVII	16.777	0.273±0.036	0.351±0.047	0.351±0.047	0.350±0.047	0.381±0.051	0.381±0.051
Fe XVIII	14.205	0.275±0.021	0.349±0.027	0.349±0.027	0.349±0.027	0.350±0.027	0.350±0.027
Fe XVIII	93.923	0.264±0.019	0.338±0.024	0.338±0.024	0.337±0.024	0.346±0.025	0.346±0.025
Fe XIX*	13.521	0.670±0.024	0.824±0.029	0.825±0.029	0.835±0.029	0.824±0.029	0.824±0.029
Fe XIX	108.35	0.309±0.026	0.384±0.032	0.385±0.032	0.388±0.032	0.383±0.032	0.383±0.032
Fe XX	121.84	0.242±0.024	0.292±0.029	0.292±0.029	0.298±0.030	0.299±0.030	0.298±0.030
Fe XX	118.68	0.257±0.035	0.309±0.042	0.309±0.042	0.315±0.043	0.316±0.043	0.316±0.043
Fe XX	12.830	0.427±0.039	0.507±0.046	0.508±0.046	0.520±0.047	0.530±0.048	0.529±0.048
Fe XXI	128.75	0.252±0.019	0.291±0.022	0.291±0.022	0.301±0.023	0.318±0.024	0.318±0.024
Fe XXI	117.50	0.248±0.049	0.287±0.056	0.287±0.056	0.296±0.058	0.314±0.062	0.314±0.062
Fe XXI	12.285	0.392±0.017	0.446±0.019	0.447±0.019	0.462±0.020	0.502±0.022	0.502±0.021
Fe XXII	117.15	0.287±0.015	0.317±0.016	0.317±0.016	0.330±0.017	0.377±0.019	0.377±0.019
Fe XXII	135.79	0.292±0.025	0.323±0.028	0.323±0.028	0.336±0.029	0.384±0.033	0.384±0.033
Fe XXII	11.767	0.529±0.036	0.576±0.039	0.576±0.039	0.601±0.041	0.704±0.048	0.704±0.048
Fe XXIII	132.90	0.372±0.011	0.389±0.012	0.389±0.012	0.405±0.012	0.491±0.015	0.491±0.015
Fe XXIII	11.736	0.584±0.025	0.600±0.025	0.600±0.025	0.624±0.026	0.759±0.032	0.759±0.032
Fe XXIV	11.171	0.655±0.094	0.637±0.092	0.637±0.092	0.649±0.094	0.718±0.104	0.718±0.104
Fe XXV*	1.8560	1.968±0.190	1.915±0.184	1.914±0.184	1.862±0.179	1.692±0.163	1.692±0.163

Table 6.55: Abundances derived for individual lines from the DEM calculated from H-like to He-like ratios for all mentioned Algol datasets combined.

	measured	2nd order	3rd order	4th order	5th order	6th oder	7th order
N VII / N VI	9.372±2.671	22.944	0.776	54.210	-NaN	0.000	0.000
O VIII / O VII	6.735±1.217	13.028	2.281	27.087	0.000	0.000	0.000
Ne X / Ne IX	3.801±0.472	4.624	3.426	5.788	0.000	0.000	0.000
Mg XII / Mg XI	2.409±0.298	2.878	3.103	3.398	0.000	0.000	0.000
Si XIV / Si XIII	1.677±0.127	1.813	2.129	2.477	2.649	2.743	2.745
S XVI / S XV	1.220±0.235	1.165	1.347	1.687	1.856	1.951	1.953
3-4 Å	8.397±0.188	8.238	8.362	8.396	8.410	8.417	8.418
2-3 Å	6.980±0.927	6.124	6.158	6.255	6.287	6.301	6.301
1-2 Å	2.812±0.158	3.152	2.932	2.860	2.832	2.814	2.812
red. χ^2		10.01	8.79	8.44	8.75	9.35	10.07

Table 6.56: Fit results from iron lines from all mentioned Algol datasets combined: Photon flux ratios and continuum flux [10^{-4} cts s^{-1} cm^{-2}] in specified wavelength bands.

element	2nd order	3rd order	4th order	5th order	6th oder	7th order
N	4.593±1.684	0.231±0.242	6.811±3.933	-NaN	0.000	0.000
O	0.605±0.167	0.222±0.123	0.897±0.435	-NaN	0.000	0.000
Ne	1.913±0.173	1.960±0.116	2.776±0.515	0.000	0.000	0.000
Mg	0.615±0.047	0.695±0.074	0.841±0.119	0.000	0.000	0.000
Al	1.683±0.156	1.804±0.168	2.124±0.197	2.246±0.209	2.301±0.214	2.301±0.214
Si	0.607±0.022	0.647±0.071	0.750±0.131	0.789±0.159	0.806±0.174	0.806±0.174
S	0.543±0.047	0.531±0.046	0.550±0.075	0.553±0.095	0.552±0.105	0.552±0.105
Ar	3.223±0.543	3.019±0.637	2.877±0.888	2.783±0.978	2.721±1.019	2.719±1.019
Ca	3.052±0.408	2.825±0.378	2.689±0.359	2.614±0.349	2.565±0.342	2.563±0.342
Fe	0.460±0.021	0.544±0.023	0.744±0.030	0.835±0.033	0.880±0.035	0.881±0.035

Table 6.57: Absolute abundances derived from the DEM calculated from iron lines for all mentioned Algol datasets combined.

abundance	2nd order	3rd order	4th order	5th order	6th oder	7th order
N / O	7.591±3.487	1.044±1.235	7.596±5.728	-NaN	0.062±0.117	0.041±0.078
Ne / O	3.162±0.921	8.841±4.923	3.095±1.608	-NaN	***	***
Mg / O	1.016±0.292	3.135±1.768	0.938±0.474	-NaN	***	***
Al / O	2.781±0.812	8.138±4.569	2.368±1.170	-NaN	***	***
Si / O	1.003±0.280	2.917±1.646	0.837±0.431	-NaN	***	***
S / O	0.898±0.261	2.396±1.343	0.614±0.309	-NaN	***	***
Ar / O	5.326±1.726	13.618±8.070	3.208±1.845	-NaN	***	***
Ca / O	5.044±1.551	12.741±7.258	2.999±1.509	-NaN	***	***
Fe / O	0.761±0.214	2.455±1.364	0.829±0.404	-NaN	***	***

Table 6.58: Abundances relative to oxygen derived from the DEM calculated from iron lines for all mentioned Algol datasets combined.

element	λ	2nd order	3rd order	4th order	5th order	6th oder	7th order
N VI	28.787	9.950±2.247	0.205±0.046	36.375±8.215	-NaN	0.000	0.000
N VII	24.782	4.064±0.706	2.480±0.431	6.288±1.093	0.000	0.000	0.000
O VII	21.602	1.048±0.153	0.165±0.024	3.288±0.479	-NaN	0.000	0.000
O VIII	18.970	0.542±0.058	0.487±0.052	0.818±0.087	0.000	0.000	0.000
Ne IX	13.447	2.202±0.221	1.839±0.185	3.851±0.387	0.000	0.000	0.000
Ne X	12.134	1.810±0.133	2.040±0.149	2.529±0.185	0.000	0.398±0.029	0.209±0.015
Mg XI	9.1688	0.706±0.074	0.850±0.090	1.114±0.117	0.000	0.000	0.000
Mg XII	8.4210	0.591±0.038	0.660±0.043	0.790±0.051	0.843±0.055	0.869±0.056	0.869±0.056
Al XIII	7.1730	1.683±0.156	1.804±0.168	2.124±0.197	2.246±0.209	2.301±0.214	2.301±0.214
Si XIII	6.6480	0.639±0.039	0.768±0.047	1.011±0.062	1.129±0.069	1.190±0.073	1.191±0.073
Si XIV	6.1830	0.591±0.027	0.605±0.027	0.685±0.031	0.715±0.032	0.728±0.033	0.727±0.033
S XV	5.0387	0.526±0.085	0.572±0.093	0.713±0.115	0.780±0.126	0.815±0.132	0.815±0.132
S XVI	4.7300	0.551±0.057	0.518±0.054	0.516±0.053	0.513±0.053	0.510±0.053	0.509±0.053
Ar XVII	3.9488	3.748±0.677	3.688±0.666	3.999±0.722	4.122±0.744	4.178±0.754	4.174±0.754
Ar XVIII	3.7330	2.661±0.700	2.412±0.634	2.173±0.571	2.068±0.544	2.008±0.528	2.006±0.527
Ca XIX	3.0212	2.919±0.444	2.699±0.410	2.591±0.394	2.527±0.384	2.486±0.378	2.483±0.378
Ca XX	3.1773	3.784±1.044	3.537±0.976	3.177±0.876	3.023±0.834	2.927±0.807	2.926±0.807
Fe XVII	15.015	0.442±0.027	0.486±0.030	0.680±0.042	0.783±0.048	0.814±0.050	0.815±0.050
Fe XVII	17.075	0.504±0.037	0.538±0.039	0.781±0.057	0.813±0.059	0.867±0.063	0.867±0.063
Fe XVII	15.262	0.540±0.036	0.591±0.039	0.831±0.055	0.947±0.063	0.985±0.066	0.987±0.066
Fe XVII	16.777	0.527±0.070	0.562±0.075	0.817±0.109	0.863±0.115	0.915±0.122	0.915±0.122
Fe XVIII	14.205	0.465±0.036	0.602±0.046	0.718±0.055	0.823±0.064	0.885±0.068	0.885±0.068
Fe XVIII	93.923	0.466±0.033	0.576±0.041	0.710±0.051	0.834±0.060	0.894±0.064	0.894±0.064
Fe XIX*	13.521	1.037±0.036	1.394±0.049	1.728±0.061	1.895±0.067	2.002±0.070	2.002±0.070
Fe XIX	108.35	0.492±0.041	0.657±0.054	0.796±0.066	0.885±0.073	0.941±0.078	0.941±0.078
Fe XX	121.84	0.359±0.036	0.480±0.048	0.625±0.063	0.680±0.068	0.712±0.072	0.712±0.072
Fe XX	118.68	0.380±0.052	0.508±0.070	0.662±0.091	0.720±0.099	0.754±0.104	0.754±0.104
Fe XX	12.830	0.617±0.056	0.819±0.074	1.100±0.100	1.197±0.108	1.249±0.113	1.250±0.113
Fe XXI	128.75	0.348±0.026	0.452±0.034	0.635±0.048	0.699±0.053	0.730±0.055	0.731±0.055
Fe XXI	117.50	0.343±0.067	0.445±0.087	0.626±0.123	0.689±0.135	0.720±0.141	0.720±0.142
Fe XXI	12.285	0.530±0.023	0.675±0.029	0.969±0.041	1.078±0.046	1.128±0.048	1.129±0.048
Fe XXII	117.15	0.372±0.019	0.454±0.023	0.660±0.034	0.748±0.038	0.790±0.040	0.791±0.041
Fe XXII	135.79	0.379±0.032	0.463±0.040	0.672±0.057	0.762±0.065	0.804±0.069	0.805±0.069
Fe XXII	11.767	0.671±0.045	0.798±0.054	1.152±0.078	1.315±0.089	1.394±0.094	1.396±0.094
Fe XXIII	132.90	0.447±0.013	0.498±0.015	0.673±0.020	0.760±0.023	0.804±0.024	0.805±0.024
Fe XXIII	11.736	0.686±0.029	0.737±0.031	0.954±0.040	1.062±0.045	1.118±0.047	1.119±0.047
Fe XXIV	11.171	0.707±0.102	0.684±0.099	0.731±0.105	0.749±0.108	0.757±0.109	0.756±0.109
Fe XXV*	1.8560	1.861±0.179	1.775±0.171	1.655±0.159	1.604±0.155	1.567±0.151	1.567±0.151

Table 6.59: Abundances derived for individual lines from the DEM calculated from iron lines for all mentioned Algol datasets combined.

6.3 AU Mic, a young active M-dwarf

AU Microscopii is an M1 V dwarf with $m_V = 8\overset{m}{.}61$, located at a distance of 9.94 pc. It forms a distance and proper motion pair with AT Mic, although the two stars are separated by 1.5° on the sky. Their space velocities identify both as members of the β Pictoris moving group, an association of nearby young stars. The age of AU Mic is estimated to be approximately 10–12 Myr.

Coronagraphic measurements with the Keck telescope revealed the presence of a disk around AU Mic, imaged in reflected light an thus consisting of circumstellar dust (Kalas et al., 2004). Recent coronagraphic imaging with ACS on board the *Hubble Space Telescope* proved its extend up to 150 AU with a thickness of ≈ 3 AU (Krist et al., 2005). The disk is seen nearly edge-on, the inclination angle of the inner part within 50 AU is less than 1°. Thus AU Mic is actually obscured by its own debris disk.

AU Mic exhibits many signs of activity. Optical and UV spectra show emission lines typical for chromospheric activity. Optical light curves show periodic variations (resulting in a rotation period of 4.85 days) with $\Delta m_V \approx 0\overset{m}{.}15$ that are attributed to photospheric dark spots, superimposed with phases of flare activity. Long-term variability studies indicate considerable variations of the extent of the spotted area and of the spot distribution on the surface. Strong flares on AU Mic are observable across the electromagnetic spectrum from X-ray to radio wavelengths (see e.g. Smith et al. (2005), who analyzed simultaneous *XMM-Newton* X-ray and VLA radio observations of several active M-dwarfs).

Magnetic activity phenomena are orders of magnitude more energetic on dMe stars than observed on the Sun, and AU Mic itself is one of the most active of the dMe stars. It shows a prominent ultraviolet emission line spectrum and has thus been a frequent target for satellite missions and instruments operating in the UV like *IUE* or *EUVE*. Pagano et al. (2000) reconstructed an emission measure distribution from recent observations with STIS on board *Hubble*, temperatures greater than $\log T = 5.5$ are however only poorly covered. Del Zanna et al. (2002) analyze *FUSE* data, concentrating on the transition region. Their Figure 7 shows a DEM computed for AU Mic in quiescent state from combined datasets of different UV instruments with the method now implemented in the CHIANTI routine `chianti_dem` shows – concentrating on higher temperatures – a minimum at $\log T = 6.5$ and a maximum at $\log T = 6.8$ but is afflicted with considerable uncertainties. At lower temperatures, their emission measure distributions are in conflict with those derived by Pagano et al. (2000).

AU Mic shows the highest X-ray luminosity of all stars within 10 pc ($\log L_X \approx 29.65$ in the *ROSAT* and *XMM* energy bands) and is thus a suitable target for detailed investigations of active M-dwarfs. Linsky et al. (2002) discuss the X-ray properties of AU Mic compared to solar active regions.

6.3.1 The HETGS dataset ObsID 17

Linsky et al. (2002) give a discussion with emission measure and abundance analysis of the HETGS observation of AU Mic. Results from this observation are also included in many studies containing several stars, e.g. those by Ness et al. (2003c), Ness et al. (2004), Testa et al. (2004) and Drake and Testa (2005). In none of these surveys it showed anomalous results deviating strongly from the average.

The lightcurve in Figure 6.17 displays periods of flaring during the HETGS observation. The flares are moderate or short-term events that do probably not have a lasting effect on the emission measure, a level of quiescent emission can clearly be assessed. The corresponding HEG and MEG spectra show a negligible continuum level and only weak emission lines in the short-wavelength range < 10 Å. The strongest line is O VIII, but O VII, N VII, Ne X, the Ne IX triplet

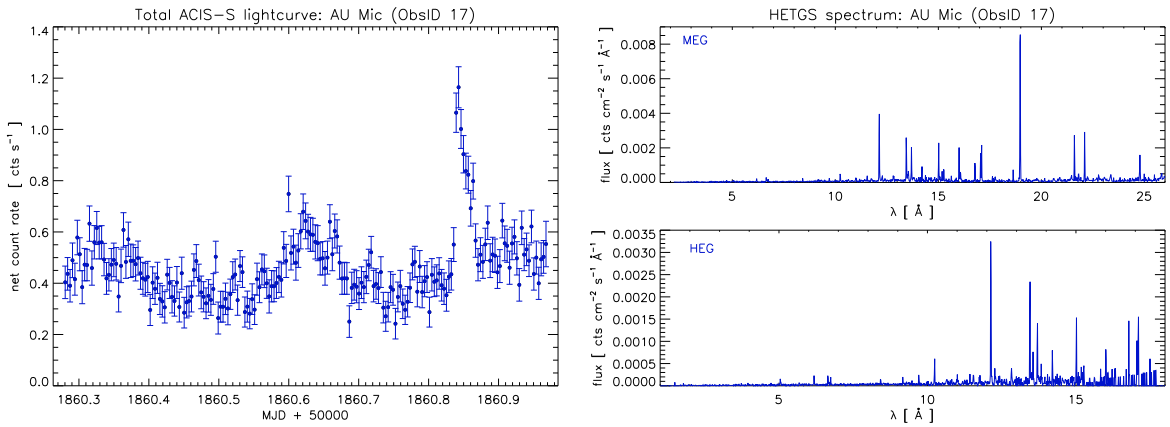

Figure 6.17: Lightcurve (left) and spectrum (right) of AU Mic from 12 November 2000 obtained with the HETGS onboard *Chandra* with a total exposure time of 58.8 ks.

and some Fe XVII lines are also visible.

The results obtained from this dataset are somehow disappointing. $DEMs$ could only be fitted in 2nd and 3rd order and the fits are not satisfactory, see Figure 6.18. The parabola from the ratio fit peaks at 5 MK at a level of logDEM≈ 45.5 cm^{-3} K^{-1}. The corresponding iron line fit is very poor, the parabola does not even have a maximum. The 3rd order ratio fit peaks at 4.5 MK, at similar temperatures as the parabola but at a much lower level of $\log DEM \approx 44$ cm^{-3} K^{-1}. The iron line fit is still not credible. It peaks at only 2 MK, at a much too low level of $\log DEM \approx 41.5$ cm^{-3} K^{-1}. 2nd and 3rd order polynomials would not be able to reproduce the complex structure of the DEM obtained by Del Zanna et al. (2002), and the reconstructed emission measures (see Figure 6.22) are only vaguely similar to the previous results from Linsky et al. (2002).

The third order ratio fit gives the smallest reduced χ^2 I have ever seen (see Table 6.60), it is much "too good". Shape and maximum temperature of the polynomial are suitable for a differential emission measure of an active M-dwarf like AU Mic but the level of maximum emission is approximately an order of magnitude to low. It is also no wonder that none of the two iron line fits can reproduce the measured ratios, and that the abundances derived from these fits are too high (Tables 6.63 and 6.61). The 3rd order ratio fit also gives systematically too high abundances, indicating the wrong normalization. The values obtained from the ratio fit parabola though have the correct order of magnitude. Relative to oxygen both ratio fits give similar results, indicating the neon overabundance reported by Drake and Testa (2005). Nevertheless they do not match the two-temperature component global fit.

Linsky et al. (2002) derived abundances relative to Grevesse and Sauval from their emission measure distribution that was constructed from iron lines based on APEC emissivities. Converted to the values by Asplund et al., they obtain absolute values of 0.62, 2.76, 0.25, 0.54 and 0.4 for oxygen, neon, magnesium, silicon and iron respectively; these correspond to 4.44, 0.4, 0.87 and 0.65 relative to oxygen. These values do neither match those computed from my DEM fits nor the global fit.

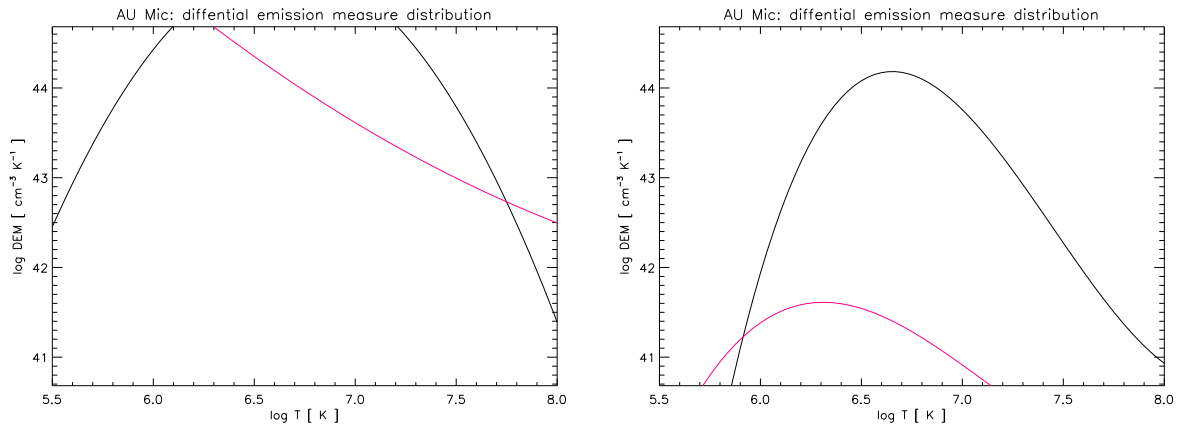

Figure 6.18: Differential emission measures for AU Mic modeled with a parabola (left) and a 3rd order polynomial (right), calculated from the HETGS dataset 604.

	measured	2nd order	3rd order
O VIII / O VII	4.257±0.635	3.567 (1.113)	4.270 (21.938)
Ne X / Ne IX	1.689±0.121	1.774 (1.117)	1.685 (36.129)
Mg XII / Mg XI	1.084±0.185	1.206 (1.284)	1.092 (73.720)
Si XIV / Si XIII	0.910±0.103	0.817 (1.385)	0.909 (***)
2-3 Å	0.343±0.034	0.343 (0.343)	0.343 (0.343)
red. χ^2		1.47 (2.71)	0.03 (3.04)

Table 6.60: Fit results from H-like to He-like ratios from the AU Mic HETGS dataset 17: Photon flux ratios and continuum flux [10^{-4} cts s^{-1} cm^{-2}] from 2 to 3 Å. The corresponding results from the iron line fit are given in brackets.

element	2nd order	3rd order	2T fit
N	1.115±0.198 (7.571±1.346)	20.646±3.670 (***±***)	2.005
O	0.645±0.037 (4.349±2.896)	11.393±0.517 (***±***)	0.812
Ne	1.622±0.044 (30.276±5.415)	27.990±0.768 (***±***)	1.034
Mg	0.161±0.013 (3.494±0.279)	3.047±0.243 (29.353±***)	0.098
Al	0.645±0.190 (11.959±3.525)	12.728±3.751 (74.033±***)	0.267
Si	0.368±0.021 (6.930±1.451)	7.323±0.414 (27.412±***)	0.220
S	0.866±0.219 (7.127±1.803)	10.050±2.542 (18.165±4.595)	0.434
Fe	0.199±0.016 (4.128±0.229)	3.551±0.267 (***±***)	0.149

Table 6.61: Absolute abundances derived from the DEM calculated from H-like to He-like ratios and a corresponding global fit with two temperature components for the AU Mic HETGS dataset 17. The corresponding results from the iron line fit are given in brackets.

abundance	2nd order	3rd order	2T fit
N / O	1.729±0.323 (1.741±1.200)	1.812±0.332 (1.734±0.557)	2.469
Ne / O	2.514±0.161 (6.961±4.799)	2.457±0.130 (1.368±0.701)	1.273
Mg / O	0.249±0.025 (0.803±0.539)	0.267±0.025 (0.062±0.045)	0.121
Al / O	0.999±0.300 (2.750±2.002)	1.117±0.333 (0.157±0.062)	0.328
Si / O	0.571±0.046 (1.593±1.112)	0.643±0.047 (0.058±0.063)	0.271
S / O	1.342±0.348 (1.639±1.167)	0.882±0.227 (0.038±0.014)	0.534
Fe / O	0.309±0.030 (0.949±0.634)	0.312±0.027 (4.611±1.258)	0.183

Table 6.62: Abundances relative to oxygen derived from the *DEM* calculated from H-like to He-like ratios and a corresponding global fit with two temperature components for the AU Mic HETGS dataset 17. The corresponding results from the iron line fit are given in brackets.

element	wavelength	2nd order	3rd order
N VII	24.782	1.115±0.198 (7.571±1.346)	20.646±3.670 (***±***)
O VII	21.602	0.553±0.078 (2.119±0.299)	11.422±1.614 (***±***)
O VIII	18.970	0.660±0.032 (8.110±0.389)	11.390±0.546 (***±***)
Ne IX	13.447	1.690±0.110 (22.543±1.471)	27.946±1.824 (***±***)
Ne X	12.134	1.608±0.049 (34.068±1.030)	27.999±0.847 (***±***)
Mg XI	9.1688	0.174±0.024 (3.957±0.558)	3.062±0.432 (***±***)
Mg XII	8.4210	0.156±0.015 (3.339±0.323)	3.040±0.294 (29.154±2.820)
Al XIII	7.1730	0.645±0.190 (11.959±3.525)	12.728±3.751 (74.033±***)
Si XIII	6.6480	0.352±0.027 (9.003±0.698)	7.320±0.568 (***±***)
Si XIV	6.1830	0.392±0.032 (5.914±0.489)	7.325±0.606 (27.212±2.250)
S XVI	4.7300	0.866±0.219 (7.127±1.803)	10.050±2.542 (18.165±4.595)
Fe XVII	15.015	0.176±0.017 (3.453±0.337)	2.887±0.282 (***±***)
Fe XVII	17.075	0.245±0.015 (4.603±0.290)	4.011±0.253 (***±***)
Fe XVII	15.262	0.235±0.027 (4.578±0.518)	3.853±0.436 (***±***)
Fe XVII	16.777	0.194±0.021 (3.649±0.399)	3.176±0.347 (***±***)
Fe XVIII	14.205	0.222±0.030 (5.739±0.773)	3.892±0.524 (***±***)
Fe XIX	13.521	0.365±0.045 (10.416±1.298)	7.003±0.873 (***±***)
Fe XX	12.830	0.198±0.044 (5.761±1.278)	4.155±0.921 (***±***)
Fe XXI	12.285	0.107±0.021 (3.008±0.604)	2.451±0.492 (***±***)
Fe XXII	11.767	0.189±0.036 (4.855±0.919)	4.733±0.895 (***±***)
Fe XXIII	11.736	0.196±0.038 (4.097±0.788)	5.421±1.043 (***±***)
Fe XXIV	11.171	0.323±0.057 (4.247±0.746)	9.598±1.686 (***±***)

Table 6.63: Abundances derived for individual lines from the *DEM* calculated from iron lines for the AU Mic HETGS dataset 17. The corresponding results from the iron line fit are given in brackets.

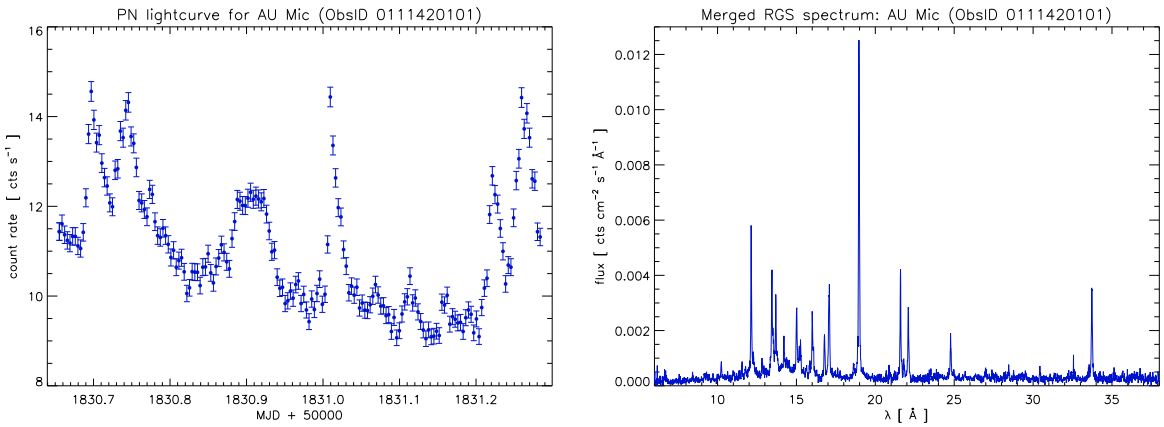

Figure 6.19: Lightcurve (left) and spectrum (right) of AU Mic from 13/14 October 2000 obtained with EPIC-PN and RGS onboard *XMM* respectively. The exposure time is 38.4 ks.

6.3.2 The RGS dataset ObsID 0111420101

The observation of AU Mic with the RGS covers a period of repeated flaring as can be seen from the lightcurve in Figure 6.19. It is difficult to assess a level of quiescence. The corresponding spectrum is very similar to the HEG and MEG spectra (apart from the pseudo-continuum typical for RGS observations). As AU Mic's HETGS dataset, this RGS spectrum has been analyzed in many studies like those by Ness et al. (2003c), Ness et al. (2003b) and Ness et al. (2004).

The differential emission measures reconstructed from this dataset give somewhat more reliable results than the HETGS dataset, although only three ratios and few iron lines covering lower to intermediate temperatures are available. At higher temperatures these fits are solely determined by the continuum measurements. The parabola obtained from the ratio fit (left panel of Figure 6.20) has its maximum at 4.5 MK at a reasonable level of $\log DEM = 45$ cm^{-3} K^{-1}. The corresponding parabola from the iron line fit is slightly narrower and its maximum is shifted to 6.5 MK. For temperatures higher than 8 MK both parabolas resemble each other very well.

The ratio fit flattens towards lower temperatures in third order and peaks at $\log T = 6.7$. The corresponding iron line fit becomes much narrower but with a level an order of magnitude higher at the maximum temperature. The fourth order iron line fit is more or less identical to the third order fit while the fourth order ratio fit forms a rise towards lower temperatures, but outside the valid temperature confidence range that starts at ≈ 2 MK.

None of the fits gives really good fit results though, the values of reduced χ^2 do not drop below 5 and 3 for ratio and iron line fit respectively, see Table 6.64. The best results are provided in both cases by the parabolas. The abundances of derived for the individual lines from the ratio fits (Table 6.67) show a broad scatter due to the poor fits. Nevertheless they indicate a neon enhancement. The global fit with two temperature components gives again deviating values, as well concerning the absolute abundances in Table 6.65 as the relative abundances in Table 6.66. The individual abundances deduced from the iron line fit (Table 6.70) are similarly scattered than those from the ratio fit, but surprisingly the average values relative to oxygen in Table 6.69 match the values from the global fit quite well. Apart from the 2nd order fit, even the absolute values in Table 6.68 agree with it. While the relative values obtained from this dataset at least roughly match the values obtained from the HETGS dataset, there are the same deviations from the values of Linsky et al. (2002).

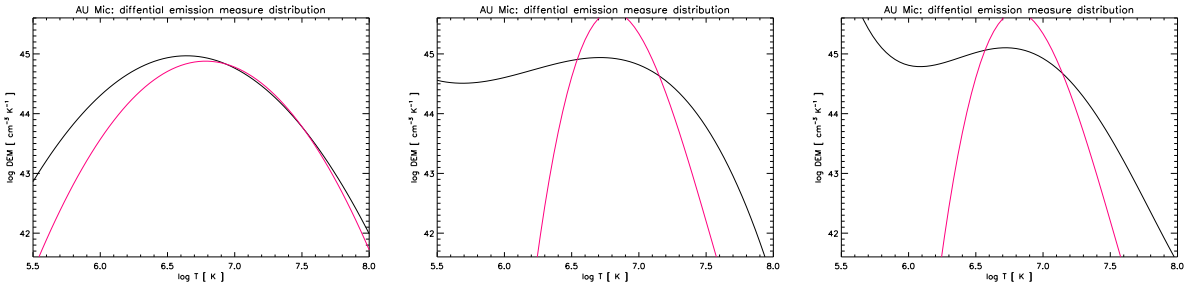

Figure 6.20: Differential emission measures for AU Mic modeled with 2nd to 4th order polynomials, calculated from the RGS dataset 0111420101.

	measured	2nd order	3rd order	4th order
N VII / N VI	3.113±0.569	4.847 (7.924)	4.360 (23.678)	4.330 (23.776)
O VIII / O VII	3.802±0.177	3.453 (5.072)	3.496 (11.506)	3.544 (11.559)
Ne X / Ne IX	1.714±0.185	1.904 (2.348)	2.081 (2.453)	1.949 (2.462)
3-4 Å	0.481±0.004	0.481 (0.481)	0.481 (0.481)	0.481 (0.481)
2-3 Å	0.290±0.026	0.305 (0.295)	0.282 (0.278)	0.299 (0.278)
1-2 Å	0.180±0.082	0.127 (0.112)	0.095 (0.247)	0.163 (0.247)
red. χ^2		5.02 (3.14)	6.48 (3.38)	8.49 (4.51)

Table 6.64: Fit results from H-like to He-like ratios from the AU Mic RGS dataset 0111420101: Photon flux ratios and continuum flux [10^{-4} cts s^{-1} cm^{-2}] in specified wavelength bands. The corresponding results from the iron line fit are given in brackets.

element	2nd order	3rd order	4th order	2T fit
C	2.311±0.212	2.188±0.201	1.656±0.152	1.385
N	2.980±0.354	2.975±0.280	2.262±0.209	1.500
O	1.993±0.070	2.014±0.062	1.516±0.039	0.876
Ne	5.880±0.234	5.665±0.380	4.312±0.196	1.252
Fe	0.720±0.043	0.730±0.042	0.515±0.030	0.192

Table 6.65: Absolute abundances derived from the DEM calculated from H-like to He-like ratios and a corresponding global fit with two temperature components for the AU Mic RGS dataset 0111420101.

abundance	2nd order	3rd order	4th order	2T fit
C / O	1.160±0.114	1.086±0.105	1.092±0.104	1.581
N / O	1.495±0.185	1.477±0.146	1.492±0.143	1.712
Ne / O	2.951±0.157	2.813±0.207	2.845±0.148	1.429
Fe / O	0.361±0.025	0.362±0.024	0.340±0.021	0.219

Table 6.66: Abundances relative to oxygen derived from the DEM calculated from H-like to He-like ratios and a corresponding global fit with two temperature components for the AU Mic RGS dataset 0111420101.

element	wavelength	2nd order	3rd order	4th order
C VI	33.737	2.311±0.212	2.188±0.201	1.656±0.152
N VI	28.787	4.513±0.776	4.066±0.699	3.071±0.528
N VII	24.782	2.898±0.179	2.903±0.180	2.207±0.137
O VII	21.602	1.839±0.079	1.878±0.081	1.429±0.061
O VIII	18.970	2.025±0.036	2.042±0.036	1.533±0.027
Ne IX	13.447	6.435±0.634	6.709±0.661	4.816±0.474
Ne X	12.134	5.792±0.252	5.527±0.241	4.236±0.184
Fe XVII	15.015	0.690±0.030	0.702±0.031	0.494±0.022
Fe XVII	17.075	0.809±0.058	0.826±0.059	0.582±0.042
Fe XVII	15.262	0.670±0.094	0.682±0.096	0.480±0.068
Fe XVII	16.777	0.655±0.080	0.669±0.081	0.472±0.057
Fe XVIII	14.205	1.017±0.100	0.980±0.096	0.703±0.069
Fe XIX	13.521	0.350±0.211	0.323±0.195	0.241±0.145

Table 6.67: Abundances derived for individual lines from the DEM calculated from H-like to He-like ratios for the AU Mic RGS dataset 0111420101.

element	2nd order	3rd order	4th order	2T fit
C	3.574±0.329	1.275±0.117	1.285±0.118	1.385
N	4.193±0.872	1.356±0.417	1.368±0.421	1.500
O	2.645±0.244	0.758±0.200	0.764±0.202	0.876
Ne	6.458±0.675	1.546±0.181	1.557±0.184	1.252
Fe	0.859±0.049	0.164±0.009	0.165±0.009	0.192

Table 6.68: Absolute abundances derived from the DEM calculated from iron lines for the AU Mic RGS dataset 0111420101.

abundance	2nd order	3rd order	4th order	2T fit
C / O	1.351±0.176	1.681±0.469	1.681±0.470	1.581
N / O	1.585±0.361	1.790±0.724	1.790±0.725	1.712
Ne / O	2.442±0.340	2.040±0.588	2.037±0.589	1.429
Fe / O	0.325±0.035	0.216±0.058	0.216±0.058	0.219

Table 6.69: Abundances relative to oxygen derived from the DEM calculated from iron lines for the AU Mic RGS dataset 0111420101.

element	wavelength	2nd order	3rd order	4th order
C VI	33.737	3.574±0.329	1.275±0.117	1.285±0.118
N VI	28.787	10.360±1.782	10.169±1.749	10.298±1.771
N VII	24.782	4.070±0.252	1.337±0.083	1.348±0.083
O VII	21.602	3.427±0.147	2.211±0.095	2.240±0.096
O VIII	18.970	2.569±0.046	0.731±0.013	0.737±0.013
Ne IX	13.447	8.549±0.842	2.132±0.210	2.154±0.212
Ne X	12.134	6.241±0.272	1.490±0.065	1.500±0.065
Fe XVII	15.015	0.827±0.036	0.157±0.007	0.158±0.007
Fe XVII	17.075	0.982±0.070	0.190±0.014	0.192±0.014
Fe XVII	15.262	0.805±0.113	0.153±0.022	0.154±0.022
Fe XVII	16.777	0.796±0.097	0.154±0.019	0.156±0.019
Fe XVIII	14.205	1.099±0.108	0.198±0.019	0.199±0.020
Fe XIX	13.521	0.356±0.215	0.073±0.044	0.074±0.044

Table 6.70: Abundances derived for individual lines from the DEM calculated from iron lines for the AU Mic RGS dataset 0111420101.

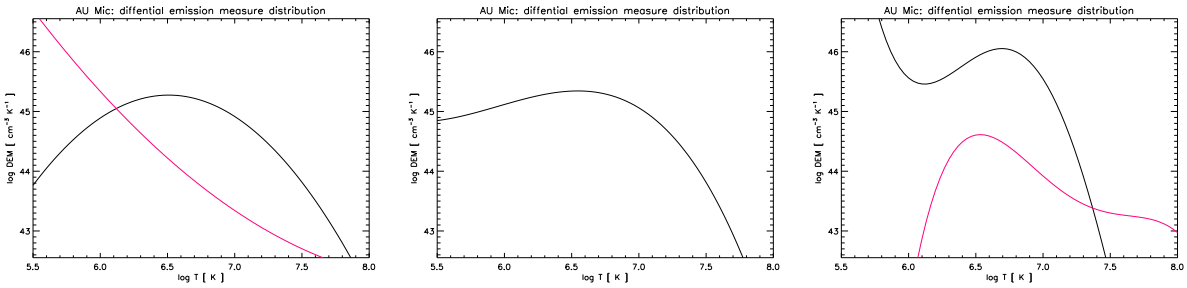

Figure 6.21: Differential emission measures for AU Mic modeled with 2nd to 4th order polynomials, calculated from both the HETGS and the RGS datasets combined.

	measured	2nd order	3rd order	4th order
N VII / N VI	3.051±0.554	3.615 (0.855)	3.499 (34.626)	3.054 (6.119)
O VIII / O VII	3.904±0.562	2.680 (0.862)	2.762 (34.492)	3.804 (3.156)
Ne X / Ne IX	1.524±0.247	1.586 (0.941)	1.676 (59.879)	1.666 (1.341)
Mg XII / Mg XI	1.084±0.185	1.199 (1.183)	1.232 (***)	0.987 (1.116)
Si XIV / Si XIII	0.910±0.103	0.888 (1.422)	0.858 (***)	0.917 (1.246)
2-3 Å	0.343±0.034	0.343 (0.343)	0.343 (0.343)	0.343 (0.343)
red. χ^2		2.09 (2.63)	3.02 (2.88)	0.64 (3.17)

Table 6.71: Fit results from H-like to He-like ratios from all AU Mic datasets combined: Photon flux ratios and continuum flux [10^{-4} cts s^{-1} cm^{-2}] in specified wavelength bands. The corresponding results from the iron line fit are given in brackets.

6.3.3 Combined datasets

Both the HETGS and the RGS datasets of AU Mic do not provide satisfactory fit results. The most obvious possibility to obtain better results from the available data seemed to be their merging. This attempt was however crowned only with moderate success. Five H-like to He-like ratios are now available, the results from their DEM fits are clearly dominated by the RGS data. The available 2nd to 4th order polynomials (Figure 6.21) resemble their counterparts from the RGS dataset discussed above. The only differences for the parabola and the 3rd order polynomial are that they peak at slightly lower temperatures of ≈ 3 MK and at a somewhat higher level of $\log DEM$. Maximum and minimum of the 4th order polynomial are more pronounced than in the RGS 4th order polynomial, and the maximum is located at a higher level of $\log DEM \approx 46$ cm^{-3} K^{-1}. The high-temperature slope of the 4th order 4polynomial starts falling at lower temperatures, similar to the iron line fits obtained from the RGS datasets.

The fit of the merged iron lines on the other hand is still dominated by the HETGS dataset, and thus it is no wonder that they provide similarly poor results. The parabola is again turned upside down and the normalization of the third order fit is too low (the maximum is located at $\log DEM \approx 41$ cm^{-3} K^{-1}) so that the corresponding polynomial is not even visible in the plot in Figure 6.21. The fourth order iron line fit has a maximum at ≈ 3 MK followed by a slow decay towards higher temperatures. A small second peak at extremely high temperatures (≈ 65 MK) appears to emerge at a level an order of magnitude lower than the maximum, which is below 45 cm^{-3} K^{-1}.

The 4th order polynomial deduced from the ratios gives the best fit results, the ratios are well-reproduced, see Table 6.71. Discrepancies arise however for the higher-temperature iron lines (Table 6.74), that have a systematically higher abundance than the lower-temperature ones. This does not occur with the 2nd and 3rd order ratio fits, thus the fitted early decrease of the differential emission measure towards higher temperatures is in conflict with the high-

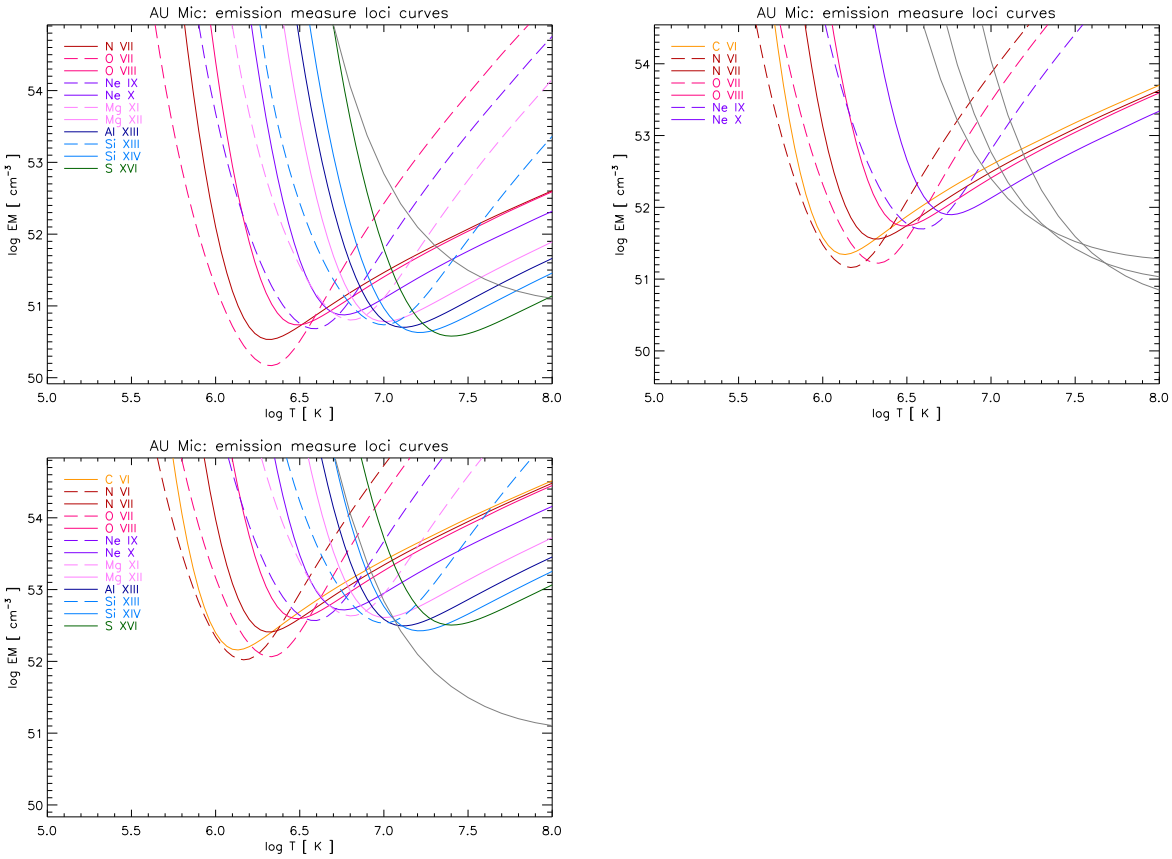

Figure 6.22: Shapes of emission measures as a lower limit from the emission measure loci curves for AU Mic. Upper panel: From the best-fit polynomial obtained from the ratio fits from the HETGS (left) and the RGS (right) observations. Underneath the same for all datasets combined.

temperature iron lines. The averaged absolute abundances in Table 6.72 derived from parabola and 3rd order fit deviate by a factor of ≈ 4 from the values of the 4th order fit. The relative values listed in Table 6.73 however show a good agreement, also with the values from the individual datasets. It is thus no wonder that they again deviate from the values derived by Linsky et al. (2002).

The emission measures shown in Figure 6.22, each constructed from the the best-fit $DEMs$ and abundances have a much more pronounced maximum than the one obtained by Linsky et al. (2002) from iron lines mainly from the HETGS dataset with two additional low-temperature lines from *EUVE*. A corresponding emission measure from the 3rd order RGS fit would resemble their data better. The emission measures computed by Del Zanna et al. (2002) (their Figure 8) match the ones shown here somewhat better.

element	2nd order	3rd order	4th order
C	1.056±0.097	0.833±0.077	0.253±0.023
N	1.438±0.080	1.165±0.065	0.312±0.017
O	0.985±0.144	0.801±0.107	0.205±0.010
Ne	2.845±0.227	2.230±0.178	0.499±0.040
Mg	0.229±0.018	0.172±0.014	0.045±0.004
Al	0.898±0.265	0.674±0.199	0.205±0.061
Si	0.518±0.029	0.389±0.022	0.117±0.007
S	1.028±0.260	0.858±0.217	0.119±0.030
Fe	0.311±0.028	0.234±0.024	0.060±0.006

Table 6.72: Absolute abundances derived from the DEM calculated from H-like to He-like ratios for all mentioned AU Mic datasets combined.

element	2nd order	3rd order	4th order
C / O	1.071±0.185	1.040±0.168	1.233±0.128
N / O	1.460±0.228	1.454±0.210	1.525±0.113
Ne / O	2.887±0.481	2.785±0.433	2.438±0.229
Mg / O	0.233±0.039	0.215±0.033	0.220±0.021
Al / O	0.912±0.300	0.842±0.272	1.003±0.300
Si / O	0.526±0.082	0.486±0.070	0.572±0.043
S / O	1.043±0.305	1.071±0.306	0.581±0.150
Fe / O	0.315±0.054	0.292±0.049	0.292±0.033

Table 6.73: Abundances relative to oxygen derived from the DEM calculated from H-like to He-like ratios for all mentioned AU Mic datasets combined.

element	wavelength	2nd order	3rd order	4th order
C VI	33.737	1.056±0.097	0.833±0.077	0.253±0.023
N VI	28.787	1.680±0.289	1.320±0.227	0.313±0.054
N VII	24.782	1.418±0.083	1.151±0.067	0.312±0.018
O VII	21.602	0.733±0.098	0.608±0.082	0.200±0.027
O VIII	18.970	1.068±0.056	0.860±0.045	0.206±0.011
Ne IX	13.447	2.914±0.362	2.366±0.294	0.527±0.065
Ne X	12.134	2.800±0.293	2.151±0.225	0.482±0.050
Mg XI	9.1688	0.247±0.035	0.189±0.027	0.042±0.006
Mg XII	8.4210	0.223±0.022	0.166±0.016	0.047±0.005
Al XIII	7.1730	0.898±0.265	0.674±0.199	0.205±0.061
Si XIII	6.6480	0.512±0.040	0.379±0.029	0.118±0.009
Si XIV	6.1830	0.525±0.043	0.402±0.033	0.117±0.010
S XVI	4.7300	1.028±0.260	0.858±0.217	0.119±0.030
Fe XVII	15.015	0.337±0.035	0.265±0.028	0.054±0.006
Fe XVII	17.075	0.416±0.045	0.330±0.036	0.067±0.007
Fe XVII	15.262	0.356±0.034	0.281±0.027	0.057±0.005
Fe XVII	16.777	0.343±0.041	0.271±0.033	0.055±0.007
Fe XVIII	14.205	0.516±0.077	0.391±0.059	0.083±0.012
Fe XIX	13.521	0.274±0.106	0.202±0.078	0.050±0.019
Fe XX	12.830	0.297±0.066	0.216±0.048	0.065±0.014
Fe XXI	12.285	0.159±0.032	0.114±0.023	0.044±0.009
Fe XXII	11.767	0.274±0.052	0.198±0.037	0.105±0.020
Fe XXIII	11.736	0.271±0.052	0.201±0.039	0.163±0.031
Fe XXIV	11.171	0.406±0.071	0.322±0.057	0.448±0.079

Table 6.74: Abundances derived for individual lines from the DEM calculated from H-like to He-like ratios for all mentioned AU Mic datasets combined.

element	2nd order	3rd order	4th order
C	2.847±0.262	***	8.315±0.764
N	5.741±3.550	***	9.300±1.500
O	5.931±4.838	***	5.937±0.463
Ne	52.613±***	***	17.201±1.378
Mg	6.122±0.489	23.430±***	1.643±0.131
Al	21.424±6.314	59.132±***	6.132±1.807
Si	12.332±2.739	21.794±***	3.517±0.552
S	11.813±2.988	14.458±3.658	3.609±0.913
Fe	7.939±0.501	***	2.166±0.126

Table 6.75: Absolute abundances derived from the DEM calculated from iron lines for all mentioned AU Mic datasets combined.

abundance	2nd order	3rd order	4th order
C / O	0.480±0.394	1.305±0.462	1.401±0.169
N / O	0.968±0.991	1.557±0.716	1.567±0.281
Ne / O	8.871±7.550	1.290±1.129	2.897±0.324
Mg / O	1.032±0.846	0.046±0.035	0.277±0.031
Al / O	3.612±3.133	0.117±0.053	1.033±0.315
Si / O	2.079±1.758	0.043±0.048	0.592±0.104
S / O	1.992±1.701	0.029±0.012	0.608±0.161
Fe / O	1.339±1.095	7.420±2.577	0.365±0.036

Table 6.76: Abundances relative to oxygen derived from the DEM calculated from iron lines for all mentioned AU Mic datasets combined.

element	wavelength	2nd order	3rd order	4th order
C VI	33.737	2.847±0.262	***	8.315±0.764
N VI	28.787	2.817±0.484	***	18.139±3.120
N VII	24.782	10.051±0.588	***	9.046±0.529
O VII	21.602	3.207±0.430	***	4.982±0.668
O VIII	18.970	14.523±0.764	***	6.162±0.324
Ne IX	13.447	43.242±5.368	***	16.059±1.994
Ne X	12.134	70.025±7.318	***	18.247±1.907
Mg XI	9.1688	6.514±0.918	***	1.676±0.236
Mg XII	8.4210	5.967±0.577	23.340±2.258	1.628±0.157
Al XIII	7.1730	21.424±6.314	59.132±***	6.132±1.807
Si XIII	6.6480	16.347±1.268	***	4.225±0.328
Si XIV	6.1830	10.464±0.865	21.707±1.794	3.087±0.255
S XVI	4.7300	11.813±2.988	14.458±3.658	3.609±0.913
Fe XVII	15.015	7.492±0.784	***	2.023±0.212
Fe XVII	17.075	8.836±0.953	***	2.461±0.265
Fe XVII	15.262	7.858±0.755	***	2.132±0.205
Fe XVII	16.777	7.277±0.877	***	2.023±0.244
Fe XVIII	14.205	15.578±2.332	***	3.723±0.557
Fe XIX	13.521	9.359±3.632	***	2.290±0.889
Fe XX	12.830	10.626±2.357	***	2.734±0.606
Fe XXI	12.285	5.678±1.140	***	1.539±0.309
Fe XXII	11.767	9.338±1.767	***	2.640±0.500
Fe XXIII	11.736	7.989±1.537	***	2.277±0.438
Fe XXIV	11.171	8.191±1.439	***	2.124±0.373

Table 6.77: Abundances derived for individual lines from the DEM calculated from iron lines for all mentioned AU Mic datasets combined.

6.4 UX Ari, an RS CVn system

RS CVn stars are a class of detached binaries typically composed of late-type (G or K), evolved stars. These systems rotate generally fast with typical orbital periods of several days. Tidal forces have coupled the rotational periods of the close components to the orbital period and thus the two stars rotate at high velocity. Consequently, these stars usually display a level of activity orders of magnitudes greater than solar, with strong chromospheric line emission and a high X-ray luminosity with a distinct tendency to flare. There is even evidence suggesting that the interaction between the two stellar magnetic fields may originate interbinary flares, interconnecting coronal loops or mass transfer. RS CVn systems often show strong rotational modulation due to large photospheric spots, the surfaces of their components can be mapped with Doppler imaging and Zeeman Doppler imaging techniques.

UX Ari is one of the best-studied RS CVn-type systems. It consists of a K0 IV and a G5 V component in a 6.44 day orbit. The orbital inclination is 60°, eclipses cannot occur. Spectroscopic measurements have additionally revealed the presence of a third component.

The X-ray luminosity of UX Ari is greater than 10^{31} erg s^{-1}. Considering its distance of 50.2 pc, this makes UX Ari – $6\overset{m}{.}47$ in m_V – to one of the brightest stellar X-ray sources in the sky. Extensive observations with previous X-ray observatories show that UX Ari is able to produce extremely strong flares. UX Ari is also one of the easiest targets for spatially resolved studies with Very Long Baseline Interferometry (VLBI) or the Very Large Baseline Array (VLBA).

Sanz-Forcada et al. (2002) calculate emission measures for UX Ari in quiescent and flaring states from XUV spectra obtained with *EUVE*. These emission measures show minima at 0.7 MK, 3 MK and 13 MK. Maxima are located at 2 MK and 8 MK. For temperatures higher than 20 MK their EM is not very well determined.

Audard et al. (2003) derive the coronal abundances of UX Ari from global fits to RGS data. They apply both APEC and MEKAL models and obtain slightly different results fro the two underlying spectral models. However, as a general trend an inverse FIP effect is clearly visible.

6.4.1 The HETGS dataset ObsID 605

The lightcurve of UX Ari obtained from this HETGS observation shown in Figure 6.23 shows no sign of variability, UX Ari was apparently caught in a state of quiescence. Ne X and O VIII are the two strongest lines in the corresponding MEG spectrum, both lines have approximately equal strength. The Ne IX and O VII triplets are also visible, as well as a relatively strong N VII line. Iron lines are rather inconspicuous and also the lines from the high-temperature ions at wavelengths shorter than 10 Å are barely visible, even in the HEG. The continuum underlying the emission lines has a moderate level of emissivity.

Five H-like to He-like ratios, of oxygen, neon, magnesium, silicon and sulfur, are available to determine the differential emission measure, polynomials up to the 4th order could be fitted, see Figure 6.24. Parabola, 3rd and 4th order polynomial show reasonable properties for an RS CVn system like UX Ari: Maxima are located at 7 MK, 9 MK and 8 MK respectively, at a high level of $\log DEM \approx 47$ cm^{-3} K^{-1}, comparable to Algol. Third and fourth order ratio fit show additional minima at 1 MK and 1.5 MK respectively, followed by a rise towards lower temperatures that are, like the minima themselves, definitely outside the valid temperature range for these fits. I would specify the lower boundary of the temperature confidence interval at 2 MK. The 4th order polynomial is somewhat narrower than the 3rd order polynomial.

The ratio fits provide values of reduced χ^2 between 1.7 and 2.4 and thus reproduce most of their input ratios well, the best-fit value is given by the simple parabola, see Table 6.78. Concerning the individual iron abundances derived from these fits (see Table 6.82), the higher values for Fe XXIII and Fe XXIV in 4th order indicate that the steep decay towards higher temperatures of

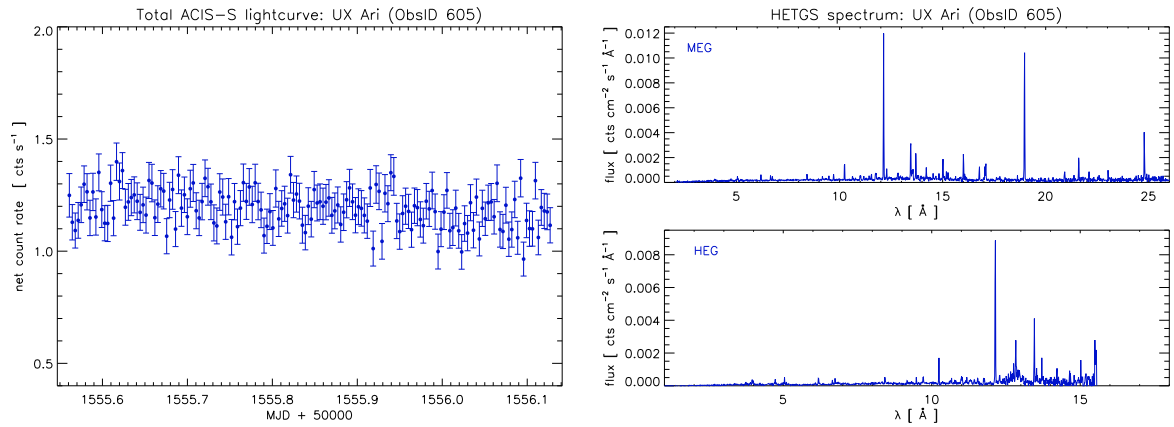

Figure 6.23: Lightcurve (left) and spectrum (right) of UX Ari from 12/13 January 2000 obtained with the HETGS onboard *Chandra*, the exposure time was 48.5 ks.

the 4th order fit starts at still too low temperatures.

The corresponding iron line fits give similar values of reduced χ^2, but they look very different and give only poor results concerning the reproduction of the measured ratios. The problem with the iron line fits is the normalization. The iron line fit parabola is broader than the one from the ratio fit, its maximum is at a similar temperature but the maximum level is lower. The 3rd and 4th order iron line fits have a shape very different from their ratio fit counterparts. They do not show the minimum, are much broader and flatten towards higher temperatures. Their temperature maxima agree with the ratio fits, but the maximum level is two orders of magnitude too low.

Thus the absolute abundances derived for these two polynomials (cf. Tables 6.84 and 6.83) are systematically too high by these two orders of magnitude. The parabola gives correspondingly lower values. The absolute abundances derived from the ratio fits given in Tables 6.82 and 6.81 also differ by certain multiplicative factors, but they have at least the correct order of magnitude.

Relative to oxygen however, as listed in Tables 6.79 and 6.80, all polynomials as well from the ratio fits as from the iron line fits show a very good agreement. Neon is clearly overabundant. The values from aluminium, sulfur and especially argon are somewhat questionable, probably they are systematically too high for the reasons discussed in Section 4.3.1. Apart from these two elements, the two-temperature component global fit nearly matches the absolute abundances deduced from the 2nd order ratio fit within the errors, indicating that the normalization is best for this fit. This simple 2T fit provides a relative good agreement with the values derived by Audard et al. (2003) from a 4T fit to the RGS dataset discussed below.

Converted to the solar photospheric reference values from Asplund et al., Audard et al. (2003) give absolute values with APEC and MEKAL models respectively of 1.1 and 1.75 for carbon, 2.17 and 3.47 for nitrogen, 0.67 and 1.04 for oxygen, 2.24 and 3.33 for neon, 0.24 and 0.34 for magnesium, 0.27 and 0.24 for silicon, 0.37 and 0.34 for sulfur, 1.94 and 2.39 for argon and 0.13 and 0.15 for iron, all with errors of approximately 10% to 20%. Relative to oxygen this results in 1.64 and 1.68 for carbon, 3.34 and 3.24 for nitrogen, 3.2 and 3.34 for neon, 0.32 and 0.36 for magnesium, 0.26 and 0.36 for silicon, 0.36 and 0.51 for sulfur, 2.39 and 2.89 for argon and 0.14 and 0.19 for iron.

A comparison of these values to the relative abundances I deduced from the *DEM* fits shows a satisfactory agreement. As mentioned above, sulfur and argon are probably too high in my measurements but additionally I obtain slightly higher neon and iron abundances.

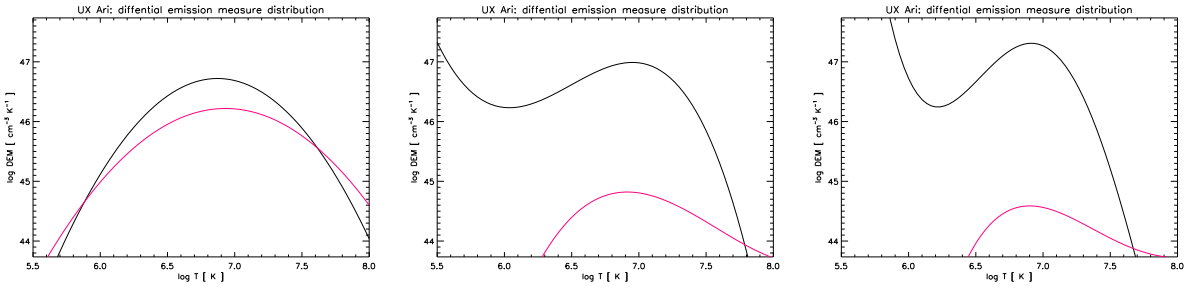

Figure 6.24: Differential emission measures for UX Ari modeled with 2nd to 4th order polynomials, calculated from the HETGS dataset 605.

	measured	2nd order	3rd order	4th order
O VIII / O VII	5.991±0.988	6.617 (6.719)	6.261 (11.678)	5.994 (16.854)
Ne X / Ne IX	3.438±0.334	2.875 (3.327)	3.072 (4.670)	3.348 (5.366)
Mg XII / Mg XI	1.666±0.197	1.919 (2.437)	1.949 (3.434)	1.820 (3.739)
Si XIV / Si XIII	1.403±0.229	1.277 (1.735)	1.155 (2.944)	1.144 (3.350)
S XVI / S XV	0.844±0.453	0.835 (1.223)	0.647 (2.999)	1.115 (3.684)
2-3 Å	1.439±0.144	1.439 (1.439)	1.439 (1.439)	1.439 (1.439)
red. χ^2		1.73 (1.78)	2.35 (2.02)	2.32 (2.40)

Table 6.78: Fit results from H-like to He-like ratios from the UX Ari HETGS dataset 605: Photon flux ratios and continuum flux [10^{-4} cts s^{-1} cm^{-2}] in specified wavelength bands. The corresponding results from the iron line fit are given in brackets.

abundance	2nd order	3rd order	4th order	2T fit
Ne / O	4.068±0.375	4.052±0.268	3.872±0.233	2.785
Mg / O	0.375±0.028	0.356±0.028	0.347±0.023	0.242
Al / O	1.183±0.263	1.137±0.253	1.180±0.262	0.380
Si / O	0.423±0.037	0.405±0.042	0.425±0.046	0.289
S / O	0.954±0.257	0.968±0.262	1.002±0.272	0.563
Ar / O	15.066±2.346	18.711±2.917	8.097±5.672	4.432
Fe / O	0.293±0.023	0.288±0.023	0.267±0.029	0.250

Table 6.79: Abundances relative to oxygen derived from the *DEM* calculated from H-like to He-like ratios and a corresponding global fit with two temperature components for the UX Ari HETGS dataset 605.

abundance	2nd order	3rd order	4th order	2T fit
Ne / O	4.119±0.248	3.902±0.702	3.770±0.929	2.785
Mg / O	0.332±0.053	0.275±0.081	0.257±0.087	0.242
Al / O	0.930±0.207	0.704±0.179	0.649±0.181	0.380
Si / O	0.332±0.035	0.239±0.079	0.217±0.084	0.289
S / O	0.642±0.175	0.329±0.204	0.276±0.195	0.563
Ar / O	7.517±2.521	2.031±1.797	1.603±1.525	4.432
Fe / O	0.314±0.018	0.366±0.050	0.378±0.068	0.250

Table 6.80: Abundances relative to oxygen derived from the *DEM* calculated iron lines and a corresponding global fit with two temperature components for the UX Ari HETGS dataset 605.

element	2nd order	3rd order	4th order	2T fit
O	0.809±0.034	0.473±0.020	0.276±0.012	1.096
Ne	3.291±0.269	1.916±0.097	1.069±0.046	3.052
Mg	0.304±0.018	0.168±0.011	0.096±0.005	0.265
Al	0.957±0.209	0.538±0.117	0.326±0.071	0.417
Si	0.342±0.027	0.192±0.018	0.117±0.012	0.317
S	0.772±0.205	0.458±0.123	0.277±0.074	0.617
Ar	12.188±1.826	8.849±1.327	2.235±1.563	4.858
Fe	0.237±0.016	0.136±0.009	0.074±0.007	0.274

Table 6.81: Absolute abundances derived from the *DEM* calculated from H-like to He-like ratios and a corresponding global fit with two temperature components for the UX Ari HETGS dataset 605.

element	wavelength	2nd order	3rd order	4th order
O VII	21.602	0.888±0.141	0.493±0.078	0.276±0.044
O VIII	18.970	0.804±0.036	0.472±0.021	0.276±0.012
Ne IX	13.447	2.911±0.243	1.770±0.148	1.048±0.088
Ne X	12.134	3.482±0.173	1.981±0.098	1.076±0.053
Mg XI	9.1688	0.339±0.034	0.190±0.019	0.102±0.010
Mg XII	8.4210	0.294±0.018	0.162±0.010	0.094±0.006
Al XIII	7.1730	0.957±0.209	0.538±0.117	0.326±0.071
Si XIII	6.6480	0.322±0.043	0.171±0.023	0.104±0.014
Si XIV	6.1830	0.354±0.034	0.208±0.020	0.128±0.012
S XV	5.0387	0.768±0.269	0.419±0.147	0.321±0.112
S XVI	4.7300	0.777±0.316	0.547±0.222	0.243±0.099
Ar XVII	3.9488	13.488±2.626	8.188±1.594	8.072±1.572
Ar XVIII	3.7330	10.971±2.541	10.342±2.395	1.817±0.421
Fe XVII	15.015	0.195±0.015	0.116±0.009	0.061±0.005
Fe XVII	17.075	0.234±0.016	0.140±0.010	0.074±0.005
Fe XVII	15.262	0.272±0.039	0.163±0.023	0.085±0.012
Fe XVII	16.777	0.214±0.026	0.129±0.015	0.068±0.008
Fe XVIII	14.205	0.300±0.035	0.168±0.020	0.084±0.010
Fe XIX*	13.521	0.591±0.069	0.315±0.037	0.161±0.019
Fe XX	12.830	0.252±0.126	0.130±0.065	0.071±0.035
Fe XXI	12.285	0.228±0.023	0.115±0.011	0.069±0.007
Fe XXII	11.767	0.317±0.038	0.161±0.019	0.112±0.014
Fe XXIII	11.736	0.315±0.063	0.170±0.034	0.146±0.029
Fe XXIV	11.171	0.390±0.042	0.245±0.026	0.277±0.030

Table 6.82: Abundances derived for individual lines from the *DEM* calculated from H-like to He-like ratios for the UX Ari HETGS dataset 605.

element	2nd order	3rd order	4th order	2T fit
O	2.259±0.096	50.954±6.637	88.836±***	1.096
Ne	9.303±0.397	***	***	3.052
Mg	0.749±0.115	14.017±3.708	22.859±6.593	0.265
Al	2.100±0.458	35.851±7.828	57.663±***	0.417
Si	0.749±0.073	12.196±3.698	19.237±6.638	0.317
S	1.450±0.392	16.769±***	24.491±***	0.617
Ar	16.980±5.647	***	***	4.858
Fe	0.709±0.029	18.664±0.751	33.572±1.343	0.274

Table 6.83: Absolute abundances derived from the *DEM* calculated from iron lines and a corresponding global fit with two temperature components for the UX Ari HETGS dataset 605.

element	wavelength	2nd order	3rd order	4th order
O VII	21.602	2.516±0.400	97.480±***	***
O VIII	18.970	2.243±0.099	50.007±2.209	87.304±3.856
Ne IX	13.447	9.083±0.759	***	***
Ne X	12.134	9.386±0.465	***±9.324	***
Mg XI	9.1688	1.027±0.104	26.656±2.700	47.326±4.794
Mg XII	8.4210	0.702±0.043	12.929±0.792	21.082±1.292
Al XIII	7.1730	2.100±0.458	35.851±7.828	57.663±***
Si XIII	6.6480	0.874±0.116	22.904±3.029	41.109±5.436
Si XIV	6.1830	0.707±0.068	10.919±1.046	17.222±1.650
S XV	5.0387	1.786±0.626	47.767±***	87.403±***
S XVI	4.7300	1.233±0.502	13.451±5.475	20.031±8.153
Ar XVII	3.9488	26.177±5.096	***	***
Ar XVIII	3.7330	13.513±3.129	89.535±***	***
Fe XVII	15.015	0.626±0.049	16.473±1.301	29.560±2.334
Fe XVII	17.075	0.751±0.052	19.884±1.381	35.909±2.493
Fe XVII	15.262	0.874±0.126	23.023±3.312	41.354±5.949
Fe XVII	16.777	0.688±0.082	18.222±2.174	32.913±3.926
Fe XVIII	14.205	0.947±0.112	24.072±2.851	41.846±4.956
Fe XIX*	13.521	1.809±0.211	45.949±5.356	79.936±9.318
Fe XX	12.830	0.740±0.369	19.025±9.488	33.530±***
Fe XXI	12.285	0.631±0.063	16.523±1.642	29.681±2.950
Fe XXII	11.767	0.814±0.098	21.785±2.629	39.976±4.824
Fe XXIII	11.736	0.711±0.141	19.353±3.849	36.092±7.178
Fe XXIV	11.171	0.709±0.076	18.574±1.980	33.195±3.539

Table 6.84: Abundances derived for individual lines from the *DEM* calculated from iron lines for the UX Ari HETGS dataset 605.

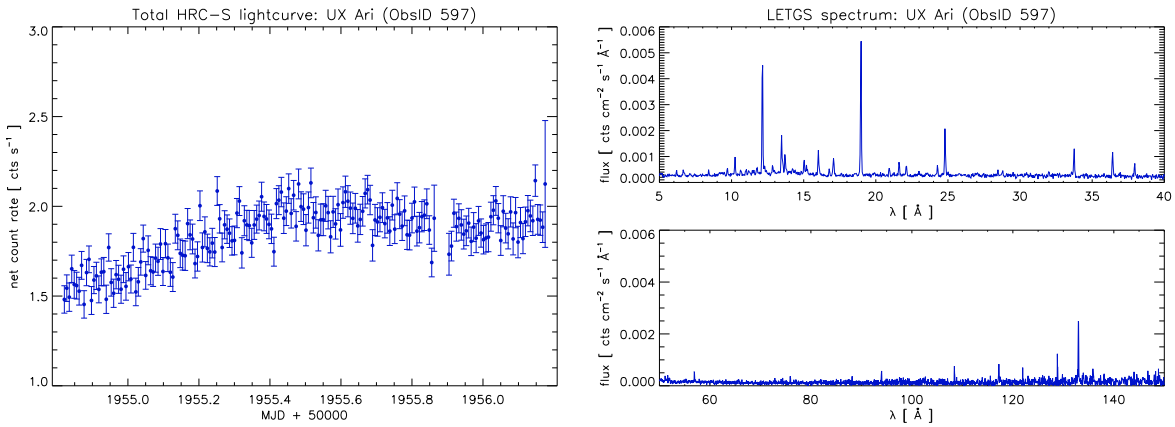

Figure 6.25: Lightcurve (left) and spectrum (right) of UX Ari obtained from 14 to 16 February 2001 with the LETGS onboard *Chandra*. Binsize of the lightcurve is 600 s with a total exposure time of 112.8 ks.

6.4.2 The LETGS dataset ObsID 597

Though quite long exposed, the LETGS spectrum of UX Ari shows again no sign of flaring activity. A slow rise in the countrate is however visible during the first half of the observation, see the lightcurve in the left panel of Figure 6.25. The corresponding spectrum in the right panel compares in the short wavelength part well with the MEG spectrum. The high-temperature iron lines in the long wavelength part are relatively weak.

Ness et al. (2002b) discussed among others this dataset. Their analysis was focused on density diagnostics but additionally they used H-like to He-like ratios for a simple temperature estimate.

Only one of the polynomials fitted to this dataset provides reasonable results. The parabola obtained from the H-like to He-like ratios provides a very poor fit (see Table 6.85), it is much too broad and peaks at $\log T = 5.9$, very much too low for an active RS CVn system like UX Ari. The fit improved a lot in 3rd order, the reconstructed DEM is much narrower and has its maximum at 8 MK, cf. Figure 6.26. An additional minimum more than one order of magnitude lower than the maximum $\log DEM \approx 47.5$ cm^{-3} K^{-1} is located at 1.3 MK; these low temperatures are barely covered by the measured carbon ratio. The 4th order polynomial is even narrower, with steeper slopes and the minimum shifted to 2 MK. This polynomial provides the best-fit result, and reproduces the measured ratios best.

The polynomials obtained from the iron lines are narrow right from start with the parabola. It peaks at 10 MK with the appropriate level of $\log DEM \approx 47.5$ cm^{-3} K^{-1}, but the ratios are only very poorly reproduced. While iron line fit parabola and 3rd order ratio fit have approximately the same width, the 3rd order iron line fit gives again an even narrower DEM. The 4th order fit looks nearly identical. Contrary to the 3rd and 4th order ratio fit, the corresponding iron line fits do not show the minimum and the rise towards lower temperatures. Differential emission measures with such a simple, parabola-like shape can apparently not reproduce the H-like to He-like ratios although the high-temperature slope of both 4th order fits are almost identical.

The abundances derived from this dataset are thus somewhat difficult to evaluate. The elements also available in the HETGS dataset show a general agreement (within the errors) in the values relative to oxygen derived from the 3rd and 4th order ratio fits. Iron gives a smaller value, matching the results from Audard et al. (2003) better. The values obtained from the 2nd order ratio fit are definitely not trustworthy due to the poor quality of the fit, nevertheless they confirm a general trend of enhanced values for nitrogen (cf. Schmitt and Ness, 2002) and neon. As for the global fit to this dataset, the thus obtained results also show this tendency.

With reservations the same applies for the relative values obtained from the iron line fits,

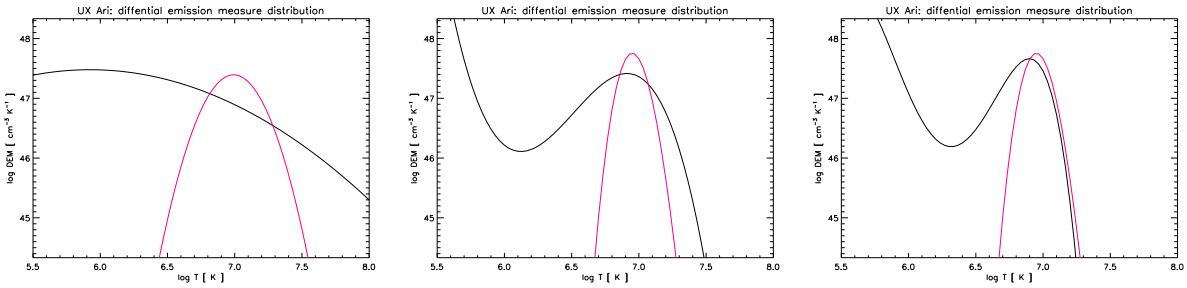

Figure 6.26: Differential emission measures for UX Ari modeled with 2nd to 4th order polynomials, calculated from the LETGS dataset 597.

	measured	2nd order	3rd order	4th order
C VI / C V	1.440±0.244	3.073 (***)	1.415 (***)	1.469 (***)
N VII / N VI	8.332±1.775	2.366 (52.835)	12.434 (***)	7.180 (***)
O VIII / O VII	9.712±0.898	2.062 (28.648)	8.782 (***)	10.256 (***)
Ne X / Ne IX	3.161±0.114	1.587 (5.446)	2.995 (***)	3.113 (***)
Si XIV / Si XIII	0.266±0.103	1.273 (0.886)	0.680 (***)	0.376 (***)
19.5-20.5 Å	8.782±1.756	8.782 (8.782)	8.782 (8.782)	8.782 (8.782)
red. χ^2		138.43 (24.68)	12.41 (23.96)	2.13 (26.36)

Table 6.85: Fit results from H-like to He-like ratios from the UX Ari LETGS dataset 597: Photon flux ratios and continuum flux [10^{-4} cts s^{-1} cm^{-2}] in specified wavelength bands. The corresponding results from the iron line fit are given in brackets.

although the low-FIP elements silicon and magnesium have systematically lower values, while iron is much too high. By and large, all the relative values obtained from the global fits and the best-fit polynomials match the values of Audard et al. (2003), confirming the finding of a distinct inverse FIP effect.

The absolute values however are more problematic. While the ratio fits show a typical scatter due to normalization, the iron line fits provide much too low values. The iron line fits are actually just as untrustworthy as the 2nd order ratio fit.

element	2nd order	3rd order	4th order	2T fit
C	0.126±0.026	0.307±0.019	0.240±0.015	0.832
N	0.552±0.247	1.231±0.081	1.081±0.045	2.756
O	0.168±0.103	0.291±0.006	0.257±0.004	0.748
Ne	1.195±0.416	1.057±0.026	0.873±0.014	1.985
Mg	0.141±0.019	0.081±0.011	0.077±0.010	0.148
Si	0.155±0.129	0.131±0.054	0.151±0.018	0.201
Fe	0.048±0.012	0.035±0.007	0.025±0.006	0.075

Table 6.86: Absolute abundances derived from the DEM calculated from H-like to He-like ratios and from a global fit with two temperature components for the UX Ari LETGS dataset 597.

element	2nd order	3rd order	4th order	2T fit
C / O	0.747±0.484	1.056±0.068	0.936±0.059	1.112
N / O	3.282±2.494	4.230±0.289	4.210±0.190	3.684
Ne / O	7.109±5.012	3.631±0.114	3.398±0.080	2.654
Mg / O	0.837±0.526	0.277±0.037	0.299±0.040	0.198
Si / O	0.921±0.950	0.450±0.185	0.589±0.072	0.269
Fe / O	0.283±0.188	0.122±0.023	0.097±0.023	0.100

Table 6.87: Abundances relative to oxygen derived from the DEM calculated from H-like to He-like ratios and a corresponding global fit with two temperature components for the UX Ari LETGS dataset 597.

element	wavelength	2nd order	3rd order	4th order
C V	40.268	0.257±0.040	0.303±0.047	0.244±0.038
C VI	33.737	0.120±0.008	0.308±0.020	0.240±0.016
N VI	28.787	0.207±0.043	1.821±0.380	0.939±0.196
N VII	24.782	0.729±0.031	1.220±0.052	1.089±0.046
O VII	21.602	0.056±0.005	0.264±0.024	0.271±0.025
O VIII	18.970	0.263±0.005	0.292±0.005	0.256±0.005
Ne IX	13.447	0.855±0.026	1.018±0.031	0.863±0.027
Ne X	12.134	1.703±0.032	1.074±0.020	0.876±0.017
Mg XII	8.4210	0.141±0.019	0.081±0.011	0.077±0.010
Si XIII	6.6480	0.366±0.046	0.178±0.022	0.160±0.020
Si XIV	6.1830	0.076±0.028	0.070±0.025	0.113±0.041
Fe XVII	15.015	0.056±0.004	0.041±0.003	0.029±0.002
Fe XVII	17.075	0.012±0.002	0.009±0.002	0.007±0.001
Fe XVII	15.262	0.116±0.012	0.087±0.009	0.062±0.006
Fe XVIII	14.205	0.055±0.010	0.027±0.005	0.018±0.003
Fe XVIII	93.923	0.113±0.010	0.064±0.006	0.043±0.004
Fe XIX	13.521	0.259±0.019	0.105±0.008	0.073±0.005
Fe XIX	108.35	0.164±0.016	0.070±0.007	0.048±0.005
Fe XX	121.84	0.085±0.013	0.033±0.005	0.025±0.004
Fe XX	118.68	0.081±0.023	0.032±0.009	0.024±0.007
Fe XX	12.830	0.131±0.015	0.051±0.006	0.041±0.005
Fe XXI	128.75	0.104±0.013	0.041±0.005	0.039±0.005
Fe XXI	117.50	0.113±0.040	0.045±0.016	0.042±0.015
Fe XXII	117.15	0.108±0.011	0.049±0.005	0.063±0.006
Fe XXII	135.79	0.095±0.017	0.043±0.008	0.056±0.010
Fe XXIII	132.90	0.116±0.006	0.073±0.004	0.145±0.008

Table 6.88: Abundances derived for individual lines from the DEM calculated from H-like to He-like ratios for the UX Ari LETGS dataset 597.

element	2nd order	3rd order	4th order	2T fit
C	0.516±0.217	0.000	0.000	0.832
N	1.982±0.338	0.000	0.000	2.756
O	0.454±0.058	0.000	0.000	0.748
Ne	1.438±0.304	0.000	0.000	1.985
Mg	0.075±0.010	0.000	0.000	0.148
Si	0.106±0.061	0.000	0.000	0.201
Fe	0.048±0.006	0.034±0.004	0.034±0.004	0.075

Table 6.89: Absolute abundances derived from the DEM calculated from iron lines and a corresponding global fit with two temperature components for the UX Ari LETGS dataset 597.

abundance	2nd order	3rd order	4th order	2T fit
C / O	1.137±0.500	0.934±0.437	0.934±0.437	1.112
N / O	4.365±0.929	3.779±1.066	3.779±1.066	3.684
Ne / O	3.165±0.781	2.869±1.848	2.869±1.848	2.654
Mg / O	0.165±0.030	0.126±0.030	0.126±0.030	0.198
Si / O	0.232±0.137	0.035±0.101	0.035±0.101	0.269
Fe / O	0.106±0.020	***	***	0.100

Table 6.90: Abundances relative to oxygen derived from the DEM calculated from iron lines and a corresponding global fit with two temperature components for the UX Ari LETGS dataset 597.

element	wavelength	2nd order	3rd order	4th order
C V	40.268	53.432±8.325	0.160±0.025	0.160±0.025
C VI	33.737	0.516±0.034	0.000	0.000
N VI	28.787	12.501±2.610	0.045±0.009	0.045±0.009
N VII	24.782	1.971±0.084	0.000	0.000
O VII	21.602	1.328±0.121	0.006±0.001	0.006±0.001
O VIII	18.970	0.450±0.008	0.000	0.000
Ne IX	13.447	2.291±0.070	0.013±0.000	0.013±0.000
Ne X	12.134	1.329±0.025	0.000	0.000
Mg XII	8.4210	0.075±0.010	0.000	0.000
Si XIII	6.6480	0.175±0.022	0.000	0.000
Si XIV	6.1830	0.053±0.019	0.000	0.000
Fe XVII	15.015	0.078±0.005	0.056±0.004	0.056±0.004
Fe XVII	17.075	0.018±0.004	0.014±0.003	0.014±0.003
Fe XVII	15.262	0.166±0.017	0.120±0.012	0.120±0.012
Fe XVIII	14.205	0.037±0.006	0.022±0.004	0.022±0.004
Fe XVIII	93.923	0.099±0.009	0.062±0.006	0.062±0.006
Fe XIX	13.521	0.118±0.009	0.069±0.005	0.069±0.005
Fe XIX	108.35	0.085±0.008	0.049±0.005	0.049±0.005
Fe XX	121.84	0.034±0.005	0.021±0.003	0.021±0.003
Fe XX	118.68	0.032±0.009	0.020±0.006	0.020±0.006
Fe XX	12.830	0.050±0.006	0.032±0.004	0.032±0.004
Fe XXI	128.75	0.037±0.005	0.028±0.004	0.028±0.004
Fe XXI	117.50	0.041±0.014	0.031±0.011	0.031±0.011
Fe XXII	117.15	0.040±0.004	0.042±0.004	0.042±0.004
Fe XXII	135.79	0.035±0.006	0.037±0.007	0.037±0.007
Fe XXIII	132.90	0.054±0.003	0.034±0.002	0.034±0.002

Table 6.91: Abundances derived for individual lines from the DEM calculated from iron lines for the UX Ari LETGS dataset 597.

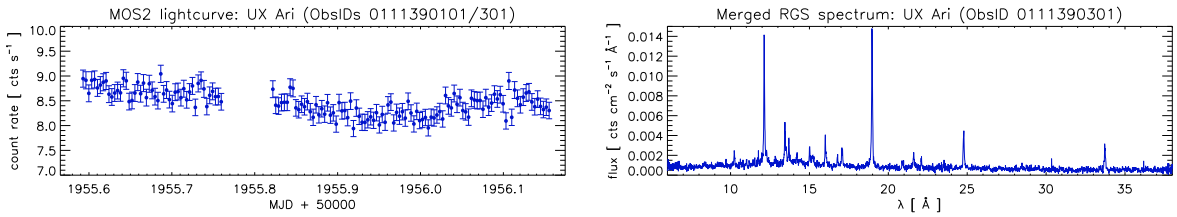

Figure 6.27: Lightcurve (left) and spectrum (right) of UX Ari from 15/16 February 2001 obtained with EPIC-MOS and RGS onboard *XMM* respectively. The spectrum is obtained exclusively from the dataset 0111390301 while the lightcurve shows additionally to the 28.5 ks in MOS 2 from observation 0111390301 also the data from the preceding observation 0111390101 providing additional 14.5 ks of exposure time.

6.4.3 The RGS dataset ObsID 0111390301

The three *XMM* observations 0111390201, 0111390301 and 0111390301 targetting UX Ari with 9.4 ks, 16.0 ks and 30.9 ks of RGS exposure time respectively have been conducted simultaneously to the *Chandra* LETGS observation of UX Ari discussed below, probably for cross-calibrational reasons. Surprisingly I could not find studies making explicitly use of this fact in the literature. Proceeding during the second half of the LETGS observation, the lightcurve of the *XMM* datasets is just as flat as the LETGS lightcurve, and the only differences in the spectra are due to the different pseudo-continua.

I concentrated my analysis on the dataset 0111390301 that has the longest exposure time. As mentioned above Audard et al. (2003) applied this dataset in their study of several RS CVn systems and derived abundances from global fits with four temperature components. The higher-temperature lines of silicon and magnesium where not measurable in this dataset, as well as the N VI line. Thus only two ratios are available to assess the DEM, and only 2nd and 3rd order polynomials could be fitted. The fit and its reduced χ^2 are therefore dominated by the three continuum measurements. There also only five iron lines available (see Table 6.95), four of them are from Fe XVII. Both fitting approaches are thus not well-determined. Nevertheless I conducted the fitting.

The two parabolas obtained from ratio and iron line fit are almost identical. They peak at 7 MK, at a reasonable level matching the previous fits. In third order, the polynomial from the ratio fit representing the DEM becomes somewhat narrower, with a slight shift of the maximum towards lower temperatures. The corresponding iron line develops a much different shape. An extremely deep minimum at 4 MK is followed by a maximum at 20 MK, resulting in a very narrow parabola-like DEM in the valid temperature range determined basically by Fe XVII.

Such a DEM is definitely not compatible with the lines from other elements, and as it can be seen from Tables 6.92 to 6.95, it provides only nonsense values for the abundances and ratios. The values derived from the other three fits compare very well with the previous measurements. The only outlier is iron that is much lower. In general, the reliable fits from all datasets for UX Ari provide absolute abundances of approximately 0.3 for carbon, 1.1 for nitrogen, 0.25 for oxygen, 1.0 for neon, 0.1 for magnesium and 0.2 for silicon; they are smaller by a factor of ≈ 3 compared to the values derived by Audard et al. (2003). Relative to oxygen there is however a good agreement.

	measured	2nd order	3rd order
O VIII / O VII	7.690±0.878	7.334 (7.433)	7.603 (0.000)
Ne X / Ne IX	2.484±0.368	2.779 (2.834)	2.574 (0.000)
3-4 Å	5.326±0.533	5.541 (5.464)	5.522 (5.288)
2-3 Å	3.335±0.334	3.180 (3.196)	3.147 (3.375)
1-2 Å	1.019±0.204	1.028 (1.071)	1.077 (0.998)
red. χ^2		0.59 (1.26)	0.60 (1.29)

Table 6.92: Fit results from H-like to He-like ratios from the UX Ari RGS dataset 0111390301: Photon flux ratios and continuum flux [10^{-4} cts s^{-1} cm^{-2}] in specified wavelength bands. The corresponding results from the iron line fit are given in brackets.

element	2nd order	3rd order	2T fit
C	0.310±0.019 (0.340±0.021)	0.258±0.016 (0.000)	1.145
N	1.130±0.055 (1.240±0.060)	0.925±0.045 (0.000)	4.644
O	0.280±0.014 (0.308±0.015)	0.227±0.011 (0.000)	1.175
Ne	1.067±0.063 (1.166±0.069)	0.866±0.051 (0.000)	3.182
Fe	0.045±0.005 (0.050±0.006)	0.034±0.004 (***)	0.204

Table 6.93: Absolute abundances derived from the *DEM* calculated from H-like to He-like ratios and a corresponding global fit with two temperature components for the UX Ari RGS dataset 0111390301. The corresponding results from the iron line fit are given in brackets.

abundance	2nd order	3rd order	2T fit
C / O	1.109±0.089 (1.104±0.088)	1.136±0.091 (***)	0.974
N / O	4.041±0.282 (4.026±0.281)	4.069±0.284 (***)	3.952
Ne / O	3.818±0.295 (3.786±0.292)	3.806±0.294 (***)	2.708
Fe / O	0.160±0.020 (0.162±0.020)	0.148±0.018 (***)	0.173

Table 6.94: Abundances relative to oxygen derived from the *DEM* calculated from H-like to He-like ratios and a corresponding global fit with two temperature components for the UX Ari RGS dataset 0111390301. The corresponding results from the iron line fit are given in brackets.

element	wavelength	2nd order	3rd order
C VI	33.737	0.310±0.019 (0.340±0.021)	0.258±0.016 (0.000±0.000)
N VII	24.782	1.130±0.055 (1.240±0.060)	0.925±0.045 (0.000±0.000)
O VII	21.602	0.270±0.027 (0.300±0.030)	0.226±0.022 (0.000±0.000)
O VIII	18.970	0.283±0.016 (0.311±0.018)	0.228±0.013 (0.000±0.000)
Ne IX	13.447	1.171±0.156 (1.301±0.173)	0.891±0.118 (0.000±0.000)
Ne X	12.134	1.047±0.069 (1.141±0.075)	0.860±0.056 (0.076±0.005)
Fe XVII	15.015	0.038±0.007 (0.043±0.007)	0.029±0.005 (***±***)
Fe XVII	17.075	0.054±0.010 (0.060±0.012)	0.041±0.008 (***±***)
Fe XVII	15.262	0.072±0.020 (0.080±0.023)	0.054±0.015 (***±***)
Fe XVII	16.777	0.044±0.009 (0.049±0.010)	0.033±0.007 (***±***)
Fe XIX	13.521	0.095±0.018 (0.104±0.020)	0.077±0.015 (15.939±3.053)

Table 6.95: Abundances derived for individual lines from the *DEM* calculated from iron lines for the UX Ari RGS dataset 0111390301. The corresponding results from the iron line fit are given in brackets.

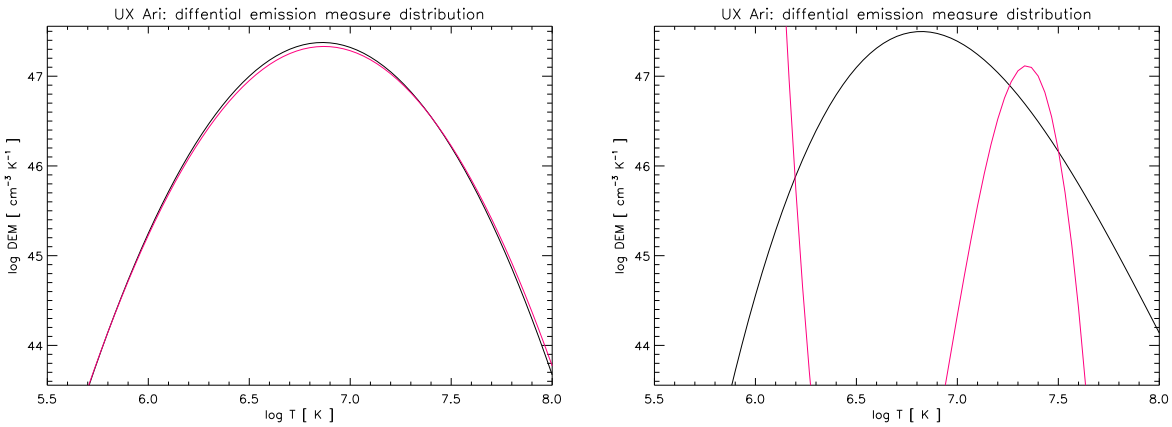

Figure 6.28: Differential emission measures for UX Ari modeled with 2nd and 3rd order polynomials, calculated from the RGS dataset 0111390301.

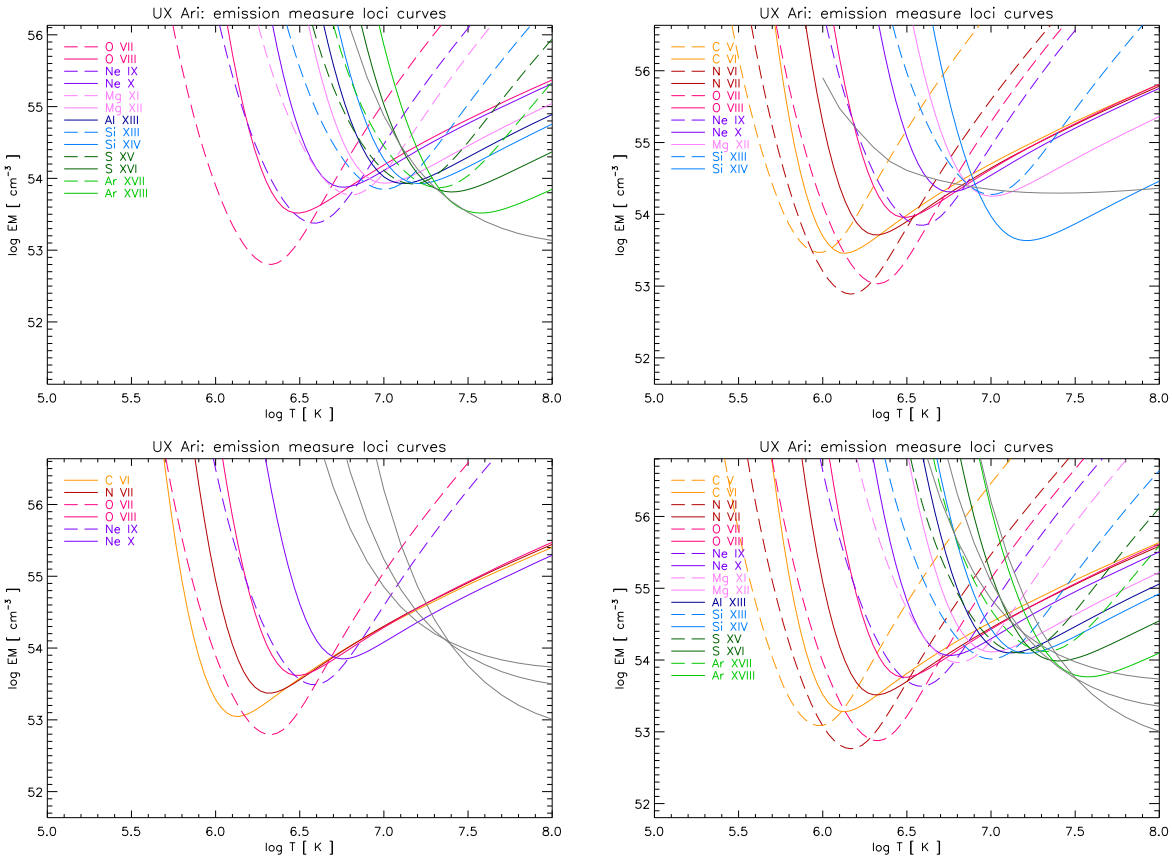

Figure 6.29: Shapes of emission measure distributions constructed from the best-fit $DEMs$ and abundances as a lower limit from the mission measure loci curves for UX Ari. From upper left to lower right: The best-fit polynomial from the HETGS, the LETGS, the RGS and all datasets combined.

6.4.4 Combined datasets

It is a little bit surprising that a well-known active RS CVn system like UX Ari showed no flaring activity during both the LETGS/RGS and the HETGS observations. Thus any of the X-ray datasets discussed here caught UX Ari in a state of quiescence. While the advantages of a combination of the LETGS and RGS datasets are obvious (a merging of the data from these simultaneous observations does not differ from the parallel treatment of HEG and MEG data and will definitely increase the quality of the fit), this allows also to add the HETGS dataset. Such an approach is affirmed by the similar relative abundances derived for the individual datasets.

The thus combined input data allows the fitting of polynomials up to the 7th order, and the results are much more promising than those obtained from the individual observations. Figure 6.30 shows the polynomials obtained from these fits. From the LETGS dataset the 2nd and 3rd order fits ratio inherit the tendency to produce a broad DEM with a maximum at low temperatures (≈ 2 MK). In 4th, 5th and 6th order, the shape of the polynomials from the ratio fits is similar to the 3rd and 4th order ratio fits from the HETGS datasets. The maximum is formed at 8 MK, and a minimum at 1.4 MK approximately an order of magnitude lower than the maximum of $\log DEM \approx 47.5$ cm^{-3} K^{-1} is added. Since the fit is calculated from ratios ranging from the low-temperature carbon to the high-temperature sulfur, the reconstructed DEM is reliable from the minimum on. Again similar to the HETGS dataset, maximum and minimum are more pronounced with higher order N. The 7th order polynomial finally develops a low-temperature minimum at 0.7 MK that is however outside the confidence range in temperature. Another maximum is formed in the high-temperature region. The initial maximum shifts to 6.5 MK and the new, smaller maximum forms at 25 MK. The initial minimum shifts to 2 MK, and another minimum forms between the two maxima at 15 MK. It is questionable if the rise towards lower temperatures following the first minimum is real, although it is now well-covered by the carbon, nitrogen and oxygen lines.

The iron line fits seem to go ahead concerning the reproduction of certain structures in the DEM with increasing order. The parabola already peaks at 7 MK and is much narrower than its counterpart from the ratio fit. The 3rd order iron line fit starts forming a minimum at lower temperatures (≈ 0.6 MK). In 4th and 5th order, the iron line fit produces a polynomial with two maxima located at 7 MK an 28 MK and a minimum at 15 MK. Ignoring the low temperature part where no iron lines to determine the DEM are available, these $DEMs$ resemble the one from 7th order ratio fit very much. The 6th and 7th order polynomials from the iron line fit unfortunately start oscillating. A third maximum forms, and maxima and minima tear orders of magnitude apart combined with very steep slopes. Such a DEM would definitely be unphysical.

The very good agreement between the independently reconstructed $DEMs$ from the 4th order iron line fit and from the 7th order ratio fit is a clear evidence for the reliability of the structures shown by the two corresponding polynomials. Additionally these two polynomials provide each the best-fit results from the ratio and iron line fits (see Tables 6.96 and 6.100). However, while the higher order ratio fits reproduce the measured ratios very well, the iron line fits suffer from missing emission measure at lower temperatures and thus cannot reproduce the ratios from carbon to magnesium. The thus arising discrepancies can easily be recognized from abundances derived for the individual lines in Table 6.103.

The averaged absolute abundances derived from the ratio fits (Table 6.97) differ again in their normalization, but in general the derived values are lower than those derived by Audard et al. (2003) by factors ranging from 3 to 6. The values relative to oxygen in Table 6.98 though show a good agreement as do the individual datasets contributing to the combined input data. Similar considerations apply to the abundances derived from the iron line fits. Despite of the poor reproduction of the low-temperature ratios, the averaged abundances of the corresponding elements are in good agreement with the values from the ratio fit. My measurements clearly

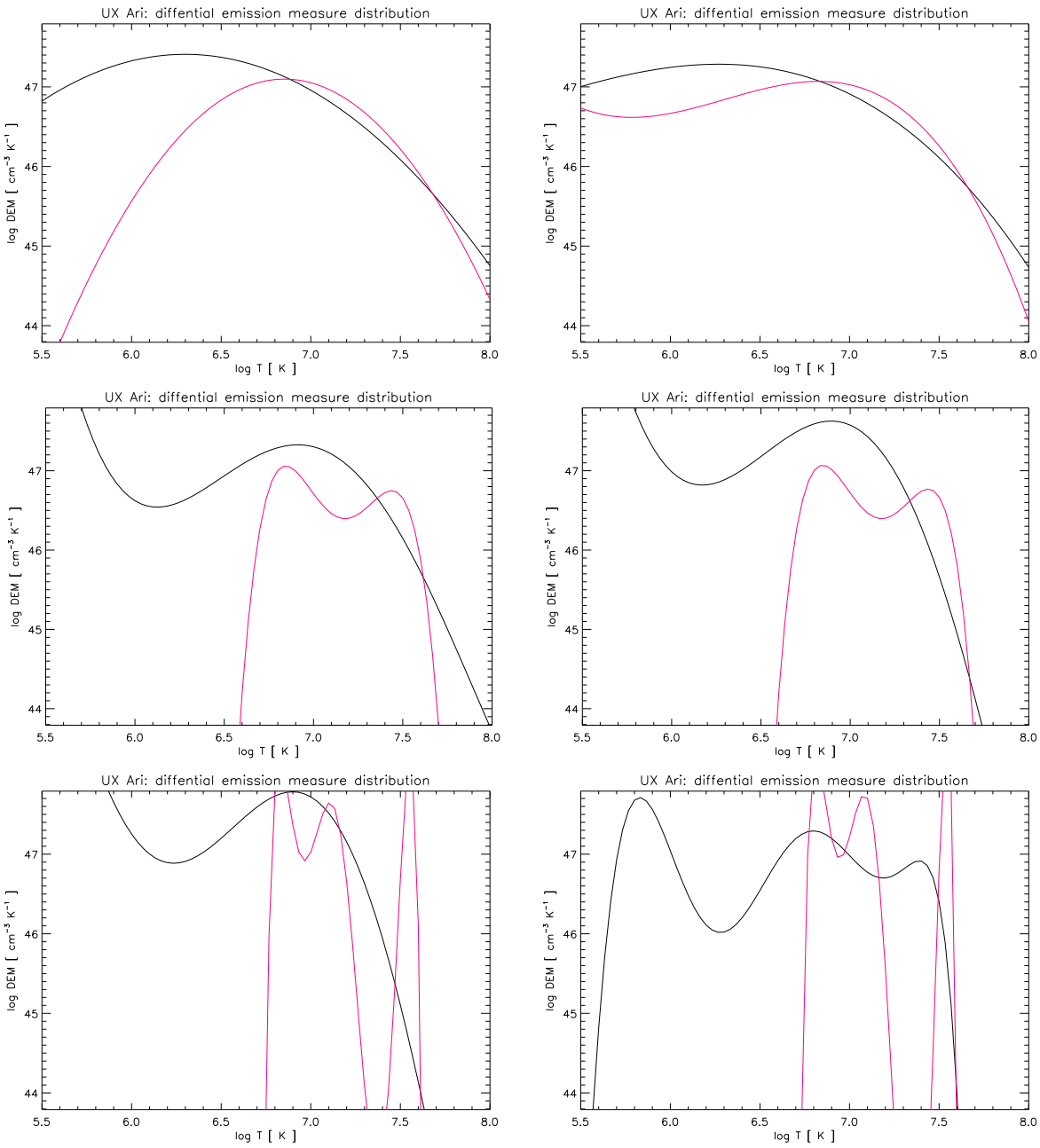

Figure 6.30: Differential emission measures for UX Ari modeled with 2nd to 7th order polynomials, calculated from all available datasets combined.

confirm an inverse FIP effect for UX Ari.

Emission measures reconstructed from the best-fit DEM (Figure 6.29) of the combined input data as well as from HETGS and LETGS confirm the maximum at $\log T = 6.9$ derived by Sanz-Forcada et al. (2002). Above 10 MK their EM is only poorly determined, so that no concluding confirmation or rejection of the second maximum found from the combined data can be given.

	measured	2nd order	3rd order	4th order	5th order	6th oder	7th oder
C VI / C V	2.311±0.528	3.996	3.860	2.304	2.294	2.283	2.313
N VII / N VI	7.033±1.424	2.769	2.835	7.990	7.904	7.553	7.017
O VIII / O VII	8.797±1.405	2.247	2.379	6.432	6.731	7.484	8.847
Ne X / Ne IX	2.910±0.354	1.537	1.670	2.944	2.978	3.110	2.869
Mg XII / Mg XI	1.606±0.186	1.290	1.416	1.807	1.752	1.688	1.637
Si XIV / Si XIII	1.403±0.229	1.040	1.131	1.081	1.143	1.078	1.344
S XVI / S XV	0.844±0.453	0.791	0.848	0.630	1.094	1.193	1.016
3-4 Å	5.326±0.533	3.993	4.010	5.231	5.303	5.315	5.234
2-3 Å	2.387±0.948	2.839	2.870	2.990	2.651	2.464	3.206
1-2 Å	1.019±0.204	1.499	1.493	1.009	1.005	1.019	0.967
red. χ^2		10.49	10.78	1.42	1.22	1.38	0.55

Table 6.96: Fit results from H-like to He-like ratios from all UX Ari datasets combined: Photon flux ratios and continuum flux [10^{-4} cts s^{-1} cm^{-2}] in specified wavelength bands.

element	2nd order	3rd order	4th order	5th order	6th ode	7th order
C	0.140±0.022	0.178±0.026	0.270±0.021	0.142±0.011	0.110±0.009	0.365±0.029
N	0.470±0.215	0.606±0.269	1.118±0.085	0.594±0.045	0.470±0.036	1.630±0.124
O	0.101±0.074	0.133±0.093	0.253±0.035	0.137±0.016	0.111±0.008	0.388±0.025
Ne	1.240±0.337	1.500±0.345	1.021±0.042	0.536±0.022	0.408±0.017	1.364±0.057
Mg	0.144±0.014	0.161±0.009	0.080±0.004	0.044±0.002	0.034±0.002	0.117±0.006
Al	0.566±0.124	0.596±0.130	0.277±0.061	0.155±0.034	0.124±0.027	0.404±0.088
Si	0.192±0.028	0.206±0.022	0.098±0.013	0.056±0.006	0.044±0.006	0.141±0.011
S	0.471±0.125	0.484±0.128	0.240±0.064	0.131±0.035	0.105±0.028	0.293±0.078
Ar	7.379±1.111	7.244±1.230	4.664±0.698	1.109±0.744	0.749±0.586	4.391±0.657
Fe	0.078±0.008	0.093±0.008	0.052±0.004	0.030±0.002	0.023±0.002	0.079±0.006

Table 6.97: Absolute abundances derived from the DEM calculated from H-like to He-like ratios for all mentioned UX Ari datasets combined.

element	2nd order	3rd order	4th order	5th order	6th oder	7th oder
C / O	1.394±1.049	1.339±0.959	1.066±0.168	1.040±0.145	0.993±0.103	0.941±0.095
N / O	4.671±4.053	4.569±3.793	4.415±0.692	4.348±0.602	4.239±0.432	4.201±0.417
Ne / O	12.333±9.682	11.311±8.344	4.031±0.576	3.928±0.482	3.680±0.292	3.516±0.267
Mg / O	1.434±1.066	1.217±0.855	0.317±0.046	0.322±0.040	0.303±0.025	0.302±0.024
Al / O	5.633±4.327	4.493±3.298	1.095±0.282	1.137±0.281	1.114±0.255	1.040±0.237
Si / O	1.912±1.436	1.554±1.102	0.386±0.072	0.408±0.062	0.398±0.058	0.362±0.036
S / O	4.687±3.669	3.650±2.736	0.947±0.285	0.962±0.281	0.949±0.264	0.756±0.207
Ar / O	73.404±***	54.641±***	18.422±3.734	8.127±5.530	6.752±5.300	11.315±1.841
Fe / O	0.777±0.578	0.702±0.496	0.203±0.031	0.218±0.030	0.205±0.023	0.203±0.020

Table 6.98: Abundances relative to oxygen derived from the DEM calculated from H-like to He-like ratios for all mentioned UX Ari datasets combined.

element	λ	2nd order	3rd order	4th order	5th order	6th ode	7th order
C V	40.268	0.234±0.050	0.286±0.061	0.269±0.057	0.141±0.030	0.109±0.023	0.366±0.078
C VI	33.737	0.135±0.011	0.171±0.014	0.270±0.023	0.142±0.012	0.110±0.009	0.365±0.031
N VI	28.787	0.283±0.052	0.367±0.068	1.247±0.230	0.656±0.121	0.500±0.092	1.627±0.300
N VII	24.782	0.718±0.060	0.909±0.076	1.097±0.092	0.583±0.049	0.465±0.039	1.631±0.137
O VII	21.602	0.063±0.009	0.082±0.012	0.202±0.029	0.112±0.016	0.098±0.014	0.390±0.056
O VIII	18.970	0.245±0.017	0.304±0.022	0.277±0.020	0.147±0.010	0.115±0.008	0.388±0.028
Ne IX	13.447	0.787±0.089	0.996±0.113	1.031±0.117	0.547±0.062	0.433±0.049	1.348±0.153
Ne X	12.134	1.491±0.066	1.736±0.077	1.019±0.045	0.535±0.024	0.405±0.018	1.367±0.061
Mg XI	9.1688	0.124±0.013	0.147±0.015	0.088±0.009	0.047±0.005	0.035±0.004	0.119±0.012
Mg XII	8.4210	0.154±0.009	0.167±0.009	0.078±0.004	0.043±0.002	0.033±0.002	0.117±0.007
Al XIII	7.1730	0.566±0.124	0.596±0.130	0.277±0.061	0.155±0.034	0.124±0.027	0.404±0.088
Si XIII	6.6480	0.163±0.022	0.182±0.024	0.084±0.011	0.049±0.007	0.038±0.005	0.137±0.018
Si XIV	6.1830	0.220±0.021	0.226±0.022	0.110±0.010	0.061±0.006	0.050±0.005	0.143±0.014
S XV	5.0387	0.459±0.161	0.485±0.170	0.218±0.076	0.150±0.053	0.128±0.045	0.322±0.113
S XVI	4.7300	0.490±0.199	0.483±0.197	0.292±0.119	0.116±0.047	0.090±0.037	0.267±0.109
Ar XVII	3.9488	8.581±1.671	8.693±1.692	4.377±0.852	3.686±0.718	3.525±0.686	4.822±0.939
Ar XVIII	3.7330	6.425±1.488	6.201±1.436	5.249±1.216	0.895±0.207	0.626±0.145	3.976±0.921
Fe XVII	15.015	0.049±0.004	0.060±0.005	0.046±0.004	0.024±0.002	0.018±0.001	0.054±0.004
Fe XVII	17.075	0.026±0.013	0.032±0.016	0.026±0.013	0.013±0.007	0.010±0.005	0.031±0.015
Fe XVII	15.262	0.088±0.008	0.108±0.009	0.084±0.007	0.043±0.004	0.032±0.003	0.099±0.009
Fe XVII	16.777	0.055±0.007	0.068±0.009	0.054±0.007	0.028±0.004	0.021±0.003	0.064±0.009
Fe XVIII	14.205	0.063±0.030	0.074±0.035	0.042±0.020	0.022±0.010	0.016±0.007	0.054±0.026
Fe XVIII	93.923	0.094±0.009	0.113±0.010	0.071±0.006	0.036±0.003	0.026±0.002	0.087±0.008
Fe XIX	13.521	0.214±0.020	0.246±0.023	0.117±0.011	0.061±0.006	0.044±0.004	0.180±0.017
Fe XIX	108.35	0.137±0.014	0.160±0.016	0.080±0.008	0.042±0.004	0.030±0.003	0.115±0.011
Fe XX	121.84	0.073±0.011	0.083±0.013	0.037±0.006	0.020±0.003	0.014±0.002	0.063±0.010
Fe XX	118.68	0.069±0.019	0.078±0.022	0.035±0.010	0.019±0.005	0.014±0.004	0.060±0.017
Fe XX	12.830	0.121±0.032	0.135±0.036	0.058±0.015	0.032±0.008	0.023±0.006	0.107±0.028
Fe XXI	128.75	0.091±0.012	0.100±0.013	0.042±0.005	0.024±0.003	0.018±0.002	0.084±0.011
Fe XXI	117.50	0.100±0.035	0.110±0.038	0.046±0.016	0.026±0.009	0.020±0.007	0.092±0.032
Fe XXI	12.285	0.129±0.013	0.140±0.014	0.057±0.006	0.033±0.003	0.026±0.003	0.119±0.012
Fe XXII	117.15	0.098±0.010	0.106±0.011	0.043±0.004	0.026±0.003	0.021±0.002	0.089±0.009
Fe XXII	135.79	0.087±0.015	0.093±0.017	0.038±0.007	0.023±0.004	0.019±0.003	0.079±0.014
Fe XXII	11.767	0.193±0.023	0.206±0.025	0.083±0.010	0.053±0.006	0.044±0.005	0.169±0.020
Fe XXIII	132.90	0.113±0.006	0.118±0.006	0.050±0.003	0.035±0.002	0.031±0.002	0.086±0.005
Fe XXIII	11.736	0.203±0.040	0.210±0.042	0.091±0.018	0.068±0.013	0.062±0.012	0.141±0.028
Fe XXIV	11.171	0.254±0.027	0.253±0.027	0.133±0.014	0.124±0.013	0.131±0.014	0.142±0.015

Table 6.99: Abundances derived for individual lines from the DEM calculated from H-like to He-like ratios for all mentioned UX Ari datasets combined.

	measured	2nd order	3rd order	4th order	5th order	6th oder	7th oder
C VI / C V	2.311±0.528	23.169	6.947	***	***	***	***
N VII / N VI	7.033±1.424	9.970	5.121	52.962	53.118	62.363	59.623
O VIII / O VII	8.797±1.405	6.233	4.187	28.192	28.299	32.264	34.365
Ne X / Ne IX	2.910±0.354	2.752	2.509	5.019	5.036	5.881	5.479
Mg XII / Mg XI	1.606±0.186	1.845	1.870	2.163	2.163	2.189	2.574
Si XIV / Si XIII	1.403±0.229	1.232	1.290	1.711	1.706	2.051	1.936
S XVI / S XV	0.844±0.453	0.806	0.842	1.382	1.374	1.780	3.069
3-4 Å	5.326±0.533	4.698	4.791	4.833	4.868	5.171	5.298
2-3 Å	2.387±0.948	3.066	3.104	3.276	3.286	3.004	2.931
1-2 Å	1.019±0.204	1.281	1.239	1.198	1.188	1.049	0.965
red. χ^2		6.16	6.46	5.01	5.35	5.02	5.33

Table 6.100: Fit results from iron lines from all UX Ari datasets combined: Photon flux ratios and continuum flux [10^{-4} cts s^{-1} cm^{-2}] in specified wavelength bands.

element	2nd order	3rd order	4th order	5th order	6th oder	7th oder
C	0.440±0.155	0.328±0.083	1.149±0.450	1.131±0.443	0.230±0.090	0.209±0.082
N	1.717±0.201	1.284±0.170	4.330±1.660	4.262±1.635	0.912±0.359	0.713±0.279
O	0.376±0.057	0.280±0.101	1.015±0.323	0.999±0.318	0.221±0.075	0.162±0.056
Ne	1.590±0.066	1.588±0.085	2.828±0.429	2.782±0.424	0.580±0.107	0.473±0.081
Mg	0.128±0.007	0.130±0.008	0.199±0.023	0.196±0.023	0.041±0.005	0.032±0.006
Al	0.425±0.093	0.424±0.093	0.619±0.135	0.609±0.133	0.117±0.026	0.106±0.023
Si	0.151±0.012	0.151±0.012	0.217±0.020	0.214±0.019	0.041±0.007	0.037±0.005
S	0.347±0.092	0.340±0.090	0.391±0.107	0.385±0.105	0.073±0.027	0.039±0.024
Ar	5.612±0.839	5.379±0.805	4.729±1.317	4.698±1.274	0.496±0.317	0.443±0.201
Fe	0.084±0.006	0.085±0.006	0.163±0.009	0.160±0.009	0.033±0.002	0.030±0.002

Table 6.101: Absolute abundances derived from the *DEM* calculated from iron lines for all mentioned UX Ari datasets combined.

abundance	2nd order	3rd order	4th order	5th order	6th oder	7th oder
C / O	1.171±0.450	1.169±0.515	1.132±0.571	1.132±0.571	1.043±0.541	1.291±0.677
N / O	4.573±0.876	4.582±1.759	4.265±2.125	4.265±2.127	4.125±2.145	4.406±2.308
Ne / O	4.233±0.666	5.664±2.064	2.786±0.982	2.784±0.984	2.624±1.014	2.927±1.135
Mg / O	0.340±0.055	0.463±0.169	0.196±0.066	0.196±0.066	0.183±0.066	0.200±0.078
Al / O	1.132±0.301	1.513±0.638	0.610±0.235	0.610±0.236	0.529±0.214	0.655±0.270
Si / O	0.402±0.069	0.539±0.199	0.214±0.071	0.214±0.071	0.186±0.070	0.226±0.085
S / O	0.924±0.283	1.211±0.542	0.385±0.161	0.385±0.162	0.330±0.166	0.240±0.169
Ar / O	14.945±3.185	19.189±7.491	4.659±1.970	4.702±1.968	2.244±1.622	2.738±1.569
Fe / O	0.224±0.037	0.303±0.111	0.160±0.052	0.160±0.052	0.151±0.052	0.184±0.065

Table 6.102: Abundances relative to oxygen derived from the *DEM* calculated from iron lines for all mentioned UX Ari datasets combined.

element	λ	2nd order	3rd order	4th order	5th order	6th oder	7th oder
C V	40.268	4.345±0.922	0.952±0.202	74.891±***	73.904±***	17.27±3.663	15.31±3.248
C VI	33.737	0.433±0.037	0.317±0.027	1.146±0.097	1.128±0.095	0.230±0.019	0.208±0.018
N VI	28.787	2.343±0.432	1.012±0.187	31.85±5.873	31.44±5.798	7.924±1.461	5.915±1.091
N VII	24.782	1.653±0.138	1.390±0.116	4.230±0.354	4.163±0.349	0.894±0.075	0.698±0.058
O VII	21.602	0.294±0.042	0.184±0.026	3.092±0.442	3.055±0.437	0.773±0.111	0.604±0.086
O VIII	18.970	0.416±0.030	0.386±0.027	0.965±0.069	0.950±0.068	0.211±0.015	0.155±0.011
Ne IX	13.447	1.515±0.172	1.402±0.159	4.709±0.533	4.647±0.526	1.130±0.128	0.860±0.097
Ne X	12.134	1.603±0.071	1.626±0.072	2.730±0.122	2.685±0.120	0.559±0.025	0.457±0.020
Mg XI	9.1688	0.143±0.014	0.147±0.015	0.256±0.026	0.251±0.025	0.053±0.005	0.049±0.005
Mg XII	8.4210	0.124±0.007	0.126±0.007	0.190±0.011	0.187±0.010	0.039±0.002	0.030±0.002
Al XIII	7.1730	0.425±0.093	0.424±0.093	0.619±0.135	0.609±0.133	0.117±0.026	0.106±0.023
Si XIII	6.6480	0.140±0.018	0.143±0.019	0.250±0.033	0.246±0.032	0.055±0.007	0.047±0.006
Si XIV	6.1830	0.159±0.015	0.156±0.015	0.205±0.020	0.202±0.019	0.038±0.004	0.034±0.003
S XV	5.0387	0.340±0.119	0.339±0.119	0.527±0.185	0.517±0.181	0.122±0.043	0.113±0.040
S XVI	4.7300	0.357±0.145	0.340±0.138	0.322±0.131	0.318±0.129	0.058±0.024	0.031±0.013
Ar XVII	3.9488	6.089±1.185	5.891±1.147	6.654±1.295	6.532±1.272	1.506±0.293	0.865±0.168
Ar XVIII	3.7330	5.133±1.189	4.882±1.131	3.828±0.886	3.813±0.883	0.397±0.092	0.347±0.080
Fe XVII	15.015	0.071±0.005	0.071±0.005	0.138±0.011	0.136±0.011	0.028±0.002	0.025±0.002
Fe XVII	17.075	0.040±0.020	0.040±0.019	0.081±0.040	0.080±0.039	0.016±0.008	0.015±0.007
Fe XVII	15.262	0.129±0.011	0.129±0.011	0.254±0.022	0.250±0.022	0.051±0.004	0.046±0.004
Fe XVII	16.777	0.083±0.011	0.083±0.011	0.170±0.023	0.168±0.023	0.034±0.005	0.031±0.004
Fe XVIII	14.205	0.069±0.033	0.073±0.035	0.107±0.051	0.105±0.050	0.023±0.011	0.020±0.010
Fe XVIII	93.923	0.114±0.010	0.119±0.011	0.187±0.017	0.184±0.017	0.041±0.004	0.034±0.003
Fe XIX	13.521	0.200±0.019	0.212±0.020	0.323±0.031	0.316±0.030	0.073±0.007	0.067±0.006
Fe XIX	108.35	0.136±0.013	0.144±0.014	0.212±0.021	0.207±0.020	0.045±0.004	0.043±0.004
Fe XX	121.84	0.064±0.010	0.067±0.011	0.113±0.018	0.111±0.017	0.025±0.004	0.023±0.004
Fe XX	118.68	0.060±0.017	0.064±0.018	0.107±0.030	0.105±0.029	0.024±0.007	0.022±0.006
Fe XX	12.830	0.101±0.027	0.107±0.028	0.194±0.051	0.190±0.050	0.044±0.012	0.038±0.010
Fe XXI	128.75	0.072±0.009	0.075±0.010	0.154±0.020	0.151±0.020	0.031±0.004	0.027±0.004
Fe XXI	117.50	0.079±0.028	0.082±0.029	0.169±0.059	0.166±0.058	0.034±0.012	0.030±0.010
Fe XXI	12.285	0.099±0.010	0.102±0.010	0.223±0.022	0.219±0.022	0.043±0.004	0.037±0.004
Fe XXII	117.15	0.073±0.007	0.074±0.007	0.168±0.017	0.165±0.017	0.031±0.003	0.028±0.003
Fe XXII	135.79	0.064±0.011	0.065±0.012	0.148±0.026	0.146±0.026	0.027±0.005	0.025±0.004
Fe XXII	11.767	0.139±0.017	0.141±0.017	0.315±0.038	0.311±0.037	0.059±0.007	0.054±0.007
Fe XXIII	132.90	0.079±0.004	0.079±0.004	0.149±0.008	0.147±0.008	0.032±0.002	0.029±0.002
Fe XXIII	11.736	0.141±0.028	0.138±0.028	0.234±0.047	0.230±0.046	0.054±0.011	0.045±0.009
Fe XXIV	11.171	0.177±0.019	0.170±0.018	0.189±0.020	0.186±0.020	0.034±0.004	0.030±0.003

Table 6.103: Abundances derived for individual lines from the DEM calculated from iron lines for all mentioned UX Ari datasets combined.

A The `fit_dem` routine

```
1  ;fit_dem reconstructs differential emssion measures and abundances
2  ;
3  ;calls:
4  ;cut (by Jan-Uwe Ness)
5  ;convertname, ion2spectroscopic, ion_interp, g_of_t, freefree, freebound, two_photon (all
    from Chianti)
6  ;ismtau (PINTofALE)
7  ;err_weight_average, err_mean, checksum, get_flength (edited version of Jan-Uwe Ness'
   get_flen counting lines of an ascii file, now accepting the ';' as a comment symbol),
   read_lines, read_corafile
8  ;
9  ;input:
10 ;name            name of the star the calculation should be done for
11 ;
12 ;keywords:
13 ;interp          number of interpolation values to the temperature array
14 ;all             auto-select every dataset found by the routine individual datasets can be
    confirmed or rejected if not set
15 ;psplot          make the plots as PS-files
16 ;fefit           doing an analogous fit for the iron lines only
17 ;maxslope        force the slope at log T = 8 to some value - sometimes helps to avoid
   raising slopes
18 ;minslope        like maxslope, but for log T = 5
19 ;startorder      starting point for higher oder fits - influences slightly the initial
   conditions!
20 ;order           maximum order to fit
21 ;
22 ;file history:
23 ;2005 08 23 by Carolin Liefke
24
25
26 ;predict_ratios computes a theoretical line flux ratio from the integral of the
   contribution function and a polynomial without the coefficient c_0 for the DEM
27 function predict_ratios, x, y, c, x_shift
28 x=double(x)      ;x is the temperature array
29 y=double(y)      ;y is a 3D array of contribution functions: (interp*30+1, 2, n_ratios)
30 order=n_elements(c)-1
31 exponent=0.d0
32 for i=1,order do exponent=exponent+c(i)*x^(i)    ;define the exponent as a polynomial
   without the cofficient c_0
33 ratio=dblarr(n_elements(y(0,0,*)))
34 for j=0,n_elements(ratio)-1 do begin
35  good0=where(y(*,0,j) gt 0) ;calculate integral only where gofts are not zero
36  good1=where(y(*,1,j) gt 0)
37  int0=int_tabulated(x(good0),y(good0,0,j)*10^(exponent(good0)+x(good0)+x_shift),/double)
38  int1=int_tabulated(x(good1),y(good1,1,j)*10^(exponent(good1)+x(good1)+x_shift),/double)
39  ratio(j)=int0/int1
40 endfor
41 return, ratio
42 end
43
44 ;theoflux computes a theoretical line or continuum flux from the integral of the
   contribution function and a complete polynomial
45 function theoflux, x, y, c, distance, x_shift, line=line
46 x=double(x)      ;x is the temperature
47 y=double(y)      ;y is a 2D array of conribution functions: (n_elements(c_temp),
   n_elements(c_wave))
48 integral=dblarr(n_elements(y(0, *)))
49 for j=0,n_elements(integral)-1 do begin
50  good=where(y(*,j) gt 0) ;calculate integral only where gofts are not zero
51  integral(j)=int_tabulated(x(good),y(good,j)*10^(poly(x(good),c)+x(good)+x_shift), /
```

```
    double)
endfor
theoflux=integral*alog(10)/distance^2    ;don't forget ln 10 ...
if keyword_set(line) then theoflux=theoflux/(4*!pi)
;contribution functions for lines and continuum are defined differently in CHIANTI
return, theoflux
end

;chi_square is to be minimized by Powell. Needs the common block because Powell can not
    deal with functions with parameters. The polynomial coefficients are free to vary
function chi_square, a
common ratiofit, t, t_shift, gofts, measured, measured_errors, c_t, c_gofts, c_flux,
    c_fluxerror, distance, fe_gofts, fe_measured, fe_measured_errors, max_slope, min_slope
theoretical=predict_ratios(t, gofts, a ,t_shift)          ;compute theoretical ratios
c_theoretical=theoflux(c_t, c_gofts, a, distance, t_shift) ;compute theoretical continuum
chi_square=total((measured-theoretical)^2/measured_errors^2)+total((c_flux-c_theoretical)
    ^2/(c_fluxerror)^2)
maxslope=dblarr(n_elements(a))
minslope=dblarr(n_elements(a))
for i=0,n_elements(a)-1 do maxslope(i)=a(i)*i*max(t)^(i-1)        ;max log T is 8,so 1 in
    units of t
for i=0,n_elements(a)-1 do minslope(i)=a(i)*i*min(t)^(i-1)        ;min log T is 5,-2 in
    units of t
if total(maxslope) gt max_slope then chi_square=10000.
if total(minslope) lt min_slope then chi_square=10000.
return, chi_square
end

;the minimization function for the iron lines. No ratios are needed but fluxes for the
    iron lines. The iron abundance is another fit parameter instead.
function chi_square_fe, params
common ratiofit, t, t_shift, gofts, measured, measured_errors, c_t, c_gofts, c_flux,
    c_fluxerror, distance, fe_gofts, fe_measured, fe_measured_errors, max_slope, min_slope
fe_abund=params(0)        ;divide the iron abundance from the parameter vector
a=params(1:n_elements(params)-1)          ;the rest are the polynomial coefficients
fe_theoretical=fe_abund*theoflux(t, fe_gofts, a, distance, t_shift, /line)
c_theoretical=theoflux(c_t, c_gofts, a, distance, t_shift)
;compute iron line flux and theoretical continuum
chi_square_fe=total((fe_measured-fe_theoretical)^2/fe_measured_errors^2)+total((c_flux-
    c_theoretical)^2/(c_fluxerror)^2)
maxslope=dblarr(n_elements(a))
minslope=dblarr(n_elements(a))
for i=0, n_elements(a)-1 do maxslope(i)=a(i)*i*max(t)^(i-1)
for i=0, n_elements(a)-1 do minslope(i)=a(i)*i*min(t)^(i-1)
if total(maxslope) gt max_slope then chi_square=1000.
if total(minslope) lt min_slope then chi_square=1000.
return, chi_square_fe
end

;-------------------------------------------------------------------------------
;main program
;-------------------------------------------------------------------------------

pro fit_dem, name, interp=interp, order=order, all=all, psplot=psplot, fefit=fefit,
    maxslope=maxslope, minslope=minslope, startorder=startorder, tshift=tshift, journal=
    journal
common ratiofit, t, t_shift, gofts, measured, measured_errors, c_t, c_gofts, c_flux,
    c_fluxerror, distance, fe_gofts, fe_measured, fe_measured_errors, max_slope, min_slope

loadct, 38, file='/home/hslxrsrv3/st1h314/IDL/colors.tbl'

;predefined linelist, indices for chianti 5.0!
linelist=['C_5','C_6','N_6','N_7','O_7','O_8','Ne_9','Ne_10','Mg_11','Mg_12','Al_12','
    Al_13','Si_13','Si_14','S_15','S_16','Ar_17','Ar_18','Ca_19','Ca_20','Fe_9','Fe_10','
    Fe_15','Fe_16','Fe_17','Fe_17a','Fe_17b','Fe_17c','Fe_18','Fe_18a','Fe_18b','Fe_19','
    Fe_19a','Fe_19b','Fe_20','Fe_20a','Fe_20b','Fe_21','Fe_21a','Fe_21b','Fe_22','Fe_22a','
    Fe_22b','Fe_23','Fe_23a','Fe_24','Fe_25']
;indices of lines to select allowing g_of_t to run without widget
indexlist=[[3, 3], [6, 8], [6, 6], [6, 8], $     ;C V r, C VI Ly a, N VI r, N VII Ly a
[6, 6], [6, 8], [6, 6], [20, 22], $      ;O VII r, OVIII Ly a, Ne IX r, Ne X Ly a
[6, 6], [6, 8], [6, 6], [6, 8], $        ;Mg XI r, Mg XII Ly a, Al XII r Al XIII Ly a
```

```
[6,6],[6,8],[6,6],[6,8],$        ;Si XIII r, Si XIV Ly a, S XV r, S XVI Ly a
[6,6],[6,8],[6,6],[6,8],$        ;Ar XVII r, Ar XVIII Ly a, Ca XIX r, Ca XX
[238,238],[1381,1381],[2061,2061],[19,19],$      ;Fe IX 171.1, Fe X, 174.5, Fe XV 69.68, Fe XVI 63.7
[55,55],[68,69],[58,58],[67,67],$        ;Fe XVII 15.01, 17.07, 15.26, 16.78
[440,441],[5892,5892],[6389,6389],$        ;Fe XVIII 14.20, 93.9, 103.9
[2008,2008],[17198,17198],[16449,16449],$ ;Fe XIX 13.52, 108.4, 101.5
[23724,23724],[23408,23408],[3874,3898],$ ;Fe XX 121.8, 118.7, 12.83
[16291,16291],[15894,15894],[3693,3693],$ ;Fe XXI 128.1, 117.5, 12.28
[13431,13431],[13818,13818],[2964,2964],$ ;Fe XXII 117.1, 135.8, 11.76
[5022,5022],[1083,1083],[69,70],[6,9]]    ;Fe XXIII 132.9, 11.73, Fe XXIV 11.17, Fe XXV 1.86
;wavelengths of lines (needed for effective area interpolation)
wavelengthlist=[40.268,33.737,28.787,24.782,21.602,18.97,13.447,12.1345,9.1688,$
8.421,7.7573,7.173,6.648,6.183,5.0387,4.73,3.9488,3.733,3.0212,3.1773,$
171.073,174.5,69.682,63.711,15.015,17.075,15.262,16.778,14.205,93.923,103.937,$
13.521,108.355,101.5498,121.845,118.6801,12.83,128.75,117.5,12.285,117.154,$
135.791,11.7675,132.9065,11.7363,11.171,1.856]

if n_elements(maxslope) eq 0 then max_slope=!VALUES.F_INFINITY else max_slope=maxslope
if n_elements(minslope) eq 0 then min_slope=-!VALUES.F_INFINITY else min_slope=minslope
;if keyword not set, allow any slope

if keyword_set(journal) then begin
 journalfile=''
 read,journalfile,prompt='Enter journal file name : '
 if journalfile eq '' then journalfile=name
 journal,journalfile+'.out'
endif
;pipe the standard output to a file

;-----collect available data
print,'-------------------------'
print,'Searching for available line data'
rootdir='/data/hspc58/st1h314/'
filename=findfile(rootdir+'*/'+name+'/*/lines*.dat')
n_files=n_elements(filename)
;filename contains now all filenames of the chosen star with measured line counts
if filename(0) ne '' then begin ;security check if any line count data found

;---- choosing datasets to include in calculations
 if not keyword_set(all) then begin
  print,'Which of these datasets shall be included?'
  print,'Confirm with "y" or "n"'
  select=intarr(n_files)
  input=''
  for m=0,n_files-1 do begin
   read,input,prompt=filename(m)+' : '
   if input ne 'n' then select(m)=1
  endfor
  chosen=where(select eq 1,n_chosen)
  if n_chosen eq 0 then begin   ;filename gets undefined when all data rejected
   print,'All line count data rejected. Aborting.'
   return
  endif
  filename=filename(chosen)
  n_files=n_elements(filename)
 endif

 fluxtab=dblarr(n_elements(linelist),n_files)
 fluxerrortab=dblarr(n_elements(linelist),n_files)
 fluxlist=dblarr(n_elements(linelist))
 fluxerrorlist=dblarr(n_elements(linelist))
;fluxes calculated for the lines measured with the different detectors will be entried in fluxtab, their errors in fluxerrortab.
;fluxlist will contain weightend means for each line, fluxerror the standard deviation of this mean

 dataset=''
 for m=0,n_files-1 do begin
  split_filename=strsplit(filename(m),'lines_',/extract,/regex)
```

```
174     dir=split_filename(0) ;get expanded directory name of file
175     file='lines_'+split_filename(1)        ;get expanded filename
176   ;find cora spectrum file belonging to data file
177     invalid=0
178     case file of
179       'lines_MEG.dat': corafile=dir+'meg.dat'
180       'lines_HEG.dat': corafile=dir+'heg.dat'
181       'lines_LETG.dat': corafile=dir+'leg.dat'
182       'lines_RGS1_1.dat': corafile=dir+'RGS/rgs1_m1.spec'
183       'lines_RGS1_2.dat': corafile=dir+'RGS/rgs1_m2.spec'
184       'lines_RGS2_1.dat': corafile=dir+'RGS/rgs2_m1.spec'
185       'lines_RGS2_2.dat': corafile=dir+'RGS/rgs2_m2.spec'
186       else: invalid=1       ;safety check if filename is allowed
187     endcase
188     if invalid eq 1 then begin
189       print, filename(m), ': invalid file name'
190       continue      ;jumps to m+1 in loop
191     endif
192   ;read each file containing line counts
193     read_lines, filename(m), counts, counts_err, lines, starname, distance, nh, data
194     dataset=[dataset, data]
195   ;read cora spectrum file to get effective areas
196     read_corafile, corafile, wave, cts, cts_err, back, back_err, eff, exposure
197   ;cut empty space from linenames
198     lines=strcompress(lines, /remove_all)
199   ;for each line listed in data file find corresponding line in linelist
200     for n=0, n_elements(lines)-1 do begin
201   ;safety check: If line mentioned in file that is not in list ignore and message
202       if total(strcmp(linelist, lines(n))) eq 1 then begin
203         k=where(strcmp(linelist, lines(n)) eq 1)
204         ion2spectroscopic, linelist(k), label
205         print, 'Found data for line '+label+', '+cut(wavelengthlist(k), 6)+' Angstrom'
206   ;took this kind of calculation von Jan-Uwe's routine get_aeff
207   ;it's just a linear interpolation
208         l=0
209         while wavelengthlist(k) ge wave(l) do l=l+1
210         aeff=eff(l-1)+(eff(l)-eff(l-1))/(wave(l)-wave(l-1))*(wavelengthlist(k)-wave(l-1))
211   ;aeff=spline(wave, eff, wavelengthlist(k), 0.1)
212   ;but calculation of aeff by spline results sometimes in arithmetic error messages
213         flux=counts(n)/(exposure*aeff)       ;calculate flux...
214         fluxerr=counts_err(n)/(exposure*aeff)        ;...and error of flux
215         fluxtab(k, m)=flux   ;fill fluxtab...
216         fluxerrortab(k, m)=fluxerr   ;...and fluxerrortab
217       endif else begin
218         print, lines(n), ': invalid line designation'
219         continue      ;jump to n+1 loop
220       endelse
221     endfor
222   endfor
223
224   ;compute transmission factors due to ISM attenuation
225   attenuationlist=exp(-ismtau(wavelengthlist, nh=nh, /bam))
226   ;apply flux correction considering attenuation
227   for i=0, n_elements(linelist)-1 do begin
228     fluxtab(i, *)=fluxtab(i, *)/attenuationlist(i)
229     fluxerrortab(i, *)=fluxerrortab(i, *)/attenuationlist(i)
230   endfor
231   ;calculating a weighted mean that considers the flux errors (and therefore indirectly the
      exposure time and effective area)
232   for j=0, n_elements(fluxlist)-1 do begin
233     measured=where(fluxtab(j, *) gt 0, num)
234     if num ne 0 then begin
235   ;     fluxlist(j)=mean(fluxtab(j, measured), /double)
236       err_weight_average, fluxtab(j, measured), fluxerrortab(j, measured), average,
        average_err
237       fluxlist(j)=average
238       fluxerrorlist(j)=average_err
239     endif
240   endfor
241   distance=double(distance*3.09e+18)
242   measured=where(fluxlist gt 0)
```

```
243   flux=fluxlist(measured)
244   fluxerror=fluxerrorlist(measured)
245   lines=linelist(measured)
246   index=indexlist(*, measured)
247
248  ;---- calculating gofts and emission measure loci curves
249   print, '-------------------------'
250   print, 'Calculating contribution functions and emission measure'
251
252   if n_elements(interp) eq 0 then begin
253    interp=3       ;default for how many interpolation values between the default values
254    print, 'Number of interpolation values set to 3 (default value)'
255   endif else print, 'Number of interpolation values set to ',strcompress(string(interp), /
      remove_all)
256   n_lines=n_elements(lines)
257   temp=findgen(41)/10+5
258  ;For each measured line the line information, flux, expanded contribution function
      goft_interp, and log_em is stored in the structure linedata
259   linedata=replicate({line:'', iz:0, ion:0, flux:dblarr(1), fluxerror:dblarr(1),
      goft_interp:dblarr(interp*40+1), log_em:dblarr(interp*40+1)}, n_lines)
260  ;linedata has n_lines entries, goft_interp and log_em interp*40+1
261   for i=0, n_lines-1 do begin
262    indices=intarr(index(1, i)-index(0, i)+1)
263    for j=0, n_elements(indices)-1 do indices(j)=index(0, i)+j
264    convertname, lines(i), iz, ion
265    ion2spectroscopic, lines(i), label
266    linedata(i).line=lines(i)
267    linedata(i).iz=iz
268    linedata(i).ion=ion
269    linedata(i).flux=flux(i)
270    linedata(i).fluxerror=fluxerror(i)
271    print, 'Calculating line: '+label+','+cut(wavelengthlist(where(lines(i) eq linelist))
       ,6)+' Angstrom'
272    goft=g_of_t(iz, ion, index=indices, ioneq_file=!ioneq_file, abund_file=!abund_file, /
       no_de, /quiet)
273    goft=goft(10:50)       ;reduce size of goft array by cropping log T from 4 to 5
274    bad=where(goft lt 1e-30)       ;strange numbers appear with Fe IX that confuse
       ion_interp
275    if bad(0) ne -1 then goft(bad)=0.
276    ion_interp, temp, goft, temp_interp, goft_interp, interp
277    temp_interp=double(temp_interp)
278    sel=where(goft_interp gt 0)
279    log_em=dblarr(interp*40+1)
280    log_em(sel)=alog10(4*!pi*distance^2*flux(i)/goft_interp(sel))
281    linedata(i).goft_interp=goft_interp
282    linedata(i).log_em=log_em
283   endfor
284
285  endif else begin
286   print, 'No files containing line counts found. Aborting.'
287   return
288  endelse
289
290  ;------ continuum
291  print, '-------------------------'
292  print, 'Searching available continuum data'
293  file_1=findfile(rootdir+'XMM/'+name+'/*/continuum*.dat')
294  file_2=findfile(rootdir+'Chandra/'+name+'/*/[hml]eg.dat')
295  n1=where(file_1 ne '', n_file_1)        ;counters n_file_1 and n_file_2 have to be
      defined that way
296  n2=where(file_2 ne '', n_file_2)
297
298  ;filename contains now all filenames of the chosen star with measured continuum flux
299  if n_file_1+n_file_2 gt 0 then begin     ;security check if any flux data found
300
301   ;---- choosing datasets to include in calculations
302   if not keyword_set(all) then begin
303   print, 'Which of these datasets shall be included?'
304   print, 'Confirm with "y" or "n"'
305    if n_file_1 gt 0 then begin
306     select=intarr(n_file_1)
```

```
307     input=''
308     for m=0, n_file_1 -1 do begin
309      read, input, prompt=file_1(m)+' : '
310      if input ne 'n' then select(m)=1
311     endfor
312     chosen=where(select eq 1, n_file_1)
313     if n_file_1 gt 0 then begin  ;file_1 gets undefined when all EPIC data rejected
314      file_1=file_1(chosen)
315     endif else file_1=''
316    endif
317    if n_file_2 gt 0 then begin
318     select=intarr(n_file_2)
319     input=''
320     for m=0, n_file_2 -1 do begin
321      read, input, prompt=file_2(m)+' : '
322      if input ne 'n' then select(m)=1
323     endfor
324     chosen=where(select eq 1, n_file_2)
325     if n_file_2 gt 0 then begin   ;file_2 gets undefined when all HEG data rejected
326      file_2=file_2(chosen)
327     endif else file_2=''
328    endif
329   endif
330   if n_file_1+n_file_2 eq 0 then begin
331    print, 'All continuum data rejected. Aborting.'
332    return
333   endif else begin
334
335    c_fluxtab=dblarr(4, n_file_1+n_file_2)
336    c_fluxlist=dblarr(4)
337    c_fluxerrorlist=dblarr(4)
338    for m=0, n_file_1 -1 do begin
339
340  ;---- EPIC files
341     read_lines, file_1(m), flux, flux_err, wrange, starname, distance, /continuum;, data
342     distance=double(distance*3.09e+18)
343  ;for each wavelength range listed in data file
344     for n=0, n_elements(wrange)-1 do begin
345  ;safety check: If wavelength range is not in list ignore and message
346      invalid=0
347      case strcompress(wrange(n), /remove_all) of
348       '3-4': c_fluxtab(0, m)=flux(n)
349       '2-3': c_fluxtab(1, m)=flux(n)
350       '1-2': c_fluxtab(2, m)=flux(n)
351       else: print, wrange(n), ' Angstrom: invalid wavelength range'
352      endcase
353     endfor
354
355    endfor
356  ;---- HEG files
357    for m=0, n_file_2 -1 do begin
358     read_corafile, file_2(m), wave, counts, counts_err, background, back_err, aeff,
       exposure
359     counts=counts-background
360     if strmid(file_2(m), 6, /reverse) eq 'heg.dat' then range=where(wave gt 2.0 and wave
       le 3.0) else range=where(wave gt 19.5 and wave le 20.5)
361     flux=counts(range)/(exposure*aeff(range))
362     flux=total(flux)
363     if strmid(file_2(m), 6, /reverse) eq 'heg.dat' then c_fluxtab(1, n_file_1+m)=flux else
        c_fluxtab(3, n_file_1+m)=flux
364    endfor
365
366    percenterror=[0.1, 0.1, 0.2, 0.2]
367    for j=0, n_elements(c_fluxlist)-1 do begin
368     measured=where(c_fluxtab(j, *) gt 0, num)
369     if num ne 0 then begin
370      c_fluxlist(j)=mean(c_fluxtab(j, measured))
371      if num gt 1 then c_fluxerrorlist(j)=err_mean(c_fluxtab(j, measured)) else
       c_fluxerrorlist(j)=percenterror(j)*c_fluxlist(j)
372     endif
373    endfor
```

```
374
375     c_wavelist=[3.5, 2.5, 1.5, 20.]
376     measured=where(c_fluxlist gt 0)
377     flux=c_fluxlist(measured)
378     fluxerror=c_fluxerrorlist(measured)
379     c_wave=c_wavelist(measured)
380     c_temp=findgen(30)/10+6
381     n_c=n_elements(c_wave)
382     continuumdata=replicate({wave:'', flux:dblarr(1), fluxerror:dblarr(1), continuum:dblarr
        (n_elements(c_temp)), log_em:dblarr(n_elements(c_temp))}, n_elements(flux))
383
384     for k=0, n_c-1 do begin
385      continuumdata(k).wave=c_wave(k)
386      continuumdata(k).flux=flux(k)
387      continuumdata(k).fluxerror=fluxerror(k)
388
389   ;the factor 4*!pi is not needed for continuum processes
390   ;but multiplication with 0.83 to convert from N_e N_H to N_e^2
391   ;(see definitions in gofnt, g_of_t, freefree etc. and the User's Guide)
392      freefree, 10^c_temp, c_wave(k), ff, /photons, /no_setup
393      ff=ff*1.0e-40
394      freebound, 10^c_temp, c_wave(k), fb, /photons, /no_setup
395      fb=fb*1.0e-40
396      two_photon, 10^c_temp, c_wave(k), tp, /photons, /no_setup
397      tp=tp*1.0e-40
398      continuum=(ff+fb+tp)*0.83
399      log_em=alog10(distance^2*flux(k)/continuum)
400      continuumdata(k).continuum=continuum
401      continuumdata(k).log_em=log_em
402     endfor
403    endelse
404
405   endif else begin
406    print, 'No files containing continuum data found. Aborting.'
407    return
408   endelse
409
410   ;------ making the EM loci plot
411   em_min=min((linedata.log_em)(where(linedata.log_em gt 0)))
412   offset=0
413   for i=0, n_lines-1 do begin
414    ion2spectroscopic, linedata(i).line, label
415    case linedata(i).iz of
416     linedata(i).ion: style=0       ;H-like ions
417     linedata(i).ion+1: style=5     ;He-like ions
418    else: style=((linedata(i).iz-linedata(i).ion) mod 4)+1
419    endcase
420    sel=where(linedata(i).goft_interp gt 0)
421    if i eq 0 then begin
422     if keyword_set(psplot) then begin
423      set_plot, 'ps'
424      device, filename=name+'_EM.ps', /color
425     endif else wset, 0
426     plot, /nodata, temp_interp(sel), linedata(i).log_em(sel), yrange=[em_min-1.5,em_min
        +3.5], /ystyle, xrange=[5.0,8.0], /xstyle, title=starname+': raw emission measure loci
        curves', xtitle='log T [ K ]', ytitle='log EM [ cm!U-3!N ]'
427    endif
428    if linedata(i).iz ne 26 then begin
429     oplot, temp_interp(sel), linedata(i).log_em(sel), linestyle=style, color=linedata(i).iz
430     if strmatch(linedata(i).line, '*[a-z]') and strcmp(linedata(i).line, linedata((i-1)>0).
        line, strlen(linedata(i).line)-1) then offset=offset+1 else  label_line, 5.1, 5.3,
        em_min+3.20-0.17*(i-offset), label, color=linedata(i).iz, linestyle=style
431    ;the >0 stuff is need to avoid comparison with linedata(-1) for i=0
432    endif
433   endfor
434   for i=0, n_c-1 do begin
435    oplot, c_temp, continuumdata(i).log_em, color=250
436   endfor
437
438   if !D.NAME eq 'PS' then device, /close  ;close file only when plot created
439
```

```
;------ derive and plot ratios
print, '------------------------'
print, 'Collecting ratio data'
izlist=[6, 7, 8, 10, 12, 13, 14, 16, 18, 20]
;elements used for ratio fitting, equivalent to [C, N, O, Ne, Mg, Al, Si, S, Ar, Ca]
ratiodata=replicate({cmp:[0, 0], ratio:'', fluxratio:dblarr(3), fluxratioerror:dblarr(1)
, fluxratiotemp:dblarr(3), gofts:dblarr(interp*40+1, 2), goftratio:dblarr(interp*40+1)},
n_elements(izlist))

for i=0, n_elements(izlist)-1 do begin
 cmp_up=where(izlist(i) eq linedata.iz and izlist(i) eq linedata.ion)          ;H-like
 cmp_down=where(izlist(i) eq linedata.iz and izlist(i) eq linedata.ion+1)      ;He-like
 if cmp_up ge 0 and cmp_down ge 0 then begin
  ion2spectroscopic, linedata(cmp_up).line, label_up
  ion2spectroscopic, linedata(cmp_down).line, label_down
  ratiodata(i).ratio=label_up+' / '+label_down
  print, 'Calculating ratio '+ratiodata(i).ratio
  fluxratio=linedata(cmp_up).flux/linedata(cmp_down).flux
  fluxratioerror=sqrt((linedata(cmp_up).fluxerror)^2+(fluxratio^2)*(linedata(cmp_down).
  fluxerror)^2)/linedata(cmp_down).flux
  ratiodata(i).cmp=[cmp_up, cmp_down]
  ratiodata(i).fluxratio(1)=fluxratio
  ratiodata(i).fluxratioerror=fluxratioerror
  ratiodata(i).fluxratio(0)=fluxratio-fluxratioerror
  ratiodata(i).fluxratio(2)=fluxratio+fluxratioerror
  sel=where(linedata(cmp_up).goft_interp gt 0 and linedata(cmp_down).goft_interp gt 0)
  ratiodata(i).goftratio(sel)=linedata(cmp_up).goft_interp(sel)/linedata(cmp_down).
  goft_interp(sel)
 endif
endfor

available=where(ratiodata.ratio ne '')
ratiodata=ratiodata(available)
izlist=izlist(available)
n_ratios=n_elements(ratiodata)

for i=0, n_ratios-1 do begin
 sel=where(ratiodata(i).goftratio gt 0 and ratiodata(i).goftratio lt 100)
 fluxratiotemp=spline(ratiodata(i).goftratio(sel), temp_interp(sel), ratiodata(i).
 fluxratio)
 ratiodata(i).fluxratiotemp=fluxratiotemp
 if i eq 0 then begin
  if keyword_set(psplot) then begin
   device, filename=name+'_ratios.ps', /color
  endif else begin
   window, 1
   wset, 1
  endelse
  plot, /nodata, temp_interp(sel), alog10(ratiodata(i).goftratio(sel)), xrange
  =[5.0,8.], /xstyle, title=starname+': Ratios of H-like Ly!4a!3 to He-like r', yrange
  =[-2.,2.], /ystyle, xtitle='log T [ K ]', ytitle='log photon flux ratio'
 endif
 oplot, temp_interp(sel), alog10(ratiodata(i).goftratio(sel)),color=izlist(i),linestyle=2
 label_line, 5.1, 5.3, 1-0.2*i, ratiodata(i).ratio, color=izlist(i), linestyle=2
 oplot, replicate(ratiodata(i).fluxratiotemp(1), 1), replicate(alog10(ratiodata(i).
 fluxratio(1)), 1), psym=2, color=izlist(i)
 plots, ratiodata(i).fluxratiotemp(0), alog10(ratiodata(i).fluxratio(0))
 plots, ratiodata(i).fluxratiotemp(2), alog10(ratiodata(i).fluxratio(2)), /continue,
 thick=2, color=izlist(i)
endfor
if !D.NAME eq 'PS' then device, /close  ;close file only when plot created

;------ calculate fit

;---- choosing ratios to include in ratio fit calculations
if not keyword_set(all) then begin
 print, '------------------------'
 print, 'Which line ratios and continuum intervals shall be included in the ratio fit?'
 print, 'Confirm with "y" or "n"'
 select=intarr(n_ratios)
 input=''
```

```
502   for m=0, n_ratios-1 do begin
503    read, input, prompt='Ratio '+ratiodata(m).ratio+' : '
504    if input ne 'n' then select(m)=1
505   endfor
506   chosen=where(select eq 1, n_ratios)
507   if n_ratios gt 0 then begin     ;only start fitting when not all ratios rejected
508    ratiodata=ratiodata(chosen)
509   endif else begin
510    print, 'All line ratios rejected. Aborting calculations.'
511    return
512   endelse
513
514   select_c=intarr(n_c)
515   input=''
516   for m=0, n_c-1 do begin
517    read, input, prompt='Continuum from '+cut(c_wave(m)-0.5,4)+' to '+cut(c_wave(m)+0.5,4)+
      ' Angstrom : '
518    if input ne 'n' then select_c(m)=1
519   endfor
520   chosen_c=where(select_c eq 1, n_c)
521   if n_c gt 0 then begin
522    continuumdata=continuumdata(chosen_c)
523   endif else begin
524    print, 'All continuum intervals rejected. Aborting calculations.'
525    return
526   endelse
527
528  endif
529
530  gofts=linedata(ratiodata.cmp).goft_interp
531  measured=ratiodata.fluxratio(1)
532  measured_errors=ratiodata.fluxratioerror
533  c_flux=continuumdata.flux
534  c_fluxerror=continuumdata.fluxerror
535  c_gofts=continuumdata.continuum
536
537  print, '_____________________'
538  print, 'Start fitting the H-like / He-like ratios'
539  if n_elements(order) eq 0 then begin
540   order=3         ;default order of polynomial to fit to the data
541   print, 'Order of polynomial to fit the ratios set to 3 (default value)'
542  endif else print, 'Order of polynomial to fit the ratios set to ',strcompress(string(
     order),/remove_all)
543
544  if n_elements(tshift) eq 0 then t_shift=7. else t_shift=tshift
545  ;setting the zero point to log T = 7 to make make fitting easier (avoid integration with
     high numbers in the exponent, leading to overflows)
546  t=temp_interp-t_shift
547  c_t=c_temp-t_shift
548  if n_elements(startorder) eq 0 then startorder=3 ;default for order of polynom to start
     the fit
549  coefficients=replicate({p:dblarr(order+1), theoretical:dblarr(n_ratios), theoretical_c:
     dblarr(n_c)}, order-startorder+1) ;defining this as a structure makes it eassier to
     overwrite the array with a smaller one
550
551  for j=startorder, order do begin        ;increase fit order by 1 until order value is
     reached
552   if j eq startorder then begin
553    print, 'Start initial fit with order=', strcompress(string(startorder), /remove_all)
554    p=dblarr(startorder+1);
555    p(0)=45.       ;starting point for normalization. Avoids strange local minima in chi
       square
556   endif else begin
557    print, 'Fitting order=', strcompress(string(j), /remove_all)
558    p=[p, 0]
559   endelse
560   xi=dblarr(j+1, j+1)
561   for i=0, j do xi(i, i)=1.
562   powell, p, xi, 1.e-8, chi_min, 'chi_square', /double, itmax=500
563   coefficients(j-startorder).p=p
564   coefficients(j-startorder).theoretical=predict_ratios(t, gofts, p, t_shift)
```

```
565   coefficients(j-startorder).theoretical_c=theoflux(c_t, c_gofts, p, distance, t_shift)
566   if j eq startorder then red_chi=chi_min/(n_ratios+n_c-startorder-1) else red_chi=[
      red_chi,chi_min/(n_ratios+n_c-j-1)]
567  ;degrees of freedom: ratios+continuum-(order of polynomial+1) (<- coefficient a_0)
568  endfor
569
570  ;----------Fitting the iron lines
571  if keyword_set(fefit) then begin
572  ;---- choosing iron lines to include in fit calculations
573   fe_lines=linedata(where(linedata.iz eq 26)).line
574   fe_gofts=linedata(where(linedata.iz eq 26)).goft_interp
575   fe_measured=linedata(where(linedata.iz eq 26)).flux
576   fe_measured_errors=linedata(where(linedata.iz eq 26)).fluxerror
577   n_fe=n_elements(fe_measured)
578   if not keyword_set(all) then begin
579    print, '-------------------------'
580    print, 'Which iron lines and continuum intervals shall be included in the fit?'
581    print, 'Confirm with "y" or "n"'
582    select=intarr(n_fe)
583    input=''
584    for m=0, n_fe-1 do begin
585     ion2spectroscopic, fe_lines(m), label
586     read, input, prompt=label+', '+cut(wavelengthlist(where(fe_lines(m) eq linelist)), 6)+
       ' Angstrom : '
587     if input ne 'n' then select(m)=1
588    endfor
589    chosen_fe=where(select eq 1, n_fe)
590    if n_fe gt 0 then begin        ;only start fitting when not all rejected
591     fe_lines=fe_lines(chosen_fe)
592     fe_gofts=fe_gofts(*, chosen_fe)
593     fe_measured=fe_measured(chosen_fe)
594     fe_measured_errors=fe_measured_errors(chosen_fe)
595    endif else begin
596     print, 'All iron lines rejected. Aborting calculations.'
597     return
598    endelse
599
600    select_c=intarr(n_c)
601    input=''
602    for m=0, n_c-1 do begin
603     read, input, prompt='Continuum from '+cut(c_wave(m)-0.5,4)+' to '+cut(c_wave(m)+0.5,4)
       +' Angstrom : '
604     if input ne 'n' then select_c(m)=1
605    endfor
606    chosen_c=where(select_c eq 1, n_c)
607    if n_c gt 0 then begin
608     continuumdata=continuumdata(chosen_c)
609    endif else begin
610     print, 'All continuum intervals rejected. Aborting calculations.'
611     return
612    endelse
613   endif
614
615   print, '-------------------------'
616   print, 'Start fitting the iron lines'
617
618   fe_coefficients=replicate({p:dblarr(order+1),fe_abund:dblarr(1),theoretical:dblarr(
      n_ratios),theoretical_c:dblarr(n_c)},order-startorder+1)
619  ;defining this as a structure makes it easier to overwrite the array with a smaller one
620   for j=startorder, order do begin
621    if j eq startorder then begin
622     print, 'Start initial fit with order=', strcompress(string(startorder), /remove_all)
623     p_fe=dblarr(startorder+2);
624     p_fe(0)=1.    ;set initial iron abundance to 1
625     p_fe(1)=45.
626    endif else begin
627     print, 'Fitting order=', strcompress(string(j), /remove_all)
628     p_fe=[p_fe, 0]
629    endelse
630    xi=dblarr(j+2, j+2)
631    for i=0, j+1 do xi(i, i)=1.
```

```
632     powell, p_fe, xi, 1.e-8, chi_min_fe, 'chi_square_fe', /double, itmax=500
633     fe_coefficients(j-startorder).p=p_fe(1:j+1)
634     fe_coefficients(j-startorder).fe_abund=p_fe(0)
635     fe_coefficients(j-startorder).theoretical=predict_ratios(t,gofts, p_fe(1:j+1),t_shift)
636     fe_coefficients(j-startorder).theoretical_c=theoflux(c_t,c_gofts, p_fe(1:j+1),distance
        , t_shift)
637     if j eq startorder then red_chi_fe=chi_min_fe/(n_fe+n_c-startorder-2) else red_chi_fe=[
        red_chi_fe, chi_min_fe/(n_fe+n_c-j-2)]
638     ;degrees of freedom: ratios+continuum-(order of polynomial+1)-1 (<- fe_abund)
639    endfor
640    fe_abund=p_fe(0)
641    a_fe=p_fe(1:order+1)
642
643   endif
644
645   ;------ output of the fit results
646   print, '-------------------------'
647   print, 'Fit results from H-like / He-like ratios:'
648   ;calculate size of output...
649   n_columns=strcompress(string(order-startorder+1), /remove_all)
650   print, format='("      ratio", t24, "measured", t39, "predicted")'
651   for i=0, n_ratios-1 do print, format='(A,t19,f7.3," +/- ",f5.3, '+n_columns+'(4x,f6.3))'
      , ratiodata(i).ratio, measured(i), measured_errors(i), coefficients.theoretical(i)
652   print, '-------------------------'
653   print, 'Normalization and continuum flux from H-like / He-like ratios:'
654   print, format='("wavelength", t21, "measured", t45, "predicted")'
655   for i=0, n_c-1 do print, format='(t4,f4.1,t12,f6.3," +/- ", f5.3,'+n_columns+'(5x,f6.3))'
      , c_wave(i), continuumdata(i).flux/1e-4, continuumdata(i).fluxerror/1e-4, coefficients.
      theoretical_c(i)/1e-4
656
657   if keyword_set(fefit) then begin
658    print, '-------------------------'
659    print, 'Fit results from iron lines:'
660    print, format='("      ratio", t24, "measured", t39, "predicted")'
661    for i=0, n_ratios-1 do print, format='(A,t19,f7.3," +/- ", f5.3,'+n_columns+'(4x,f6.3))'
       , ratiodata(i).ratio, measured(i), measured_errors(i), fe_coefficients.theoretical(i)
662    print, '-------------------------'
663    print, 'Normalization and continuum flux from iron lines:'
664    print, format='("wavelength", t21, "measured", t45, "predicted")'
665    for i=0, n_c-1 do print, format='(t4, f4.1, t12, f6.3, " +/- ", f5.3, '+n_columns+'(5x,
       f6.3))', c_wave(i), continuumdata(i).flux/1e-4, continuumdata(i).fluxerror/1e-4,
       fe_coefficients.theoretical_c(i)/1e-4
666   endif
667
668   dem_max=max(poly(temp_interp<7.5>6.-t_shift, coefficients(n_columns-1).p))
669   ;doing the <7.5 >6 stuff to find a local maximum...
670   for j=0, n_columns-1 do begin
671    if keyword_set(psplot) then begin
672     device, filename=name+'_DEM'+strcompress(string(startorder+j), /remove_all)+'.ps', /
        color
673     plot, temp_interp, poly(t,coefficients(j).p), yrange=[dem_max-3.5,dem_max+0.5], xrange
        =[5.5,8.], xtitle='log T [ K ]', ytitle='log DEM [ cm!U-3!N K!U-1!N ]', /xstyle, /
        ystyle, title=starname+': diffential emission measure distribution'
674   ;  label_line, 5.6, 5.8, dem_max+0.25, 'ratio H-like / He-like red. !4v!3!U2!N:'+cut(
      red_chi(0), 4)
675     if keyword_set(fefit) then oplot, temp_interp, poly(t, fe_coefficients(j).p), color=8
676   ;  if keyword_set(fefit) then label_line, 5.6, 5.8, dem_max+0.1, 'iron lines red. !4v!3!
      U2!N: '+cut(red_chi_fe(j), 4), color=8
677     device, /close
678    endif else begin
679     window, 2
680     wset, 2
681     plot, temp_interp, poly(t, coefficients(j).p), xrange=[6.,8.], yrange=[dem_max-3.5,
        dem_max+0.5], xtitle='log T [ K ]', ytitle='log DEM [ cm!U-3!N K!U-1!N ]', /xstyle, /
        ystyle, title=starname+': diffential emission measure distribution'
682   ;label_line,5.6,5.8, dem_max-0.25, 'ratio H-like / He-like red. !4v!3!U2!N:'+cut(red_chi
      (0),4)
683     if keyword_set(fefit) then oplot, temp_interp, poly(t, fe_coefficients(j).p), color=8
684   ;if keyword_set(fefit) then label_line,5.6,5.8,dem_max+0.1, 'iron lines red. !4v!3!U2!N
      :'+cut(red_chi_fe(j),4), color=8
685    endelse
```

```
686 endfor
687
688 print, '-------------------------'
689 print, 'Goodness of ratio fit: ', red_chi
690 if keyword_set(fefit) then print, 'Goodness of iron line fit: ', red_chi_fe
691
692 ;--------- abundance calculations
693
694 ;--------- absolute abundance for each line
695 print, '-------------------------'
696 print, 'Line fluxes and abundances from H-like / He-like ratios:'
697 elements=['C', 'N', 'O', 'Ne', 'Mg', 'Al', 'Si', 'S', 'Ar', 'Ca', 'Fe']
698 elements_iz=[6, 7, 8, 10, 12, 13, 14, 16, 18, 20, 26]
699
700 abundance_line=dblarr(n_lines, 2, n_columns)
701 print, format='("line", t8, "wavelength", t23, "abundance")'
702 for i=0, n_lines-1 do begin
703  ion2spectroscopic, linedata(i).line, label
704  for j=0, n_columns-1 do begin
705   abundance_line(i, 0, j)=linedata(i).flux/theoflux(t, linedata(i).goft_interp,
     coefficients(j).p, distance, t_shift, /line)
706   abundance_line(i, 1, j)=linedata(i).fluxerror/theoflux(t, linedata(i).goft_interp,
     coefficients(j).p, distance, t_shift, /line)
707  endfor
708  print, format='(A,t10,A,t20,'+n_columns+'(f6.3," +/- ", f5.3, 4x))', label, cut(
     wavelengthlist(where(linedata(i).line eq linelist)),6), abundance_line(i, *, *)
709 endfor
710
711 ;--------- absolute abundance per element
712 print, '-------------------------'
713 print, 'Abundances from H-like / He-like ratios per element:'
714 print, format='("element", t13, "abundance")'
715
716 abundance_element=dblarr(n_elements(elements), 2, n_columns)
717 abund_line=dblarr(n_lines, 2, n_columns)          ; this is a dummy with the same size as
    linedata for the new em loci plot
718 for i=0, n_elements(elements)-1 do begin
719  cmp=where(linedata.iz eq elements_iz(i))
720  if cmp(0) ge 0 then begin
721   for k=0, n_columns-1 do begin
722    if elements_iz(i) eq 26 then begin    ;special treatment for iron
723     if keyword_set(fefit) then begin     ;if fe_fit set and not all Fe lines chosen for
        the fit
724      cmp_good=intarr(n_fe)               ;take only those into account that are were
        chosen
725      for j=0, n_fe-1 do cmp_good(j)=where(fe_lines(j) eq linedata.line)
726     endif else cmp_good=cmp
727    endif else cmp_good=cmp
728 ;use only the good iron lines for the mean abundance
729    err_weight_average, abundance_line(cmp_good, 0, k), abundance_line(cmp_good, 1, k),
     abund, abund_err
730    abundance_element(i, 0, k)=abund
731    abundance_element(i, 1, k)=abund_err
732    abund_line(cmp, *, k)=[[replicate(abund, n_elements(cmp))], [replicate(abund_err,
     n_elements(cmp))]]
733   endfor
734   print, format='(A, t10, '+n_columns+'(f6.3," +/- ", f5.3, 4x))', elements(i),
     abundance_element(i, *, *)
735  endif
736 endfor
737
738 ;--------- abundances relative to oxygen
739 if abundance_element(2, 0, 0) ne 0 then begin
740 ;security check: the unlikely case that no oxygen lines were measured
741  relative=where(elements ne 'O')
742  other_elements=elements(relative)
743  other_abundance=abundance_element(relative,*,*)
744  relative_abundance=dblarr(n_elements(other_elements), 2, n_columns)
745  for i=0, n_columns-1 do begin
746   relative_abundance(*,0,i)=other_abundance(*,0,i)/abundance_element(2,0,i)
747   relative_abundance(*,1,i)=sqrt(other_abundance(*,1,i)^2+(abundance_element(2,1,i)^2)*(
```

```
      relative_abundance(*,0,i)^2))/abundance_element(2, 0, i)
748   endfor
749   print, '-------------------------'
750   print, 'Abundances from H-like / He-like ratios relative to oxygen:'
751   print, format='("element", t11, "abundance ratio")'
752   for i=0, n_elements(other_elements)-1 do if relative_abundance(i) gt 0. then print,
      format='(A, " / O", t10, '+n_columns+'(f6.3, " +/- ", f5.3, 4x))', other_elements(i),
      relative_abundance(i, *, *)
753  endif
754
755  ;----------doing the same if fefit present
756  if keyword_set(fefit) then begin
757   print, '-------------------------'
758   print, 'Line fluxes and abundances from iron lines:'
759   fe_abundance_line=dblarr(n_lines, 2, n_columns)
760   print, format='("line", t8, "wavelength", t23, "abundance")'
761   for i=0, n_lines-1 do begin
762    for j=0, n_columns-1 do begin
763     ion2spectroscopic, linedata(i).line, label
764     fe_abundance_line(i, 0, j)=linedata(i).flux/theoflux(t, linedata(i).goft_interp,
      fe_coefficients(j).p, distance, t_shift, /line)
765     fe_abundance_line(i, 1, j)=linedata(i).fluxerror/theoflux(t, linedata(i).goft_interp,
      fe_coefficients(j).p, distance, t_shift, /line)
766    endfor
767    print, format='(A,t10,A,t20,'+n_columns+'(f6.3," +/- ",f5.3,4x))', label, cut(
      wavelengthlist(where(linedata(i).line eq linelist)),6), fe_abundance_line(i, *, *)
768   endfor
769  ;---------- absolute abundance per element
770   print, '-------------------------'
771   print, 'Abundances from iron lines per element:'
772   print, format='("element", t13, "abundance")'
773   fe_abundance_element=dblarr(n_elements(elements), 2, n_columns)
774   fe_abund_line=dblarr(n_lines, 2, n_columns)
775   for i=0, n_elements(elements)-1 do begin
776    cmp=where(linedata.iz eq elements_iz(i))
777    if cmp(0) ge 0 then begin
778     for k=0, n_columns-1 do begin
779      if elements_iz(i) eq 26 then begin  ;the new determination of the iron abundance
       would not be
780       if keyword_set(fefit) then begin   ;necessary if there was not the error...
781        cmp_good=intarr(n_fe)
782        for j=0, n_fe-1 do cmp_good(j)=where(fe_lines(j) eq linedata.line)
783       endif else cmp_good=cmp
784      endif else cmp_good=cmp
785      err_weight_average, fe_abundance_line(cmp_good,0,k), fe_abundance_line(cmp_good,1,k)
       , abund, abund_err
786      fe_abundance_element(i, 0, k)=abund ;value is identical to fe_coefficients.fe_abund
787      fe_abundance_element(i, 1, k)=abund_err
788      fe_abund_line(cmp, *, k)=[[replicate(abund, n_elements(cmp))], [replicate(abund_err,
       n_elements(cmp))]]
789     endfor
790     print, format='(A, t10, '+n_columns+'(f6.3, " +/- ", f5.3, 4x))', elements(i),
      fe_abundance_element(i, *, *)
791    endif
792   endfor
793  ;---------- abundances relative to oxygen
794   if fe_abundance_element(2,0,0) ne 0 then begin
795    fe_other_abundance=fe_abundance_element(relative,*,*)
796    fe_relative_abundance=dblarr(n_elements(other_elements),2,n_columns)
797    for i=0,n_columns-1 do begin
798     fe_relative_abundance(*,0,i)=fe_other_abundance(*,0,i)/fe_abundance_element(2,0,i)
799     fe_relative_abundance(*,1,i)=sqrt(fe_other_abundance(*,1,i)^2+(fe_abundance_element
      (2,1,i)^2)*(fe_relative_abundance(*,0,i)^2))/fe_abundance_element(2,0,i)
800    endfor
801    print, '-------------------------'
802    print, 'Abundances from iron lines relative to oxygen:'
803    print, format='("element", t11, "abundance ratio")'
804    for i=0, n_elements(other_elements)-1 do if fe_relative_abundance(i) gt 0. then print,
      format='(A, " / O", t10, '+n_columns+'(f6.3, " +/- ", f5.3, 4x))', other_elements(i),
      fe_relative_abundance(i, *, *)
805   endif
```

```
806  endif
807
808  ;------ making the new EM loci plots
809
810  em_m=fltarr(n_lines)
811  for i=0, n_lines-1 do begin
812  em_m(i)=min((linedata(i).log_em-alog10(abund_line(i, 0)))(where(linedata(i).log_em gt 0))
     )
813  endfor
814  em_min=min(em_m)
815  offset=0
816  for i=0, n_lines-1 do begin
817   ion2spectroscopic, linedata(i).line, label
818   case linedata(i).iz of
819    linedata(i).ion: style=0       ;H-like ions
820    linedata(i).ion+1: style=5     ;He-like ions
821   else: style=((linedata(i).iz-linedata(i).ion) mod 4)+1
822   endcase
823   sel=where(linedata(i).goft_interp gt 0)
824   if i eq 0 then begin
825    if keyword_set(psplot) then begin
826     set_plot, 'ps'
827     device, filename=name+'_EM_korr.ps', /color
828    endif else begin
829     window, 3
830     wset, 3
831    endelse
832    plot, /nodata, temp_interp(sel), linedata(i).log_em(sel)-alog10(abund_line(i,0,
       n_columns-1)), yrange=[em_min-1.5,em_min+3.5], /ystyle, xrange=[5.0,8.0], /xstyle,
       title=starname+': emission measure loci curves', xtitle='log T [ K ]', ytitle='log EM
        [ cm!U-3!N ]'
833   endif
834   if linedata(i).iz ne 26 then begin
835    oplot, temp_interp(sel), linedata(i).log_em(sel)-alog10(abund_line(i, 0, n_columns-1))
       , linestyle=style, color=linedata(i).iz
836    if strmatch(linedata(i).line, '*[a-z]') and strcmp(linedata(i).line, linedata((i-1)>0).
       line, strlen(linedata(i).line)-1)then offset=offset+1 else  label_line, 5.1, 5.3,
       em_min+3.20-0.17*(i-offset), label, color=linedata(i).iz, linestyle=style
837   endif
838  endfor
839  for i=0, n_c-1 do begin
840   oplot, c_temp, continuumdata(i).log_em, color=250
841  endfor
842  if !D.NAME eq 'PS' then begin
843   device, /close
844   set_plot, 'x'
845  endif
846
847  ;-----------------------------------------------
848  if keyword_set(journal) then begin
849   print, coefficients.p
850   if keyword_set(fefit) then print, fe_coefficients.p
851   journal
852  endif
853
854  end
```

Bibliography

Allen, C. W., *Astrophysical quantities*. London: University of London, Athlone Press, —c1973, 3rd ed.

Anders, E. and Grevesse, N., 'Abundances of the elements - Meteoritic and solar'. *Geochim. Cosmochim. Acta* **53**, 197–214, 1989

Argiroffi, C., Drake, J. J., Maggio, A., Peres, G., Sciortino, S., and Harnden, F. R., 'High-Resolution X-Ray Spectroscopy of the Post-T Tauri Star PZ Telescopii'. *ApJ* **609**, 925–934, 2004

Asplund, M., Grevesse, N., and Sauval, A. J., 2005, 'The Solar Chemical Composition'. In: *ASP Conf. Ser. 336: Cosmic Abundances as Records of Stellar Evolution and Nucleosynthesis*. pp. 25–38

Audard, M., Güdel, M., Sres, A., Raassen, A. J. J., and Mewe, R., 'A study of coronal abundances in RS CVn binaries'. *A&A* **398**, 1137–1149, 2003

Brinkman, A. C., Behar, E., Güdel, M., Audard, M., den Boggende, A. J. F., Branduardi-Raymont, G., Cottam, J., Erd, C., den Herder, J. W., Jansen, F., Kaastra, J. S., Kahn, S. M., Mewe, R., Paerels, F. B. S., Peterson, J. R., Rasmussen, A. P., Sakelliou, I., and de Vries, C., 'First light measurements with the XMM-Newton reflection grating spectrometers: Evidence for an inverse first ionisation potential effect and anomalous Ne abundance in the Coronae of HR 1099'. *A&A* **365**, L324–L328, 2001

Burnham, R., *Burnham's Celestial Handbook. An Observers Guide to the Universe Beyond the Solar System*. New York: Dover, 1978, Rev.ed.

Catura, R. C., Acton, L. W., and Johnson, H. M., 'Evidence for X-ray emission from Capella'. *ApJ* **196**, L47–L49, 1975

Chandra X-ray Center, *Chandra* Project Science, and *Chandra* IPI Teams, 'The *Chandra* Proposer's Observatory Guide'. Version 7.0, 2004

Chung, S. M., Drake, J. J., Kashyap, V. L., Lin, L., and Ratzlaff, P. W., 'Doppler Shifts and Broadening and the Structure of the X-Ray Emission from Algol'. *ApJ* **606**, 1184–1195, 2004

Craig, I. J. D., 'The use of a-priori information in the derivation of temperature structures from X-ray spectra'. *A&A* **61**, 575–590, 1977

Craig, I. J. D. and Brown, J. C., 'Fundamental limitations of X-ray spectra as diagnostics of plasma temperature structure'. *A&A* **49**, 239–250, 1976

Del Zanna, G., 'CHIANTI – User Guide'. Version 5.0, 2005

Del Zanna, G., Landini, M., and Mason, H. E., 'Spectroscopic diagnostics of stellar transition regions and coronae in the XUV: AU Mic in quiescence'. *A&A* **385**, 968–985, 2002

Dere, K. P., Landi, E., Mason, H. E., Monsignori Fossi, B. C., and Young, P. R., 'CHIANTI - an atomic database for emission lines'. *A&AS* **125**, 149–173, 1997

Dere, K. P., Landi, E., Young, P. R., and Del Zanna, G., 'CHIANTI-An Atomic Database for Emission Lines. IV. Extension to X-Ray Wavelengths'. *ApJS* **134**, 331–354, 2001

Desai, P., Brickhouse, N. S., Drake, J. J., Dupree, A. K., Edgar, R. J., Hoogerwerf, R., Kashyap, V., Wargelin, B. J., Smith, R. K., Huenemoerder, D. P., and Liedahl, D. A., 'An Assessment of the Fe XVIII and Fe XIX Line Ratios from the Chandra Grating Observations of Capella'. *ApJ* **625**, L59–L62, 2005

Drake, J. J., 'From the Heart of the Ghoul: C and N Abundances in the Corona of Algol B'. *ApJ* **594**, 496–509, 2003

Drake, J. J., Brickhouse, N. S., Kashyap, V., Laming, J. M., Huenemoerder, D. P., Smith, R., and Wargelin, B. J., 'Enhanced Noble Gases in the Coronae of Active Stars'. *ApJ* **548**, L81–L85, 2001

Drake, J. J., Kashyap, V., and Lin, L., 'The PUB – PINTofALE Users' Book'. Version 2.0, 2004

Drake, J. J. and Testa, P., 'The 'solar model problem' solved by the abundance of neon in nearby stars'. *Nature* **436**, 525–528, 2005

Edlén, B., 'Die Deutung der Emissionslinien im Spektrum der Sonnenkorona. Mit 6 Abbildungen.'. *Zeitschrift für Astrophysik* **22**, 30–64, 1943

Ehle, M., Breitfellner, M., González Riestra, R., Guainazzi, M., Loiseau, N., Rodríguez, P., Santos-Lleó, M., Schartel, N., Tomás, L., Verdugo, E., and Dahlem, M., '*XMM-Newton* Users' Handbook'. Issue 2.3, 2005

Favata, F. and Micela, G., 'Stellar Coronal Astronomy'. *Space Sci. Rev.* **108**, 577–708, 2003

Favata, F., Micela, G., Reale, F., Sciortino, S., and Schmitt, J. H. M. M., 'The structure of Algol's corona: a consistent scenario for the X-ray and radio emission'. *A&A* **362**, 628–634, 2000

Favata, F. and Schmitt, J. H. M. M., 'Spectroscopic analysis of a super-hot giant flare observed on Algol by BeppoSAX on 30 August 1997'. *A&A* **350**, 900–916, 1999

Feldman, U. and Laming, J. M., 'Element Abundances in the Upper Atmospheres of the Sun and Stars: Update of Observational Results'. *Phys. Scr* **61**, 222–252, 2000

Güdel, M., 'X-ray astronomy of stellar coronae'. *A&A Rev.* **12**, 71–237, 2004

Güdel, M., Guinan, E. F., and Skinner, S. L., 'The X-Ray Sun in Time: A Study of the Long-Term Evolution of Coronae of Solar-Type Stars'. *ApJ* **483**, 947–960, 1997

Gabriel, A. H. and Jordan, C., 'Interpretation of solar helium-like ion line intensities'. *MNRAS* **145**, 241–248, 1969

García-Alvarez, D., Drake, J. J., Lin, L., Kashyap, V. L., and Ball, B., 'The Coronae of AB Doradus and V471 Tauri: Primordial Angular Momentum versus Tidal Spin-up'. *ApJ* **621**, 1009–1022, 2005

Golub, L. and Pasachoff, J. M., *The Solar Corona*. Cambridge University Press, ISBN 0521480825, 1997.

Grevesse, N. and Sauval, A. J., 'Standard Solar Composition'. *Space Science Reviews* **85**, 161–174, 1998

Grotian, W., 'Zur Frage der Deutung der Linien im Spektrum der Sonnenkorona'. *Naturwissenschaften* **27**, 214, 1939

Gu, M. F., 'Indirect X-Ray Line-Formation Processes in Iron L-Shell Ions'. *ApJ* **582**, 1241–1250, 2003

Güdel, M., Audard, M., Briggs, K., Haberl, F., Magee, H., Maggio, A., Mewe, R., Pallavicini, R., and Pye, J., 'The XMM-Newton view of stellar coronae: X-ray spectroscopy of the corona of AB Doradus'. *A&A* **365**, L336–L343, 2001

Hussain, G. A. J., Brickhouse, N. S., Dupree, A. K., Jardine, M. M., van Ballegooijen, A. A., Hoogerwerf, R., Collier Cameron, A., Donati, J.-F., and Favata, F., 'Inferring Coronal Structure from X-Ray Light Curves and Doppler Shifts: A Chandra Study of AB Doradus'. *ApJ* **621**, 999–1008, 2005

Kalas, P., Liu, M. C., and Matthews, B. C., 'Discovery of a Large Dust Disk Around the Nearby Star AU Microscopii'. *Science* **303**, 1990–1992, 2004

Kashyap, V. and Drake, J. J., 'Markov-Chain Monte Carlo Reconstruction of Emission Measure Distributions: Application to Solar Extreme-Ultraviolet Spectra'. *ApJ* **503**, 450–466, 1998

Kashyap, V. and Drake, J. J., 'PINTofALE : Package for the interactive analysis of line emission'. *Bulletin of the Astronomical Society of India* **28**, 475–476, 2000

Krist, J. E., Ardila, D. R., Golimowski, D. A., Clampin, M., Ford, H. C., Illingworth, G. D., Hartig, G. F., Bartko, F., Benítez, N., Blakeslee, J. P., Bouwens, R. J., Bradley, L. D., Broadhurst, T. J., Brown, R. A., Burrows, C. J., Cheng, E. S., Cross, N. J. G., Demarco, R., Feldman, P. D., Franx, M., Goto, T., Gronwall, C., Holden, B., Homeier, N., Infante, L., Kimble, R. A., Lesser, M. P., Martel, A. R., Mei, S., Menanteau, F., Meurer, G. R., Miley, G. K., Motta, V., Postman, M., Rosati, P., Sirianni, M., Sparks, W. B., Tran, H. D., Tsvetanov, Z. I., White, R. L., and Zheng, W., 'Hubble Space Telescope Advanced Camera for Surveys Coronagraphic Imaging of the AU Microscopii Debris Disk'. *AJ* **129**, 1008–1017, 2005

Laming, J. M., 'A Unified Picture of the First Ionization Potential and Inverse First Ionization Potential Effects'. *ApJ* **614**, 1063–1072, 2004

Landi, E., Del Zanna, G., Young, P. R., Dere, K. P., Mason, H. E., and Landini, M., 'CHIANTI - An Atomic Database for Emission Lines. VII. New data for X-Rays and Other Improvements'. *accepted by ApJS*, 2005

Linsky, J. L., Ayres, T. R., Brown, A., and Osten, R. A., 'Comparison of the spectrum of a sunspot-like star with a sunspot'. *Astronomische Nachrichten* **323**, 321–324, 2002

Love, J., 'Reversals and excursions of the geodynamo'. *Astronomy and Geophysics* **40**, 14, 1999

Mason, H. E. and Fossi, B. C. M., 'Spectroscopic diagnostics in the VUV for solar and stellar plasmas'. *A&A Rev.* **6**, 123–179, 1994

Matranga, M., Mathioudakis, M., Kay, H. R. M., and Keenan, F. P., 'Flare X-Ray Observations of AB Doradus: Evidence of Stellar Coronal Opacity'. *ApJ* **621**, L125–L128, 2005

Mazzotta, P., Mazzitelli, G., Colafrancesco, S., and Vittorio, N., 'Ionization balance for optically thin plasmas: Rate coefficients for all atoms and ions of the elements H to NI'. *A&AS* **133**, 403–409, 1998

McIntosh, S. W., 'On the Inference of Differential Emission Measures Using Diagnostic Line Ratios'. *ApJ* **533**, 1043–1052, 2000

Mewe, R., Gronenschild, E. H. B. M., Heise, J., Brinkman, A. C., Dijkstra, J. H., Westergaard, N. J., Schnopper, H. W., Seward, F. D., Chlebowski, T., and Kuin, N. P. M., 'X-ray spectrum of Capella and its relation to coronal structure and ultraviolet emission'. *ApJ* **260**, 233–239, 1982

Ness, J., Brickhouse, N. S., Drake, J. J., and Huenemoerder, D. P., 'Modeling the Ne IX Triplet Spectral Region of Capella with the Chandra and XMM-Newton Gratings'. *ApJ* **598**, 1277–1289, 2003a

Ness, J.-U., Audard, M., Schmitt, J. H. M. M., and Güdel, M., 'Coronal densities and temperatures for cool stars in different stages of activity'. *Advances in Space Research* **32**, 937–943, 2003b

Ness, J.-U., Güdel, M., Schmitt, J. H. M. M., Audard, M., and Telleschi, A., 'On the sizes of stellar X-ray coronae'. *A&A* **427**, 667–683, 2004

Ness, J.-U., Mewe, R., Schmitt, J. H. M. M., Raassen, A. J. J., Porquet, D., Kaastra, J. S., van der Meer, R. L. J., Burwitz, V., and Predehl, P., 'Helium-like triplet density diagnostics. Applications to CHANDRA-LETGS X-ray observations of Capella and Procyon'. *A&A* **367**, 282–296, 2001

Ness, J.-U., Schmitt, J. H. M. M., Audard, M., Güdel, M., and Mewe, R., 'Are stellar coronae optically thin in X-rays?. A systematic investigation of opacity effects'. *A&A* **407**, 347–358, 2003c

Ness, J.-U., Schmitt, J. H. M. M., Burwitz, V., Mewe, R., and Predehl, P., 'Chandra LETGS observation of the active binary Algol'. *A&A* **387**, 1032–1046, 2002a

Ness, J.-U., Schmitt, J. H. M. M., Burwitz, V., Mewe, R., Raassen, A. J. J., van der Meer, R. L. J., Predehl, P., and Brinkman, A. C., 'Coronal density diagnostics with Helium-like triplets: CHANDRA-LETGS observations of Algol, Capella, Procyon, epsilon Eri, alpha Cen A & B, UX Ari, AD Leo, YY Gem, and HR 1099'. *A&A* **394**, 911–926, 2002b

Ness, J.-U. and Wichmann, R., 'CORA - emission line fitting with Maximum Likelihood'. *Astronomische Nachrichten* **323**, 129–134, 2002

Pagano, I., Linsky, J. L., Carkner, L., Robinson, R. D., Woodgate, B., and Timothy, G., 'HST/STIS Echelle Spectra of the dM1e Star AU Microscopii Outside of Flares'. *ApJ* **532**, 497–513, 2000

Pallavicini, R., Golub, L., Rosner, R., Vaiana, G. S., Ayres, T., and Linsky, J. L., 'Relations among stellar X-ray emission observed from Einstein, stellar rotation and bolometric luminosity'. *ApJ* **248**, 279–290, 1981

Perryman, M. A. C. and ESA, *The HIPPARCOS and TYCHO catalogues. Astrometric and photometric star catalogues derived from the ESA HIPPARCOS Space Astrometry Mission.* Noordwijk, Netherlands: ESA Publications Division, 1997, Series: ESA SP Series vol no: 1200, ISBN 9290923997

Pottasch, S. R., 'The Lower Solar Corona: Interpretation of the Ultraviolet Spectrum.'. *ApJ* **137**, 945–966, 1963

Pottasch, S. R., 'On the chemical composition of the solar corona'. *MNRAS* **128**, 73–92, 1964a

Pottasch, S. R., 'On the Interpretation of the Solar Ultraviolet Emission Line Spectrum'. *Space Science Reviews* **3**, 816–855, 1964b

Press, W. H., Teukolsky, S. A., Vetterling, W. T., and Flannery, B. P., *Numerical recipes in C. The art of scientific computing*. Cambridge University Press, 1992, 2nd ed.

Raassen, A. J. J., Mewe, R., Audard, M., Güdel, M., Behar, E., Kaastra, J. S., van der Meer, R. L. J., Foley, C. R., and Ness, J.-U., 'High-resolution X-ray spectroscopy of Procyon by Chandra and XMM-Newton'. *A&A* **389**, 228–238, 2002

Raassen, A. J. J., Ness, J.-U., Mewe, R., van der Meer, R. L. J., Burwitz, V., and Kaastra, J. S., 'Chandra-LETGS X-ray observation of α Centauri: A nearby (G2V + K1V) binary system'. *A&A* **400**, 671–678, 2003

Ribas, I., Guinan, E. F., Güdel, M., and Audard, M., 'Evolution of the Solar Activity over Time and Effects on Planetary Atmospheres. I. High-Energy Irradiances (1-1700 Å)'. *ApJ* **622**, 680–694, 2005

Rosner, R., Tucker, W. H., and Vaiana, G. S., 'Dynamics of the quiescent solar corona'. *ApJ* **220**, 643–645, 1978

Sanz-Forcada, J., Brickhouse, N. S., and Dupree, A. K., 'Quiescent and Flaring Structure in RS Canum Venaticorum Stars'. *ApJ* **570**, 799–819, 2002

Sanz-Forcada, J., Favata, F., and Micela, G., 'Coronal versus photospheric abundances of stars with different activity levels'. *A&A* **416**, 281–290, 2004

Sanz-Forcada, J., Maggio, A., and Micela, G., 'Three years in the coronal life of AB Dor. I. Plasma emission measure distributions and abundances at different activity levels'. *A&A* **408**, 1087–1102, 2003

Schmitt, J. H. M. M., 'Coronae on solar-like stars.'. *A&A* **318**, 215–230, 1997

Schmitt, J. H. M. M. and Favata, F., 'Continuous heating of a giant X-ray flare on Algol.'. *Nature* **401**, 44–46, 1999

Schmitt, J. H. M. M. and Liefke, C., 'NEXXUS: A comprehensive ROSAT survey of coronal X-ray emission among nearby solar-like stars'. *A&A* **417**, 651–665, 2004

Schmitt, J. H. M. M. and Ness, J.-U., 'Carbon and nitrogen abundances in the coronae of Algol B and other evolved stars: Evidence for CNO-cycle processed material'. *A&A* **388**, L13–L16, 2002

Schmitt, J. H. M. M. and Ness, J.-U., 'Coronal abundances from high-resolution X-ray data: The case of Algol'. *A&A* **415**, 1099–1112, 2004

Schmitt, J. H. M. M., Ness, J.-U., and Franco, G., 'A spatially resolved limb flare on Algol B observed with XMM-Newton'. *A&A* **412**, 849–855, 2003

Schwabe, S. H., 'Sonnenbeobachtungen im Jahre 1843. Von Herrn Hofrath Schwabe in Dessau'. *Astronomische Nachrichten* **21**, 233–234, 1844

Smith, K., Güdel, M., and Audard, M., 'Flares observed with XMM-Newton and the VLA'. *A&A* **436**, 241–251, 2005

Telleschi, A., Güdel, M., Briggs, K., Audard, M., Ness, J., and Skinner, S. L., 'Coronal Evolution of the Sun in Time: High-Resolution X-Ray Spectroscopy of Solar Analogs with Different Ages'. *ApJ* **622**, 653–679, 2005

Testa, P., Drake, J. J., and Peres, G., 'The Density of Coronal Plasma in Active Stellar Coronae'. *ApJ* **617**, 508–530, 2004

Vaiana, G. S., Cassinelli, J. P., Fabbiano, G., Giacconi, R., Golub, L., Gorenstein, P., Haisch, B. M., Harnden, F. R., Johnson, H. M., Linsky, J. L., Maxson, C. W., Mewe, R., Rosner, R., Seward, F., Topka, K., and Zwaan, C., 'Results from an extensive Einstein stellar survey'. *ApJ* **245**, 163–182, 1981

Vedder, P. W. and Canizares, C. R., 'Measurement of coronal X-ray emission lines from Capella'. *ApJ* **270**, 666–670, 1983

Whitehouse, D. R., *The sun. A biography*. Wiley, 2005, ISBN 0-470-09296-3

Wood, B. E., Redfield, S., Linsky, J. L., Müller, H.-R., and Zank, G. P., 'Stellar Lyα Emission Lines in the Hubble Space Telescope Archive: Intrinsic Line Fluxes and Absorption from the Heliosphere and Astrospheres'. *ApJS* **159**, 118–140, 2005

Young, P. R., Del Zanna, G., Landi, E., Dere, K. P., Mason, H. E., and Landini, M., 'CHIANTI-An Atomic Database for Emission Lines. VI. Proton Rates and Other Improvements'. *ApJS* **144**, 135–152, 2003

many thanks to

– Professor Hansen –
für eine Woche mehr Zeit

– Dieter Kasan –
ohne den ich wahrscheinlich nie zur Astrophysik gekommen wäre

– Jürgen H.M.M. Schmitt –
der mich vor mehr als viereinhalb Jahren aus heiterem Himmel gefragt hat, ob ich nicht
an der Hamburger Sternwarte als studentische Hilfskraft anfangen möchte.
Die letzten Jahre wären ansonsten für mich völlig anders verlaufen,
und ich hätte das vergangene Jahr nicht mit diesem ungemein interessanten Thema verbracht.

– dem CHIANTI Team –
dessen Datenbasis und dazugehörige Auswerteroutinen die Grundlage für diese Arbeit bilden

– Birgit Fuhrmeister, Jan Robrade und Jan-Uwe Ness –
meine fleißigen Korrekturleser

– Jan Robrade –
immer hilfsbereiter Zimmergenosse

– Jan-Uwe Ness –
für die ganzen Skripte und Rat und Tat auch aus der Ferne

– Moritz Günther, Christian Schröder, ... der ganzen Arbeitsgruppe zuzüglich Chris Wawrzyn –
für diese unvergleichliche Arbeitsatmosphäre

– Henrika Liefke –
für alles

デニス
愛してる

Erklärung zur Diplomarbeit

Hiermit versichere ich, daß ich die vorliegende Arbeit selbständig und nur unter Verwendung der angegebenen Quellen verfaßt habe. Desweiteren erkläre ich mich mit einer Veröffentlichung der Arbeit einverstanden.

Hamburg, den 30. Oktober 2005